London Centre for Nanotechnology

University College London

University of London

Biophysical properties of the transport barrier in the nuclear pore complex

Aizhan Bestembayeva

Submitted in partial fulfilment of the requirements

For the degree of Doctor of Philosophy

At University College London

February 4, 2016

I declare that the work presented in this thesis is my own. Where information has been obtained from other sources, I declare this has been clearly indicated in this thesis.

Abstract

The Nuclear Pore Complex (NPC) is a large protein structure found in eukaryotic cells, perforating the nuclear envelope. It mediates bidirectional selective transport between the nucleus and the cytoplasm. The NPC contains a permeability barrier consisting of unstructured nuclear pore proteins. The structure of the permeability barrier is not well defined. As a consequence, various models have been proposed for its structure and functionality. Typically, these models consider the unstructured nuclear pore proteins as weakly or strongly interacting polymers: In the first case nuclear pore proteins protrude from the pore creating an entropic barrier; in the second case they may form a meshwork occupying the central channel, resembling a hydrogel.

In this thesis, I measure the nanomechanical properties of this barrier in intact NPCs, and compare them to the properties expected for entropic brushes and gel-like materials. To this end, I carried out nanometre-scale force spectroscopy measurements using Atomic Force Microscopy (AFM). Prior to the measurements the pores were treated with reagents that activated the transport process, thus flushing out the pores to ensure that I was probing the barrier itself instead of cargo stuck in transit. I carried out Laser Scanning Confocal Microscopy experiments to verify this procedure, as well as to measure transport properties of the pores in isolated nuclei.

For comparison, I also measure nanomechanical properties of artificial polymer brushes, and set the first steps towards creating protein-coated solid-state nanopores as a reductionist model system for the NPC. My results indicate that the proteins in the NPC form a condensed network, more closely resembling a hydrogel than a brush dominated by entropic interactions.

Acknowledgments

First of all, I'm very grateful to my supervisor Dr. Bart Hoogenboom from the London Centre for Nanotechnology for being supportive and helpful throughout all four years of my PhD. He initiated my training in Munster Physiology Institute II, where I would like to thank Dr. Ivan Liashkovich and Dr. Armin Kramer, who helped me to gain skills in terms of handling and preparation of the nuclear envelopes.

I'm also grateful to my second supervisor Dr. Ariberto Fassati and to the postdoc in his group Dr. Aksana Labokha from Infection and Immunity division, University College London for advices and informative discussions in designing the experiments.

I would like to thank all the collaborators for support: Dr. Guillaume Charras, London centre for Nanotechnology, Prof. Stewart Murray from MRC Laboratory of Molecular Biology, University of Cambridge, Dr. Joshua Edel from Chemistry Department, Imperial College London, Dr.Julien Gautrot from School of Engineering and Materials Science, Queen Mary University.

I'm extremely grateful to Sofya Mikhaleva and George Stanley for designing the script for analysis of the AFM force data. I also would like to thank my group who have always been supportive and helpful, Carl, Armin, Richard, Alice, Hasan, Dino, George, Sofya, Alex and Adrian.

I would also like to acknowledge the Centre for International programmes "Bolashak" (Astana, Kazakhstan) who assigned me funding and scholarship and gave me this opportunity work in a great team.

Finally, I would like to thank my family who were always caring and supporting me throughout my PhD, my mom and dad, my grandparents Mendesh, Raya, Shymyr ata and my aunt Gulmira. I'm very grateful to all my beloved friends for helping me to go through my course, especially Saad, Akmaral, Gulsim and Zhibek.

Content

List of Figures

List of Tables

List of abbreviations

AFM – atomic force microscope

LSCM – laser scanning confocal microscope

NPC – nuclear pore complex

NE – nuclear envelope

Nup – nucleoporin

FG – phenylalanine-glycine

NLS – nuclear localization sequences

NES – nuclear export sequences

NTR – nuclear transport receptor

PDMAEMA – Poly (2-(dimethylamino) ethyl methacrylate)

MBP - maltose-binding protein

IBB – Importinβ binding domain

WGA – wheat germ agglutinin

CHD – cyclohexanediol

NTF2 – nuclear transport factor 2

PEG – polyethylene glycol

Chapter 1 Introduction into the Nuclear Pore Complex

In eukaryotic cells the nucleus is separated from the cytoplasm by a double membrane, the nuclear envelope (NE) (Figure 1-1 a). The nuclear envelope is formed by an inner and an outer membrane, both consisting of a phospholipid bilayer. In the nucleus, there are nuclear laminas (proteins) attached to the inner membrane of the nuclear envelope to maintain the structure of the nucleus (Figure 1-1 b). The outer membrane continues into endoplasmic reticulum membrane outside the nucleus. On the surface of the endoplasmic reticulum membrane there are small molecular machines – ribosomes – which take part in protein synthesis [1].

The inner and outer membranes of the nuclear envelope connect at the nuclear pore complex. The nuclear pore complex (NPC) is a vital nanometer-scale biological machine that regulates all macromolecular traffic (e.g., messenger RNA) between the nucleus and cytoplasm of all eukaryotic cells. Nucleocytoplasmic transport occurs via the central channel of the NPC (~50 nm in diameter). Furthermore, the NPC participates in the regulation of gene expression. It assists as a quality control check of RNA during its export to cytoplasm. Thus, the NPC not only regulates the molecular traffic between nucleoplasm and cytoplasm, but also separates the DNA transcription process from the cytosol [1].

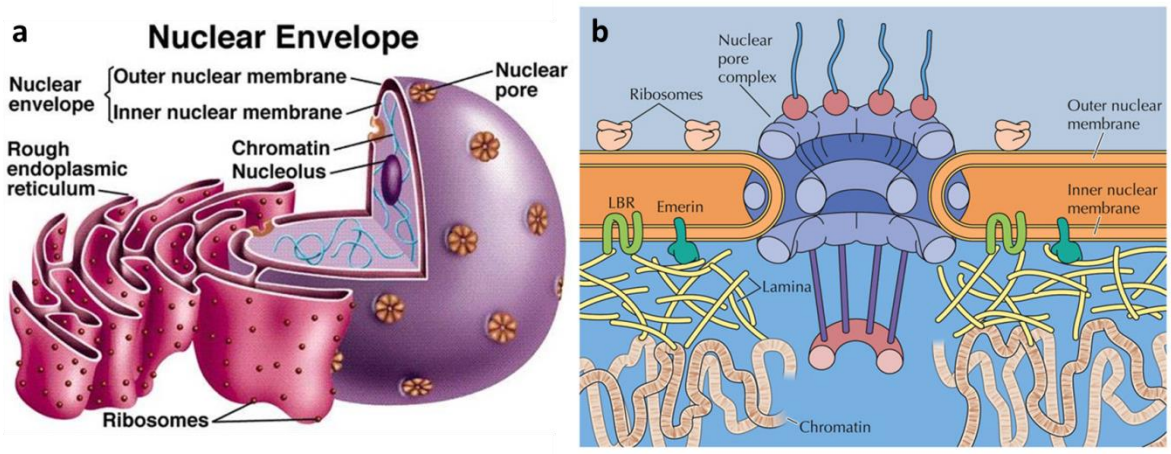

Figure 1-1 a) Illustration of the nucleus separated from the cytoplasm by nuclear envelope which is perorated by nuclear pore complexes. The nucleus is partially surrounded by an endoplasmic reticulum [2]; b) Cross section view of the nuclear envelope and nuclear pore. The outer membrane surface has ribosomes served as

protein synthesis sites; the inner membrane is connected to the lamina which supports the structure of the nucleus [1].

1.1 Background

NPCs of all eukaryotic cells from yeast to human are similar to each other in terms of functionality, biochemical composition and structure. This has been shown using electron microscopy [3], [4], [5], [6]. The examination of the discrete NPC parts supports a theory of conservation of NPC structure among different species [6], [7] (Figure 1-2). NPCs have largely been investigated using different model organisms: human [8], yeast (*Saccharomyces cerevisiae)* [9], African clawed frog (*Xenopus laevis*) [10] and amoeboid (*Dictyostelium discoideum*) [11]. It is important that all types of NPCs possess the analogous structural components for functional NPCs. Although there are some differences in structure, mass and bio-chemical composition between these two, the selectivity mechanism remains the same.

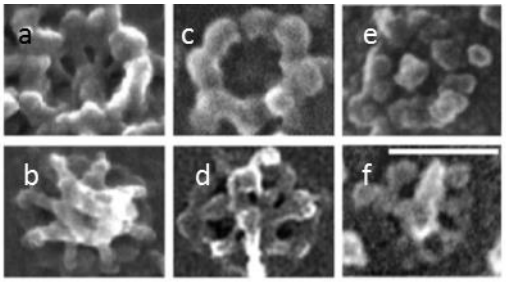

Figure 1-2 Electron microscopy images of NPC derived from (a), (b) Xenopus laevis; (c), (d) Drosophila melanogaster; (e), (f) Saccharomyces cerevisiae. The top row (a), (c), (e) represents the cytoplasmic side, the bottom row (b), (d), (f) – the nucleoplasmic side. The scale bar equals to 100 nm [12].

1.2 Physical characterisation of NPCs

Qualitatively NPCs from different species illustrate a similar architecture. However, quantitatively, there are variations in dimensions and masses from one organism to another. For instance, the yeast cells are generally smaller than the vertebrate ones (50 MDa and 125 MDa respectively) [7]. The dimensions of the human and vertebrate NPCs are similar, except for the outer diameter which is smaller in human NPCs (105 nm). Amoeboid NPCs are slightly larger than human or vertebrate ones in terms of height and inner diameter (see Table 1-1). The nuclear envelope thickness is the largest

in human and amoeboid NPCS (~60 nm), whereas in yeast it is the smallest (20-30 nm). Likewise, yeast NPCs exhibit the smallest height (35 nm) and outer diameter - 80 nm, whereas the rest of the species show around 120 nm for the outer diameter [8]. Interestingly, the inner diameter seems to match among the species ~50-60 nm. In a Table 1-1 below the main parameters are highlighted. The functional diameter, the diameter of the cargoes allowed to pass the NPC, and physical inner diameter of the NPC are most likely coinciding as it was shown elsewhere [9], [10].

Table 1-1 Physical characteristics NPCs across species [8], [10],[17],[18].

	Human	**Vertebrate**	**Yeast**	**Amoeboid**
Height	80 nm	80-100 nm	35 nm	110 nm
Outer Diameter	105 nm	125-150 nm	80 nm	125 nm
Inner diameter	50 nm	48-50 nm	49 nm	60 nm
NE thickness	40 nm	50-60 nm	20-30 nm	60 nm

1.3 General Structure of the NPC

The NPC has a cylindrical shape with an 8-fold rotational symmetry [4], [16]. There are eight spokes which create co-axial rings along the z-axis of the NPC. The spokes are divided into two parts connected at the joint plane of the NPC with NE. The nucleoplasmic filaments form a distal ring and creates the nuclear basket (Figure 1-3 a). At the cytoplasmic side the spokes form short eight filaments. There are two external rings at both the cytoplasmic and the nucleoplasmic sides and two neighbouring inner rings at the luminal domain. In addition to these four rings, which is a core scaffold of NPC, there are also connecting rings between the nuclear envelope and the outer rings – membrane ring; and between outer rings and the inner rings. The rings are built from the nuclear proteins termed nucleoporins (Nups). The nucleoporins from the outer rings are called coat nucleoporins, while the ones that connect coat nucleoporins with the nuclear envelope are called pore membrane proteins (POMs). The inner rings are represented by so-called channel nucleoporins, whilst the connector Nups between the

outer and inner rings are called linkers or adaptor Nups [13], [19]. Within the central channel there is an accumulation of the nucleoporins which contain natively unfolded phenylalanine-glycine repeats (FG-repeats) [20] (Figure 1-3 b). These Nups are connected either to the inner ring or to the linker Nups and facing the central channel. This is the general structure for both vertebrate and yeast NPCs [5], [13].

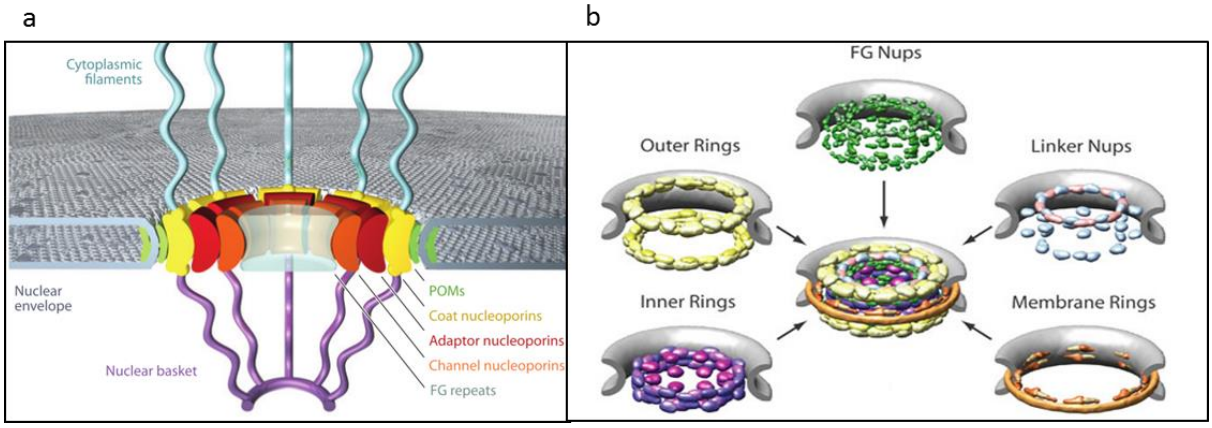

Figure 1-3 a) a schematically illustrated cross section of a vertebrate NPC which consists of the nuclear basket, cytoplasmic filaments and the core scaffold built by a few rings structured from the pore membrane proteins, coat proteins, adaptor Nups, channel Nups and FG Nups [19]. *(b) Visualisation of the Nups distribution within the rings of the pore's scaffold* [13].

1.3.1 Nucleoporins

The NPC contains about 30 different types of proteins, with each one being present in multiple copies. In total the NPC has about 500-1000 protein molecules. The majority of Nups are the same for all eukaryotic cells from yeast to human. Nups are named according to the convention of appending the molecular mass in kDa to the word Nup, e.g. Nup98 corresponds to a mass of 98 kDa. Nearly 30% of all the Nups in the NPC are partially unstructured and possessing FG-repeats [19].

The FG-repeats are classified according to the amino acids separating the repeats, so-called spacer sequences [21]. There are three types of the FG repeats in Nups with different spacers: Gly-Leu-Phe-Gly (GLFG), Phe-any-Phe-Gly (FxFG) and Phe-Gly (FG) repeats. The FxFG-repeats contain charged amino acids as the spacers (threonine and serine) and the FG domains. *In-vitro* experiments have provided evidence for cohesive and presumably weak hydrophobic interactions between these FG domains [22], [23]. . On the other hand, the GLFG-repeats do not have charged elements,

instead enriched with asparagine and glutamine which are polar uncharged amino acids. Overall, GLFG-repeats show non-cohesive interaction between FG domains. As for the FG-repeats, they can have both charged and uncharged spacers. Due to these differences the FG Nups have distinction in functions.

It is known that FG Nups are the crucial components of the permeability barrier which can be formed *in vitro* [24], [25], [26]. It is not only accommodating the passive diffusion of small molecules [27] but also mediating the transport of larger cargoes. The selectivity requires the FG domains to be cohesive along the full length of the FG Nup. If a cohesive FG Nup was removed from the barrier, as it was done in vertebrate NPC lacking specifically cohesive Nup98, the permeability barrier would no longer be functional [28], [29]. A similar experiment was performed with the partially cohesive pNsp1 nucleoporin, which resulted in a breakdown of the selectivity barrier [21]. Moreover, it may be thanks to the cohesiveness of the FG-repeats that some molecular density could be identified in the central channel at a resolution of 2 nm [10], because they appear to contain more ordered domains than typical for the unstructured nucleoporin in the permeability barrier [30].

However, there are some nucleoporins which have non-cohesive FG domains, located primarily at the periphery of the central channel. It was suggested that they are not involved in the structuring of the permeability barrier, but take part in disassembling the import and export molecules from transport receptors required to start the translocation across the pore [31], [32]. For example, the following complex of FG Nups in the cytoplasmic outer ring – vNup88–Nup214–Nup62 (in vertebrates) – is involved in ceasing mRNA export [33].

Another function of non-cohesive FG domains is to blend the exceptionally cohesive FG repeats, to prevent the formation of an impenetrable meshwork, and also preserve the selective functioning of the permeability barrier [25]. For example, some cohesive FG-domains within yeast nucleoporins Nup100 and Nup116 are separated with non-cohesive parts. As it was shown later [23], these types of Nups have a bimodal distribution: the sequence of high changed amino acids (non-cohesive domain) is alternated by low charged amino acids (cohesive domain). This exhibits that even

nucleoporins with highly cohesive FG-domains along their disordered structure have non-cohesive spacers.

Nups can also regulate the selectivity by having the binding sites for transport receptors required to start the translocation across the pore. It has been suggested that cytoplasmic Nup358 serve as a binding site for the transport receptors. When this Nup was depleted, the translocation rate of the transport receptors decreased [34].

1.3.2 Nuclear Transport Receptors

In eukaryotic cells, nucleoplasmic transport of macromolecules is mediated by nuclear transport receptors from the Karyopherin family of proteins, which are conserved across the different species [8], [32]. Macromolecules bind to the karyopherins in order to pass across the barrier. According to the directionality of transport the karyopherins are categorised into importins and exportins. The most abundant import karyopherin is Importinβ. It is structured from 19 HEAT repeats, which in turn is formed by two alpha helices [35] (Figure 1-4 a).

Importinβ binds to cargo from its inner side and with its outer side interacts with FG-repeats in the NPC (Figure 1-4 c) [33], [34]. The binding of Importinβ to the macromolecule occurs via the nuclear localisation signal (NLS), a special sequence of amino acids in macromolecules, or via an adaptor protein Importinα which in turn binds to the macromolecule using the NLS [36]. Importinα consists of 10 armadillo (ARM) repeats of helical shape with two binding sites for NLS [35] (Figure 1-4 b). Importinβ binds to Importinα via importin beta binding domain (IBB) which is a part of Importinα (Figure 1-4 c, d).

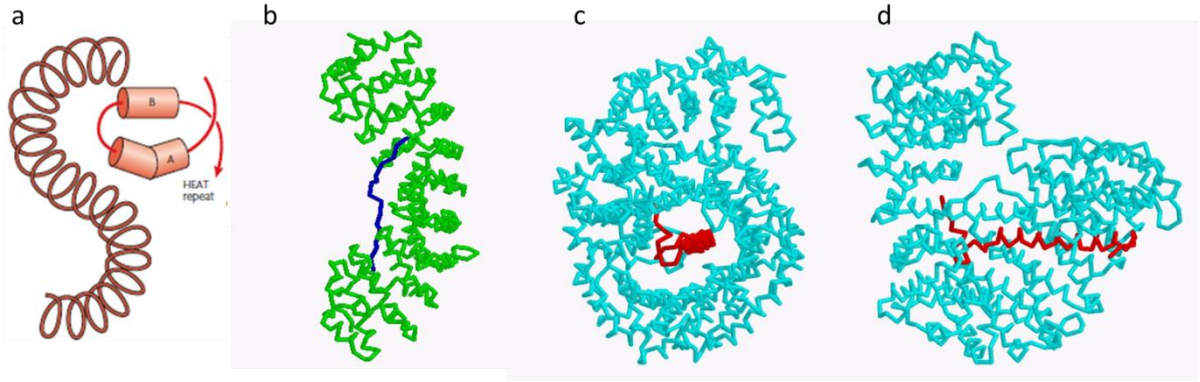

Figure 1-4 a) Structure of Importinβ consisting of 19 HEAT repeats (red helices). Individual HEAT repeat consists of two α-helices. (b) Importinα (green) represents a "banana"- like structure consisting of 19 ARM repeats and interacting with nuclear localisation signal (blue) from the inner side of the curvature. (c) Importinβ conformation upon interaction with IBB (red). (d) Previous image of Importinβ with IBB tilted to 90^{o} to the right [35].

The presence of Importinβ increases the translocation rate significantly, as it was shown elsewhere [24] by observing the penetration of the macromolecule (IBB-RedStar) through the gel of FG Nups in presence and absence of Importinβ. In was found that with Importinβ the translocation rate increased 25 000 times compared to insufficient penetration of IBB-RedStar alone. Also, the cargoes with more nuclear transport receptors (NTR) on its surface translocate the pore faster.

1.4 NPC transport

Nucleocytoplasmic transport is a crucial function of eukaryotic cells. There are two distinguishable types of nucleocytoplasmic transport established: passive and active. Small molecules (smaller than about 5 nm) can be transported through the NPC via passive diffusion [3], [37]. Larger molecules and proteins require additional factors to be translocated through the pore.

1.4.1 Passive diffusion

From studies on the ion conductivity through the NPC it was concluded that there are separate pathways for passive and active transport [38]. In particular, it was suggested that there are eight narrow periphery channels apart from central channel for passive diffusion [39]. But it has also been suggested that the barrier at the central channel is

designed to facilitate both active and passive diffusions [27]. Overall, there is some evidence that two types of transport are carried out via segregated routes [40], [41].

In the mid 70s, it was assumed that the cut off of the molecules size for passive diffusion was about 7 nm in diameter [42]. The experiment showed that dextrans of diameters from 2.4 nm to 7 nm could freely diffuse across the nuclear envelope. This was measured using ultra-low temperature autoradiography. The same value was found later [43]: in this case, PEG coated gold nanoparticles of size 4 – 24 nm in diameter were microinjected into the HeLa cells, which were fixed 5 and 30 minutes after injection and scanned on TEM. It was found that only small PEG particles (4-7 nm) translocated through the pore, however only 0.7% of all small PEG golds were found on the nuclear side of the NPC rather than in the nucleoplasm.

In further studies the diameter proposed was 5.2 nm of the channel for passive diffusion [27]. Authors were monitoring the entry rate of the labelled particles of different sizes (Stokes radii ranging from 0.67 nm to 2.85 nm) imaged on confocal microscope. By using thioredoxin, (Stokes radius 1.97 nm) as a reference particle, they quantified the ratio between the entry rates of these particles and their Stoke radii, and fitted the data with the models for finding the radius of the channel based on the Stokes-Einstein equation and concentration gradient. Most data fitted the model best for a channel of 5.2 nm diameter.

Currently it is accepted that the macromolecules of less than 5 nm in diameter can freely diffuse across the pore. In addition, transport of some small proteins such as Histone H1 and P(Lys)cytochromes is mediated using nuclear transport receptors [44]. It was found by monitoring the passage of receptor mediated large proteins under chilled and energy-depleted conditions using fluorescence microscopy. In particular, it was observed that large proteins were arrested in the nuclear envelope under chilled and energy depleted conditions, and small proteins surprisingly were stuck as well, whereas all other small molecules passively diffused across the nuclear envelope. Thus, after titration of transport factors, it was concluded that these small proteins used nuclear transport receptors (Importinβ and Importin7) to import actively [45]. This facilitated diffusion also applies to the export of tRNA, possibly to facilitate an efficient control of newly made tRNA functionality [46].

1.4.2 Active transport

Active transport is fast, selective and energy-dependent. The flow rate of substances during facilitated transport may reach up to 1000 translocations per second [47]. Cargoes of up to 39 nm can be translocate this way [15], [37]. In active transport, in order for the cargo to go through the nuclear envelope in both directions (to the nucleoplasm or to the cytoplasm) it needs to be recognised by the NPC. The cargo carries transport signals classified as either nuclear localization sequences (NLS) or nuclear export sequences (NES), for import and export respectively. These sequences can bind to transport receptors, the majority of which belongs to the karyopherin family (importin and exportin), which in turn binds to the FG Nups in the NPC.

Apart from transport receptors, presence of Ran is prerequisite for active nuclear transport (Figure 1-6), as it provides the energy to maintain the directionality of transport [48]. Ran encourages the assembly or disassembly of cargo bound to transport factors. Ran is a small nuclear GTPase molecule, which is highly conserved among different species. It freely translocates between the cytoplasm and the nucleoplasm. Ran can switch between two states: Ran GTP (guanine triphosphate) can be converted into Ran GDP (guanine diphosphate) by hydrolysis (Figure 1-5 a) [49]. This Ran cycle is necessary to release the cargo from Importin in the nucleoplasm and release the Importin in the cytoplasm under the hydrolysis.

Ran can switch between two states: Ran GTP (guanine triphosphate) can be converted into Ran GDP (guanine diphosphate) by hydrolysis [41]. Upon altering the state of Ran-bound molecule, there is a dramatic change in the conformation of the key switches I and II (Figure 1-5 a), which control the interaction with nuclear transport receptors [50]. This Ran cycle is necessary to release the cargo from Importin in the nucleoplasm and release the Importin in the cytoplasm under the hydrolysis.

The release of the cargo bound to Importinβ is achieved by changing the conformational state of Importinβ upon interaction with RanGTP (Figure 1-5 b). The induced structural change affects the helicoidal pitch of HEAT repeats in Importinβ. As a result, it no longer matches the helix of IBB domain. Thus, the efficiency of IBB binding to the Importinβ lowers significantly: following the conformational change of Importinβ, it releases the IBB with cargo and binds to RanGTP (Figure 1-5 c) [35].

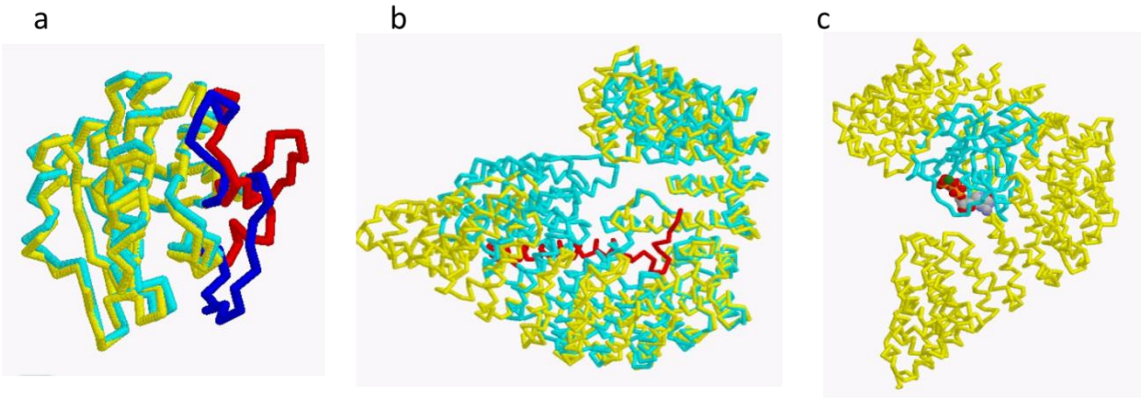

Figure 1-5 (a) RanGTP (cyan) with larger switch I (red) is overlaid with RanGDP (yellow) with smaller switch II (blue) to show the differences in conformation. (b) Conformational changes of Importinβ when it is interacting with IBB (cyan) or RanGTP (yellow). The IBB domain is shown in red. (c) Conformational state of Importinβ (yellow) coiling around RanGTP (cyan, switch I in red) [35]

As depicted in Figure 1-6 there is a host of proteins that regulate the switch between two states of Ran. Ran GTP is hydrolysed to Ran GDP with the help of RanGAP (GTPase-activating protein) and RanBPs (Ran-binding proteins) in the cytoplasm. Meanwhile, in the nucleoplasm, it is RanGEF (guanine-nucleotide exchange factor, RCC1) which contributes to formation of Ran GTP. As a result, RanGTP is dominant in the nucleoplasm, whereas RanGDP is located mainly in the cytosol. Since RanGDP is constantly hydrolysed into RanGTP which then travels into the nucleus, there is a RanGTP gradient across the NE. This Ran compartmentalization guides the directionality of nucleocytoplasmic transport.

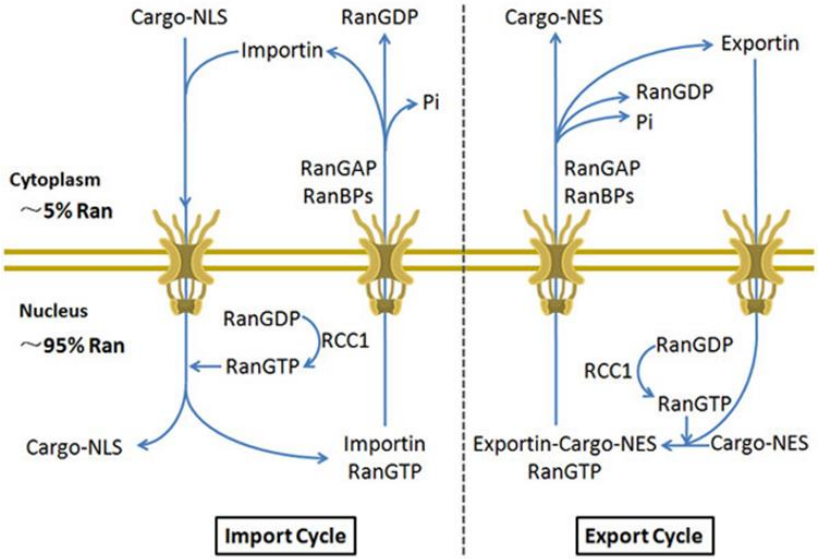

Figure 1-6 Nuclear import and export cycle [51]. *The import cycle starts with creation of a cargo-Importin complex in the cytoplasm. Then the complex interacts with the NPC. After the translocation into the nucleus, the complex interacts with RanGTP and gets released from the cargo. The remaining part (Importin-RanGTP) travels back to the cytoplasm.In the cytoplasm the complex is disassembled by RanGAP which promotes hydrolysis of RanGTP into RanGDP. Here RanBP1 serves as catalysis of the hydrolysis. After the separation another protein RanGAP is able to bind to RanGTP and promotes hydrolysis of RanGTP into RanGDP. The new RanGDP translocates back to the nucleoplasm by binding to a nuclear transport factor. In the nucleus it transforms into RanGTP with the help of a protein RCC1. The export cycle is initiated by the binding of RanGTP to an Exportin–cargo complex in the nucleus. They are then all transported into the cytoplasm where the complex breaks down into independent units by RanBPs. RanGTP again experiences the hydrolysis into RanGDP and travels into the nucleus. In the nucleus it transforms into RanGTP by RCC1 and the cycle starts over. The concentration of Ran in the nucleus is much higher than in the cytoplasm due to the hydrolysis of RanGDP into GTP and transport into the nucleus.*

Cargo import starts with the formation of a cargo-karyopherin complex on the cytoplasmic side (Figure 1-6). The docking sites for the transport receptor attached to the cargo are the areas of large FG-repeats density within FG nucleoporins [13], [52]. On the surface of karyopherins there are multiple sites for FG domain binding [21]. Therefore, the FG nucleoporins act as mediators of molecular traffic through the NPC [13]. Once the interaction between karyopherin and FG domains has been established, the complex passes through the pore. The translocation occurs via reversible binding of the karyopherin to the FG-repeats of the nucleoporins.

The cargo-karyopherin complex decomposes under the interaction of RanGTP on the nucleoplasmic side. Since RanGTP and FG-repeats bind to different sites of Importinβ, RanGTP is thought to release Importins from FG nucleoporins by inducing a conformational change [53]. Thus, the RanGTP-Importin bond breaks the bond between the Importin and the FG-repeat, as well as between the Importin and the cargo. The new RanGTP-Importin complex travels back into the cytoplasm. However, it is not necessary for the transport receptor to interact with Ran since it is able to bind directly to FG Nups [54]. However, it was shown that in presence of Ran, the amount of Importinβ decreases in the pore [55]. It has also been suggested that FG domains change topological position or even breakdown after transport receptor binding. The effect of this on the transport mechanism remains unknown [21], [56].

The export mechanism is similar to import. The cargo, with corresponding export sequences, binds to an exportin, which in turn is bound to Ran-GTP on the nucleoplasmic side. Then the complex passes through the NPC and falls apart on the cytoplasmic side by RanGTP hydrolysis. Ran returns to the nucleus by binding to the nuclear transport factor 2 (NTF2), which has an affinity to RanGDP. It imports the Ran molecule into the nucleoplasm. Due to this reutilizing process, the number of Ran-GDP and Ran-GTP remains large in the cell [51]. However, NTF2 abundance appears to be the limiting factor in active nuclear passage, restricting the maximum capacity of Ran-transport [57].

The cargo translocation time across the pore is quite fast. The transport time of mRNA, for example, is 5-20 ms, excluding the nucleoplasmic docking and cytoplasmic release which takes about 80 ms [7], [58]. The dwell time of transport receptors on the NE was revealed by means of single-molecule microscopy as being 6 - 11 ms [59]. It could be limited to 1 ms if there were more karyopherins in the cycle.

1.5 Transport Models of the permeability barrier

The selectivity barrier resides in the central channel, which is occluded with unstructured and natively unfolded FG-repeats. To explain the selective transport macromolecules (>40 kDa) through the NPC several models have been proposed. They

are based on the studies of structure, functionality and the mechanical properties of the NPC. The main models are described below (Figure 1-7).

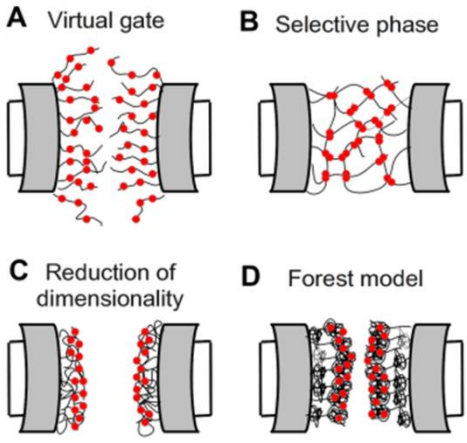

Figure 1-7 Transport models of the permeability barrier. A) Virtual gate (polymer brush) model; B) Selective phase (hydrogel model); C) Reduction of dimensionality; D) Forest model [60].

1.5.1 Virtual gating (Entropic brush)

The virtual gating model suggests that entrances into the central channel and the walls of the channel are decorated with a loose and highly fluctuating brush of FG Nups (Figure 1-7 **Error! Reference source not found.** a). According to this model, the large cargo entering the pore should overcome an entropic barrier created by fluctuating FG-repeats inside the central channel [48], [9]. The entropic barrier can be overcome by the binding of transport receptors to the FG repeats which collapse under this interaction. The energetic gain of the binding can pay the entropic penalty. It has been suggested that a cargo may be translocated along the channel by being in a constant interaction with FG-repeats. On the other hand, the small molecules pass through the brush without affecting the movement of FG Nups. Such brush behaviour was observed by AFM *in vitro* when FG-repeats of Nup153 were tethered to gold nanodots [61], [62]. To mimick the NPC dimensions, the size of the nanodots were about 100 nm in diameter. Moreover, to bring the design of the substrate closer to the NPC, the gold nanorings were introduced [63] (Figure 1-8 a,b). The brush-like conformation of anchored FG-repeats was confirmed by force spectroscopy, which showed an exponential increase of the force upon indentation of the tip (Figure 1-8 c). Furthermore, these experiments shows a “reversible collapse” of the FG-domains upon interaction with Importinβ [62].

However, this behaviour was not found in other experimental setups with different type of FG-repeats [64]. A more detailed description of this type of experiments can be found in section 1.7 of this chapter.

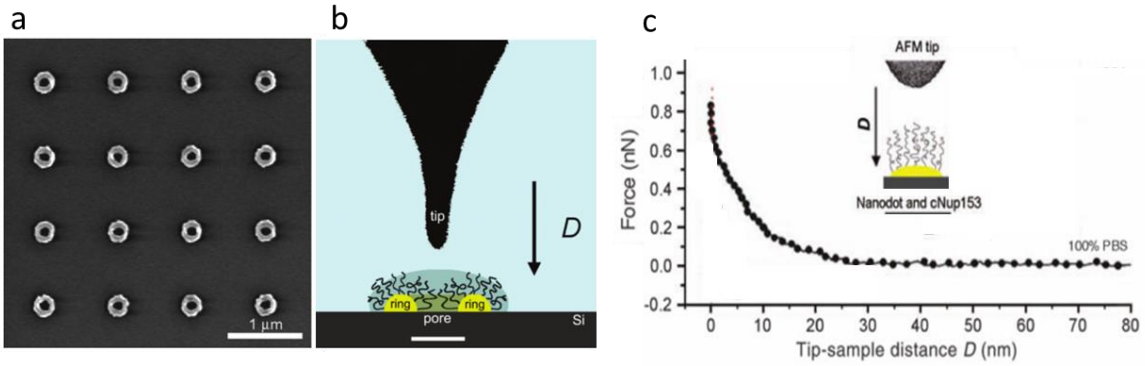

Figure 1-8 a) SEM image of gold nanorings; inner diameter - 87 nm, outer diameter - 213 nm. (b) Illustsration of the AFM tip approaching the polymer brush anchored to the nanoring shown in cross section [63]. *(c) Force curve obtained from the polymer brush formed out of FG-domains of Nup153* [62].

1.5.2 Selective Phase (Hydrogel)

The "selective phase" model describes the NPC channel as a sieve-like meshwork, resulting from cohesive hydrophobic interactions between FG-repeats [37], [65], [66] (Figure 1-7 b).

In this model the FG-repeats extend across the channel and restrict the translocation of molecules larger than the mesh size. Therefore, small molecules pass through the mesh without interacting with FG-repeats, whilst large cargoes may only translocate if the transport receptors dissolve the meshwork. Local dissolution of the meshwork occurs when transport receptors are competing with the weak attractions between the FG-repeats. The formation of new FG-domain – NTR bonds results in low activation energy required to mediate the high flow rate of diffusion (120 MDa per second).

This model is partly based on the observation that FG-domains can form a hydrogel *in vitro*. FG-repeats of Nsp1 were triggered to form a gel when an alkaline solution with FG-repeats was kept at physiological pH. The resulting structure was formed due to the hydrophobic and aromatic interactions and occurred in transparent and homogeneous gel-form [67]. Moreover, these gels formed from FG-repeats were shown to facilitate active, transport-receptor mediated transport [25]. It was shown that the GLFG gel

blocked entry of the inert MBP-mCherry fusion protein, but at the same time permitted >1000-fold quicker the entry of an Importinβ-cargo complex (Figure 1-9). Further experiments illustrated that only cohesive FG-domains could form a functioning barrier [28]. To confirm this, hydrophobic residues of cohesive Nup98 were mutated, and as a result Importinβ failed to bind to FG-repeats, which was shown on Western Blot. The broken permeability barrier was additionally confirmed on the nuclei which were treated with immobilized lectin wheat germ agglutinin (WGA) to deplete original Nup98 and complemented with mutant Nup98. Confocal microscopy showed that neither active transport nor passive exclusion was sustained with non-cohesive FG-domains (Figure 1-10). Thus, during the transport it is not only the interaction between Importinβ and FG-repeat that matters, but also the interactions between the FG-repeats.

To sum up, the "hydrogel" model is supported by experiments that showed that cohesive FG-domains can spontaneously form a hydrogel. This hydrogel functions as a permeability barrier of NPC by excluding the inert cargoes but allowing fast passage of the cargo with nuclear transport receptors and passive diffusion of small molecules. However, the role of non-cohesive FG-domains is not described within the model.

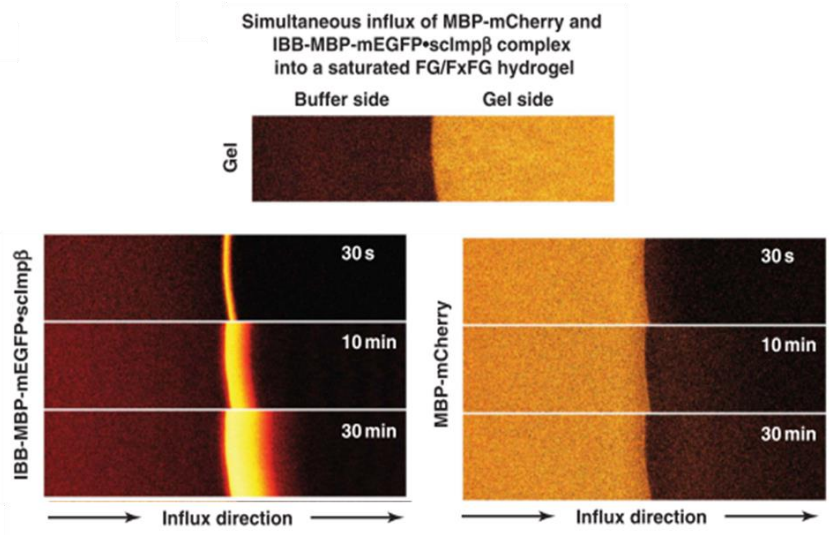

Figure 1-9 The experiment showed a simultaneous influx of an inert molecule MBP-mCherry and another cargo IBB-MBP-mEGFP carrying the transport receptor – Importinβ. The upper panel shows a piece of the sample, where the right half is the gel and the left half is the buffer solution. The imaged were obtained using the confocal microscopy and the influx was recorded over time (30 s, 10 min and 30 min) [25].

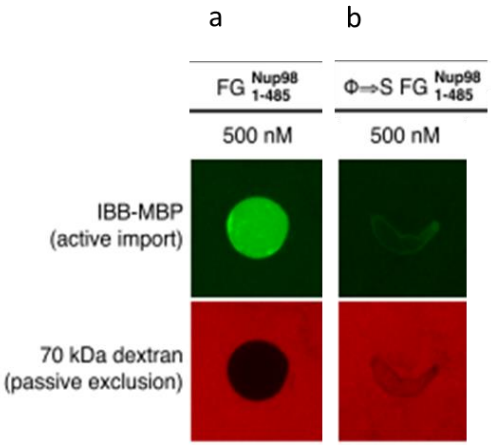

Figure 1-10 WGA-depleted nuclei represent a closed nuclear envelope containing nuclear pores and supplemented with (a) cohesive Nup98 and (b) non-cohesive mutant Nup98. Both nuclei in (a) and (b) were subjected to the fluorescent IBB-MBP (to test active transport) and fluorescent 70 kDa dextran influx (to test passive exclusion). The final concentration of Nup98 used in both forms was 500 nM [28].

1.5.3 Reduction of Dimensionality

In the reduction-of-dimensionality model, the FG-repeats are presented as a hydrophobic layer of flexible FG Nups that covers the walls of the central channel (Figure 1-7 c). FG-Nups collapse towards the outer edge of the NPC scaffold, creating a surface of exposed FG repeats and leaving a corridor of 10 nm diameter in centre of the pore for passive diffusion [68]. Cargo bound with transport factors "slides" across this surface reducing the diffusion to a two dimensional space (i.e., on the surface of exposed FG repeats), as opposed to the three dimensions of inert cargoes.

The model assumes that karyopherins are in constant contact with FG-repeats. This was confirmed by a bead-spring model simulation, which were used to calculate the time of the interactions between FG-repeats and Importins. It was found that the complex is in contact with FG-repeats in 97% of their time [69]. Another study, using fluorescence correlation spectroscopy, observed that the number of nuclear transport receptors in NPCs is high, and that they are immobile [70]. However, in a different experiment it was detected that Importins rather replace each other within NPC than resting there [55].

1.5.4 Forest model

In this model the FG Nups are described as polymers that can be in collapsed and extended states (Figure 1-7 d). Thus, the collapsed Nups are residing at the walls, while

Nups in the extended state are stretched into the central channel, walls resembling shrubs, while Nups in the extended state are stretched into the central channel, resembling trees and therefore similar to forest-like configuration [71]. It was confirmed that FG-repeats can be cohesive and non-cohesive by examining *in-vitro* assays built from bead-immobilized FG-domains in of interaction with other FG-domains [72] (Figure 1-11 a). In a further study three conformations of FG-repeats were identified and described as collapsed-coil and extended-coil or both of them. The collapsed-coil conformation corresponds to shrubs and two-component configuration to trees. This was deduced from the measured Stoke radii of FG-nucleoporins and comparing to the theoretical value corresponding to particular conformations [23].

The "forest" model distinguishes two zones for transport are differentiated. Side channels are designed for the diffusion of small molecules, whereas the central channel is for the large cargoes. It is assumed that the narrow central channel is hydrophobic and mainly positively charged, thus it would attract the negatively charged cargo with hydrophobic properties such as Importins. In addition, it is suggested that the central channel is able to expand rapidly to let large cargo pass. In order to translocate, the macromolecule-Importin complex pushes the FG Nups from the central channel towards the walls. However, this may be in conflict with some experimental evidence from single-molecule tracking, showing that karyopherins pass near the walls, while small molecules diffuse through the central channel [73]. On the other hand, there is also evidence on the large cargoes translocating through the central part of the channel [74], for instance by monitoring a single-molecule translocation across the pore and its position [75] (Figure 1-11 b).

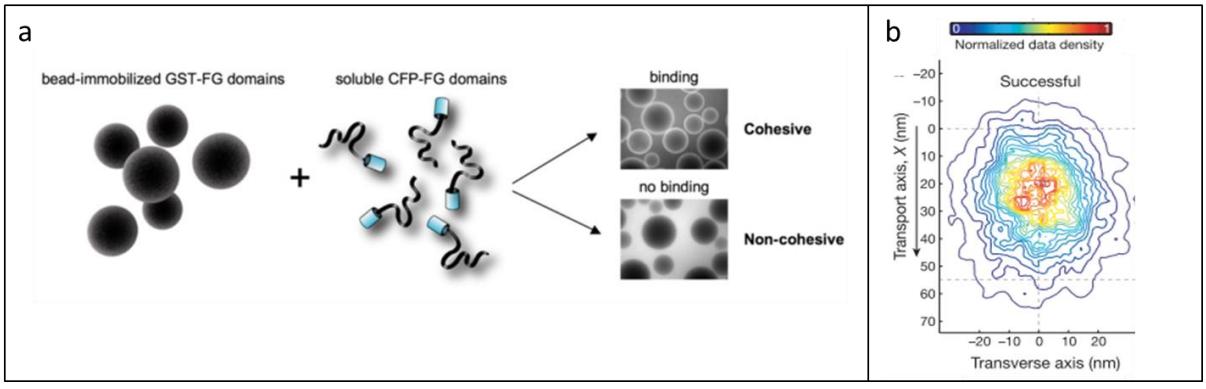

Figure 1-11 a) Bead-immobilized GST-FG nucleoporins incubated with soluble fluorescent FG-repeats to identify under the fluorescent microscope binding between

mixed FG-repeats. In case of binding the fluorescent signal emerges from the rim of the beads, while non-binding is determined due to dark non-fluorescent beads [72]. *(b) Density map of cargoes locations within the central channel which were successfully translocated across the nuclear pore. The map is colour coded illustrating normalized density* [75].

1.5.5 Other models

Other models more or less coincide with the highlighted earlier models. Some of them represent the joint mechanism of a few models such as those proposed elsewhere [76]. For instance, there was a suggestion that the "selective phase" model is applied to explain the behaviour of polymers within the central channel and the "virtual gating" model is used to describe the FG-repeat interactions at the periphery of the pore. Some models propose that the directionality of the transport might be due to the gradual rise of FG-Importin affinity from the cytoplasm to the nucleoplasm [77]. Additionally, there is a hypothesis that the tuneable cohesiveness of the FG-repeats can determine the permeability barrier since it is dependent on the FG-repeats [22].

1.6 Translocation across the NPC

Due to the high affinity of Importinβ to the nucleoporins which are predominantly located at the periphery of the channel [77], some have suggested [73] that the mediated transport occurs in the peripheral area of the channel (Figure 1-12 a), whilst the passive diffusion occurs via the central channel. However, in another study [39], it was claimed that the periphery of the pore is designed for passive diffusion, while the centre is dedicated to the active transport (Figure 1-12 b). However according to Density Function Theory calculations the transport route depends on the interaction strength between the FG domains and FG domains with NTRs. When both of these interactions are not high enough, the NTRs tend to accumulate at the periphery of the pore [78] while the centre remains free for FG domains (Figure 1-12 c). However, when they are large, the NTRs try to occupy all the space available (Figure 1-12 d).

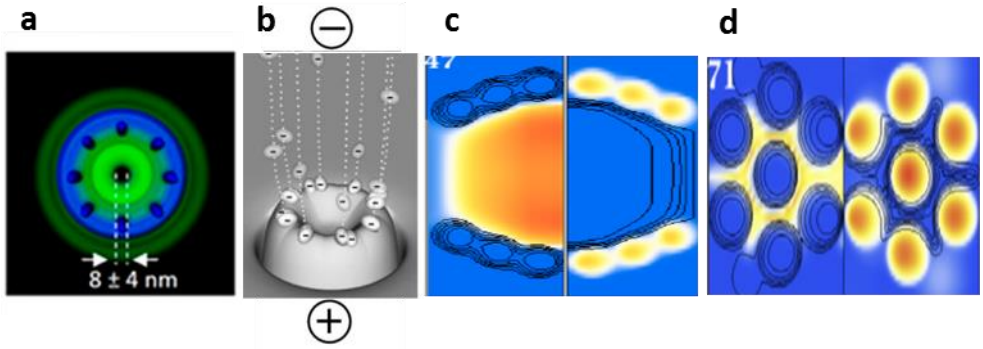

Figure 1-12 a) Top view of the NPC, where blue corresponds to the scaffold of the pore, and green – to the Importinβ accumulation [73]*; b) schematic view of the pore showing the ions diffusion into the peripheral channels upon direct current application* [39]*; c) top view of the pore generated by a simulation with weak interactions between the FG domains and between NTRs and FG-repeats. In the same manner (d) shows strong interactions between the FG domains and FG domains with NTRs. In (c) and (d) the pore is divided into two parts: the colourmap on the left panel refers to the interaction between the polymers in the central channel, whilst the right panel refers to the NTRs distribution* [78].

1.7 Characterisation methods to study NPCs

Since the discovery of NPC in 1959 [79], its structure and function has been extensively studied by various means. The structural characterisation was mainly implemented by electron microscopy coupled with X-ray crystallography to resolve the configuration of nucleoporins. High-resolution confocal microscopy allows to measure transport across the pores, whereas atomic force microscopy provides access to the topography and nanomechanics of the pores. All the methods combined are able to provide structural information of the nucleoporins that form the NPC, their configuration, flexibility, and along with that, transport kinetics and suggestions on the thermodynamics of the process.

1.7.1 Electron Microscopy

Electron Microscopy (EM) is one of the most used techniques to study the structure of the NPC. Some of the first EM images were recorded in the late 1950s, where NPCs were imaged as cylindrical formations embedded into the nuclear membrane [79]. Later, in 1967, the eight-fold symmetry of the pore was discovered by EM [80]. The NPCs were derived from *Xenopus* laevis oocytes and imaged by cryo-electron microscopy in

frozen buffers by obtaining 64 slices along the z-axis with a separation of 25Å [4]. Since then, the resolution of the image has increased significantly. Figure 1-13 shows the evolution of the EM imaging of the NPC from 1993 to 2015. In the initial images the distal ring of the basket, the cytoplasmic ring and molecular density within the central channel were identified [3], [4] and the dimensions for the outer and inner diameter were estimated as 125 and 55 nm respectively [18]. Later, in 2013 the configuration of some Nups was resolved to up to 3.5 nm [81], and in 2015 the resolution increased to 2 nm which is highest resolution to date [10]. By imaging the NPCs in transport inhibited state it was found that some nucleoporins in the nuclear basket change their conformation depending on whether there is a cargo translocating or not. Although the images are more detailed, the structure of the central channel is still vague and sometimes excluded from analysis, because the disordered, natively unfolded nature of the FG Nups compromises the used averaging procedures.

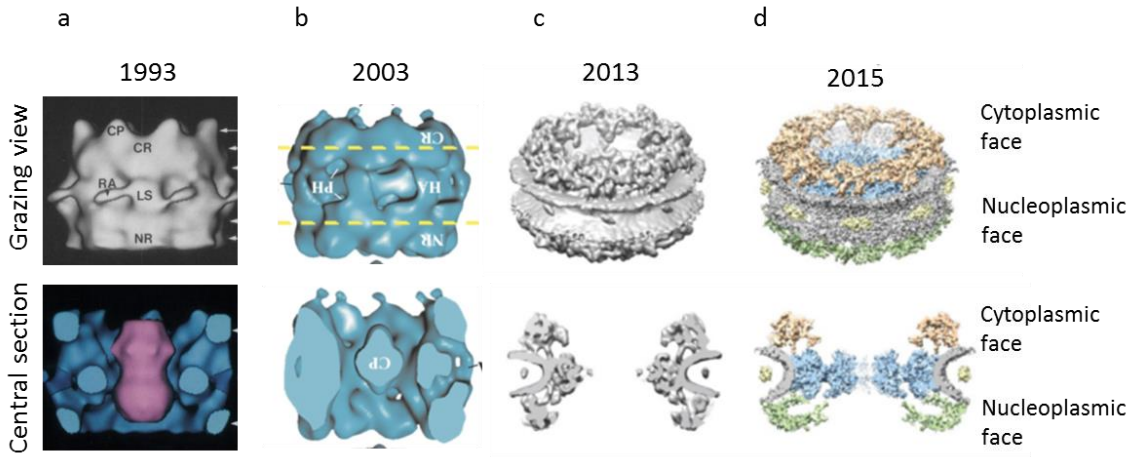

Figure 1-13 The development of the spatial resolution in molecular density maps as determined by EM. (a), (b) and (d) illustrations are for Xenopus laevis NPCs and (c) is for human NPCs. The resolution increased from: a) ~10 nm [4]; *b) 12 nm* [3]; *c) 3.5 nm* [81] *to d) 2 nm* [10].

1.7.2 X-ray crystallography

X-ray crystallography is a high resolution technique which enables to resolve structure of the proteins at atomic level. X-Ray crystallography was problematic to implement on NPCs, due to their large size and mobility of some parts. Instead, the individual proteins or complex of proteins were crystallised and then put together to build the pore. This

approach also complements the EM results. For example, 85% of the Nup84 structure was resolved due to combination of EM and crystallography [19].

EM and crystallography have been effectively combined to gain structural information of NPC, as exemplified by the structure of the Y-complex. The Y-complex is a key component of the NPC scaffold (Figure 1-14). It consists of several different Nups formed into Y shape configuration shown by negative-stain EM [82], [83].

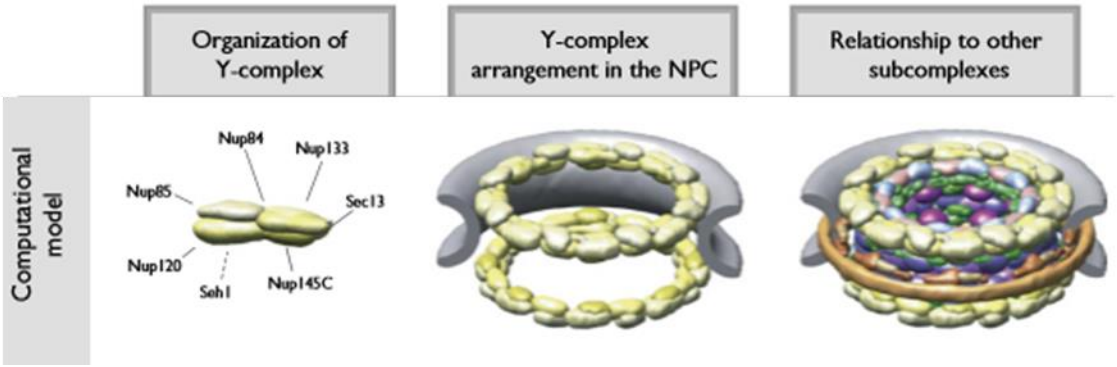

Figure 1-14 Representation of Y-complex as an assembly of Nups, their position within the NPC scaffold shown in relation to other subcomplexes. The first panel shows a computational representation of Y-complex consisting of the following Nups: Nup84, Nup133, Sec13, Nup145C, Seh1, Nup120, Nup85. The second panel exhibits the assemblies of Y-complex organised into two rings along Z-axis. The third panel shows the position of other Nups and complexes within NPC [12].

The three-dimensional structure of the Y-complex was imaged in yeast NPCs using negative stain EM. In this method the sample was imaged in tilted (50^{o}) and untilted positions to obtain different projections of the structure. Resulting 3D maps were mapped with known crystal structures of yeast nucleoporins – Nup85, Seh1 and Nup145 (Figure 1-15). The space that was not mapped with the crystal structures was left empty because currently there is no crystal structure developed so far. Moreover, instead of yeast Nup133 and Nup84, the human analogues were used (Nup133 and Nup107), because no crystal structures were available for these yeast Nups. The resolution of the structure achieved in EM images was 3.5 nm, whereas the resolution of the crystal structures, for example of Nup85-Seh1 dimer was 3.5 Å [84]. It is quite possible that the estimated position of Nups might still change with the emergence of new Nup structures and of higher-resolution EM data.

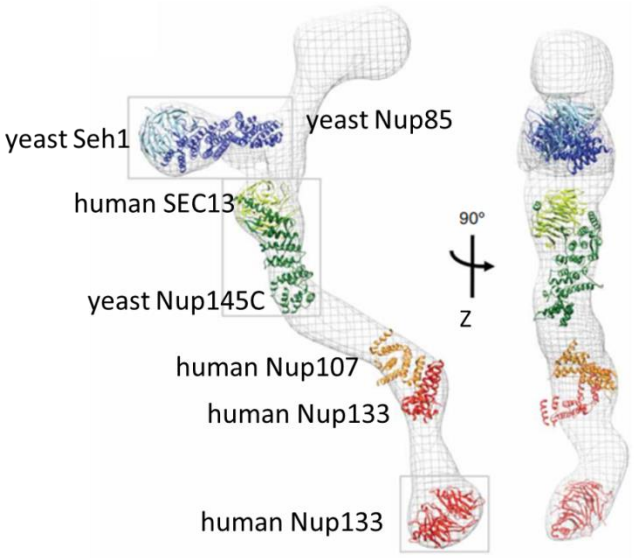

Figure 1-15 Mapping of available crystal structures of yeast and human nucleoporins into the 3-dimensional EM representation of Y-complex. Another view of the complex is rotated to 90^{o} around Z-axis. Crystal structures of the following Nups were fitted into the 3D model of Y-complex: dimer of yeast Nup85 and Seh1 (dark blue and light blue respectively), complex of yeast Nup145C and human SEC13 (dark green and light green respectively), complex of human Nup107 and Nup133 (analogous of yeast Nup84 and Nup133, orange and red respectively) and human Nup133 (red) [85].

Overall, by combining high resolution crystallography of individual nucleoporins and relatively low resolution of EM data, the location and orientation of Nups could be determined within the NPC scaffold. The low degree of order in the central channel, however, complicates similar approaches to solving the structure of the selectivity barrier.

X-ray crystallography has also been used extensively to study the interactions between FG-repeats and transport receptors [86]. Moreover, it was also possible to study the Ran binding interface when anchoring to the FG-repeats [87]. However, the nucleoporins within the central channel, which form the permeability barrier, cannot be crystallised due to their unstructured domains that natively unfolded.

1.7.3 High-resolution confocal microscopy

High-resolution imaging of the NPC has been done by many groups in recent years using different variations of confocal microscopy. One of the first attempts to image NPCs at high resolution with a confocal microscope was done in 1996 on 3T3 cells

stained by a fluorescent anti-nucleoporin antibody [88]. However, due to the diffraction limitation of light, the NPCs were captured only as the bright spots.

Another attempt to differentiate a single NPC was done on a whole nucleus of human HeLa cells in 2008. As a result, only the distribution of NPCs on the surface of a nucleus was determined [89] (Figure 1-16 a). However, recently the approach on managing the diffraction limit has changed due to the method of single-particle localisation technique. Thousands of subsequent images collected by stochastic optical reconstruction microscopy (STORM) were averaged and individual NPCs could clearly be resolved [90] (Figure 1-16 b).

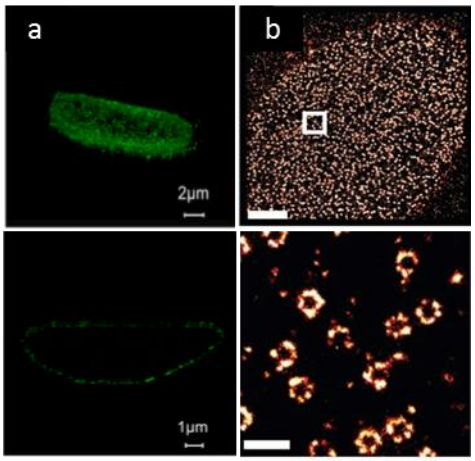

Figure 1-16 a) Human HeLa cells nuclei scanned by two-photon 4Pi microscope [89]*; b) Human U2OS nuclei scanned by STORM. The scale bar is 3 µm and 300 nm respectively* [90].

In 2012-2013 two independent groups determined the 8-fold symmetry of a gp210 membrane protein of *Xenopus laevis* NPCs by using direct (d)STORM, which creates a separate snapshot of each condition of the 'blinking' fluorophore (Figure 1-17 a, b) [91]; and stimulated emission depletion fluorescence microscope (STED), which achieve a high resolution due to de-exciting the area around the centre of the excited spot (Figure 1-17 c, d, e, f) [92], [93]. The lateral resolution was 15 nm. By averaging the collected images of hundreds of NPCs, the internal diameter of the pore was identified as 41±7 nm [91]. Additionally, the dwell times of cargoes were measured [94], [75].

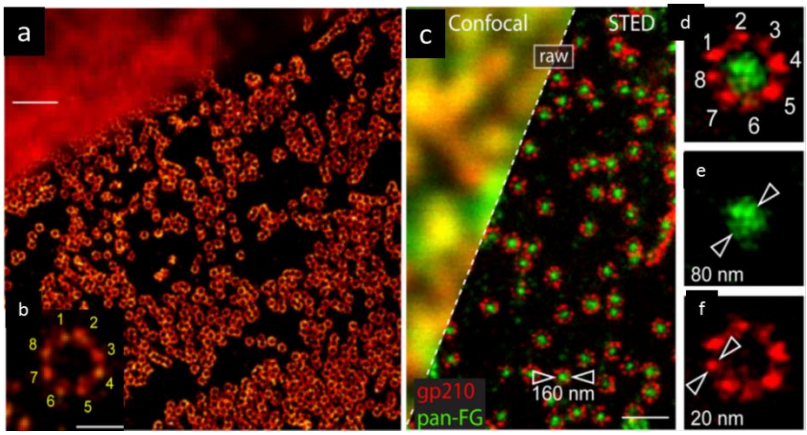

Figure 1-17 a), (b) STORM and (c), (d), (e), (f) STED high resolution images of nuclear envelopes, showing the 8-fold symmetry of the NPC [91], [93].

Apart from identifying the position of the nucleoporins and the overall structure of the NPC, the high-resolution confocal microscope also contributed into studying the transport process and its kinetics at the single-molecular level. For example, it was found that the importin complex moves fast (2 ms) within the central channel and the movement is bidirectional [94], whereas the mRNA export takes longer (1 s) [54]. Overall, high-resolution imaging of translocation gives more details of the cargo's docking and passage across the pore. Thus, by observing the transport process and its kinetics, the properties of the permeability barrier can be inferred but not be identified directly.

1.7.4 Atomic force microscopy

AFM has been widely applied for investigation of conformational and mechanical changes of NPCs under different conditions such as variation of temperature, addition of calcium, carbon oxide, and exposure to drugs, in particular alcohol, glucocorticoids and dexamethasone. .

AFM Imaging of the nuclear pores

Effect of CO_2

The increase of carbon dioxide in the atmosphere may directly affect the living organisms. In this sense it is interesting to find out how the nuclear pores react to the carbon dioxide exposure. The conformational changes of the NPCs such as flattening and narrowing were observed in the AFM topography after exposure to 5% CO_2 [95] . The diameter of the pore which was 84 nm appeared to reduce and the rim was blended

with the central channel. After CO_2 removal, the NPC returned to its original shape (Figure 1-9). However, there remain so questions about the appropriateness of the sample preparation: samples were dried and only rehydrated for the AFM measurements.

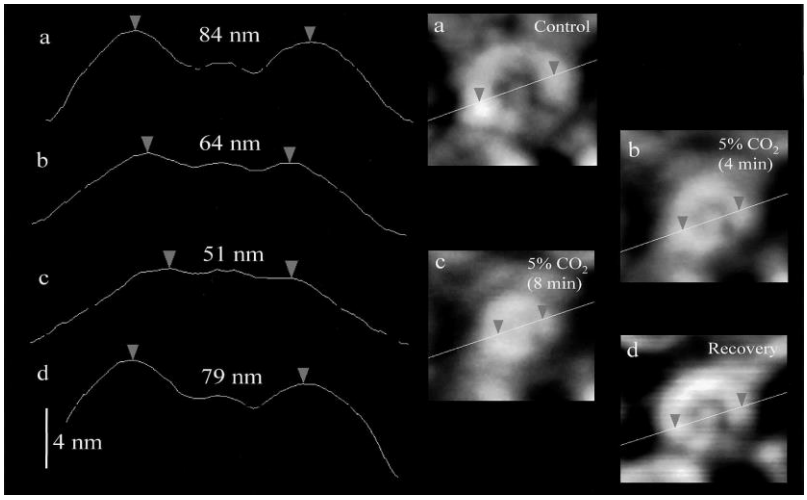

Figure 1-18 Effect of CO_2 on NPC over time captured by AFM (a) control sample, the diameter of NPC was 84 nm, the shape of central channel was recognisable. In (b) and (c) 4 and 8 minutes after CO_2 addition, the diameters of the pore appears reduced to 64 nm and 51 nm respectively. The central channel blended with the rim. In (d), the pore has returned to its initial state after CO_2 removal, the diameter enlarged to 79 nm. [95]

Effect of Calcium

It was found that the nuclear calcium store regulates the transport of molecules [96]. Depletion of calcium inhibited diffusion of 10 kDa molecules [97]. However, as has been reported elsewhere [98] AFM time-lapse measurements did not identify any dramatic changes in topography upon calcium treatment. At low concentrations of calcium (~10 nM), the pore showed opened and closed phases corresponding to the presence or absence of calcium respectively which has been confirmed by another study [99] where the cytoplasmic face showed an increase in the number of plugged pores under calcium depletion. At a reduced concentration over 80% of the NPCs were plugged. It was also established that the process of blocking the pore was reversible [98] (Figure 1-19). The same sample was imaged after each manipulation with calcium. The force was calibrated prior to scanning. The set point was set to be zero at the engaging step to save the sample from damage.

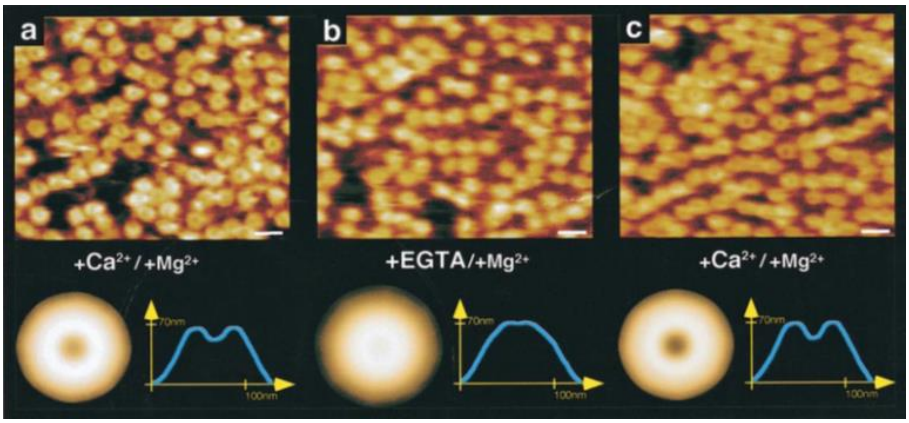

Figure 1-19 The reversible effect of Ca^{2+} treatment on NPCs (a) in presence of calcium; (b) calcium depletion and (c) addition of calcium again [98].

Effect of Glucocorticoids

Glucocorticoids are the anti-inflammatory and immunosuppressive substances which are used in drugs [100]. They cause leakage of the NE barrier. This is probably due to changes in hydrophobicity and dilation of the NPC. In this study [101] the triamcinolone (TA), which is recognised as a glucocorticoid analogue, was used. Significant changes in the structure and permeability of the membrane, such as a notable opening of NPCs, appearance of clusters (Figure 1-20) and intense leakage of the transport barrier (Figure 1-21) were all measured. The changes were observed after 5 minutes of TA injection. The process was reversible measurements of permeability performed an hour after treatment yielded results similar to those observed in the initial state. It is believed that the increase in the hydrophobicity of the NPC might be due to the binding of the hydrophobic TA with hydrophobic transport receptors to FG nucleoporins. Thus, the accumulation of TA in the NPC may change the hydrophobicity, which in turn promotes the dissociation of the FG rich nucleoporins in the pore and leads to NPC opening. Therefore, it was concluded that the NPC is sensitive to hydrophobic molecules. Moreover, it was suggested that the NPCs undergo lateral movement in response to TA because the nucleoporins limit NPC movement.

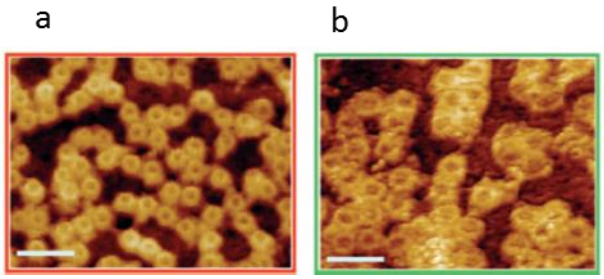

Figure 1-20 The NPCs (a) before and (b) after the injection of Glucocorticoids. The scale bar: 500 nm [101].

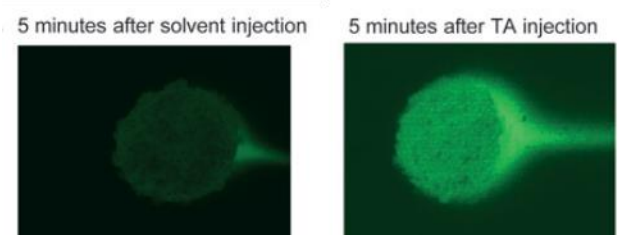

Figure 1-21 Permeability experiments observed on fluorescent microscope with solvent and TA [101].

Effect of Temperature

It is known that at low temperature the nucleoplasmic transport can be paused [102], [103], [104]. If the NE was kept at low temperature (4^0C) the cargo can be caught in the central channel. Consequently, the NPC would appear to be plugged. This was shown by implementing time-lapse AFM on NEs prepared at 4^oC and 25^oC yielding 45% and 12% of plugged pores respectively [3] (Figure 1-22). This conclusion was drawn from the results of a 3D tomography experiment of the NPC fixed in ice. Lowering the temperature acts as an inhibitor of the transport, reducing the translocation rate. Increasing the temperature leads to an increase in transport rate.

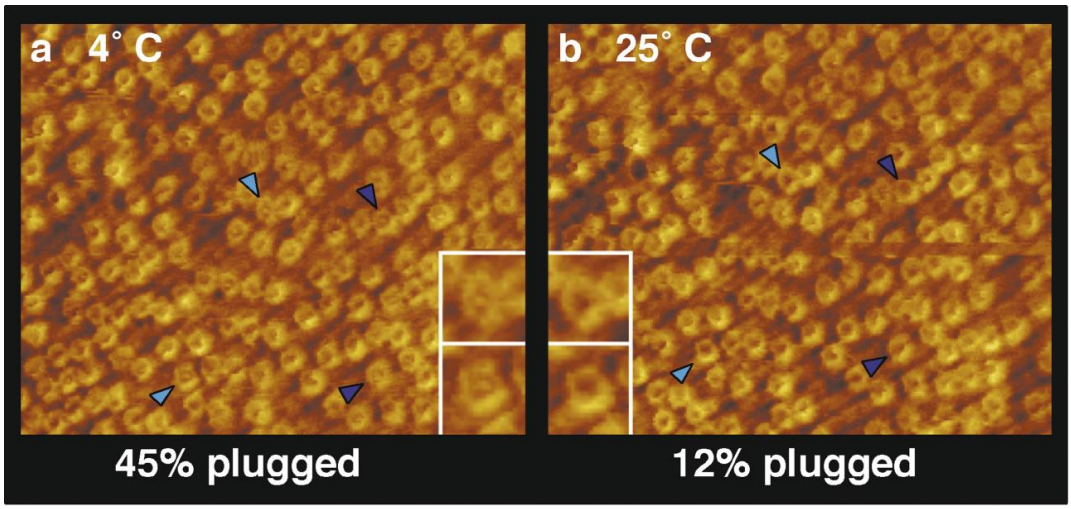

Figure 1-22 AFM scan done at (a) 4^0C and (b) 25^0C in contact mode of the same area of cytoplasmic NE [3].

AFM imaging of individual NPCs

Along with the topography image, where the conformational change of the pores can be identified, a phase image is used as well to differentiate the properties of the material as adhesion, surface charge, elasticity and etc. The phase image is recorded by registering the phase shift between the cantilever's oscillation and exciting signal in the tapping mode of AFM. In the experiment conducted in reference [37], the nuclear pores were imaged in height and phase channels. It was found that the central channel appeared differently in these two types of images (Figure 1-23 a, b). It was suggested that the difference could be due to the hydrophobicity of FG-repeats trapped in central the channel. The phase image showed larger contrast in the central channel was observed. To confirm the interpretation of the phase image in terms of enhanced hydrophobicity in the central channel, a mutant of Importin β known for its hydrophobic properties was incubated with nuclei, prior to AFM imaging. Figure 1-23 (c) shows the topography image where the central channel is filled with Importin β, however in the phase image (Figure 1-23 d) the contrast appears more pronounced than in the non-importin phase image which might mean the structure is more hydrophobic that FG-repeats. Thus, AFM is capable of resolving the difference which was not visible in the topography data alone. However, it should be emphasised that the interpretation of such phase images is not trivial.

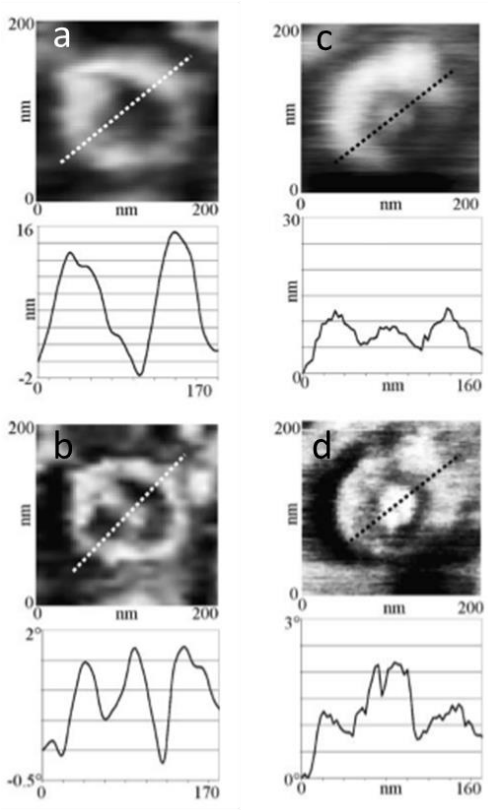

Figure 1-23 (a) and (b) are height and phase images of individual pores with the corresponding cross section. (c) and (d) show the height and phase images of the pores pre-incubated with Importin β [37].

AFM force spectroscopy on nuclear pores

AFM force spectroscopy can also differentiate between the states of the pores according to the stiffness data. In particular it was shown that under the ethanol treatment (0.05 - 2%) [105] the pores formed clusters on the nuclear envelope. AFM measurements of the interaction forces between the sample and the tip showed that the pores grouped in clusters were stiffer than pores independently spread on the membrane. For instance, for a deformation of 10 nm, the forces applied to clusters versus free NPCs were ~300 pN and ~100 pN respectively (Figure 1-24). The pores were scanned by 10 nm diameter tip. Although the diameter of the tip allowed the authors to resolve individual nuclear pores, force curves were averaged over larger areas to show the enhanced stiffness of the clusters of nuclear pores.

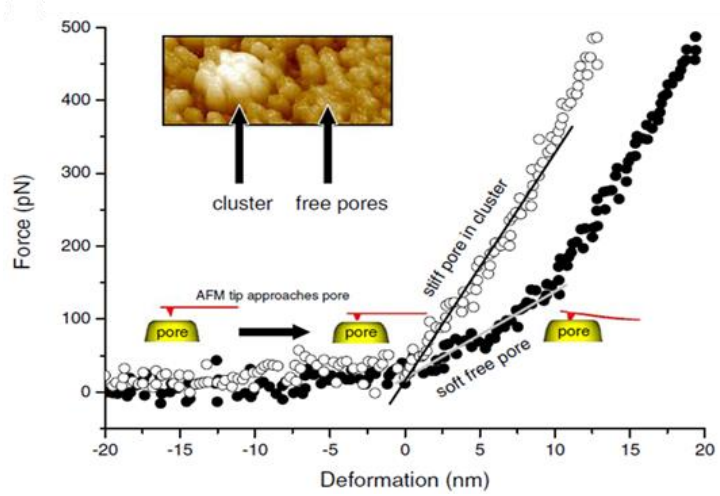

Figure 1-24 Force curves of stiff and soft pores [106]. *The clusters of NPCs formed under ethanol treatment appeared to be stiffer than the freely distributed NPCs. The force curve corresponding to the stiff pores is edgy and the contact point between the sample and the tip is seen clearly. Meanwhile the force curve of soft pores highlights the softness of the probed material. The AFM topography image of clusters and independent pores is given at the top of the diagram.*

Summary

Some preparation methods of the samples mentioned above involve the drying of the sample, in order to achieve better adhesion to the substrate, followed by rehydration prior imaging. The majority of the AFM experiments described were done with either chemically fixed samples, samples exposed to some detergents, or air-dried samples. Thus, the discussion on the effect of various chemicals upon the NPC was done when it was no longer in a functional state. Ideally, the sample should always be in the buffer, hydrated and with no chemical fixation as it was described in [37] and [3]. Both contact and tapping mode worked fine for NPC imaging.

AFM imaging on the model systems

There is another cluster of work done by AFM on artificial systems mimicking the permeability barrier and FG-conformations.

Polymer brush behaviour as observed by AFM

The AFM Force Volume technique was used to determine the nanomechanics of polymer brushes formed by FG-domains (Nup153) covalently anchored to the gold nanodots (100 nm in diameter) [62]. It was assumed that individual FG-domains from

one type of nucleoporin behaves in the same manner as other FG-domains within the NPC (from different nucleoporins). Such brushes showed a (presumably steric) repulsive force resulting from the compression of the polymer chain by the AFM tip (Figure 1-25, top curve). Upon addition of Importinβ this brush seemed to collapse. Moreover, the effect of collapsed state was stronger with increase of Importinβ concentration. Thereby, at the highest concentration used (33 nM), the force curves were steeper than at lower concentrations (115 fM and 2.5 pM) (Figure 1-25). The applied force was the same for each measurement - 0.8 nN. It was suggested that this transition in polymer brush state is due to the FG-repeats collapsing upon interaction with Importinβ. When RanGTP was added to the buffer the polymer brush was restored due to the RanGTP effect of dissociation of Importinβ-FG-repeat interaction. The interpretation of these experiments has been complicated by the fact that the collapse was observed at Importinβ concentrations that were far below the physiological (μM) conditions; and rather problematically, this large Importinβ-induced collapse was not observed in various follow-up experiments [107], [108].

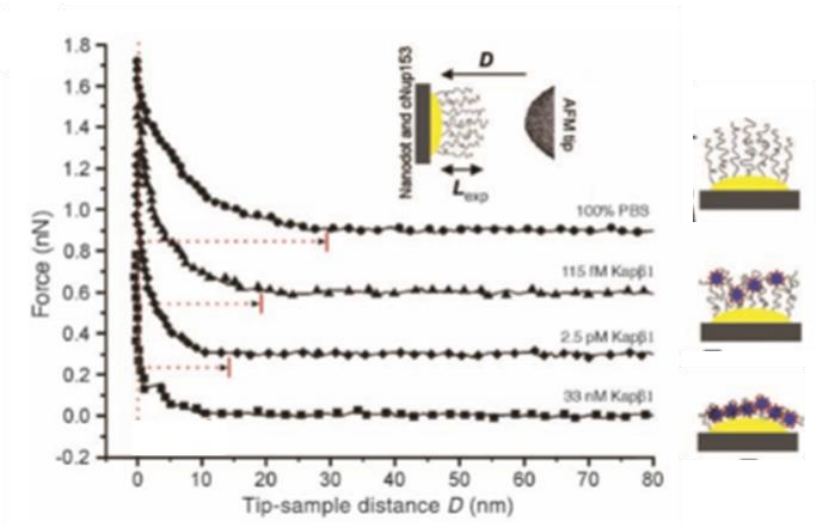

Figure 1-25 The top curve was acquired in the PBS buffer and represented the extended FG-repeats of cNup153 by showing exponential behaviour. The following three curves show the polymer brush under the Importinβ interaction at various concentrations (115 fM, 2.5 pM and 33 nM). The higher the concentration, the steeper the force curves, meaning stiffer sample. The state of the polymer brush is illustrated on the left from the curves [62].

An apparently similar collapse of FG-repeats (from Nup153) was also observed upon exposure to 5% 1,2-hexandiol [61]. The results were shown in form of force curves and

stiffness maps. The same sample as described above was probed in Force Volume with similar force applied (1.2 nN) for both extended and collapsed states. As it was expected in the relaxed state of the brush, force curves showed repulsive forces with approximately exponential behaving Figure 1-26 a, black line), while after the treatment with hexanediol force curves appeared steeper and showed strong attraction to the surface (Figure 1-26 c, red line). Moreover, when the tip is unloading from the collapsed brush, the curve showed sudden jumps, indicative of unfolding events of the FG-repeat caused by the retracting AFM tip.

Along with force curves, the relative stiffness of extended and collapsed brushes was quantified and represented in stiffness maps. Figure 1-26 (b) shows clear difference in stiffness between the nanodot and surrounding area. The nanodot covered with FG-repeats appeared twice softer than the area around it. Conversely, the nanodot with collapsed FG-repeats under hexanediol shows the stiffness close to the surrounding area (Figure 1-26 d).

In another study by means of confocal microscopy, it was shown that hexanediol disrupts the interaction between FG-repeats [72]. Taking this into account one can suggest that collapsed state of the brush corresponds to the “open” state of the nuclear pore.

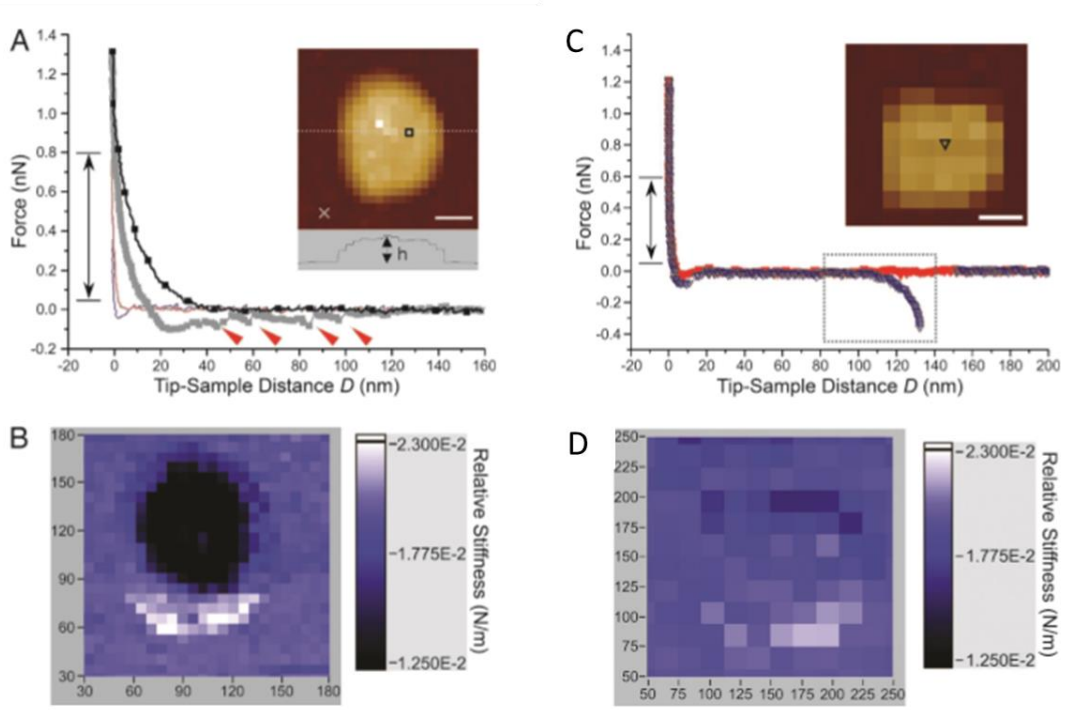

Figure 1-26 a) The tip-sample interaction was recorded on FG-repeats tethered to the nanodot. The black line corresponds to the trace (loading) force curve, exhibiting a repulsive force, and grey line representing the retrace curve with few stretches corresponding to unfolding of FG-repeats. Red and blue curves show trace and retrace force curves respectively collected from the surrounding area. The illustration on the left shows height image of the nanodot. (b) Stiffness map (32x32) shows in dark the nanodot indicating its softness and in light blue the surrounding area which appears harder. (c) Trace (red) and retrace (blue) force curves collected from the nanodot (height image on the left) with FG-repeats subjected to the hexanediol. The shape of the force curves indicates the hard surface. The sudden jump in the retrace curve shows the height at which the FG-repeat detached from the AFM tip. (d) Stiffness map of the same nanodot (16x16) showing the stiffness of the FG-repeats exposed to hexanediol, which is comparable to the stiffness of the surrounding area [61].

AFM imaging of polymer brushes formed by PEG

Similar experiments were done on the gold nanorings which were used as a substrate for polyethylene glycol (PEG) anchoring [63]. The size of the ring was close to the size of real NPC - 87 nm and 213 nm for inner and outer diameters. PEG was used as a model system for the polymer brush formed from the FG-repeats due to the similarities in their nanomechanical behaviour, as confirmed by analogous force curves. As it can be seen from Figure 1-27 (a), the force curves collected from the functionalised nanoring also show a long-range repulsion as the FG-domains in the experiments described above

[61]. Force curves acquired from the silicon substrate illustrated a steep increase of the force which indicates a hard surface. The applied force in all cases was 300 pN. A corresponding stiffness map was also presented where the nanopore appeared softer than the surrounding area (Figure 1-27 b). The same result was achieved before with the FG-domains instead of PEG chains. In the same manner the collapse of PEG was observed as the collapse of FG-domains. The compact state fo the PEG brush was acheived after exposure to poor solvent (10% 2-propanol). As a result "open" and "closed" configuration of the pore was obsered when the brush was in collpased and extended state respectively (Figure 1-28). This is in agreement with the previous suggestion that upon collapse of the brush, the pore does not have a selectivity barrier. The brush was restored to its original extended state by changing the buffer with no 2-propanol.

These results show that synthetic polymer brush have similar nanomechanical behaviour as the natural FG-repeats from nucleoporins and may construct a physical repulsive barrier.

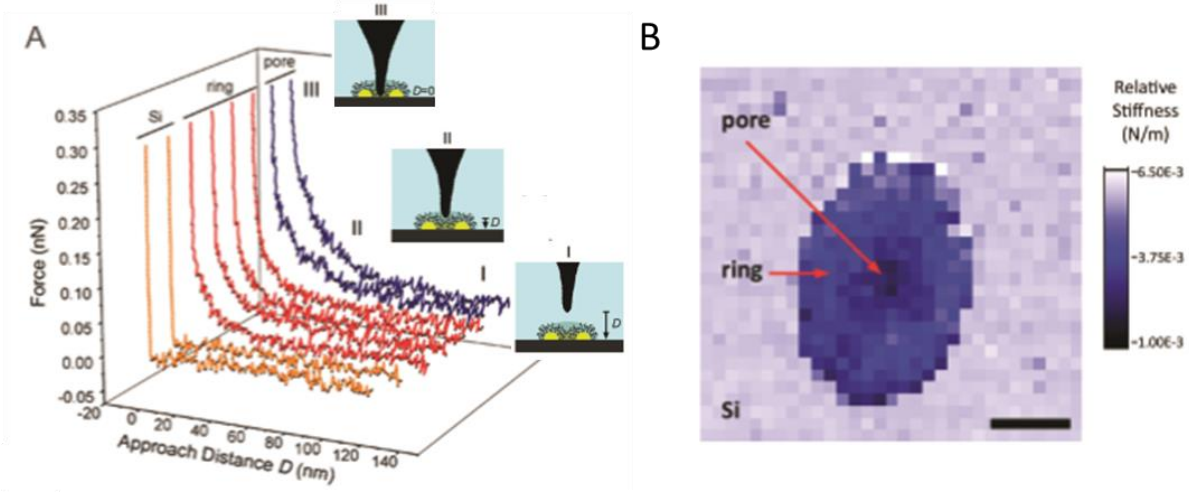

Figure 1-27 a) Force curves obtained from silicon surface (orange), rim of the nanoring/nanopore functionalised with PEG (red), and the inner part of the nanoring/nanopore (blue). The latter one has the demonstration of the tip-sample interaction depending on the position of the tip with regard to the pore. (I) shows non-contact area, when the tip is far above the pore. (II) shows the long-range repulsion of the tip when it started to interact with the brush. (III) illustrates the case when the tip penetrates the brush and measures the hard substrate, which was shown as rapid increase of repulsion. (b) Stiffness map of the nanopore functionalised with PEG where the surrounding area appeared stiffer than the nanopore [63].

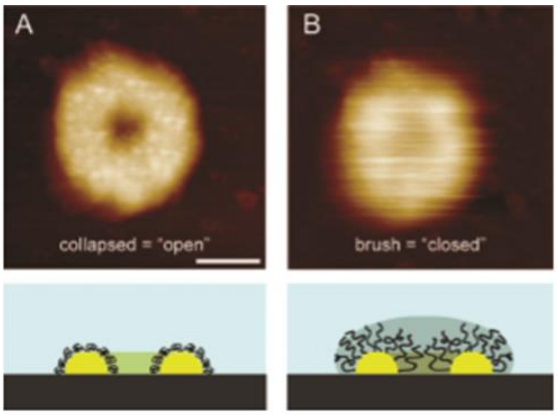

Figure 1-28 a) Collapsed PEG tethered to the nanopore upon change of the buffer to poor solvent – 10% 2-propanol – formed "open" state of the nanopore. (b) Extended state of PEG on the nanopore, showing "closed" state of the nanopore. Scale bar 100 nm [63].

Hydrogel behaviour as observed by AFM

In a more collapsed state, polymer brushes of FG-repeats can also form thin films or hydrogels. The FG-domains were grafted with one end to the supported lipid bilayer. Few aspects were kept similar to the NPC such as grafting only from one end of FG-domain, density of FG-repeats and dimensions (thickness of the film) which is comparable to the size of NPC. It was shown that extremely cohesive FG-Nups such as Nup98 formed stiffer films than partially cohesive Nsp1-WT, and non-cohesive Nsp1-FILV-S FG-domains [22]. Two latter FG-domains illustrated long-range repulsive forces during AFM tip indentation (Figure 1-29 a). This result shows that depending on cohesiveness of FG-repeats they may be arranged into the steric polymer brush-like conformation or form cross-linked hydrogels which are stiffer. Based on this results it was concluded that the polymer brush and the gel are the two extremes of the range of states which can be tuned by cohesiveness of FG-repeats.

Interestingly, these results did not show any significant collapse upon interaction with Importinβ [64] (Figure 1-29 b), as it was shown previously with polymer brush of FG-repeats from Nup153 on gold nanodot substrates (see above). Only a slight increase in thickness was observed upon incubation with Importinβ. It was suggested that Importins displace FG-domains and interact only with nearby FG-repeats.

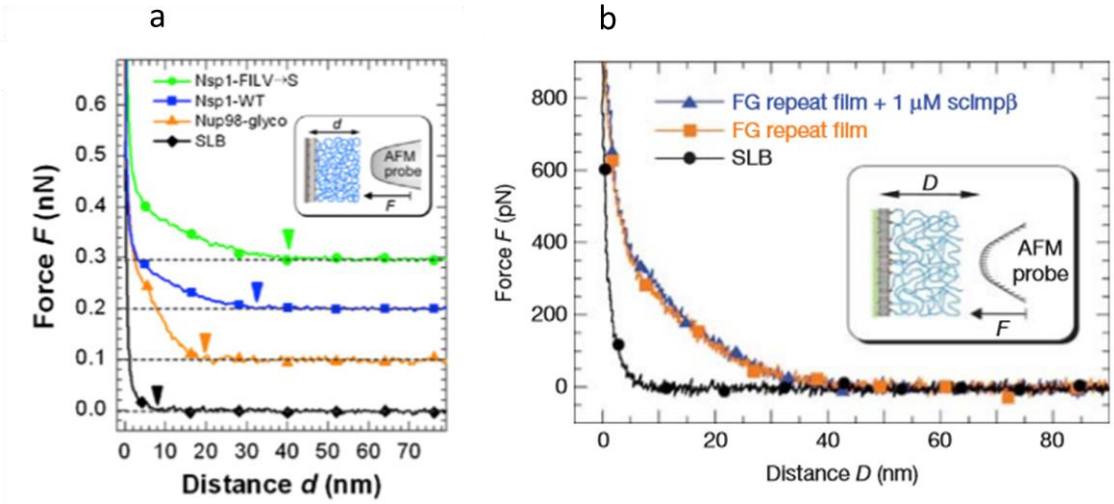

Figure 1-29 Force curves obtained in Force Volume from the supported lipid bilayer (black) and (a) FG-domains: Nup98-glyco (O-GlcNAc-modified Nup98, orange), Nsp1-WT (blue), Nsp1-FILV-S (mutant, green) [22]. *(b) Force curves recorded in presence and absence of 1 μM Importinβ in films formed from Nsp1p FG-domains (blue and orange respectively). Force applied – up to 0.7-0.8 nN* [64].

Summary

AFM measurement on model systems thus showed rather diverse nanomechanical behaviour, where it requires further study to determine to what extent such results can be extrapolated to the permeability barrier in the NPC.

Conclusion

As illustrated above, many AFM experiments been carried out have to investigate conformational changes of NPCs via topography imaging under different conditions. The investigation of the nanomechanical properties of the permeability barrier was done only using the model systems, providing indications of polymer brush and hydrogel behaviour of FG-repeats or synthetic polymers. In this thesis, we use AFM not only to achieve high-resolution imaging, but also extract the nanomechanical data from the individual NPCs, including their central channel that contains the permeability barrier.

1.8 Thesis outline

In this thesis the permeability barrier of the nuclear pore complexes (NPCs) was studied with atomic force microscopy and laser scanning confocal microscopy. The nuclear envelope preparation for measurements is described in detail in Chapter 2. The general

setup of the microscopes, operational principles and protocols of the experiments are described in Chapter 3.

In the chapter 4 the AFM method called Force Volume is described and validated on the model system – polymer brushes which is responsive to the pH change and can occur in two states: collapsed and extended. The nanomechanical properties of both brush types were compared to the NPCs central channel, in Chapter 5, to identify what its material is like in the permeability barrier: more brush-like or gel-like, where the latter roughly corresponds to the collapsed state of a brush. However, since there have been several claims that the appearance of native NPC is affected by the presence of cargoes stuck in transport, it was decided to 'wash' the pores, meaning to remove cargo and karyopherins, with the reagents that enhance the transport process and digest the nucleic acid. This leads to the Chapter 6 where the nanomechanical data acquired from NPCs in their 'washed' state is discussed.

Chapter 7 approaches the study of the NPCs via new advanced AFM technique called Peak Force Quantitative Nanomechanical Mapping. This technique is faster and has higher resolving power, and may thus also provide a route to a higher throughput nanomechanical characterisation of NPCs. The nanomechanical data of NPCs collected from both new and conventional Force Volume are compared.

An alternative route to understand the NPCs transport mechanism is to manufacture and study silicon-based biomimetic nanopores. These nanopores are built from silicon and can be functionalised with proteins to mimic the properties of the true NPC. Chapter 8 describes preliminary results on nanopores characterisation and the also required surface passivation.

Chapter 2 Sample Preparation

2.1 Preparation of the nuclear envelope

Stage IV *Xenopus* laevis oocytes, which are in the middle of their development cycle, were used as the material for studying the nuclear pore complexes. Their large cells (~1 mm in diameter) with huge enclosed nuclei (~300 µm in diameter) are very convenient for manual isolation [109]. To characterise the physical parameters of the nuclear pore complex (NPC) using AFM, the nuclei and nuclear envelopes must first be isolated. This protocol for AFM sample preparation is also the basis for other experiments involving NPCs, such as the temperature dependence experiments, and the confocal microscopy experiments. The glass coverslips used as a substrate during the sample preparation differ depending on the microscope used. For the AFM experiments, circular glass coverslips of 13 mm diameter were used; whereas for the LSCM experiments, 22x30 mm rectangular coverslips or 45 mm diameter glass bottomed Petri dishes were utilized. The glass was 0.13-0.16 mm thick. All the coverslips were cleaned with 70% ethanol, rinsed in MilliQ water and dried with Kim-wipes. 6-8 Petri dishes (plastic with a diameter of 35 mm) for sample preparation were first incubated with 1% BSA for at least 20 minutes to prevent nuclei sticking to the bottom of the dish.

2.1.1 Nuclei isolation

The oocytes were stored at 4^0C in Barth's solution (88 mM NaCL, 1 mM KCl, 0.41 CaCl2, 10 mM HEPES, 0.33 mM $Ca(NO_3)_2$, 0.82 mM $MgSO_4$, 2.4 mM NaHCO3, pH 7.6) [110]. Defolliculation of oocytes was performed manually in Barth's solution in a Petri dish using tweezers under the stereomicroscope (Figure 2-1 a, b). After the oocytes had been separated from each other, they were transferred into a 3 ml solution of a nuclear isolation medium (NIM: 17 mM NaCl, 90 mM KCl, 10 mM MgCl2, 10 mM TRIS, pH 7.4) supplemented with 1.5% Polyvinylpyrrolidone 40 (PVP). For isolation, two types of Dumont tweezers (World Precision Instruments) were used: #5 (tip 0.10 x 0.06 mm) – to hold up the oocyte at one particular position; and #55 (tip 0.05 x 0.01 mm) – to penetrate the cell and open it up. The single oocyte was fixed between the two legs of tweezers #5, whilst the fine tweezers (#55) were used to gently pierce the oocyte just off the equator line, into the darker coloured tissue. The fine tweezers were then

slowly opened up to enlarge the tear in the oocyte. This was done ensuring that the tweezers were held perpendicular to one another at all times (Figure 2-1 c, d). After enlarging the hole (Figure 2-1 e), the oocyte was pushed, using tweezers #5, from the side of the oocyte situated opposite to the tear, to make the nucleus protrude from the cytosol (Figure 2-1 f, g). The nucleus was washed away from the cytosol into the surrounding medium using a pipette functionalised with a glass capillary tip (Figure 2-1 h). It is inadvisable to touch the nucleus with the tweezers or to let the air interfere with it, to prevent it from being damaged. The excess cytosol on the nucleus was washed away by continuous pipetting. This is an important step which helps to avoid contamination during the microscopy measurements. The isolated nucleus was transferred to another Petri dish with NIM containing 1.5% PVP. Nuclei were transferred using the glass capillary tip only.

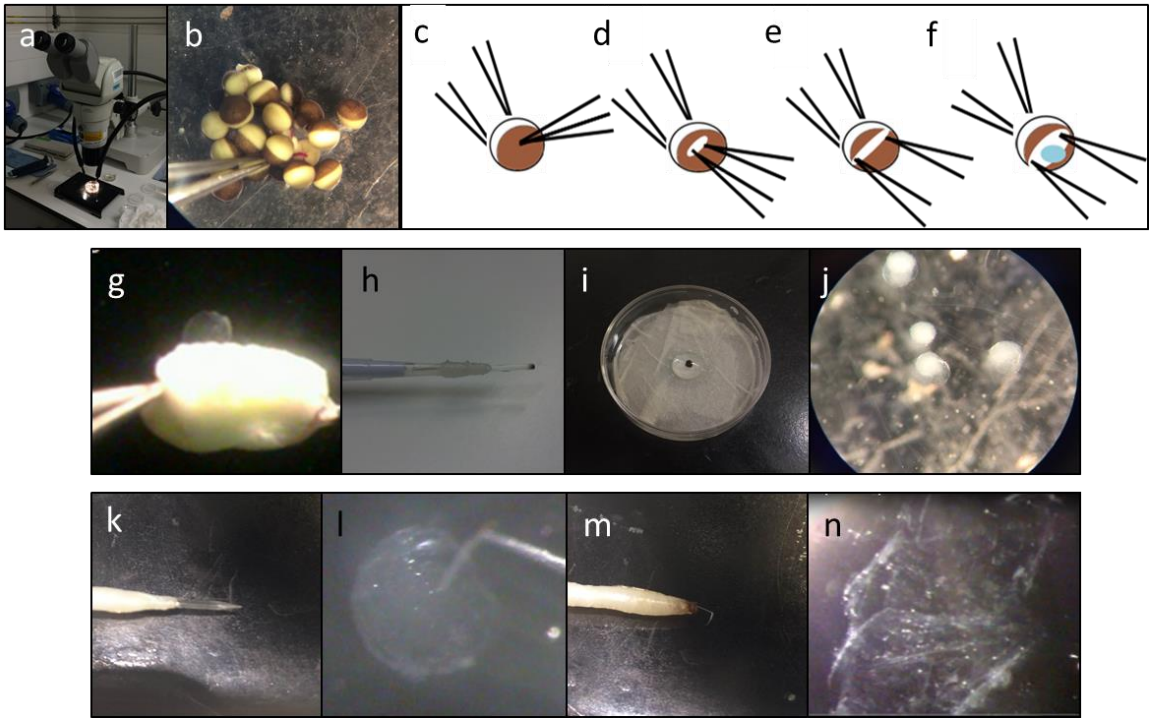

Figure 2-1 a) a stereomicroscope; b) manual defolliculation of oocytes connected with their ovarian follicles. Schematic representation of nuclei isolation using two pairs of tweezers; c) fixation of oocytes with tweezers; d) piercing the oocyte in the area perpendicular to the "equator" with the sharpest tweezers and (e) widening up the hole by opening the tweezers; f) pushing the back of the oocytes with the blunt tweezers to squeeze out the nucleus; g) nucleus popping out of the oocyte; h) glass pipette tip connected to the 200 µl plastic pipette tip with parafilm. The end of the tip was exposed to fire to smoothen the glass tip; i) Petri dish with damp tissue at the bottom to store the

glass coverslip with the sample; j) swollen nuclei in NIM; k) glass rod with a rounded end; l) the nucleus pierced with a metal needle; m) the metal needle as a hook; n) isolated nuclear envelope on a glass coverslip. Images in (g), (l) and (n) are courtesy of Munster Institute of Physiology, Germany.

2.1.2 Nuclear envelope isolation

Prior to the isolation of the nuclear envelope, coverslips were cleaned in 70% EtOH, rinsed in pure water and dried with Kim-wipes. Afterwards, they were incubated with 60 µl of 0.01% Poly-l-Lysine (Sigma-Aldrich, UK) for 20 minutes and washed with NIM. The coverslips were stored in a humid Petri dish (Figure 2-1 i). For the AFM samples the coverslips should be marked with a small spot on the underside of the coverslip with a black indelible marker to identify the area for isolation; this also helps to find the sample on the AFM camera when imaging.

The isolated nuclei were placed into the Petri dish with NIM for about half a minute (Figure 2-1 j). When the nucleus had started to swell, it was gently pipetted a few times and transferred onto the coverslip, pre-treated with Poly-l-lysine. The nuclei were then gently pressed with the rounded point of the glass needle (Figure 2-1 k) to attach them to the substrate. When the chromatin detached from the membrane, the nucleus was pierced with a metal needle (Figure 2-1 l, m). By dragging the needle across the nucleus, the membrane was ripped, so that the chromatin can be pulled out from the nucleus; meanwhile, the membrane was stretched in the direction of the needle. The remaining membrane was spread as flat as possible with the cytoplasmic side facing upwards, with special care taken to flatten the edges. The centre of the membrane was left untouched to prevent it from being damaged prior to imaging (Figure 2-1 n).

Next, the NIM buffer was changed to NIM supplemented with 8% PVP to attach the NE to the glass. For further AFM measurements, the sample was stored overnight at 4^{o}C in a humid Petri dish. If fixation was needed, the sample was incubated in 1% glutaraldehyde for 30 minutes the next day, followed by a wash in NIM 8% PVP. Prior to AFM measurements, the buffer was changed to NIM once again. The same procedure was repeated for each nucleus.

2.1.3 Instrumentation for nuclear envelope preparation

Some of the tools were adapted specifically for the purpose of nuclear isolation such as needles and glass capillary tips. This section describes the fabrication, handling and cleaning of the tools used for nuclear isolation.

Fabrication of needles for nuclear envelope preparation:

The narrow end of a glass Pasteur pipette (150 mm in length) was filled with an epoxy glue reaching a depth of 5-7 mm. A thin needle (or Minutien needle) was inserted into the tip using tweezers so that only 5 mm of the needle was protruding. This was left for 2 days to allow the glue to dry. Afterwards, the end of the needle was bent into the shape of a hook using tweezers under the stereomicroscope.

Fabrication of a 'capillary' for nuclei transfer:

Since the nucleus is a very delicate material, it requires careful handling. In order to transfer nuclei carefully from one buffer into another a thin glass capillary tip should be used. It can be made by taking a glass capillary of 5 cm in length, with outer diameter 1.65 mm and inner diameter 1.1 mm; and a regular tip of volume 200 µl. The regular tip was cut at the top so that the capillary can go through it. The capillary was protruding from the tip by 3 cm, and parafilm was used to firmly bind them together. The end of the capillary was smoothed using the flame from a Bunsen burner.

Coating of materials with Bovine Serum Albumin (BSA)

Incubation of tools in 1% BSA prevents adhesion of proteins to their surfaces [111]. Small petri dishes (diameter 35-40 mm, height 10-20 mm) were filled with 700 µl of 1% BSA solution and left overnight at 4^{o}C. The next day before the experiment, they were upturned onto tissues, and left to air-dry for 30 min. Alternatively, dishes may be incubated for at least 2 hours at room temperature and then dried for 30 min. Needles are incubated in a horizontal position by filling a test tube (1.5 ml) with 500 µl 1% BSA. Needles are always kept in 1% BSA, at room temperature. The same procedure should be undertaken for tweezers: one Eppendorf vial (1.5 ml) for each pincer (tip), should be incubated one hour prior to experiments. Capillaries for nuclei transfer are incubated in a vertical position in a test tube filled with 500 µl of 1% BSA. Every day, it

is necessary to check the amount of solution in the vials to ensure they do not dry out (otherwise the needles and capillaries will stick to the vials).

Cleaning tools

After the experiment has been completed, tool cleaning should be undertaken. The tweezers were cleaned by wiping them with ultrapure water. Needles were cleaned by scratching their surface at the edge of the tweezers to remove the pieces of membrane and chromatin which were attached. Capillaries do not require the cleaning procedure: the pipetting in NIM is enough.

2.2 Preparation of nanopore devices

The fabrication procedure was performed in collaboration with Imperial College London, Chemistry department. The aim of this preparation was to develop a channel lined with a ring of gold: a metal which enables protein adsorption.

2.2.1 Fabrication of nanopore devices

This section describes the fabrication of the nanopores, which was carried out by Dr. Agnieszka Rutkowska and Dr.Joshua Edel from Chemistry Department, Imperial College London.

A nanopore is a hole or a channel made from biological or solid state materials. In this project silicon nitride (Si_3N_4) was used as a substrate to prepare a nanopore device. The nanopore may vary in size from 1 to >100 nm. The channel could be conical, cylindrical or hour-glass shaped depending on the preparation method [112], [113]. In this work the nanopores were prepared using the focused ion beam technique.

The pores were produced on a membrane fabricated from SiO/Au/Ti/SiN with a total thickness of 210 nm. The membrane was held on a 300 μm thick silicon layer with a 75 nm layer of Si_3N_4 coated on both sides. Figure 2-2 (a) shows the image from the AFM camera of the nanopore device. The part of the device that appears as a blue square is a membrane, 70 μm x 70 μm in size. Figure 2-2 (b) illustrates an SEM image of the membrane with an array of pores regularly spaced at a distance of 4 μm.

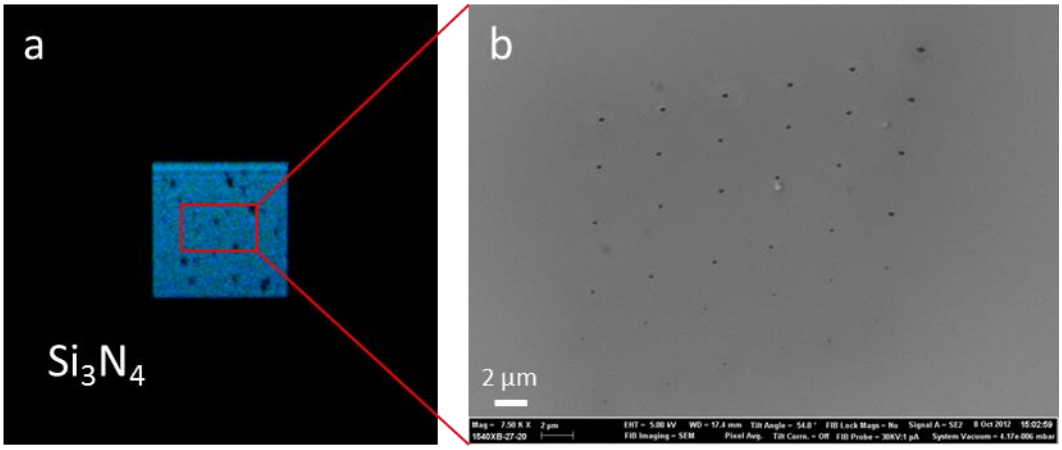

Figure 2-2 a) A JPK Nanowizard camera shows the nanopore device from underneath. The blue square represents the membrane; (b) An SEM image of the membrane from above, showing the nanopore array (SEM image: courtesy of Dr. Agniezska Rutkowska).

The fabrication process of the membrane started by coating the silicon wafer - on both the top and bottom surfaces - with silicon nitride (75 nm) using plasma enhanced chemical vapour deposition (Figure 2-3 a). The bottom surface of the newly deposited silicon nitride was carved by reactive ion etching (Figure 2-3 b). The titanium (3 nm) and gold (100 nm) were deposited by a physical vapour deposition technique on top of the Si wafer (Figure 2-3 c). Ti was used as an adhesion layer for the gold. The silicon surface on the underside of the device was etched using a potassium hydroxide solution (Figure 2-3 d). On top of the gold, the silicon oxide (30 nm) was deposited using plasma enhanced chemical vapour deposition. Finally, the pores were drilled on the surface using the Focused Ion Beam directed from the bottom to the top of the device penetrating the layers of silicon nitride, titanium, gold and silicon oxide (Figure 2-3 e).

The nanopores were drilled from the bottom through layers of Si_3N_4, Ti, Au and SiO_2 using the focused ion beam method (Figure 2-3 d). The shape of the channel after ion beam treatment usually appears as a cone with a larger diameter at the beam entrance [112] (Figure 2-4 a). The nanopores were characterised from the top layer (SiO_x) which is the exit site of the ion beam. Finally, a ring of gold was formed by drilling into the centre of the channel (Figure 2-4 b).

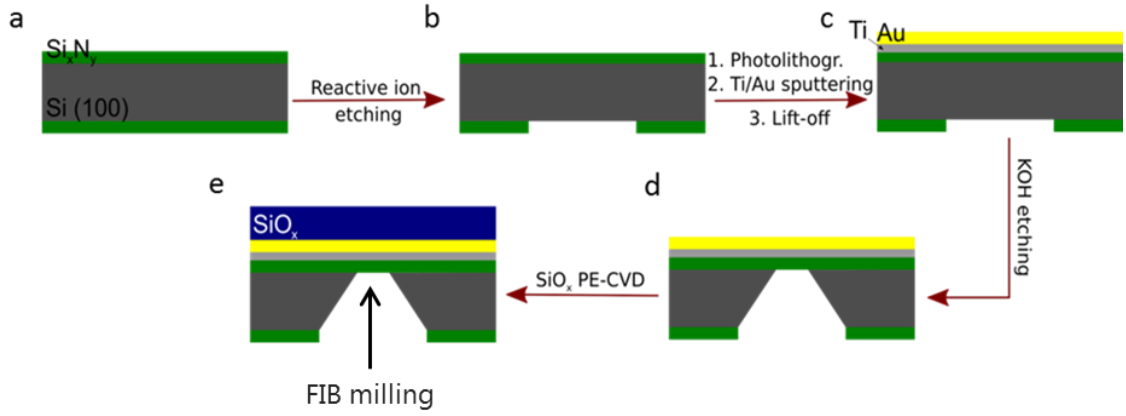

Figure 2-3 The fabrication steps for nanopore preparation: a) plasma enhanced chemical vapour deposition of Si_3N_4 onto Si wafer; b) reactive ion etching of Si_3N_4 bottom layer; c) physical vapour deposition of Ti and Au onto the top of Si_3N_4 layer; d) potassium hydroxide etching of the bottom layer of Si wafer; e) plasma enhanced chemical vapour deposition of SiO_x and Focused Ion Beam milling of the pores from the bottom of the device through the layers of Si_3N_4, Ti, Au and SiOx (Image courtesy of Dr. Agniezska Rutkowska).

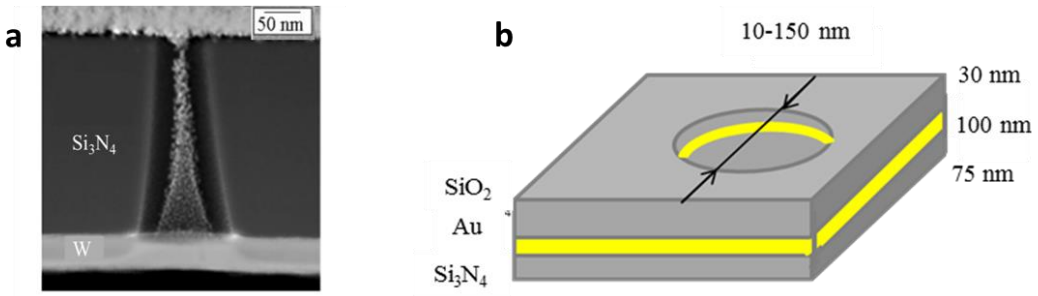

Figure 2-4 a) A TEM image of a cross section of the conically shaped channel drilled by focused ion beam in a silicon nitride layer at 1 pA current. The channel was filled with Platinum (Pt) in order to visualise the nanopore. The FIB was directed from bottom to top in this image. Tungsten (W) coating was implemented to avoid the charging effect of silicon nitride at the beam entrance [112]. *(b) Geometry of the silicon nanopore with a thin layer of gold in the middle (100 nm). The lower silicon nitride layer is 75 nm thick, and the upper silicon oxide layer is 30 nm thick. The diameter can vary from 10 – 150 nm.*

The diameter of the nanopores can be controlled by regulating the current, voltage and drilling time. With a smaller current, a smaller diameter is formed. For example, at 1 pA, and a beam exposure time of 10 s, a diameter of about 17 nm can be achieved; whereas at 10 pA with the same exposure time, the diameter is 60 nm; and at 50 pA, an

80 nm diameter pore is formed. This was done at a constant voltage of 30 kV (Table 2-1).

Table 2-1 Average diameters of pores formed using the ion beam with different values of exposure time and current, at a constant voltage of 30 kV (data were provided by Department of Chemistry, Imperial College London).

Time, s	0.5	2.5	5	10	15	20	30	40	100
1 pA			15 nm	17 nm		25 nm		30 nm	45 nm
10 pA	10 nm	30 nm	40 nm	60 nm					
50 pA	28 nm	50 nm	60 nm	80 nm	100 nm		>100 nm		

The final sizes of pores chosen for characterisation were 60 nm, 80 nm, 100 nm and >100 nm. Such a variation in size is important for testing the confinement of proteins in different volumes in order to examine the behaviour of polymer phases.

2.2.2 Cleaning of nanopore devices

Prior to imaging, the nanopore devices should be cleaned appropriately. To remove trapped air, the samples were incubated in acetone for 30 minutes, followed by subsequent washes in 75% and 50% ethanol, and rinsing in MilliQ water. The samples were dried with cleanroom cloth. Each side of the device was subsequently plasma cleaned for 5 minutes to remove any organic impurities and increase its hydrophilicity. Devices were stored in 50% ethanol.

2.2.3 Cleaning, passivation and functionalisation of gold and silicon chips

For simplicity, the gold and silicon chips were used to test the success of the functionalization and passivation processes, rather than using the nanopore devices.

The cleaning of gold and silicon chips involved the following steps: incubation in acetone for 30 minutes, rinsing with Isopropanol and then drying with a nitrogen gun.

Afterwards, the samples were exposed to UV light for 45 minutes to desorb carbon-oxygen-based compounds [114]. At the end, samples were kept for 30 minutes in ethanol and dried with a nitrogen gun.

As a passivation agent, polyethylene glycol (PEG), which self assembles on the surface, was used. To cover a silicon surface, PEG is functionalised with a silane group (2-[Methoxy(polyethyleneoxy)propyl]trimethoxysilane), to form covalent bonds with silicon. On the other hand, when passivating a gold surface, the PEG is functionalised with a thiol group (HS-C16-EG3-OMe), which can bond covalently to gold.

Silicon was passivated first to ensure no binding of yeast nucleoporin Nsp1to anywhere apart from the gold in the nanopore devices, and then the gold was passivated to guarantee that the Green Fluorescent Protein-labelled nuclear transport factor 2 (NTF2-GFP) will bind to Nsp1 exclusively. Cleaned Si chips were incubated overnight with PEG silane (40 mg/ml in absolute EtOH), and then the following day, were incubated with 600 µg/ml Nsp1 nucleoporin for 30 minutes in HEPES buffer (10 mM KCl, 90 mM HEPES, pH 7.5); then incubated for 1.5 hours in PEG-thiol (10 mg/ml in EtOH) if required; and finally with 100 µg/ml NTF2-GFP for 15 minutes prior to imaging.

The PEG was washed off with ethanol, and the excess ethanol was removed with the nitrogen gun. After Nsp1 incubation, the samples were dried with the nitrogen gun. Nsp1 has a tag containing four cysteines at the N-terminus and was provided by Dr. Murray Stewart, Medical Research Council Laboratory of Molecular Biology, Cambridge. Cysteines have a thiol group which can covalently bind to the gold surface [115].

2.2.4 Characterisation of nanopore devices and gold/silicon chips

AFM: The non-functionalised nanopore device or functionalised gold chip was glued to the glass coverslip with silver paint prior to imaging the pores. The HEPES buffer of 40 µl volume was added on top of the device. The AFM scan was conducted on a JPK Nanowizard 1 in a HEPES solution in contact mode, covering a large area of up to 25x25 μm^2. The individual pores were imaged at a scan size of 5x5 μm^2. The functionalised gold surface was characterised using Force spectroscopy on AFM.

Confocal microscopy: In order to test the capability of imaging the nanopore devices on a confocal microscope, 30 µl DiI-Alexa546 with molecular mass of 4 kDa was used. The HeNe laser with an excitation wavelength of 543 nm was used to identify the DiI signal. Prior to this, the nanopore arrays were checked with scanning electron microscopy at Imperial College London.

To test the specificity of Nsp1 binding to gold and silicon surfaces via the NTF2-GFP signal, the custom built[1] confocal microscope was used. It had a set of filters, in particular, a 488 nm StopLine® single-notch filter, and a 525/30 nm BrightLine® single-band bandpass filter, both of which were located before the detector. The single-notch filter was used to block the excitation light of 488 nm coming from the sample, whilst the single-band bandpass filter was used to allow only emission light to reach the detector.

[1] Home-built by Dr. Alan Lowe in Division of BioSciences, UCL

Chapter 3 Characterisation Methods

3.1 Atomic Force Microscope (AFM) operational principles

The sphere of influence of atomic force microscopes has expanded a lot since its invention in 1985 by Binnig [116]. AFM is a part of the scanning probe microscopy family and is able to measure both insulating and conducting materials. It can also scan samples in ambient air and liquid . The ability to scan at high resolution and its power to sense forces at the molecular levels in buffer solution makes AFM a valuable tool for the characterisation of biological samples. Thus, high resolution images of biological substances such as cells, nuclear membranes, proteins and nucleic acids can be obtained. Resolution can also be improved by increasing the sharpness of the probe and the stability of the system. Moreover, AFM can be utilized in force spectroscopy mode, which allows measurements of intramolecular forces, acquisition of elasticity and adhesion data, providing new vision into structural and functional properties of biological samples.

The main compartments of the AFM setup are: piezoelectric scanner, a signal detecting system which consists of a photodiode and a laser beam (Figure 3-1), a cantilever with mounted sharp tip (of diameter 2 - 10 nm) and a feedback system to maintain the cantilever's deflection. The cantilever's deflection gives information about the sample, such as the mechanical properties and the topography of the surface. The cantilever bends when the tip is in contact with the sample. The deflection is detected by the 4 quadrant photodiode using a laser beam which is reflected from the gold/silver coated back of the cantilever, which serves as a mirror, to the photodetector. The photodiode measures the deflection of the cantilever in both the vertical and the lateral directions by comparing the readings from the top-bottom segments and right-left segments respectively [117].

The signal, measured at the photodiode, is analysed by a feedback circuit. The feedback loop controls the force applied to the sample. If the force can be maintained at the set value, then the cantilever deflection can be maintained as well, since the cantilever behaves as a spring.

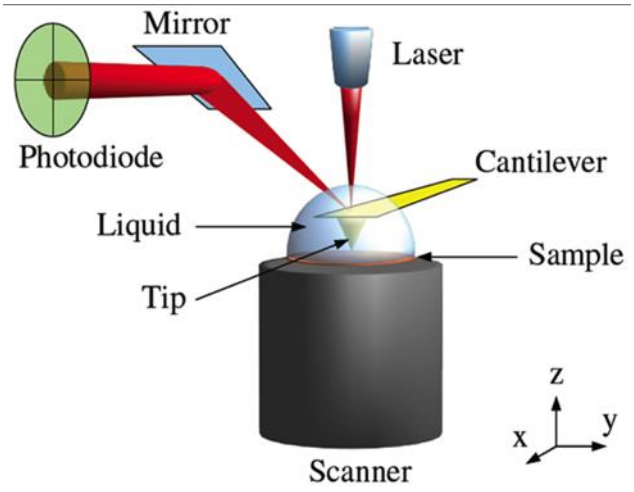

Figure 3-1 The AFM set up. The laser is focused onto the reflective back of the cantilever and passes onto the photodiode and is then processed by a feedback circuit to maintain the defection of the cantilever. The piezo tube ensures the movement of the sample along X, Y and Z – axes [118].

The main parts of the feedback loop along with cantilever and optical system are a feedback circuit and a piezo scanner. The optical system obtains the height of the surface; the feedback circuit maintains the deflection of the cantilever at a set value by managing the voltage applied to a piezo scanner (Figure 3-2). In many AFM systems the piezo scanner is made in form of a cylinder (and hence called piezo tube) which provides high stability and controls the movement of the sample in the X, Y, Z-directions during measurements. The tube is made of piezocrystals which tend to expand or contract when there is a voltage gradient applied [119]. In the tube there is a cylindrical whole piece of one electrode which expands or shrinks in the Z-direction. It is surrounded by 4 other electrodes which are responsible for the X and Y-movements. When a voltage is applied to the electrodes the piezoceramics extend or contract to move the sample in three dimensions. The measurement of the piezo tube movement along Z-axis corresponds to sample height. The images can be obtained faster if the feedback system can correct the variations of cantilever deflection faster.

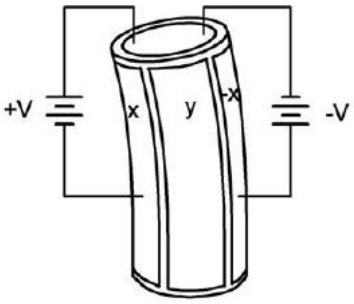

Figure 3-2 A tube scanner. If the voltage is applied to one of the external quadrants the tube tilts away from the central axis. In case of voltage application to the inner electrode, the tube moves in Z-direction (Image courtesy of Park Systems, Korea)

The closer the tip approaches the sample surface the larger the attraction between the surface and the tip (Figure 3-3). At a distance of few nanometres there are far range forces exerted on the tip such as: van der Waals forces, electric and magnetic, and capillary forces. These far range forces are usually greatly reduced in salt-containing aqueous solutions. When the distance between the tip and the sample becomes about a few angstroms the repulsive forces dominate.

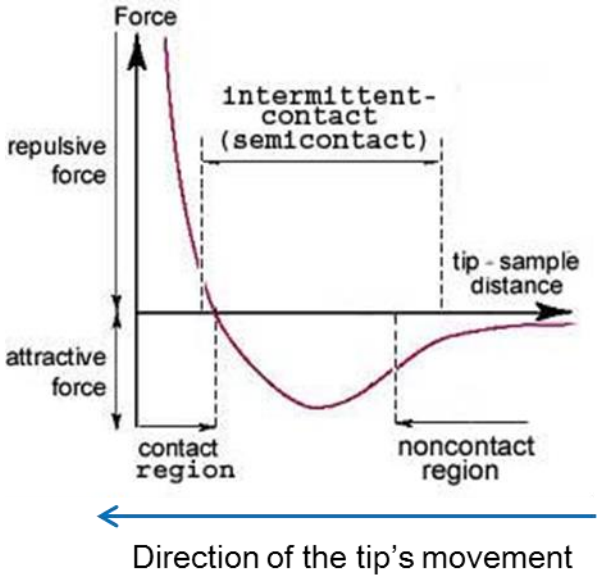

Figure 3-3 The force diagram, showing which interactions tip and sample undergo while the distance between them is getting smaller. There is no cantilever deflection at non-contact region. However, at a smaller tip-sample distance (few nm) the attractive forces are prevalent (intermittent contact) whereas when it comes to a few angstroms the repulsive forces are preponderate (contact region) [120]

3.1.1 AFM Instrumentation

In this project two types of the AFM systems were used: A Multimode (in versions IV and VIII) of Bruker (Santa Barbara, CA, USA) and a Nanowizard 1 (JPK Instruments, Berlin, Germany).

Multimode AFM

The Multimode consists from the following parts: a controller; a base which contains displays of the voltages from photodetector; a scanner, which serves as a stage for a sample; an AFM head, which contain the fluid cell, the laser system and the photodiode (Figure 3-4).

In the Multimode the piezo scanner is responsible for the movements of the sample in X, Y and Z directions. It is based on the open loop system feedback system which means the piezo scanner does not have sensors to verify the sample position during the measurement and where necessary correct the drift and creep.

The scanner also acts as a sample holder, with a magnetised top to attract the metallic disk where the sample is mounted on. The sample holder is circular shape and of 16 mm diameter, which implies an upper limit for the sample size.

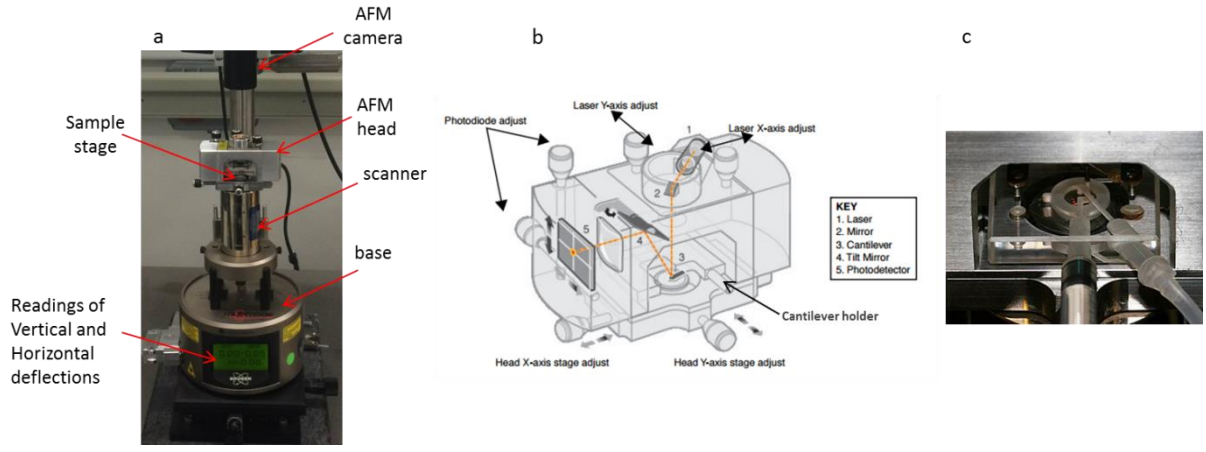

Figure 3-4 a) AFM setup with main components; b) AFM head, the orange line shows the path of the laser reflecting from the cantilever into the photodiode; c) fluid cell for cantilever fixation with channels for liquid. Images (b) and (c) are courtesy of Bruker, USA.

JPK AFM

The main parts of the JPK Nanowizard 1 are: a controller, an AFM head, which encloses all the optics, a flexure-based piezo scanner to move the tip and the fluid cell holder; sample stage which is stationary and move only in X and Y directions (Figure 3-5). The Nanowizard can be mounted on an inverted fluorescent microscope, which is often useful for biological samples.

The ('closed-loop') piezo scanner contains position sensors, which allows for an accurate position of the sample over longer times and also after large lateral offsets. This is an advantage when the same areas should be imaged after the tip retracts, since AFM accurately records the coordinates of the previous scan area. The scan size may reach up to 100x100 μm^2. The sample stage is adapted to mount a rectangular glass coverslip.

The force mapping option on the Nanowizard 1 can create a rectangular or square grid of the points to be scanned, where the force measurements are taken from each pixel. In addition, force measurements can be recorded at individually selected lateral positions on the sample.

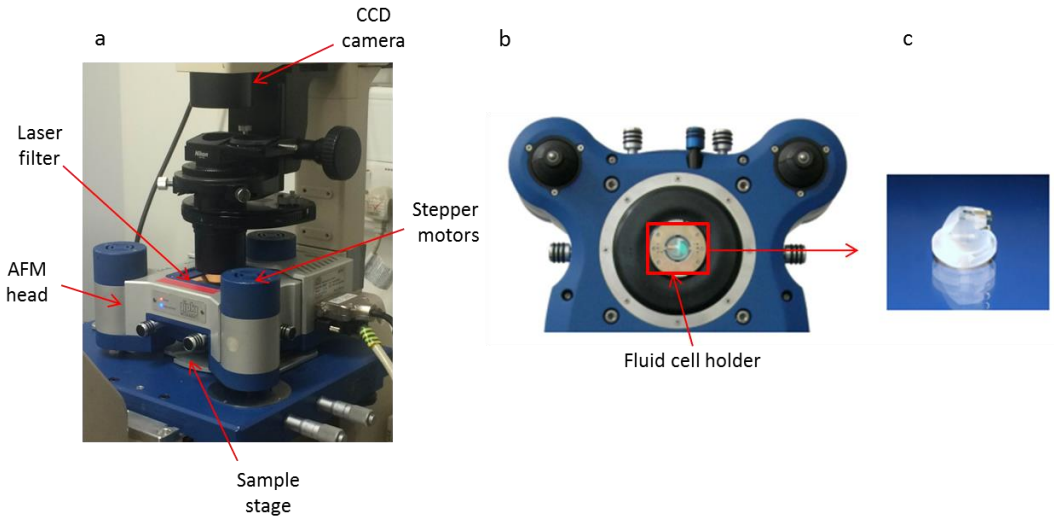

Figure 3-5 a) AFM setup with main components; b) AFM head, containing the optics including the laser, the photodiode, mirrors; also it has the piezo sensors to move the tip; red square is a place for the fluid cell; c) the fluid cell with the cantilever fixed with the clip. Images (b) and (c) are the courtesy of JPK Instruments, Germany.

Cantilevers

During the AFM experiments in this project we used three types of the cantilevers (Figure 3-6). The characteristics of each cantilever tip are shown in Table 3-1. Of the MSNL and MLCT cantilevers, from the 6 available levers the E and F cantilevers were used (Figure 3-6 c). The MSNL and MLCT cantilevers are similar in the characteristics such as resonance frequency, spring constant and a tip height, but different in the tip diameter, which is specified as 4-24 nm for MSNL cantilevers and 40-120 nm for MLCT cantilevers. The ShoconG-SS cantilever is mounted as a single lever on its support chip, and is of rectangular shape. It is qualified as a super sharp high aspect-ratio tip, with a tip diameter of 4-8 nm.

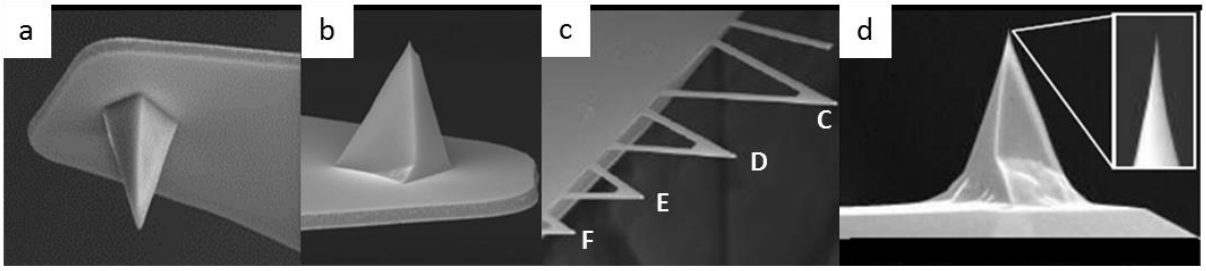

Figure 3-6 a) MLCT cantilever; b) MSNL cantilever; c) an array of MLCT/MSNL cantilevers on the chip (Images are courtesy of Bruker, USA); d) ShoconG-SS cantilever (Image courtesy of AppNano, USA).

Table 3-1 Characteristics of the cantilever tips[2]

Characteristics of the tip	**MLCT-E/F**	**MSNL-E/F**	**ShoconG-SS**
Material	Silicon Nitride	Silicon Nitride	Silicon
Shape	Pyramidal	Pyramidal	Pyramidal
Tip diameter (nominal), nm	40	4	4
Tip height, µm	2.5 - 8	2.5 - 8	14 - 16
Resonance frequency (nominal), kHz	38/125	38/125	28

[2] MSNL and MLCT cantilevers are manufactured by Bruker (Santa-Barbara, US); ShoconG cantilevers are manufactured by AppNano (CA, US)

Spring constant (nominal), N/m	0.1/0.6	0.1/0.6	0.1

3.1.2 Operational modes

AFM can operate in various different modes. The following sections describe the main modes that are relevant for this thesis: Contact, Tapping, Peak Force Tapping, Peak Force Quantitative Nanomechanical Mapping and Force Volume.

Contact mode

Contact mode is the most common and conceptually simplest method of AFM imaging. It is used for large scans of rigid samples. During imaging the probe is in constant contact with the sample. The topography of the sample surface is acquired by adjusting the Z-piezo to keep the deflection of the cantilever constant at a predefined setpoint.

Typical value for cantilever spring constant is in the range of 0.005-50 N/m [121]. Since the tip is in continuous contact with the sample during the lateral scan motion, there are relatively high lateral forces. This can affect the surface of the samples that are being imaged.

Tapping mode

Tapping mode largely avoids the lateral forces encountered in contact mode. It is therefore convenient to study the biological samples, in particular those that loosely bound to the substrate.

In tapping mode, the cantilever oscillates near its resonance frequency and is only in intermittent contact with the sample (hence the reduced lateral forces). It can be actuated by many different means such as acoustic [122], thermal [123], or magnetic actuations [124]. When the cantilever is actuated at constant amplitude and frequency, the tip-sample interaction follows from a change in the oscillation amplitude and phase. When the tip touches the surface, the amplitude of the oscillation reduces, and increases again when the tip moves away from the surface. A feedback loop adjusts the Z-piezo to keep the amplitude constant, and – as for contact mode – the sample topography follows from the position of the Z-piezo during the scan.

Force Volume

The Force Volume mode is used to simultaneously collect the topography information and nanomechanical properties of the sample, by recording the force as a function of Z-piezo position on a grid of points on the sample surface. One of the pioneering works of biomolecular force mapping was done on the enzyme lysozyme. It was demonstrated that a single protein can be differentiated on the force curve [125]. The force resolution can be as low as 10 pN, or even better if a smaller cantilevers is used [101]**.**

To record the force curves, the tip-sample distance is varied by ramping the Z-piezo. It follows a sawtooth trajectory between being in contact with the sample and withdrawal. (Figure 3-7). The rate of the linear ramping is restricted to low frequencies 1-10 Hz (i.e. 1-10 ramps per second), since higher rate tend to cause excitation of the mechanical resonance from the cantilever and/or the scanner. The ramp size is set such that the tip can completely retract from the sample, yielding a well-defined baseline of zero force where the tip is sufficiently far from the sample to not detect any force due to the presence of the sample surface. The cantilever acts as a force sensor, and typically a trigger threshold is set to define the maximum cantilever deflection and thus the maximum force and indentation into the sample. The lateral movement of the tip takes place when the cantilever retracted from the sample, thus reducing the load of lateral forces on the sample surface.

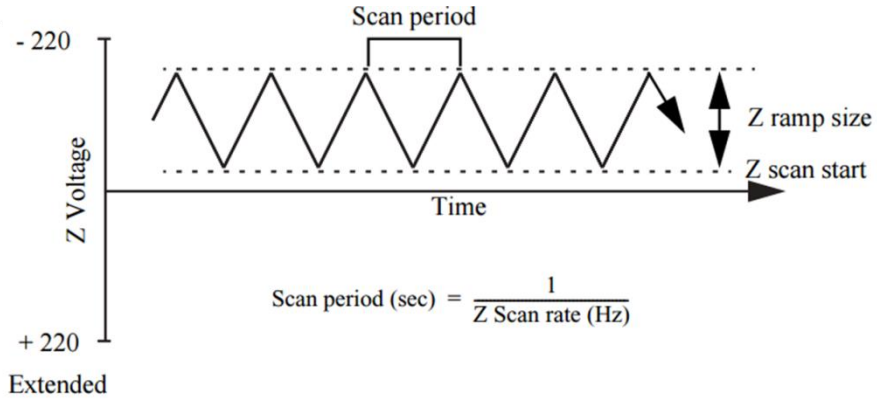

Figure 3-7 The movement of the tip over time during ramping over the surface represented in the triangular wave [126].

Thus, acquired force curves relate the measured force to the position of the tip with respect to the sample. It thus describes the interaction force between the tip and the

sample, providing information on adhesion and stiffness, as well as on chemical and electrical properties of the sample [127].

Force curves can be divided into six parts (Figure 3-8): during the approach stage (1) (non-contact region), the tip moves towards the surface with constant velocity; in the contact region (2), the tip may experience long-range attraction to the surface (electrostatic, capillary, van der Waals forces [128]); on closer approach (3), the force curve shows the short-range repulsion between the probe and the sample, the tip is now in contact with the sample surface; on retracting the cantilever, the tip re-enters the region of attractive forces again, which due to tip-sample adhesion can be larger than during the approach (hysteresis, 4); on further retraction, the tip snaps back from the surface (5), returning to its initial state with no detectable attraction and zero force applied. The local sample stiffness is derived from the force curve and specifically from the contact region; whereas the hysteresis provides information on the adhesion or binding forces that need to be overcome to release the tip from the sample [129], [130].

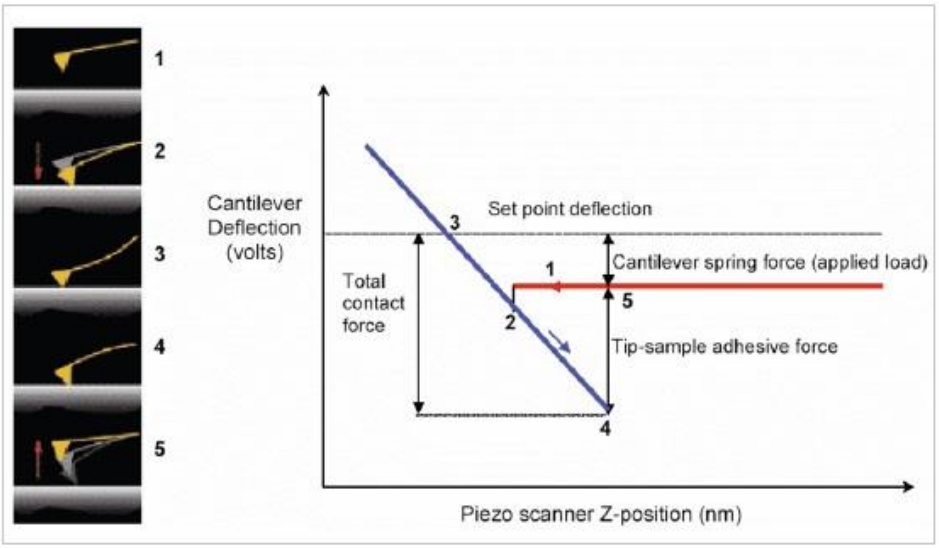

Figure 3-8 Schematic of a force curve. The horizontal axis on the diagram represents the Z-piezo position. The vertical axis represents the force detected by the cantilever. The tip approaches the surface from right to left in the diagram. The flat line indicates that there is no deflection of the cantilever (hence zero force) when the tip is away from the sample (1). At some point (2) the transition from non-contact region to contact region occurs under long range attractive forces: electrostatic, capillary and van der Waals forces. Region (3) represents repulsion forces which appear when the tip approaches the surface within a few nanometres. On retracting the tip from the surface, it again experiences far range attractive forces (4). In order for the tip to retract from

the sample, the adhesion should be overcome (5), and the tip returns to its initial state with no deflection. The image courtesy of Bruker, USA.

In Force Volume mode, the scanned surface is visualised in a topography channel, while the force curves are being collected. A force curve is stored for each pixel of the image. Taken together, the measured force curves form a two-dimensional array of curves (i.e., a three-dimensional array of force data points).

There are two main drawbacks encountered during these measurements. Firstly, because the force acquisition is relatedly slow (e.g, typically >10 minutes for a 64x64 pixel per image), thermal drift can lead to a significant inaccuracies in the measurement of the sample topography. At the start of the experiment, it usually takes 20-30 minutes for the system to stabilize before one can collect the force curves. Secondly, because the measurement time is long, the experiments are rather time-consuming.

Peak Force Tapping and Peak Force QNM

Peak Force Tapping is essentially a rapid version of Force Volume mode. Force curves are continuously recorded at frequencies 1-8 kHz, as illustrated in Figure 3-9 (a) and (b). Compared to Force Volume mode, the speed enhancement is largely due to the sinusoidal instead of sawtooth tip trajectory.

This sinusoidal shape is less prone to excite higher mechanical resonances of cantilever and/or scanner, and reduces the approach speed when coming closer to the surface [131]. The ‘peak force’ is defined as the maximum force measured with respect to the baseline reference. Since the maximum force and the baseline are measured continuously, this provides a measurement of the tip-sample interaction that is highly robust against cantilever drift. The peak force is kept constant by adjusting the position of the Z piezo while scanning. Peak Force Tapping mode is primarily an imaging mode, but the corresponding force curves can be used to determine Nanomechanical properties of the sample using an extension Peak Force Quantitative Nanomechanical Mapping (PF QNM).

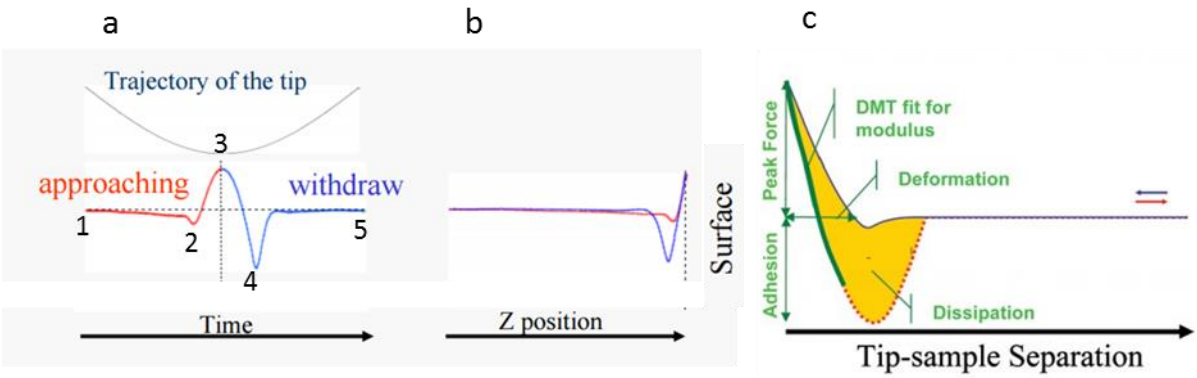

Figure 3-9 a) The motion of the tip in sinusoidal movement to collect the force curves. The trace and retrace curves are shown here as a function of time: (1) is a non-contact region during approach; (2) attraction of the tip to the surface; (3) the peak force (maximum applied force); (4) adhesion during the retract; (5) non-contact area after tip retracts from the surface; b) the same force curves shown as a relation of force over time; c) Force curve divided into sections for calculating the nanomechanical parameters. Images are courtesy of Bruker, USA.

It allows for a quantitative characterisation of the surface in terms of an adhesion and elasticity during high-resolution topography imaging (Figure 3-9 c). It is in particularly useful for fragile samples and for keeping the tip sharp, since it can use small and well-defined forces. Because of the higher speed of Peak Force QNM, this allows for nanomechanical characterisation in a way that compared to Force Volume is much less sensitive to thermal drift of the sample with respect to the tip. However, the more rapid recording of force curves usually leads to a somewhat lower signal to noise.

3.1.3 AFM Imaging

The parameters used during imaging of polymer brushes, NPCs and the nanopore devices are described in this section. These parameters include the applied force, the scan rate, the image resolution and cantilevers.

AFM imaging of the Polymer brush

The imaging of the polymer brushes grafted onto silicon surface was done on the AFM Multimode IV in tapping mode, using pyramidal shape MLCT-E cantilevers with a (relatively blunt) tip of 40 nm diameter, and a spring constant of 0.1 N/m. A large sample area 5x5 μm^2 was scanned using the lowest possible force at a scan rate of 1.97 Hz.

AFM imaging of the NPC

The NPC images were acquired on the AFM Multimode IV in the tapping mode. The nuclear envelope was attached to a glass substrate and the cytoplasmic side of the nuclear envelope was imaged. Prior to imaging, a flat area of the nuclear envelope was found aided by the optical top view of the sample. A large scan range of 5x5 μm^2 was imaged with 200 µm long, silicon-nitride cantilevers with pyramidal tips with a diameter 4 - 24 nm at their end (MSNL-E,-F cantilevers, Bruker, US). Scan line rates were 1 - 2 Hz. The nominal spring constant value of the cantilevers varied from 0.1 - 0.6 N/m.

Peak Force Tapping imaging of NPCs was done on a Multimode VIII system (Bruker, Santa-Barbara, US) with MSNL-F cantilevers. Force curves of 1024 data points were acquired in this mode, oscillating the tip-sample distance at 2 kHz frequency and an amplitude of 40 nm. Forces were applied up to 100 pN, sufficiently low to prevent damage to tip or sample. The line scan rate was 1-1.5 Hz.

The images from both microscopes were analysed on NanoScope Analysis software (Bruker, US). Prior to the height and width measurements the images were flattened, applying a baseline correction which eliminates image artefacts due to sample tilt and scanner drift in the Z direction.

AFM imaging of nanopore devices

Large scan areas 25x25 μm^2 of the nanopore device were imaged on a JPK Nanowizard 1 in contact mode. MSNL-type cantilevers, in particular the C and D-cantilevers (tip diameter ~4-24 nm, height 2.5-8 µm), were used. For individual nanopore imaging the scan size was reduced to 5x5 μm^2. To detect the presence of proteins on the sample surface, the sample was probed in force spectroscopy mode. The maximum applied force was ~500 pN. The images were analysed using JPK Data Processing software (JPK Instruments AG, Germany), in particular for extracting the topography profiles of the nanopores.

3.1.4 AFM Force Spectroscopy on NPCs

Procedure of collecting Force curves from NPCs

In this project, the stiffness map from the NPC was required to compare the stiffness in the NPC central channel to the stiffness of a polymer brush. Individual NPCs were probed by a MSNL-E and ShoconG super-sharp tips (diameter <8 nm), using the Force Volume mode of the Multimode IV. Moreover, to assess the new faster method of acquiring the force data, Peak Force QNM mode was used on scanning NPCs on the Multimode VIII.

The appropriate area of the sample was selected for imaging using the Multimode camera, where the sample surface should appear darker than the glass surface. The dark colour indicates firm adhesion to the glass (Figure 3-10).

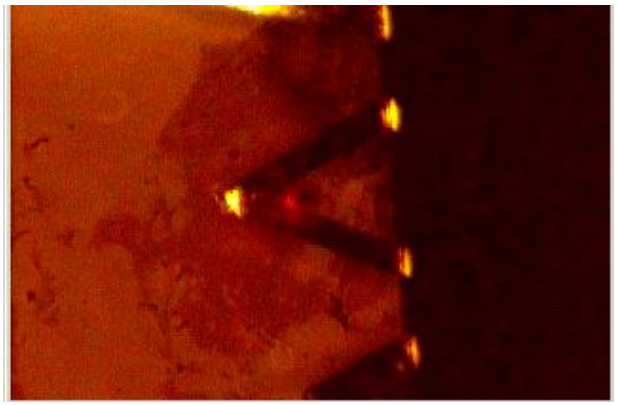

Figure 3-10 View from AFM Multimode IV camera on sample surface with an MSNL-cantilever approached. The sample surface appears on the camera as dark brown, which indicates adhesion of the nuclear envelope to the glass surface.

Prior to any force volume measurements on the NPC, the sample was imaged to reveal roughness and contamination (Figure 3-11 a). The images were obtained with regular MSNL-10 cantilevers, in particular, the E and F-cantilevers (Bruker AFM Probes, CA). Images were initially acquired in tapping mode, at a resonance frequency of 7-10 kHz and an amplitude setpoint of 800-1000 mV, before/after Force Volume measurements. Peak Force QNM was carried out with a 2 kHz oscillation frequency and 40 nm Peak Force amplitude. The scan size was about 3-5 μm at 256 samples per line. As soon as a few scans were acquired and the flatness and cleanliness of the sample was ensured

(Figure 3-11 b), the cantilever was exchanged for a ShoconG-SS super sharp cantilever (AppNano, USA) with an aspect ratio > 3.5:1, tip diameter < 8 nm.

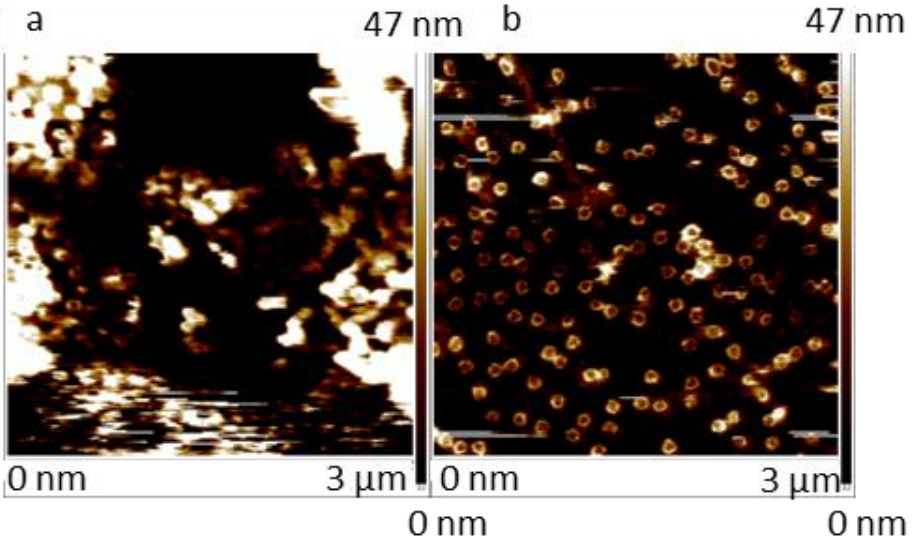

Figure 3-11 Topography AFM image of 3x3 µm^2 scan size. a) rough and messy sample surface; b) clean sample surface covered with NPCs. Images were acquired in Tapping mode with MNSL-cantilevers at 256 lines per samples on Multimode IV.

Force Volume protocol

With the new cantilever the operation was started with the "false" approach (as defined in the AFM software) in contact mode. When approached, the mode was switched from "Imaging" to "Force-Advanced" to ensure a careful engage of the tip to the surface: In this mode the cantilever approached the surface by ramping the piezo in the range of 1.6 µm, each curve followed by an 800 nm step of the approach motor, until the measured deflection reached a predefined setpoint (trigger threshold) of about 3 nm. The ramp step should be about significantly smaller than the ramp size, such that tip-sample contact was only reached by ramping the Z piezo and not by the much coarser stepping of the approach motor. The trigger channel was set to "Deflection" to indicate which channel was to be used as a trigger. The trigger mode was set as "Relative" for gentler probing since the threshold is calculated relative to free-air deflection voltage. The "Start" and "End" modes of the scan were set as "Motor Step" and "Retract" respectively. Once the cantilever was engaged, a single force curve was collected to verify if the tip had indeed reached the sample surface. The force curve should clearly show the contact point between the tip and the surface.

Afterwards, the mode was switched from "Force-Advanced" to "Force Volume". An area of 200x200 nm^2 was scanned to capture a single pore. The ramp size was changed to 100 nm, and the deflection setpoint to a few nm, to apply a maximum force of about 400-500 pN (with the cantilevers used in these experiments). In some cases, the value for the trigger threshold was increased to 5 nm for a deeper indentation. The backward velocity (the speed the tip retracts) was higher than the forward velocity (5.58 µm/s and 1.86 µm/s respectively) to reduce the total time of the measurement. The pixel resolution of the topography image and the force image were the same. For locating the pores at the sample surface, force volume data were acquired at a minimum of 16x16 pixels, and as soon as the pore was found, the number of pixels was increased to a maximum of 64x64 (Figure 3-12). At this resolution the time spent per Force Volume scan for single pore was about 12 minutes. During this time the pore might drift away due to the thermal drift. Therefore some pores can appear distorted compared to their ideal, rotationally symmetric shape as recorded in AFM images at time scales for which drift was not a significant factor.

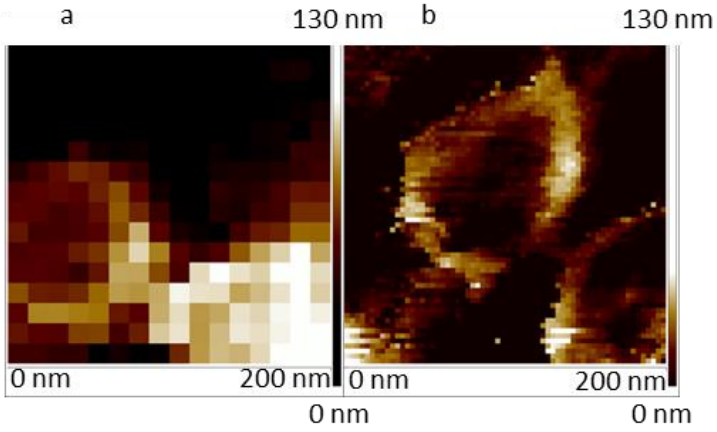

Figure 3-12 Examples of (a) 16 x 16 and (b) 64 x 64 resolution of topography image during Force Volume of the same pore scanned with ShoconG-SS super sharp cantilevers.

The same settings were used to probe the Polymer brushes, although the resolution was 32 pixels per line and three different tips were used MLCT, MSNL and ShoconG-SS.

Peak Force QNM Protocol

In Peak Force QNM, after finding the appropriate area and exchanging the cantilever for the super sharp one, the tip started approaching the surface with a Peak Force tapping

frequency of 2 kHz amplitude of 100 nm. After completion of the approach, scans of 1x1 μm^2 or 2x2 μm^2 were initiated to choose the pores that were to be scanned at higher resolution. For measurements with 2 kHz Peak Force tapping frequency, the scan size was chosen to be around 400x400 nm^2, whereas for the 0.25 kHz the scan size was 200x200 nm^2. The reasons behind these choices are the pixel resolution and the speed of acquiring the data: In Force Volume, images were recorded at 64x64 pixels for 200x200 nm^2, which can be reproduced at 0.25 kHz Peak Force tapping frequency. At 2 kHz, the same pixel resolution can be obtained for 128x128 pixels for 400x400 nm^2, without the image time becoming too long. The line scan rates were adjusted accordingly to 0.5 Hz and 1.5 Hz for the Peak Force tapping frequencies of 0.25 kHz and 2 kHz, respectively. The maximum force applied was 400-500 pN. An individual force curve in the Force Volume requires ~64 ms, while in the Peak Force QNM it takes from 0.45-3.6 ms. Thus, with Peak Force QNM multiple pores (up to 24, 128x128 pixels) can be imaged in the time that is required for imaging a single pore in the Force Volume (at 64x64 pixels) with the same resolution (1 pixel = 3.13 nm).

3.1.5 The force curves analysis

The raw force curves represent the cantilever deflection (in Volts) as a function of *Z-piezo position* (in nm). To extract nanomechanical properties from these curves, they must be converted into curves representing force versus *tip-sample separation*. The deflection is converted into force by multiplying the deflection (in V) by the deflection sensitivity (nm/V) and the spring constant of the cantilever (nN/nm); and the tip-sample separation is obtained by adding the deflection (in nm) to the Z-piezo position.

Although the spring constant is given by the manufacturer, it is given as a range, and so each cantilever requires calibration individually. This is done at the end of an experiment by pressing the tip against a hard surface (usually glass) and detecting the Z-piezo movement (in nm) that is required per V of deflection signal.

Contact point identification

The contact point is the Z-position at which the tip first interacts with the sample surface. This was identified in the force curves via the following steps: the force curve is divided into 20 equal intervals and the mean and standard deviation of the force values are saved for each interval. The minimum standard deviation is multiplied by a

factor (in this case two), and used later as a reference. The absolute difference between the adjacent mean values is calculated and compared against the reference. If the difference between adjacent mean values is less than the reference value, it is assigned the value 0; if it is greater than the reference value, it is assigned a 1. If the result is a series of zeroes (resulting from the baseline region), followed by a series of ones (from the contact region), with only one transition between them, the force curve is cropped, taking only the baseline region and the first interval after the transition point (Figure 3-13 a). If there is more than one transition point, the script returns to the beginning of the analysis, divides the force curve into 19 intervals, and repeats the analysis. This process continues, reducing the number of intervals by one with each successive failure, until only one transition point is found, and the force curve is cropped. The result is a force curve containing only the baseline region and the initial indentation after contact, ignoring much of the non-linear behaviour of the force curve at deeper indentation. Once this has been achieved, a linear piecewise function is fitted - by the least-squares regression method - to the cropped force curve, which is presumed to contain the contact point. A horizontal line is fitted to the baseline, and a sloped line fitted to the contact region, with the break point representing the contact point (Figure 3-13 b).

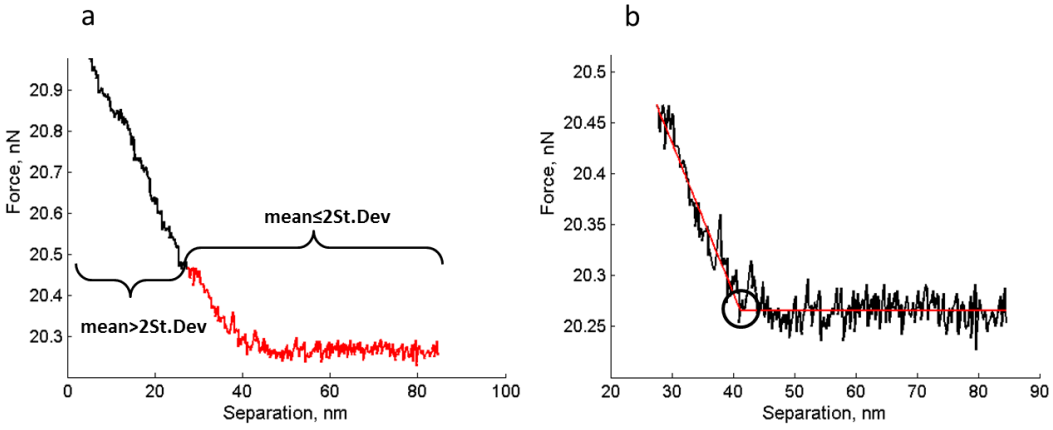

Figure 3-13 a) A close look of the force curve shown as a relationship of the force (nN) and the tip-sample separation (nm). The curve is divided into 20 intervals (final 2 shown here in black and red). The interval where the contact point located is highlighted in red and show that the mean deflection values differ by less than 2 times the reference standard deviation. For the interval in black, these differences are more than 2 times this reference. b) The 'piecewise' fit (see text) is shown as a red line. The found contact point is indicated by the black circle.

Analysis of the force curves from featureless samples

When the force-distance curves were acquired with a known contact point, the force curves were aligned to the contact point and averaged. The force curves were also fitted with either the Hertz or Sneddon model (depending on the shape of the AFM tip) – techniques commonly employed to extract an effective Young's modulus. Additionally, stiffness curves were generated by taking the numerical derivatives of the force curves. Although this analysis is simple for featureless samples, in which all the available force curves could be added together and averaged, the analysis of samples with features, as is the case for the NPC, a few more steps are required to complete the analysis.

Analysis of the force curves from the NPC

Force Volume and Peak Force QNM data of individual NPCs represent a topography image (Figure 3-14 a) coupled with force data stored at each pixel. It was important to extract the force curves from particular areas of the image, for example, to distinguish between force curves of the cytoplasmic ring from those of the central channel. Therefore, taking into account the rotational symmetry of the pore, the force curves were extracted from radial bins extending out from its central axis of rotation. However, due to the slow rate of data acquisition in imaging modes such as Force Volume, some pores appear distorted due to lateral drift, removing their rotational symmetry.

In order to restore the rotational symmetry of the NPC around the central axis, the shape of the pore's scaffold was traced manually, and assigned the radial value 1 (this bin was assigned the value of 42.5 nm, as estimated from low-drift tapping-mode AFM images). Using the polar coordinates system, radial bins with a width of 4 nm, were then created, relative to the manually traced bin on the scaffold (Figure 3-14 b). These bins were assigned an *r* value. The unindented, 'true' height image (Figure 3-14 c) followed by adding the indentation depth (as determined from the contact point in the force curves as a function of tip-sample distance) to the height images (as was recorded at the maximum force applied during the data acquisition). All force curves were aligned such that their contact point corresponded to the average true height within a shell.

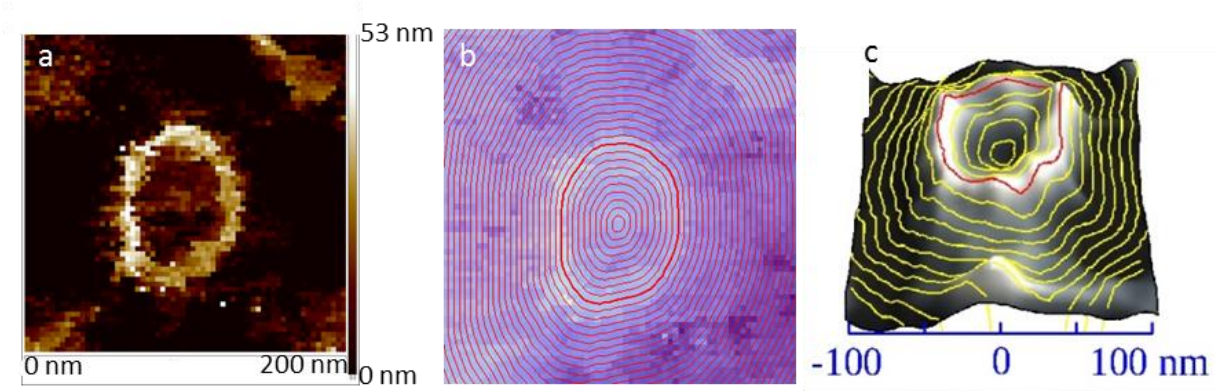

Figure 3-14 a) Flattened AFM topography image of NPC. Scan size 200x200 nm^2; b) NPC rim traced in thick red; c) 3D representation of NPC mapped with concentric circles

Building up the height cross section of the NPC

Figure 3-15 (a) shows the average force curve at R=2.3 (which correspond to a radial coordinate of 97 nm), where the contact point corresponds to the true heights in the rotationally symmetrised data. Since the images were obtained at maximum indentation force, the height indented after the contact with the surface is called a deformed height and extracted from the values of Z at the maximum force stored in the height image. The red arrows in Figure 3-15 (b) show the indentation.

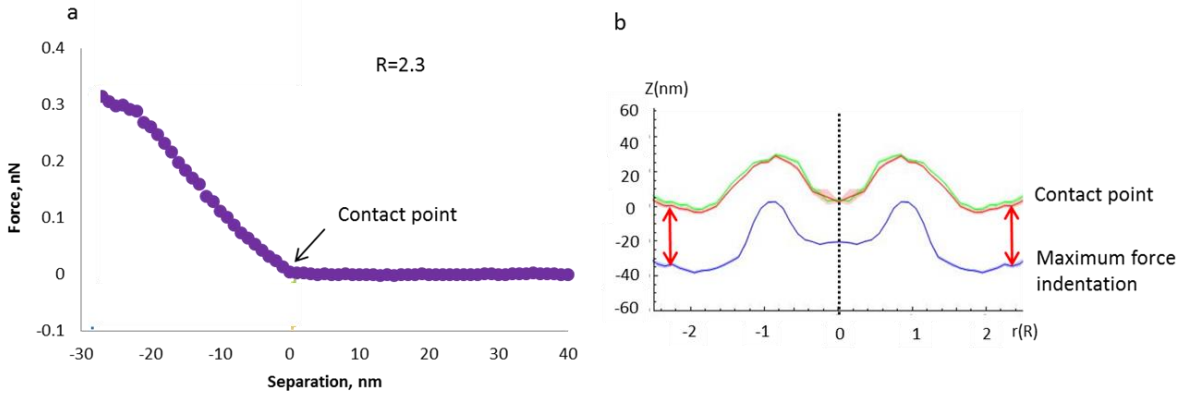

Figure 3-15 a) The average force curve produced from the shell of radius 97 nm, position R=2.3. The contact point on the force curve corresponds to the contact height (orange/green lines) shown on (b) the cross section of the NPC. The height at the maximum force indentation is a deformed height (blue). The red arrows in the cross section represent the indentation into the sample.

Building up the stiffness cross section of the NPC

The obtained derivative of the force gradient $\frac{-\partial F(r,z)}{\partial z}$ was represented as a heat map in a stiffness cross-section of the pore. Figure 3-16 (a) shows the stiffness curve from the radius of 97 nm. The information we are interested is the indentation, thus the contact and deformed heights, and also the maximum stiffness value, which is represented in a colourmap on the stiffness cross section (Figure 3-16 b). The values in the colourmap increases from blue (0 pN/nm) to red (maximum stiffness value, or a value roughly corresponding to it).

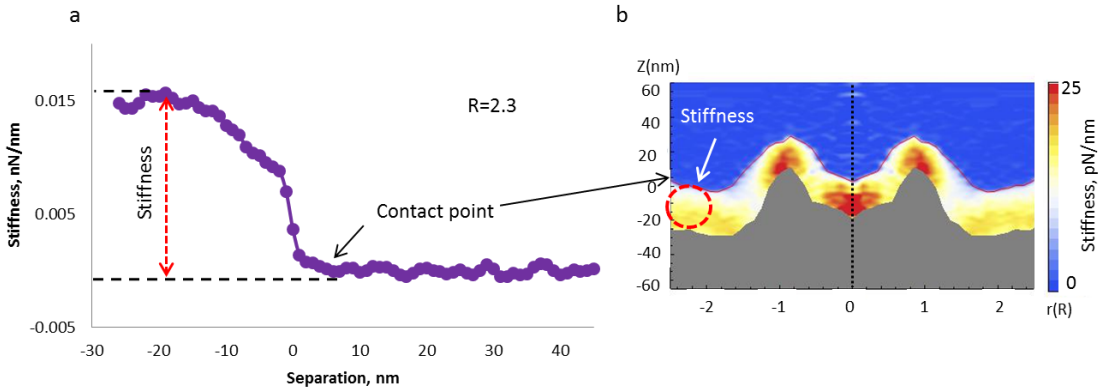

Figure 3-16 a) The average stiffness curve from the radius of 97 nm. The height data (the beginning and the end of the indentation) were used to build the height cross section in the (b) stiffness map. The actual stiffness value (marked with red arrows) is represented in the colourmap, where zero corresponds to blue and the maximum stiffness to red (25 pN/nm).

Building up the elasticity cross section of the NPC

An effective Young modulus was extracted by applying the Hertz or Sneddon model over the first 20 nm of indentation in the force curves. Figure 3-17 (a) shows a force curve, where the fit is applied to the slope of the curve. From such fits, the Young's modulus cross section of the pore was generated (Figure 3-17 b). The limits for Young's modulus were set from 0.1 to 10 MPa. It should be emphasised that this measurement of the Young's modulus only provide an effective stiffness parameter. Due to the structural heterogeneity of the NPC, the obtained values are unlikely to bear a straightforward relation to a Young's modulus in a bulk material.

It should be noted that the Hertz model can be used instead of the piecewise function, described in the section entitled '*Contact point identification*', as a method of finding the contact point [132].

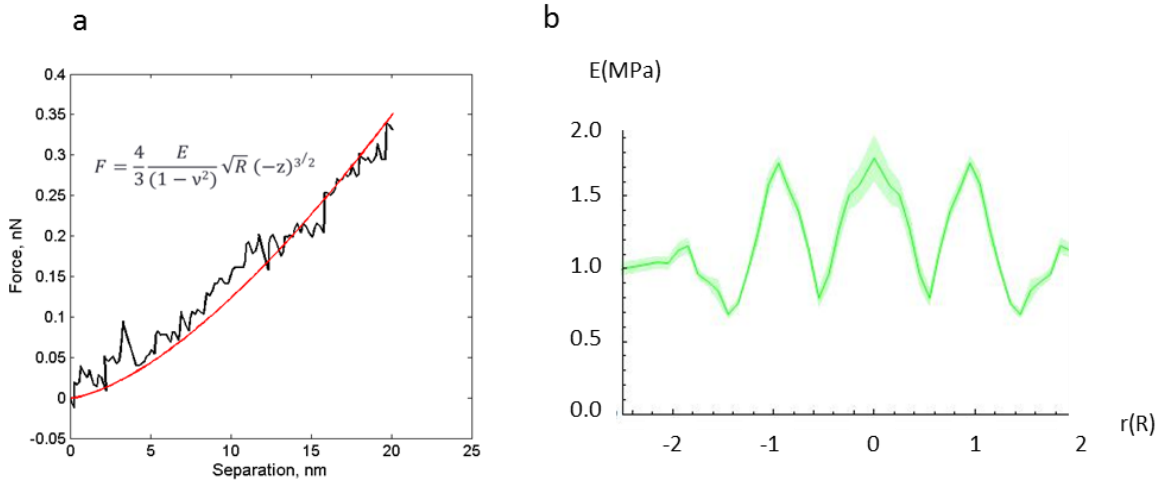

Figure 3-17 a) An example of the force curve (black) fitted with Hertz model (red) in the first 20 nm of indentation; b) cross section of the elastic modulus values according to the radial position.

3.2 Laser Scanning Confocal Microscopy (LSCM)

3.2.1 Background

Laser scanning confocal microscopy (LSCM) has established itself as a valuable tool in biological and biomedical research. It has a major advantage of imaging thin slices of living samples without destroying them [133]. Unlike conventional fluorescence microscopy, in which the entire specimen is illuminated, confocal microscopy only illuminates a selected focal plane with a well-defined depth, known as a 'slice'. As a result, instead of obtaining a blurry image of the whole sample, a sharp image of the chosen slice is generated (Figure 3-18).

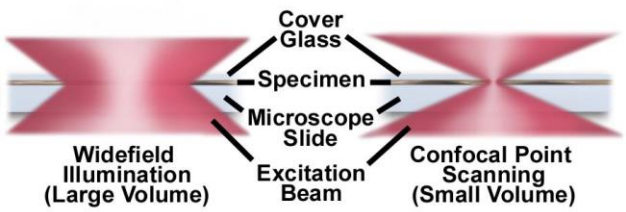

Figure 3-18 A comparison of the amount of illumination of a sample in both wide field optical microscopy, and laser scanning confocal microscopy [133].

The idea of the confocal microscope is to illuminate a sample point by point and register the emitted light. This idea emerged from the need to improve the spatial resolution. This resolution is hindered by the diffraction limit, which stops any optical system from resolving two objects that are too close. A distance greater than half of the wavelength of the illumination light is required to simultaneously resolve two objects - Figure 3-19 shows examples of small objects which render resolved, poorly resolved, and unresolved images. The resolved object is depicted as a diffuse circular disc with a number of concentric rings surrounding it. The disc is called the 'Airy disc', and the pattern produced from the concentric rings is known as the 'Airy pattern'. When the separation is no longer explicit, the object is defined as unresolved.

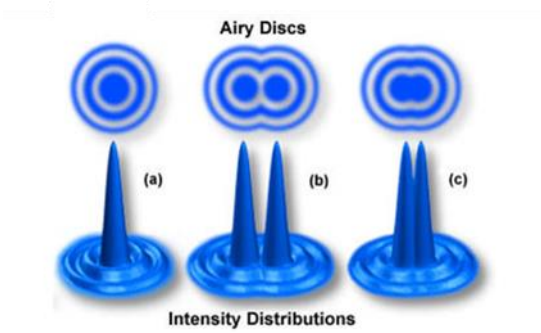

Figure 3-19 Schematic illustration of Airy discs when the object is (a) resolved, (b) poorly resolved and (c) unresolved.

The improvement in resolution lies in registering only the light coming from the centre of the Airy disc and eliminating all out-of-focus light by using the small radius aperture in front of the detector.

The first prototype of the confocal microscope was developed in 1957 by Marvin Minsky for imaging brain tissue [134], [135]. A zirconium arc lamp was used as a source of light to illuminate the sample. He put an objective lens before the sample to form a focused point of light and captured the same light with the second objective which led the light to the detector (Figure 3-20). In front of the detector he set the small pinhole to record only the centre of the Airy disc, reconstructed from the second objective. This meant a small point of light was focused onto a fluorescent screen. Unlike modern designs, in his prototype the stage was moving during scanning to generate an image of the whole sample.

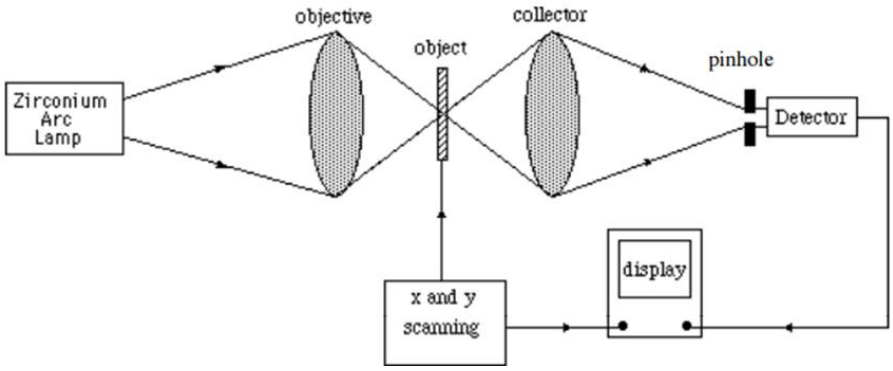

Figure 3-20 The schematic representation of Marvin Minsky setup of confocal microscope [136].

In the late 1970s and 1980s, the first laser scanning confocal microscopes started to emerge [133], mainly thanks to the growing development of laser and computer technologies, which enabled considerable improvement in the speed and quality of imaging. In modern systems the stage is fixed and a laser is used instead of the lamp.

3.2.2 Principle of Fluorescence

Scanning in confocal microscopy uses intense monochromatic light to excite fluorophores that are bound to the molecules of interest. A fluorophore is an organic or non-organic molecule that can absorb photons of a particular wavelength, and consequently emit light at longer and distinctly different wavelengths. The effect is based on a fluorescence phenomenon in which excitation occurs by supplying the fluorophore with an excess of energy when exposing it to a photon of a certain wavelength. This excess energy promotes an electron to a higher energy state, creating an excited singlet state, S_1', which lasts for a finite amount of time (Figure 3-21). This excited state turns, via internal conversion, into the relaxed singlet excited state, S_1, from which point a photon is emitted at a wavelength corresponding to the energy difference between this singlet state, and the ground state, S_0. Thus emitted light is always of a longer wavelength than the excited one. Each fluorophore has its own excitation and emission spectra, such that a sample can be stained with one or more fluorophores to label different moieties.

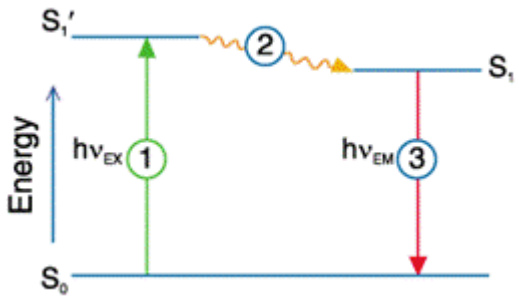

Figure 3-21 After being exposed to photons with sufficient energy, an electron is promoted from the ground state, S_0, to the excited singlet state, S_1'. Afterwards, it transfers to the relaxed singlet excited state, S_1, due to energy dissipation. From this state, it relaxes to the ground state, emitting energy in the form of a photon [137]

3.2.3 Components of the LSCM

Lasers

The heart of the microscope is the laser system. It may consist of one or more lasers. Laser light has a several advantages over the conventional lamp arcs used for illumination. The light produced by a laser is of one particular wavelength. This reduces the need of filters for producing excitation light. The laser light is coherent: the waves are of the same frequency, phase, direction and speed; therefore the laser light is well-focused and has a high intensity. The laser light scans the surface by changing its position using electronically controlled mirrors.

Acousto-optic tuneable filters

The high intensity light source is controlled and modulated by acousto-optic tuneable filters (AOTFs), which ensure both precise wavelength and intensity of the excitation light. AOTFs are solid state electro-optical filters. They are made of a birefringent crystalline material, which is capable of changing its optical properties when interacting with acoustic waves. When acoustic waves spread across the crystal, the lattice structure periodically compresses and relaxes due to the applied oscillation. This alternating motion causes refractive index fluctuations in the crystal, and hence the diffraction of propagated light.

The generators of the high-frequency acoustic waves in AOTFs are the piezoelectric transducers connected to the crystal. The changes in the applied frequency cause a periodic redistribution of the refractive index, which leads to the alternation of the diffracted wavelength. Thus, the combination of oscillating frequency and periodical change of refractive index tunes and modulates the laser wavelength [133], [138]. Moreover, ATOFs are useful in controlling the defined area of illumination and its intensity. It is also useful for regulating the wavelength and intensity of the laser beam at high speed, allowing sequential or simultaneous scans by multiple lasers. This is all due to the fast tuning of the wavelength and intensity of the laser light.

Objectives

The image in the microscope is formed by the laser beam focused on the sample using the objective lens, which is one of the most important components of the microscope. Objective lenses vary in magnification and numerical aperture (NA), which determine the depth of field and resolving power.

The numerical aperture shows the capacity of the objective to gather light. It is a dimensionless unit, which is expressed as follows (Equation 1):

$$NA = n * Sin(\mu), \qquad (1)$$

where μ is the half of the angle formed at the tip of the focused light cone entering the sample and where n is the refractive index of the medium between the specimen and the objective.

It is not possible to continually increase the numerical aperture to improve the resolution - this has its limits. The refractive index is also a restricting factor in resolution (Figure 3-22): the resolution can be improved by using immersion lenses. The scanning medium before the specimen can be water, glycerine or oil. Their refractive indices are higher than the refractive index of air, allowing higher NA and higher resolution.

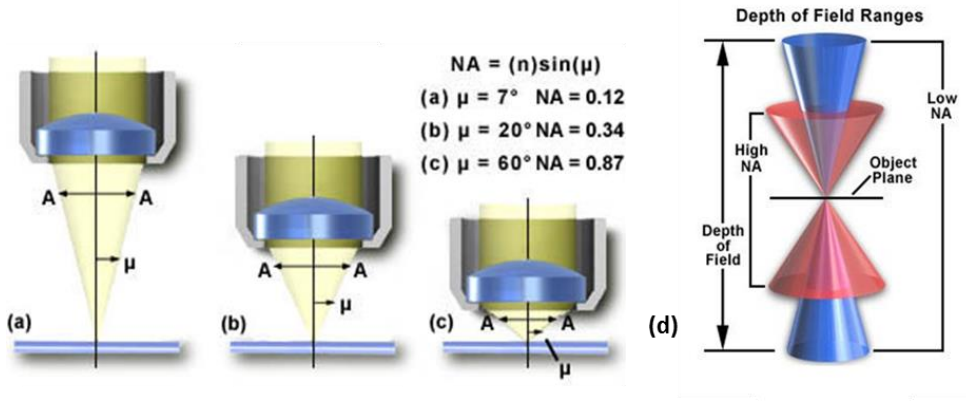

Figure 3-22 The NA increases when the half angle of the light cone increases from (a) 7°, to (b) 20° and (c) 60°. For larger angle, the focal length becomes prohibitively short. d) Corresponding depth of field with regard to numerical aperture [139], [140].

The depth of field of the objective is defined as the distance between the two furthest object planes where the object is still in focus. It is highly dependent on numerical aperture. The higher the numerical aperture, the shorter the focal length and the smaller the depth of field. (Figure 3-22 d).

3.2.4 Operational principle of the LSCM

The laser beam is brought to the fluorescent sample through the objective lens (Figure 3-23), which focuses the light on a focal plane. The emission light from the excited fluorophore goes back to the objective. After passing the objective lens, it goes through the dichroic mirror and is detected by the photomultiplier. The excess of scattered out-of-focus light is excluded by the pinhole aperture located before the detector, helping to reduce the background noise. Thus all emitted fluorescent light in the area below or above the focal plane is not recorded. The range of emission wavelength that the microscope can register is 400-750 nm.

In case when the recorded intensity is too low, the photomultiplier tube can enhance the signal by producing more electrons from photons using a photocathode. The sensitivity of the photomultiplier is controlled by a dynode voltage (HV).

The signal is then digitized into an image, the sensitivity values of which values are regulated by the gain and offset parameters.

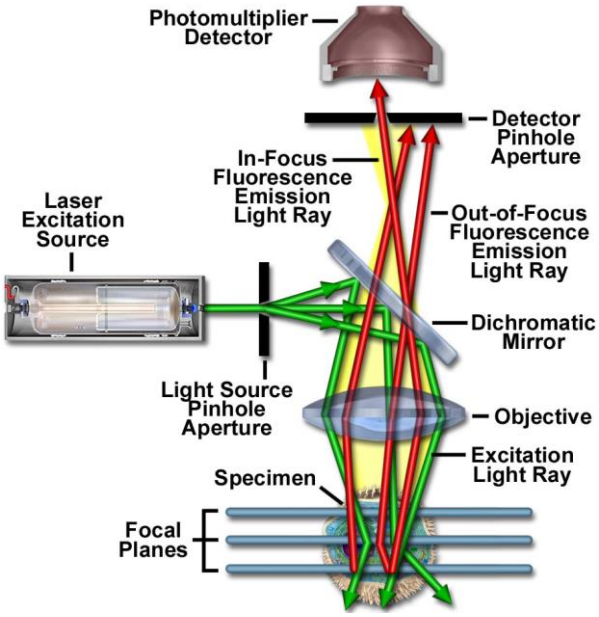

Figure 3-23 A schematic view of the light path in a confocal microscope, and its main components [133]

3.2.5 Imaging modes

There are three imaging modes in the FluoView1000 programme software of the Olympus microscope: Lambda, Depth and Time. Depth mode collects stacks of thin optical slices along the Z-axis. These stacks are of a particular thickness which can be set manually by indicating a step size. Time mode collects data over time at one particular focal plane, which is maintained by an autofocus control. Finally, Lambda mode is used to find the peak of the emission spectrum by scanning over a range of wavelengths. Image modes can be coupled, for example, to scan a range of slices over time or over wavelength spectra.

3.2.6 Limitations

Along with some great advantages that the confocal technique holds over wide-field optical microscopy, there are also some limitations. Firstly, the microscope is restricted by the diffraction limitation. Secondly, the high-intensity laser light might bleach the fluorophore and thus, less fluorescence would be detected. And thirdly, in some cases the fluorescent probe in the excited state directly or indirectly distorts or damages the sample. This effect is called phototoxicity [141].

3.2.7 LSCM Experiments

NPC permeability upon trans-1,2-cyclohexanediol (CHD) addition

The permeability barrier of the nuclear pore results from the interactions between FG-repeats amongst themselves, and between FG-repeats and karyopherin [142]. Below is the summary of the sample preparation protocols for the experiments which aimed to modify the permeability barrier of the NPC by exposure to CHD tested using laser scanning confocal microscope.

In the permeability measurements, the main objective was to capture the fluorescence intensity change over time at the same focal plane, and subsequently calculate the influx rate.

In other experiments, the aim was to observe the change in intensity due to fluorescent cargo and NTRs in the nuclear envelope.

Sample preparation and Imaging parameters

Dextran permeability test: The isolated nuclei were incubated with 0.2 mg/ml 70 kDa-Dextran Texas Red (Sigma-Aldrich) in 50 µl NIM 1.5% PVP for 10 minutes. The scan was done every 8 seconds in "Time" mode on an Olympus FluoView 1000 CLSM at 10x magnification for 35 minutes. Afterwards, the sample was incubated in 5% CHD for 2 minutes. Then the buffer was exchanged to 0.2 mg/ml 70 kDa Dextran and scanned again for another 35 minutes. The HeNe laser with excitation wavelength 543 nm was used to identify the dextran signal. In order to scan in the same focal plane the Autofocus mode was applied.

Cargo and NTR test: The isolated nuclei were incubated in either 1µM Rch1-IBB-MBP-GFP and 0.5µM hsImpβ[3], or 0.5µM hsImpβ-GFP for 15 minutes, where MBP is a maltose-binding protein from Escherichia coli and IBB is Importinβ binding domain. Then they were washed in NIM supplemented with 1.5% PVP. The second incubation was performed with 5% trans-1,2-cyclohexanediol (CHD) for 20 minutes and then washed with NIM 1.5% PVP. Meanwhile the negative control sample was incubated in NIM 1.5% PVP only. The structural integrity of the nuclei was tested by the addition of

[3] Importinβ and Ran-Mix were kindly gifted by Prof. Dirk Gorlich from Max Plank Institute for Biophysical Chemistry, Germany.

0.2 mg/ml 70 kDa-Dextran Texas Red (Sigma-Aldrich). The samples were scanned on the Olympus FluoView 1000 CLSM in Depth mode at 10x magnification. An argon laser with an excitation wavelength of 488 nm was used to detect cargoes and nuclear transport receptors; and a HeNe laser with an excitation wavelength of 543 nm was used to detect the dextran.

Confocal test** on **permeability of nuclei and NE to NTR or/and cargo upon Ran cycle:

The aim of this experiment was to check whether the NPC import could be activated by adding the reagents required for transport. Ran-mix (0.3 µM Ran, 0.3 µM GDP, 0.06 µM NTF2, 0.03 µM RanGAP, 4 nM Ran BP1) and Energy-mix (0.75 mM ATP, 0.75 mM GTP, 15 mM creatinP, 0.075 mM $Mg(OAC)_2$, 0.075 mM DTT, 0.075 mg/ml creatin kinase in HEPES/KOH pH 7.5) were used to enhance the translocation process of the cargo. Additionally, by running the enhanced transport process through NPCs, hence 'flushing' the pores multiple times, the pores could be depleted from cargo and NTRs. Thus, the same procedure was applied for nuclei that were subsequently used to isolate the nuclear envelope. Moreover, the cargo in NPCs (for the nuclear envelope) was treated with Benzonase to digest any remaining ribonucleoproteins in the NPCs.

Sample preparation and Imaging parameters

The isolated nuclei were incubated in either 1 µM Rch1-IBB-MBP fluorescently labelled with GFP and 0.5 µM hsImpβ, or 0.5 µM hsImpβ fluorescently labelled with GFP for 15 minutes. Then they were washed in NIM supplemented with 1.5% PVP. Afterwards the procedure of incubation with Ran-, E-Mix was followed. The integrity of the nuclei was checked by the addition of 0.2 mg/ml 70 kDa-Dextran Texas Red (Sigma-Aldrich). The sample was incubated with Dextran for 10 minutes prior to measurements. The samples were scanned in NIM 1.5% PVP on the Olympus FluoView 1000 CLSM in Depth mode at 10x magnification using an argon laser with an excitation wavelength of 488 nm to detect cargoes and nuclear transport receptors; and a HeNe laser with an excitation wavelength of 543 nm was used to detect the dextran.

The Benzonase effect on NEs was tested using confocal microscopy with the help of RNA staining agent (SYBR Gold). In order to observe the envelope Wheat Germ Agglutinin (WGA) was used. The NEs were prepared from nuclei treated with Ran-/E-

Mix as described above. However, no labelled cargo or Importin were added. The NEs were incubated with 25 units/µl Benzonase (Sigma-Aldrich) for 30 minutes in NIM supplemented with 8% PVP. Subsequent incubation with 1:5000 SYBR Gold to stain the RNA and 0.04 µM WGA-Alexa 647 to label the NE was performed for 10 minutes. Samples were measured with CLSM using an argon laser to detect SYBR Gold-labelled RNA and a HeNe laser to detect WGA-Alexa647 signal.

Incubation of the nuclei for positive and negative controls was done separately.

3.2.8 Data analysis from LSCM

Images from the confocal laser scanning microscopy were analysed in Fiji (Open source, http://fiji.sc/Fiji), FluoView and MatLab (MathWorks, Inc., R2011b) software.

Nuclei processing

The evaluation of the intensity in the confocal images was done in Matlab. In order to select an area of interest, an image was converted into a binary one: presenting the image in black and white. This was done by normalising the pixels intensity values to the maximum value and setting a threshold. The mask of the binary image was applied to the raw image and the average grey pixel value was acquired. The intensity acquisition from the different parts of the nucleus (periphery and inside) was performed by eroding the mask of the nucleus with a disc width of 7 pixels (Figure 3-24). Then the eroded mask was subtracted from the original one. Both masks were applied to the raw image and the mean grey pixel value was obtained. The value of 7 pixels as a width of erosion was chosen approximately, by sight, to select the nuclear envelope.

Figure 3-24 Image analysis representation in MatLab: (a) raw image; b) binary image of eroded nuclei (nuclei without the nuclear envelope); c) binary image of nuclei periphery, width 7 pixels.

The contrast/brightness settings of the images used in the figures were changed to the same degree to visually enhance the signal. Each set of images corresponds to the same values of contrast.

The intensity data of dextran images were obtained using the Olympus FluoView software.

NE processing

The fluorescence images of NEs were analysed as described above. However, prior to conversion into the binary image, the contrast of the images was enhanced, though the intensity values were obtained from the raw images. The signal from the NE was strongly dependent on the layout of the membrane. If there were more folds on the membrane as a result of isolation, then it would appear brighter. To compensate for this artefact, the signal of the RNA fluorescent tag (SYBR Gold-YoYo) was normalised to the wheat germ agglutinin (WGA) signal that marked the nuclear envelope.

Influx rate determination

The influx rate was determined based on the following equation (2) which describes the intensity change over time.

$$I=I_0(1-e^{-kt}) \qquad (2),$$

where $I\ (t)$ is the intensity in the nuclei, $I_0\ (t)$ is the intensity of the background, k is the influx rate, t is the duration of measurements.

The logarithm of the equation (2) was taken. The plot for $log(1-I/I_0)$ versus t was generated and correlated with the best fit for the function $(ka+b)$. The rate was extracted from the slope of the function.

Chapter 4 Nanomechanical Characterisation of the Polymer Brush

4.1 Introduction

Standard biochemical and structural methods have struggled to determine the biophysical nature of the unstructured proteins in the NPC. Various scenarios have been proposed, including suggestions that the nucleoporins with FG-repeats form a meshwork of cross-linked filaments, which resembles the hydrogel; or that they may behave as an entropic brush, with constantly fluctuated filaments of which the entropy is reduced on the spatial constriction caused by the presence of a cargo.

A priori, one would expect that such scenarios lead to largely diverging nanomechanical properties. To test and validate this prediction, this chapter describes the nanomechanical characterisation of a simple model system, a responsive polymer brush. It was chosen because it is relatively simple to prepare and because it is possible to alter the conformational state by changing the pH. In particular, these polymer brushes can be induced to appear in either collapsed or expanded conformation, which are the two extremes of the difference configurations that have been proposed for unstructured proteins in the NPC.

The polymer brush in this study was anchored by silane chemistry to the silicon surface at high grafting density. It carried an electrostatic charge, and thus qualifies as a polyelectrolyte polymer. The crucial difference between a neutral and a polyelectrolyte brush is the large amount of counterions that are attracted to within the charged brush layers [143].

In this project we used the weak polyelectrolyte brush Poly (2-(dimethylamino) ethyl methacrylate) (PDMAEMA), containing a basic group. At higher concentrations of hydrogen ions at pH 5.0, the protonation of the PDMAEMA brush takes place via the formation of NH^+ bonds, which gives a positive charge to the polymer (Figure 4-1 a). The resulting repulsive electrostatic force between the branches causes the polymer to

stretch and the brush to swell. On the other hand, in a basic environment, the surrounding OH^- groups are dissociating the excess hydrogen ions from the polymer brush (Figure 4-1 b). The loss of hydrogen ions leads a reduction of electrostatic repulsion and thus to the collapse of the polymer string [144]. These kind of responsive properties of the brushes may be useful in smart surface applications such as biomolecular switches [145], controlled wettability of the surfaces [146] and microactuators [147].

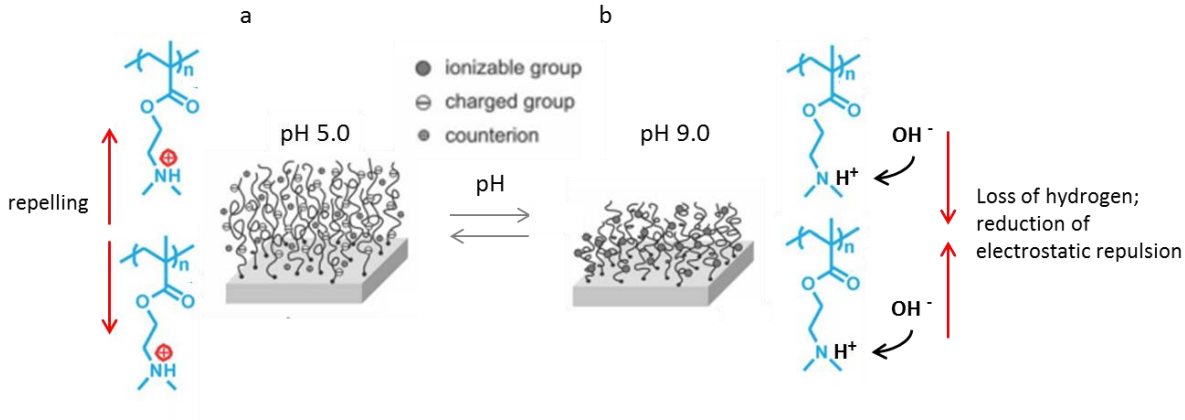

Figure 4-1 Collapsed (at pH 9.0) and expanded state (at pH 5.0) of the PDMAEMA polymer brush [148]**,** [149]**.**

The nanomechanical characterisation of both states of the brush was carried out by applying Force Volume mode in AFM, which records the force curves as a measure of the interaction between the probe and the brush.

4.2 Preparation of the polymer brushes

The polymer brushes were prepared in Queen Mary University, School of Engineering and Material Science, by Mahentha Krishnamoorty, PhD student. The preparation starts from mixing 6.6 g DMAEMA, 18mg $CuBr_2$, 320 mg bipyridine in 30 ml of 25% Ethanol. It was left bubbling in argon whilst stirring for 20 minutes. After adding 82 mg CuCl the mixture was degassed and stirred for another 20 minutes before applying to the substrate, which is under argon in a polymerisation carousel [150].

The polymers were grafted onto silicon chips of 1x1 cm^2 size using silane initiator [144]. By using polymers of three different lengths, three different brushes were

formed, and characterised via their thickness (20 nm, 30nm and 60 nm) as measured in a dry state using ellipsometry. The silicon substrate was attached to the metal specimen holder of 15 mm diameter for AFM measurements. Prior to imaging the sample was rinsed in ethanol and dried with nitrogen gun, before immersion in aqueous solution. The scanning was performed in 10 mM sodium acetate solution at pH 5.0, and 10 mM TRIS buffer at pH 9.0, with no additional salts.

4.3 Results and Discussion

The topography and nanomechanical properties of the PDMAEMA polymer brushes in two distinct states were measured using the AFM Multimode IV in Tapping mode and Force Volume.

4.3.1 Topography of the Polymer brush

To visualise two different states of the brush, the AFM images (Figure 4-2) were acquired in the Tapping mode to avoid the lateral forces occurring in the Contact mode, which might deform or damage the brush. An area of 5x5 μm^2 was measured with an MLCT-E (40 nm in diameter) cantilever at a scan line rate of 1.5 Hz and 512 samples per line. The amplitude setpoint was optimised separately for both states of the brush for minimal-force and highest-contrast imaging. The maximum amplitude setpoint was ~2 V for scanning a collapsed brush of 60 nm thickness.

The AFM topography (height data, Figure 4-2) shows large clusters of polymer brushes (of ~300 nm lateral size) at pH 5.0, compared to smaller ones at pH 9.0 (of ~90 nm lateral size). The roughness of the surface is illustrated with profiles of the surface. Interestingly, the same area scanned the second time shows a different location for the clusters. Thus, the polymer brush is dynamic and it is hard to reproduce exactly the same image.

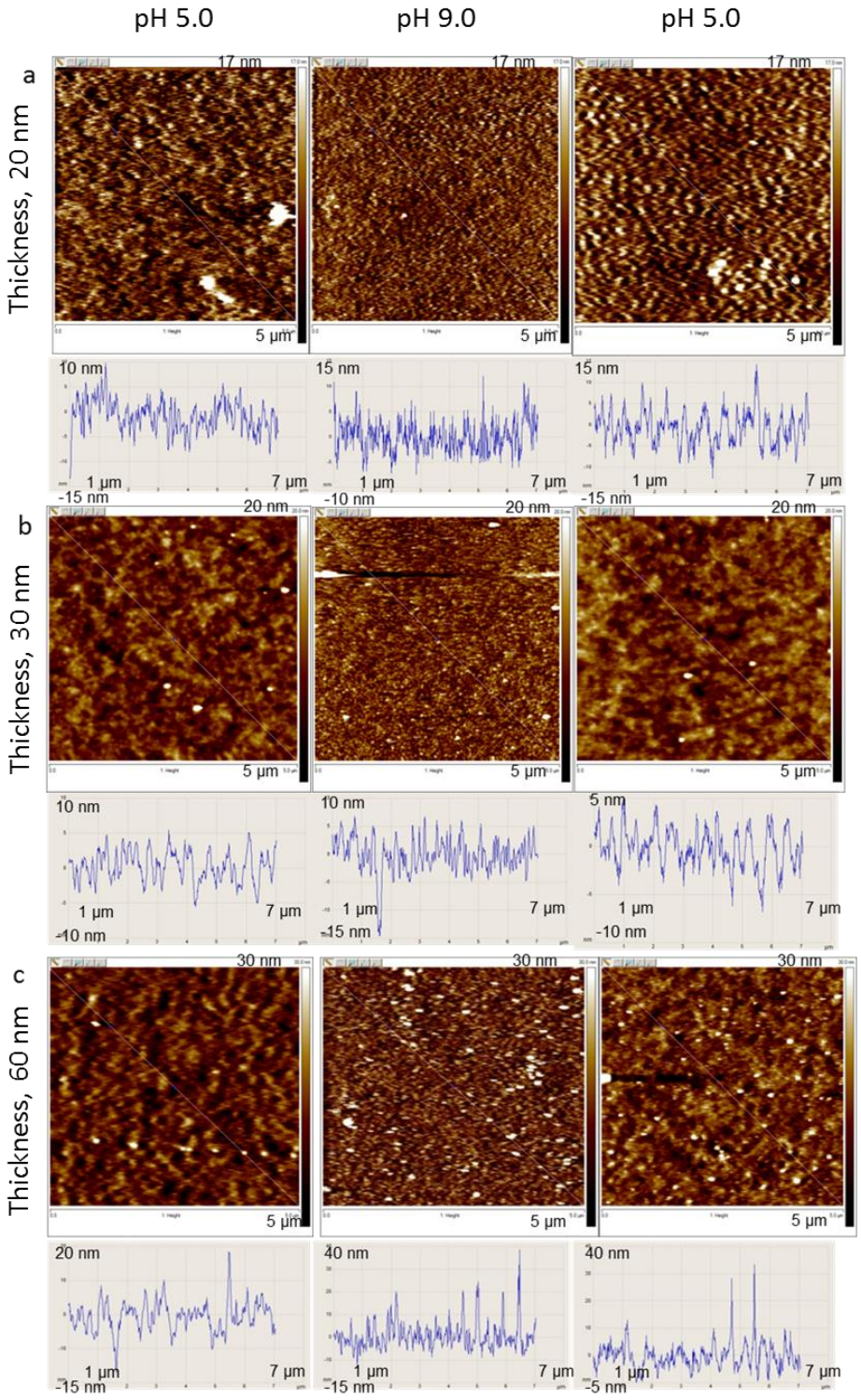

Figure 4-2 AFM height images (5x5 µm^2) in a solution of a PDMAEMA polymer brush at pH 5.0, pH 9.0 and pH 5.0 again with (a) 20 nm, (b) 30 nm and (c) 60 nm thickness (as measured in the dry state) acquired in tapping mode with an MLCT-E cantilever in liquid. Each AFM image has a corresponding profile below.

The larger clusters at pH 5.0 may be interpreted as resulting from the swollen state of the polymers but it may also be an artefactual deformation of the soft polymer brush caused by the AFM tip. Clusters in the collapsed state (pH 9.0) are considered as layers of overlapped chains represented in so-called pinned micelles [151]. Their small-size cluster can be interpreted as a signature of the compacting of the polymer in this state [63].

There are at least two ways to determine the thickness of the polymer brush in a wet condition using an AFM. The first one uses the mask at the grafting stage. For example, in the experiment described in [152], the polymer brushes were grafted onto the gold chip with a elastomeric PDMS stamp which deposited a self-assembled polymer brush in a certain pattern. Thereby, a gold surface with no brush served as a control during an AFM imaging in fluid for identifying the brush height in a wet state (Figure 4-3). Another method of finding the thickness of the brush is to use an AFM in force mode and determine the indentation of the tip from the force curves. However, it might be inaccurate due the repulsive forces between the polymer brush and an AFM tip. Additionally, a suitable loading force should be worked out in order to sense the brush instead of penetrating or compressing it. Furthermore, apart from finding the minimal force, the large tip diameter (in range of micrometres) should be used in order to increase sensitivity towards the brush since the smaller diameters tend to penetrate it [153]. Besides, the contact point of the force curve should be found accurately which is generally challenging with soft samples as the polymer brush.

In this study we could not use either of the methods since in our samples the brush covered the entire space of a silicon chip and as a result, there was no control for the height measurements. Therefore, we did not measure the thickness of the polymer brush in liquid, but used as a reference the thickness obtained in the dry state by an ellipsometry. According to our results shown later, all the polymer brushes used in this study showed the same behaviour regardless of the thickness.

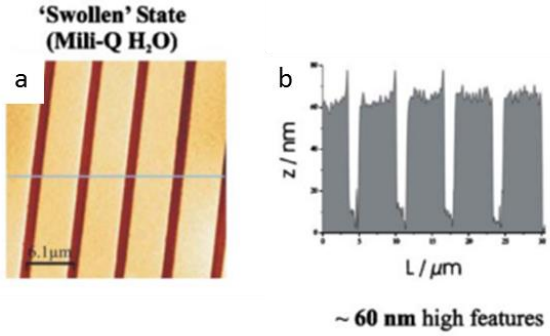

Figure 4-3 (a) Height image obtained in liquid of the polymer brush deposited in strips onto a gold surface. (b) Cross section of the polymer brush image showing a distinct difference in height between the gold surface and the brush [152].

Polymer brush as a model system

It is known that *in vitro* FG-domains may form both brush- and gel-like conformations. We decided to find a model system which can represent both configurations. It is also known that responsive polymer brushes made of synthetic material according to their physical properties are similar to the FG-domains. In the extended state they exhibit long range steric repulsion which is a characteristic of the FG-brush; and in the collapsed state they avoid an interaction with the solvent as FG-repeats according to the hydrogel model.

Polymer brushes formed from PDMAEMA can be compared to the hypothesised states for assemblies of FG-Nups, as they can assumed both collapsed/cohesive (gel-like) states and more extended, entropic-brush states. In addition, the PDMAEMA brush is grafted to the surface from one end and extended from another as the FG-domains within the NPC. The extension of the brush is enhanced by the high density of grafting, when little space between the points of grafting implies significant chain-chain interactions. The PDMAEMA brush in the extended state shows long-range steric repulsive forces in the AFM Force Volume measurements, similar to the FG-repeats in a brush-like conformation anchored to a gold substrate [62]. For a comparison with FG-Nups in the NPC, however, these samples do not include the same type of nanopore confinement as the NPC.

4.3.2 Comparative nanomechanical study of collapsed and swollen polymer brushes

To measure the mechanical properties of the sample, the force curves were acquired in Force Volume mode. The force curves describe the interaction between the tip and the sample by measuring a force the AFM tip applies to the surface.

The typical scan area of Force Volume was 200x200 nm^2, with force curves recorded on a 32x32 pixel grid. Force/Deflection curves consisted of 512 data points and were obtained with a ramp speed 1.86 µm/s. The tip was ramping from distance of 200 nm, and subsequently ramped back again. Force curves were collected at maximum loads of 0.8 - 1 nN for MSNL-E and MLCT-E cantilevers and up to 3 nN for ShoconG-SS tips. The characteristics of each cantilever tip are shown in Section 3.1.1, Chapter 3.

In this chapter all the shown force curves are averages of 1024 force curves, i.e., of all force curves in a single scan. Each force curve was aligned to the contact point between the tip and the sample. The data analysis and averaging proceeded as for the NPC measurements in the following chapters.

The force curves provide a measure of local stiffness via their slope as a function of indentation, with stiff samples yielding steeper slopes. For softer samples, the force curves rise more gradually with increase of indentation [129] (Figure 4-4).

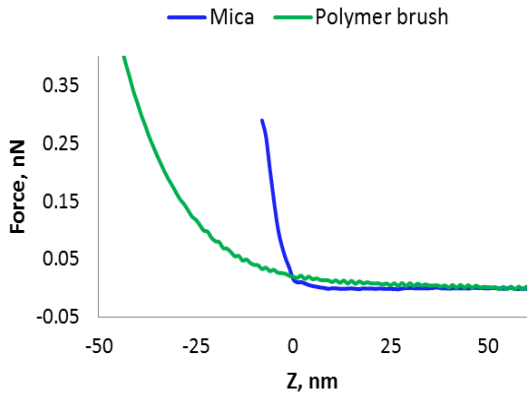

Figure 4-4 Force curves acquired with an MLCT-E cantilever on a mica surface (blue) and on a PDMAEMA brush (60 nm thickness in a dry state) in extended state at pH 5.0 (green). Z=0 refers to the approximate contact point between the tip and the sample.

Figure 4-5 shows a set of force curves acquired from polymer brush of thicknesses 20 nm, 30 nm and 60 nm using MSNL, MLCT and ShoconG-SS cantilevers which have different tip diameter (range 4-120 nm) and aspect ratio (from low to high). Each plot shows three curves corresponding to the measurements at pH 5.0, pH 9.0 and pH 5.0 again. The force curves with all cantilevers show the clear difference between the extended and collapsed states. The applied force on swollen brush (pH 5.0) increases gradually with indentation of the tip into the brush, whilst the force curves from the collapsed state (pH 9.0) appear to be steeper and show larger increase of force with the same indentation. At pH 9.0 some of the force curves have an additional attraction to the surface which is observable through the negative force which means the tip 'snapped in' to the surface. In most of the cases the force curves at pH 5.0 obtained before and after collapsed state could well be overlaid. Additionally, one of the plots in Figure 4-5 showing force curves measured with ShoconG-SS tips displays long range repulsion in non-contact area. This can be due to the unwanted optical interference between the laser light reflected form the cantilever and the light bounced off the reflective surface of the AFM sample. As a result, a sinusoidal pattern can be observed on force curves, periodic with half the laser wavelength. In some cases the re-alignment of the laser spot on the cantilever might help to remove the artefact [154], however sometimes the spillage of the laser spot (which allows the light to reflect on only from the cantilever, but also from the sample surface) is caused by the lateral warping or torquing of the cantilever during imaging [155].

These results are independent on the AFM tip and sample thickness, except for the measurements with the ShoconG-SS at the thickness of the brush 30 nm, which we therefore assign to an unknown technical issue during the experiment. The approximate indentation into the sample is about 50 nm at pH 5.0 and 10 nm at pH 9.0. This may appear large compared to the brush thickness specifications 20 nm, 30 nm, and 60 nm, but it should be emphasised that those specifications refer to the dried state of the brushes.

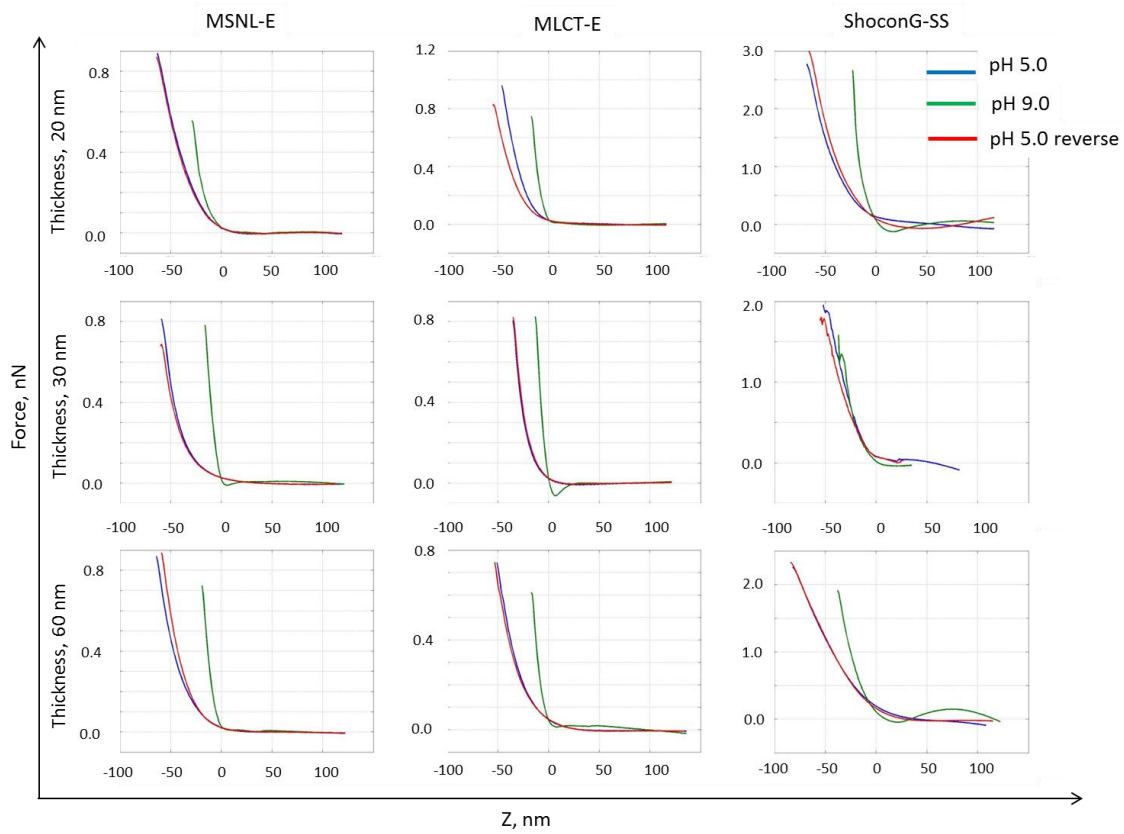

Figure 4-5 Force curves over three thicknesses of the PDMAEMA polymer brush (20 nm, 30 nm and 60 nm, one row for each) using three different cantilevers (MSNL, MLCT and ShoconG-SS) at various pH conditions (pH 5.0 and 9.0).

The overlap of the force curves at the pH 5.0 indicates that the process of swelling and collapsing is reversible. The steep force curves at pH 9.0 suggest that the polymer brush in collapsed state is stiffer than the swollen brush at pH 5.0.

The identification of the indentation into the sample highly depends on the contact point determination. Especially when indenting into a soft sample, the force increases only very gradually. Hence it is not as straightforward to determine the contact point as it is on a hard sample (Figure 4-4). Therefore, the values for the indentation depending on the method for identification of the contact point would vary.

To sum up, the discrepancy between the two brush states can be easily observed in force curves [156] regardless of the shape of the tip or diameter.

4.3.3 Assessing polymer brushes with indentation models

Indentation models can be used for a more quantitative (though not necessarily accurate) assessment of the nanomechanical properties of the brushes. There are two commonly used indentation models to acquire the Young's modulus of the sample. The original Hertz model, where two homogeneous spheres elastically deform under load, was adapted to the interaction of the small spherical indenter and a substrate with a large radius of curvature [157]. The Hertz model assumes that: (i) the tip is an elastic sphere; (ii) the substrate is isotropic and flat [104] (Figure 4-6). Therefore, the thickness of the sample is assumed to be large, whilst the indentation – is small. The relation between the applied force and elastic modulus of the substrate is described as a square root of the tip radius and indentation to the power of (3/2) (Equation 3) (Figure 4-6 a).

$$F = \frac{4\,E}{3\,(1-\nu^2)}\sqrt{R}\sigma^{3/2} \qquad (3),$$

where F is the applied force, E is a Young's modulus, ν is a Poisson ratio, R is a tip radius and σ is an indentation.

The Sneddon model, which emerged as a modification of the Hertz model, describes the interaction of a rigid conical probe with an isotropic elastic substrate by considering the tangents of the half-angle of the tip-cone and squared indentation (Equation 4) (Figure 4-6 b).

$$F = \frac{2\,E}{\pi\,(1-\nu^2)}\tan\alpha\,\sigma^2 \qquad (4),$$

where F is the applied force, E is a Young's modulus, ν is a Poisson ratio, α is a half-angle of the tip and σ is an indentation .

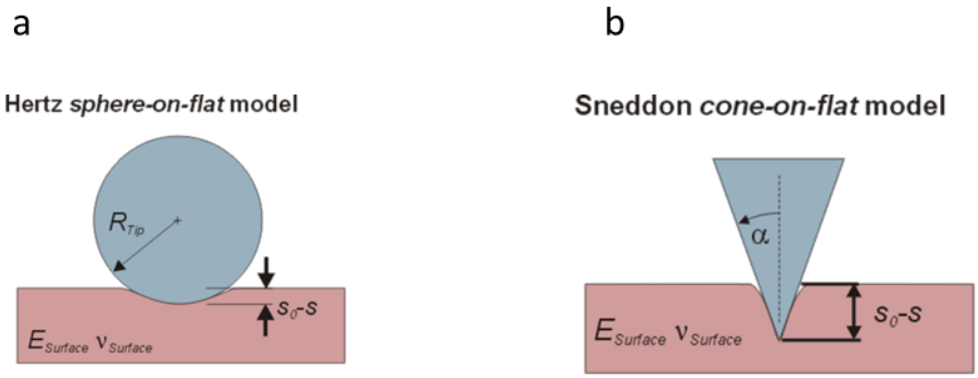

Figure 4-6 Graphic representation of the tip's requirement in (a) Hertz and (b) Sneddon models. Labelling: s_0-s – indentation into the sample, R- tip radius, ν – Poisson ratio, α – half-angle opening of the tip.

These two approaches were used to establish the difference in elasticity between the cardiac, skeletal muscle cells and vascular endothelium cells [158], normal and cancerous human bladder cells [159], the old and young mouse's hearts cells [160].

Here, the force curves from extended and collapsed polymer brushes were analysed with both indentation models.

Fitting the force curves with indentation models

Figure 4-7 shows the force curves (blue line) from the extended and collapsed states of the PDMAEMA polymer brush of various thicknesses fitted with Hertz (green) and Sneddon (red) models. The averaged force curves collected at pH 5.0 do not fit well with the experimental data. The models predict steeper behaviour of the curve. On the other hand, the fits match the force curves obtained at pH 9.0 much better.

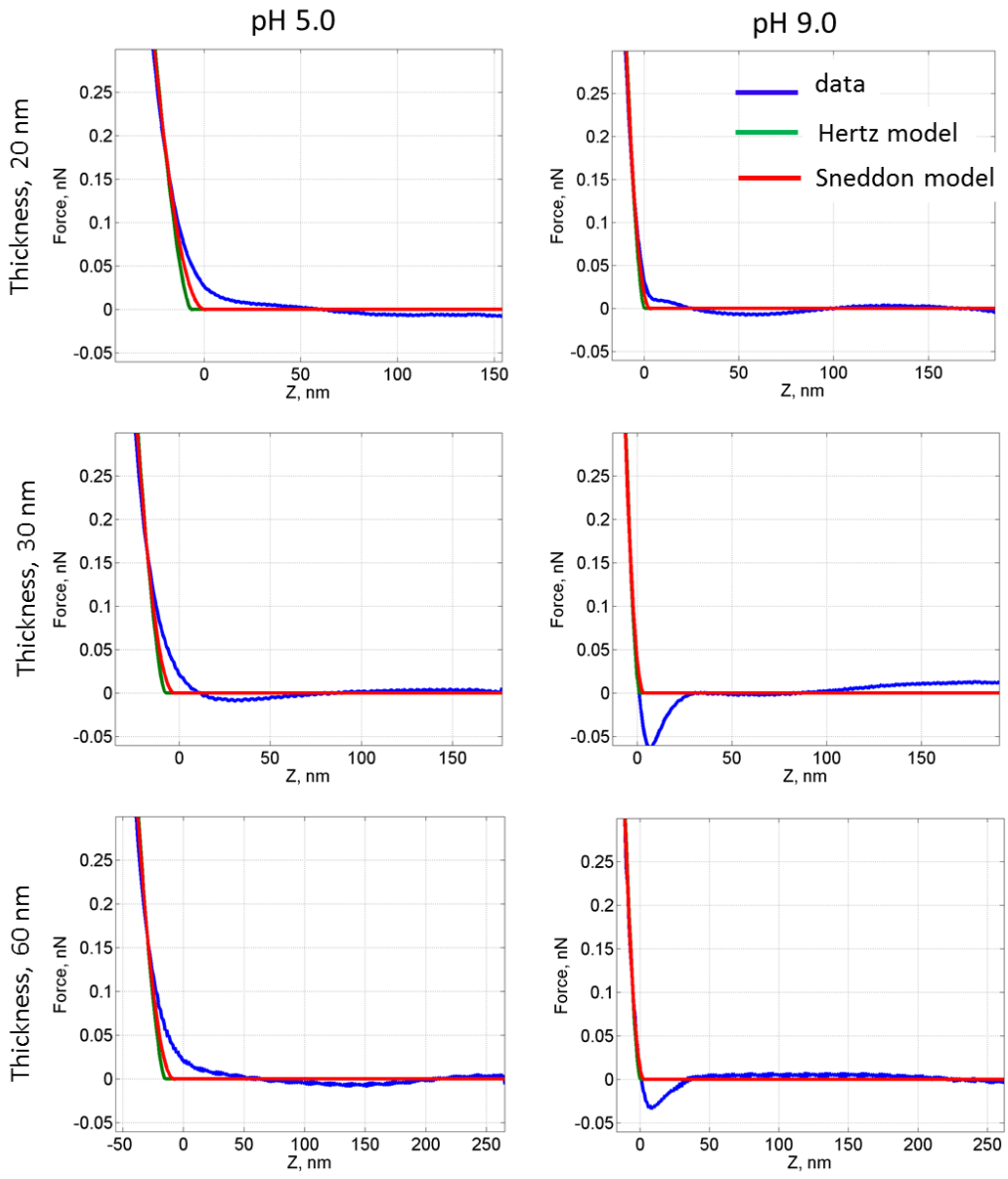

Figure 4-7 Force curves (blue) recorded on PDMAEMA brushes (of 20 nm, 30 nm and 60 nm thickness in the dried state) with MLCT cantilever at various pH conditions (pH 5.0 and 9.0), fitted with Hertz (green) and Sneddon (red) models.

The difficulties in fitting the swollen brush are largely due to the fact that the surface is soft with a smooth transition between the non-contact to contact area [161], [162]. Conversely, the force curves from the collapsed brush exhibited the behaviour of the hard surface with clear determination of the contact point. In our analysis of the force curves we determined the contact point as the point when the steric repulsion between the surface and the tip deflects the cantilever.

To further emphasise the observed differences, Figure 4-8 shows the set of the stiffness curves from the PDMAEMA polymer brush in both swollen and collapsed states of the different thicknesses, where the stiffness is defined as the force gradient (multiplied by '-1', to ensure that deeper indentations at more negative z result in higher stiffness).

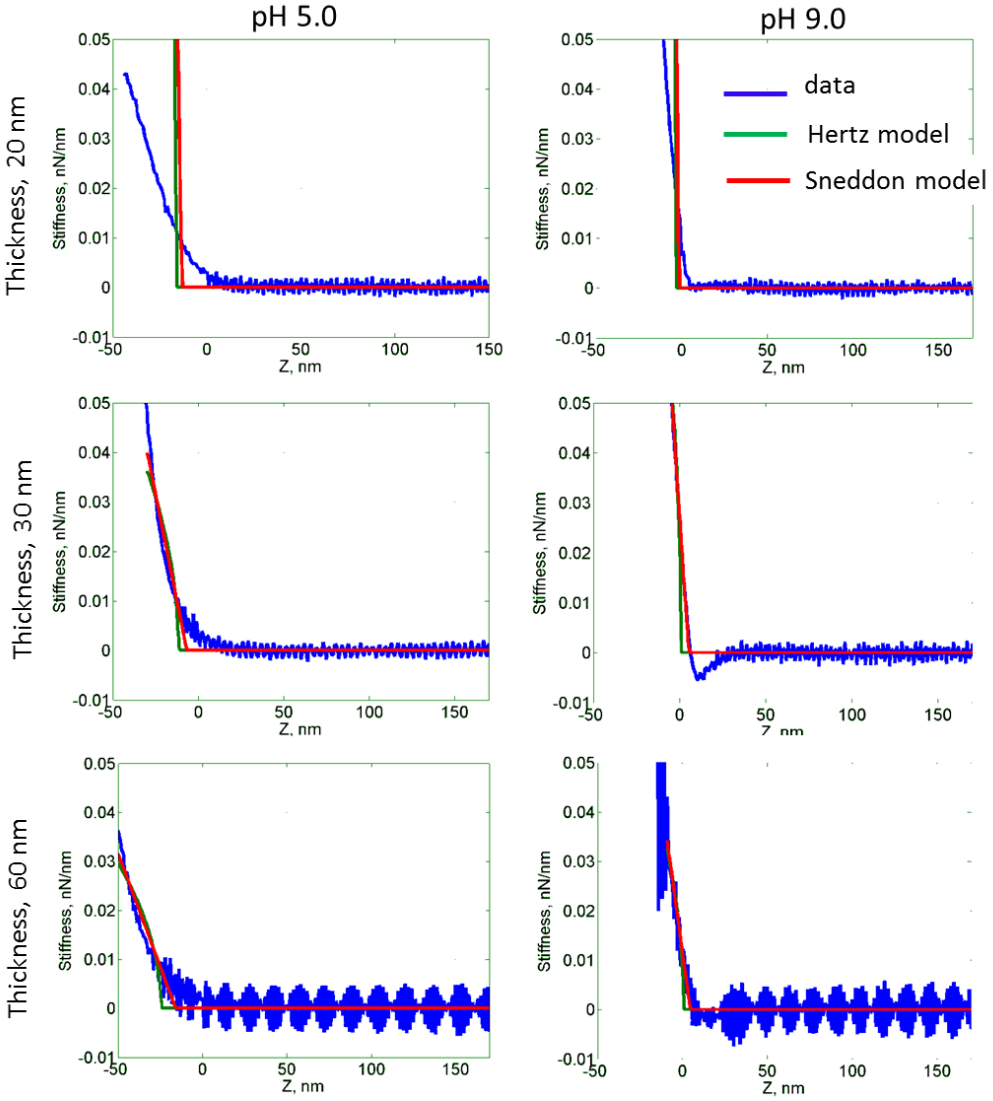

Figure 4-8 Stiffness curves (blue) derived from the force curves recorded on PDMAEMA brushes (of 20 nm, 30 nm and 60 nm thickness in the dried state) with MLCT cantilever at various pH conditions (pH 5.0 and 9.0), fitted with Hertz (green) and Sneddon (red) models.

The experimental data (blue) from the polymer brush at pH 5.0 disagree with the indentation models in exhibiting gradual increase of the stiffness at the first few

nanometres of indentation. However, the stiffness curves at pH 9.0 demonstrate the behaviour as predicted by the indentation models by showing steep increase of the stiffness, which is indication of a hard(er) surface.

These results are showing the clear difference between two states of the brush. In particular, the polymer brush measured at swollen state at pH 5.0 is soft with a smoothly increasing force as a function of indentation [163]. However, at pH 9.0 when the polymer brush is collapsed, it demonstrates a behaviour of harder and stiffer sample, with a more sudden onset of the force as a function of tip-sample approach.

As the indentation models failed to fit the swollen brushes, these brushed were instead fitted with expential behaviour, based on earlier theoretical predictions [164] (Figure 4-9). This yielded clearly better results.

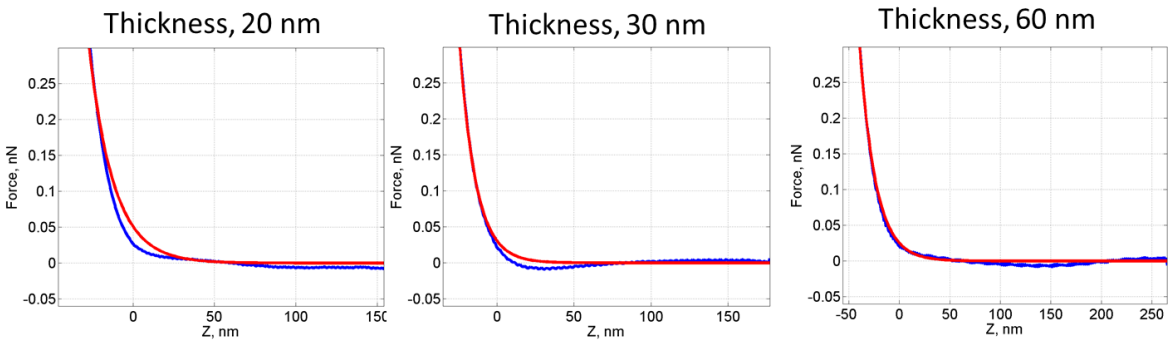

Figure 4-9 Force curves (blue) recorded on PDMAEMA brushes (of 20 nm, 30 nm and 60 nm thickness in the dried state) at pH 5.0 with MLCT cantilever, fitted with exponential model (red).

In spite of the difficulties in fitting the swollen brushed with Hertz and Sneddon indentation models, the extracted effective Young's moduli can still be used for a more quantitative comparison of the different brushes.

Figure 4-10 shows the effective Young's moduli for each sample at expanded and collapsed states scanned by MLCT, MSNL and ShoconG-SS cantilevers and analysed with both Hertz (green) and Sneddon (orange) models. The diagrams clearly demonstrate that at the collapsed state at pH 9.0, the Young's modulus of the brush is higher than the Young's modulus of the extended brush at pH 5.0 regardless of the indentation model or the tip used. However, there are differences between the models

which are most pronounced for the MLCT cantilever which has a nominal tip diameter of 40 nm. There are also discrepancies in the Young's modulus between the cantilevers (Table 4-1). Thus, ShoconG-SS cantilevers showed the highest values for Young's modulus for both states of the polymer brush in both indentation models, whereas the results obtained with MLCT cantilevers and analysed in Hertz model produced the smallest values.

The effective Young's moduli at pH 5.0 were similar before and after exposing the brush to pH 9.0, to within 25% for MSNL and MLCT cantilevers and within 12% for ShoconG-SS cantilevers.

Table 4-1 The average value for the Young's modulus for the PDMAEMA brushes, in extended (pH 5.0) and collapsed (pH 9.0) state, based on experiments and fits with different cantilevers and indentation models.

	Hertz model		**Sneddon model**	
Cantilevers	**E, MPa (pH5)**	**E, MPa (pH9)**	**E, MPa (pH5)**	**E, MPa (pH9)**
MLCT-E	0.50 ± 0.05	1.7 ± 0.3	1.7 ± 0.3	8.2 ± 2.0
MSNL-E	0.90 ± 0.06	3.2 ± 0.9	1.1 ± 0.4	5.0 ± 1.8
ShoconG-SS	1.7 ± 0.2	5.6 ± 0.3	3.3 ± 0.6	17.9 ± 10.3

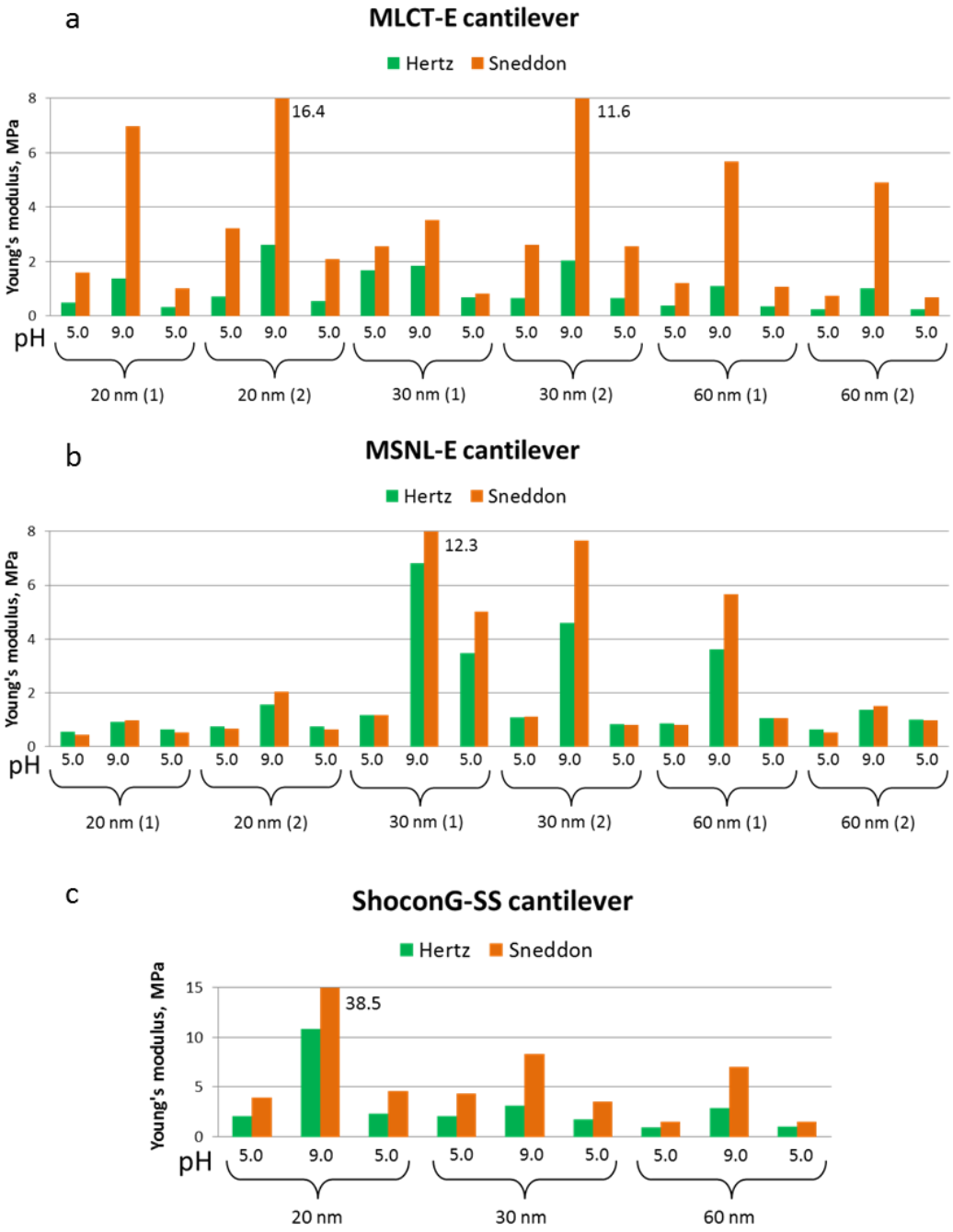

Figure 4-10 The effective Young's modulus for the PDMAEMA brushes (of 20 nm, 30 nm and 60 nm thickness in the dried state) at pH 5.0 and pH 9.0, estimated by applying Hertz and Sneddon models to the corresponding AFM force curves. The data were collected with (a) MLCT cantilevers, (b) MSNL cantilevers and (c) ShoconG-SS cantilevers.

The effective Young's modulus of the polymer brush in the literature varies a lot. For example, the high density swollen polymer brush measured in liquid resulted in 500 ± 69 kPa [165] which is close to our results, however the thickness of the brush used in that experiment was in the range from 380 to 800 nm. In another study the elasticity of the polymer brush in swollen state was 22 ± 1 kPa and 11 ± 2 kPa in the collapsed state [166]. On the other hand, the polymer brushes scanned in air resulted in the Young's modulus of 2.5 GPa [167].

Differences in the effective Young's moduli can be explained not only with identification of the contact point in the force curve, but also by the differences in the AFM probe (Figure 4-11). The probes used in this work were neither ideally spherical nor conical as it was assumed in the indentation models. Instead, the all three tips had a pyramidal shape. For example, the tips with larger diameters such as MLCT (40-120 nm) appeared to yield lower values of Young's modulus at the same indentation and applied force, compared to MSNL (4-24 nm) or ShoconG-SS (4-8 nm) probes.

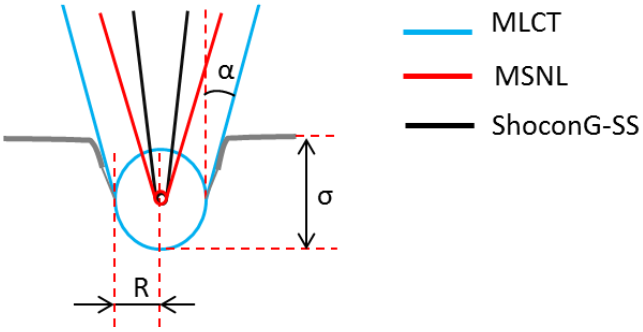

Figure 4-11 Schematic representation of the AFM tips with spherical indenter, where R is a tip radius, α is a half opening angle and σ is an indentation of the tip into the sample.

4.4 Conclusion

This chapter provides references measurements to validate simple predictions for different states of one-end grafted polymers, including their appearance in AFM measurements. The polymer brush was chosen as a model system that can show different types of behaviour that mimic different scenarios that have been proposed to describe the structure of the permeability barrier within NPCs: This includes extended

and collapsed states depending on the pH of the buffer, which would resemble an entropic brush and hydrogel respectively.

The polymer brush used in this study was grafted from one end to the silicon chip. Both the high density grafting and repulsive chain-chain interactions caused the brush to be the extended state for pH 5.0, which was confirmed by AFM Force Volume measurements by showing exponential behaviour of the tip-surface interaction. The results are similar to data on FG-domains tethered to the gold surface [168], [61]. Although, the scale of the substrate differed dramatically (100 nm and 5 mm), it did not affect the behaviour of the brush. According to the similarities in the physical properties, it was assumed that the extended brush fits well with the definition of the entropic brush model, which states that extended nucleoporin filaments fluctuate around the entrance to the pore and do not cohesively interact with each other.

On the other hand, the collapsed brush creates layers of entangled chains to avoid the interaction with a solvent which resembles the description of the hydrogel, where the nucleoporins create dense meshwork due to the hydrophobic interaction between the FG-repeats and fluctuates insignificantly. Force curves obtained from the collapsed brush showed sharp increase of the force over indentation which is a characteristic of a hard surface. Similar results were obtained on FG domain assemblies formed from cohesive FG-Nups [22].

AFM imaging and force measurements yielded results that were consistent with the expected collapse and swelling behaviour of PDMAEMA brushes. As expected, the swollen state is softer than the collapsed one, which is quantified by applying indentation models to determine effective Young's from the force curves. The trend in stiffness increase with increase of pH was shown. Overall the force curves were following the exponential behaviour in pH 5.0 conditions, following the prediction from polymer brushes [169]. At pH 9.0, the majority of curves had steeper slopes as also indicated by the calculated Young's moduli. These results demonstrate that AFM force curves can be used to distinguish between entropic brush and collapsed or cohesive brush ("gel") scenarios for the transport barrier in the NPC. Thus, knowledge about the shape of force curves for each state of the polymer brush illustrated in this chapter can

be used for further comparison of the force curves acquired from actual NPCs with the proposed model system. The comparison is demonstrated within the next chapter.

Chapter 5 Nanomechanical Characterisation of the Nuclear Pore Complex

5.1 Introduction

Nuclear pore complexes (NPCs) have been studied with a variety of approaches, including structural investigations [4], [6], [13], [17], characterisation of purified nucleoporins [9], [170], [24], and evaluation of the kinetics of the transport mechanism [52], [57], [75], [171]. However, the structure and configuration of the FG-nucleoporins, the building blocks of the permeability barrier, and their transient dynamic interaction are still poorly understood.

In this chapter we describe a nanomechanical characterisation of the permeability barrier, using AFM in Force Volume mode, which represents a new approach for studying the permeability barrier.

The Force Volume was carried out by probing individual NPCs in isolated nuclear envelope with a sharp tip to record the interaction between the tip and the sample (Figure 5-1). In particular, we were interested in the nanomechanics of the central channel of the pore, where the FG-filaments, which are the unstructured part of Nups, form the barrier.

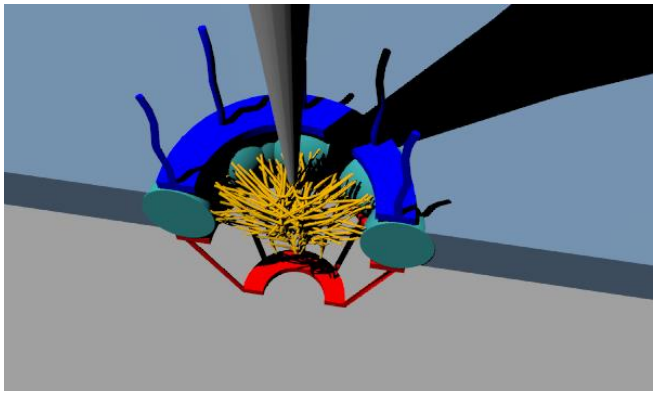

Figure 5-1 Schematic representation of the AFM tip probing the central channel of the NPC, with unstructured nucleoporins (yellow) here shown to span across the NPC channel [172].

The resulting force volume data from NPCs were compared to the force data from the polymer brush investigated in the previous chapter (Chapter 4). For this purposes the type of the tip (MSNL-E) was kept the same and the applied force was up to 700 pN. The main goal of the comparison was to find out whether the FG-repeats within the central channel behave as a polymer brush or not.

To sum up, the aims of this chapter are (i) to measure force curves on NPCs using the Force Volume method and (ii) compare the behaviour of the force curves of the polymer brush and the central channel of the NPC.

5.2 Results and Discussion

5.2.1 Acquiring the nanomechanical properties of the NPC

The Force Volume mode produces a range of force curves which show the interaction between the tip and the sample through the relation of the force and indentation. The examination of the height and stiffness cross sections of the pore, generated by the force curves (described in Section 3.1.5), can provide us with information about the topography and stiffness distribution along the pore. Additionally, the force curves were fitted with indentation models to find out the Young's modulus of the pore.

5.2.2 NPC topography and stiffness distribution

Figure 5-2 (a) shows the height cross section which is an average of 19 pores. It was generated making use of the rotational symmetry around the central axis of the pore (see Section 3.1.5, Chapter 3). The force data were assigned to the bins around the centre of the pore, as a function of their radial distance from the pore centre, to acquire an average force curve for each radial position. It displays the 'true height' of the NPC, at which the force due to tip-sample contact starts to deviate from the force baseline. This contact point was identified in two different ways (see Section 3.1.5, Chapter 3): by fitting the curves with an indentation model (Hertz model, green line) and by dividing the curve into intervals, detecting the early onset of the force at tip-sample contact, and by fitting this onset with a stepwise function (constant for baseline, and linear for the early onset; orange line). The blue line represents the deformed height of the pore under applied force. Thus, the indentation of the tip into the sample is the difference between

the true and the deformed heights. According to this cross section the MSNL-E tip indented the NPC surface by >20 nm.

Figure 5-2 (b) shows the rotationally stiffness cross section for these data, coupled with the height cross section, where the 'stiffness' is defined as the force gradient (times '-1'). The true height profile is the same as in height cross section. The grey area masks depths for which no or insufficient (i.e., less than 30% of force curves contained data in this range) force data were available. The stiffness is represented by a colour map in which red is the maximum value (here 25 pN/nm) and blue refers to zero. Interestingly, the centre of the pore as well as the edges appears stiffer than the rest of the pore. Moreover, the central part of the channel (around 20 nm in diameter) seems to be as stiff as the rim of the pore.

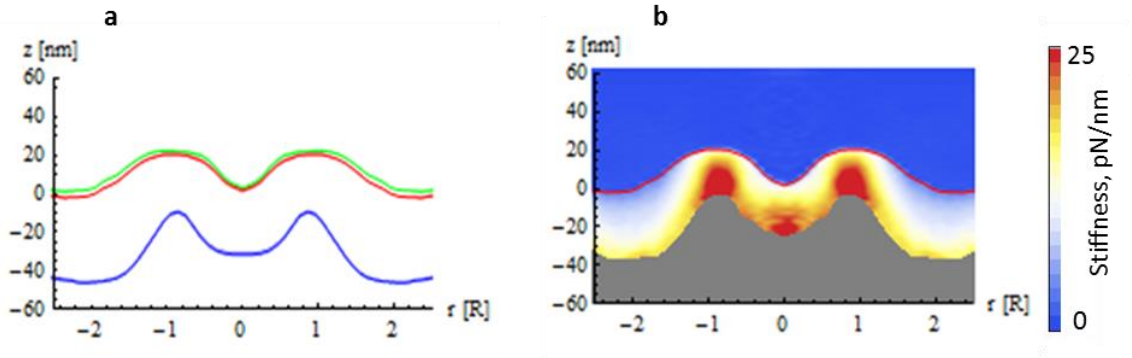

Figure 5-2 a) Height cross section of the pore representing the true and deformed heights (orange/green and blue lines respectively). b) The height cross section coupled with the stiffness values derived from the force curves. In the colour map the stiffness values increase from 0 pN/nm (blue) to 25 pN/nm (red). The grey area masks depths for which no or insufficient (i.e., less than 30% of force curves contained data in this range) force data were available. The zero point in Z-scale in both cross sections corresponds to the height of the nuclear envelope near the NPC (at 2×R). The horizontal scale represents a radial distance from the centre of the pore, normalised to the radius of the NPC scaffold R ~ 42.5 nm.

To help interpreting the measured height and stiffness cross sections, the results were compared to the images of cross sections obtained with cryo-electron tomography, which is a technique commonly used to study the structure of the NPC [4], [18], [81],

[17], [8], [173]. Since the first cryo-electron tomography image of the NPC was captured, the resolution has improved dramatically from 12 nm [3] to 2 nm [10]. EM cross sections typically resolve both nucleoplasmic and cytoplasmic ring structures [4], [18], [17], [8].

The AFM stiffness cross sections can be compared with the structure of the cytoplasmic side of the nuclear envelope, as determined by EM on the same organism (*Xenopus* oocytes). The averaged AFM stiffness cross section was overlaid with the latest molecular density EM cross section at the same scale, and the results showed a good agreement, as depicted in Figure 5-3, where it should be noted that EM densities were masked within a central tube of 17 nm diameter, and that the averaged EM data are not sensitive to disordered nucleoporins. The high stiffness at the edges of the pore is attributable to the cytoplasmic ring.

The location of the stiffness matched well with that molecular density in the pore. The locations of enhanced (red) stiffness match well with the (structured) molecular density in the pore. The rest of the central channel is filled with the molecular density corresponding to various protein structures of the NPC [10].

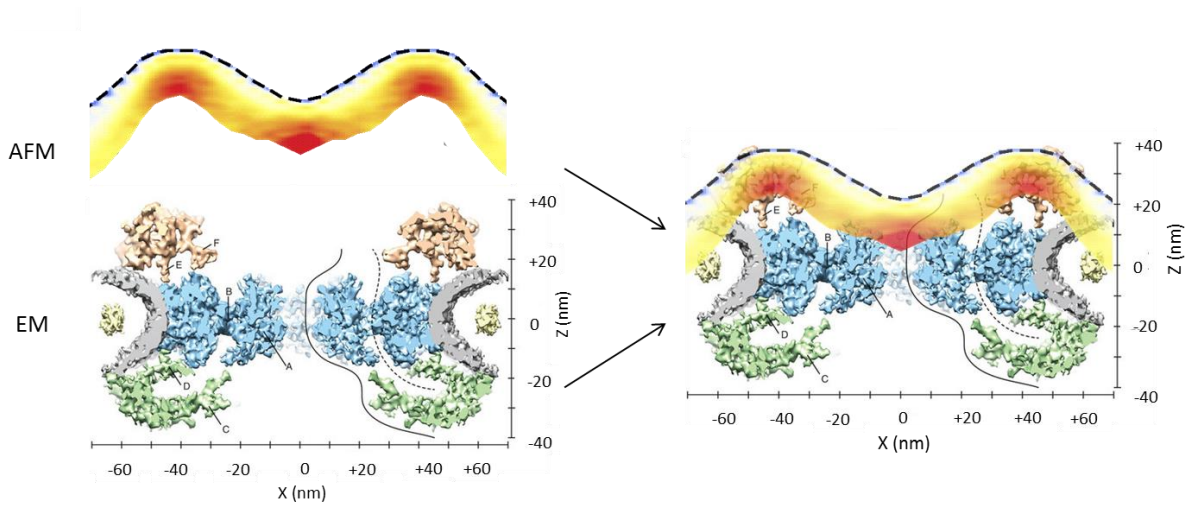

Figure 5-3 The AFM stiffness map (NPC cross-section) overlaid with cryo-electron tomography representation of the NPC (cross section) [3]. *Both representations are at the same scale. The EM image was adapted from* [10] *and the AFM cross section was adapted from* [172].

Therefore, by looking at the stiffness distribution, we can conclude that the shape of the NPC was preserved during Force Volume measurements, including the presence of central density.

5.2.3 Elasticity of the NPC defined by indentation models

The force curves were also fitted with Hertz and Sneddon models (see Section 4.3.3, Chapter 4) to obtain the effective Young's modulus for each part of the pore. Figure 4a shows the average force curve (out of 19 pores) from the centre of the pore fitted with the Hertz and Sneddon models.

The force curve obtained from the NPC central channel shows a steep increase of the force with indentation and exhibits a clear contact point (Figure 5-4 a). Both fits roughly match the experimental data and overlap with each other at the slope area, but there are discrepancies in contact point identification. Both models found the contact point in a non-contact area. The Sneddon fit identified the contact point 10 nm apart from the contact point found with our Contact Point Identification routine (see Section 3.1.5, Chapter 3), while the Hertz fit found the contact point about 4 nm away from the original point. Briefly, the indentation models show a reasonable but not perfect agreement with the experimental data.

Stiffness curves (Figure 5-4 b) derived from the force curve and model fits, conversely, show a clearer difference between the models. The Hertz model replicated the data curve better than the Sneddon model. It found the contact point at the right position and followed the trend of the curve along the indentation showing the step-like behaviour of the derived force curve, corresponding to a sudden increase of stiffness. On the other hand, the Sneddon model predicts a linear curve from the contact point to the maximum indentation.

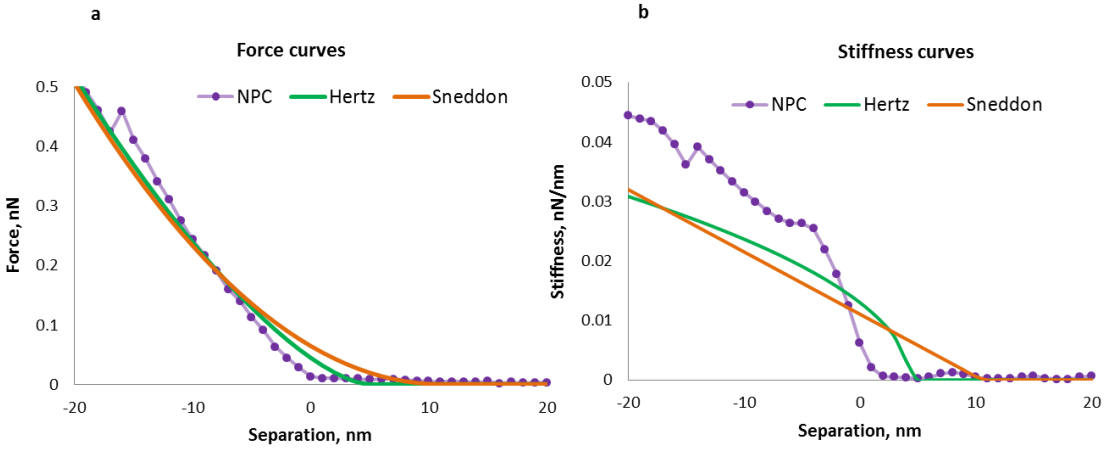

Figure 5-4 a) Data force curve and (b) stiffness curves (both purple) fitted with Hertz (green) and Sneddon (orange) models. The contact point set at zero.

Figure 5-5 shows the difference in the effective Young's modulus obtained from the force curves for the two models. Figure 5-5 (a) demonstrates the values for the elastic modulus calculated using the Hertz model. It shows high values of the modulus at the same positions where the maximum stiffness was obtained before: the cytoplasmic ring and the central channel. We can observe that the average Young's modulus of the central channel is slightly lower than the ring (about 0.4 MPa).

Conversely, the elastic modulus cross section acquired using the Sneddon model showed the stiffness profile matched neither the Hertz model nor the stiffness cross section (Figure 5-5 b). It shows a high elastic modulus for the inner side of the channel between the central stiffness and the rim. Moreover, the stiffness at the centre is not prominent anymore, although the standard deviation indicates some variation in determining the stiffness, but it still is not as high as the elastic modulus at the rim. Overall, the value of the Young's modulus is half that obtained from the Hertz model.

For the Young's modulus determination, the force curves were fitted over the baseline and only the first ~20 nm of indentation, since we expect the force curves to become more artefactual for larger indentations, due to interaction of the tip shaft with the NPC scaffold.

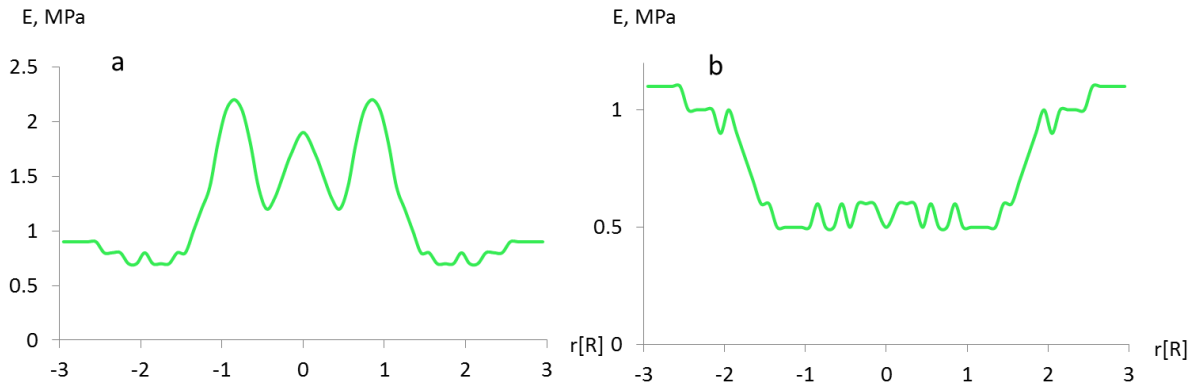

Figure 5-5 Cross sections of the elastic modulus distribution in the pore obtained by (a) Hertz and (b) Sneddon models.

In the scientific literature, the stiffness of biological cells is commonly represented by Young's moduli as determined using the Hertz and Sneddon models [174], [175], [176], [177], [178], [179]. However, since these models assume indentation in a semi-infinite, homogeneous material, it is not surprising that some data did not fit well with either model model. For example, the fitting of the Sneddon model to the force curves obtained from cardiac cells, shows a large deviation from the data points. However, the blunted conical tip used in the same analysis resulted in a good fit to the data force curves [177].

In addition, if the sample is too thin, then the underlying hard substrate could cause the stiffness measurements to yield artefactually high results [180]. For our NPC measurements, however, it was shown that the underlying substrate did not yield significant changes in the stiffness measurement, by comparison to results on NPCs of which the nuclear basket (here acting as a spacer between NPC and substrate) was removed [172].

It is not surprising that the models did not match well with the experimental data shown in Figure 5-5. In practice, it is difficult to justify a quantitative use of either the Hertz or Sneddon model due to the following reasons. Firstly, the tip shape is not as ideal as assumed in these models. Instead of a spherical or conical shape, ideally a pyramidal probe with a blunt end would be used. Secondly, the surface of the nuclear pore is not flat and homogeneous, and it has a finite thickness. Nanoscale confinement (unexpected

properties of the proteins in nanoscale) can be expected to play a role in the central channel. Moreover, the indentation depth (>20 nm) is not negligible compared to the height (thickness) of the nuclear pore, which is about 60-70 nm in vertebrates [10], [181]. As a result, the measured values of the Young's modulus should here only be used for comparative studies, and not as absolute values.

In other words, they can provide effective values of the Young's modulus, to show the difference between the elastic modulus at various locations of the pore [178], [182], [183].

5.2.4 Comparative study of the nanomechanical properties of the NPC and the Polymer brush

It is interesting to draw the comparison between nanomechanical properties of the central channel of the NPC and the polymer brush because existing models of the permeability barrier suggest that the barrier is formed by a gel or a brush. Thus, the evaluation of force and stiffness curves of the NPC and the polymer brush would be informative on the question if the barrier shows a brush-like or gel-like behaviour.

As an additional control the comparison was also made with the polymer brush in the collapsed state. As it was shown in Chapter 4 the polymer brush can be found in two states depending on the pH of the buffer solution. In the extended state the brush is stretched out from the grafted surface and fluctuates freely, which corresponds to the 'polymer brush' model, whilst in the collapsed state, the brush is compressed and tangled, which could resemble a 'hydrogel' model.

Nanomechanical properties of extended polymer brushes compared to the NPC

The force measurements were done in Force Volume mode using AFM on Multimode IV by probing individual pores and collecting the force curves from each pixel of the image. To directly compare the nanomechanical properties of the polymer brush (see the previous chapter) and the properties of the NPC central channel, the scanning conditions were kept the same, i.e., probe, applied force, scan size and resolution.

Figure 5-6 (a) shows the average force curves collected from the brush sample (red line) and NPCs (blue line). The brush sample presented here is in its extended state at pH 5.0

and has a thickness of 60 nm in a dry state (in air). The curve corresponding to the NPC was collected from the central channel, specifically from the disk-shaped area of ~8 nm diameter located at the centre of the NPC. Both force curves were aligned to the contact point (defined as zero separation).

The force curves obtained from the polymer brush sample display exponential behaviour, making it difficult to identify the contact point. On the other hand, the force curve from the NPC is much steeper and has a prominent contact point since the force increases linearly after contact with the surface, i.e., the deviation from the baseline is sudden and well-defined.

The indentation of the tip into the polymer brush sample is about 60 nm, whilst the NPC sample shows only about 30 nm of indentation.

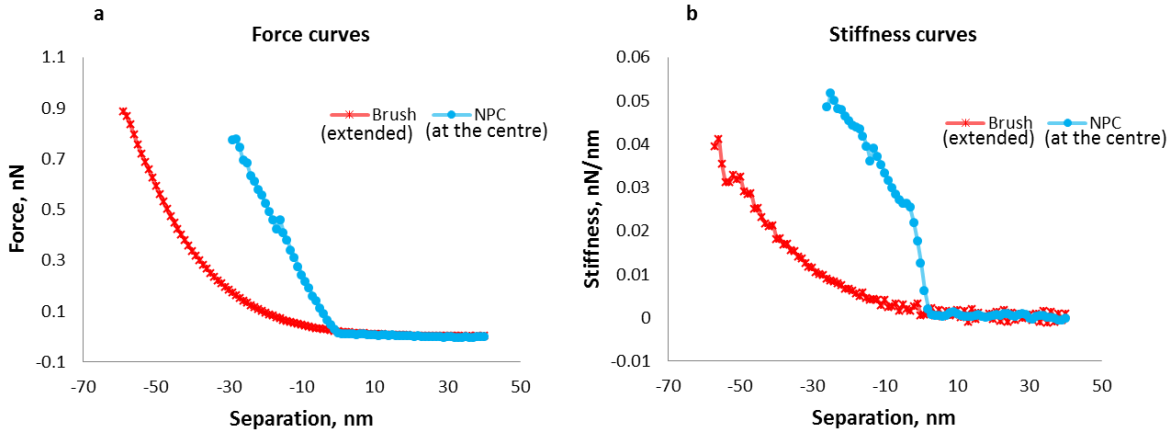

Figure 5-6 Averaged force (a) and stiffness (b) curves from the centre of NPCs (based on 76 individual curves) and from the extended polymer brush (based on 1024 curves). The red line corresponds to the 60 nm thick polymer brush at pH 5 (extended state) and the blue line - central channel of 19 NPCs.

The same observation on the behaviour of the force curves can be made by analysing the stiffness curves, which are derivatives of the force curves shown above (Figure 5-6 b). As expected, the stiffness curve of the polymer brush also displays exponential growth, as in the force curve. This is different to the behaviour of the NPC sample, which shows a steep increase in the stiffness during the first few nanometres of indentation, and then continues to increase slowly.

The steep growth of the force and the step-like increase of the stiffness, demonstrated by the central channel of the NPC, suggest that this region, in which the permeability barrier of the pore is located, is relatively stiff. On the contrary, the polymer brushes showed exponential behaviour for both force and stiffness, which is a hallmark of a material dominated by thermal fluctuations of its components (an 'entropic brush') [184].

Nanomechanical properties of collapsed polymer brushes compared to the NPC

Although a brush in an extended state is softer than the NPC barrier, a brush in a collapsed state might be of the similar stiffness. Figure 5-7 (a) shows the similarity in the behaviour of the force curves which were obtained from the collapsed polymer brush at pH 9.0 (red) and from the NPCs (blue). During the first 15 nm of indentation, the force curves are almost overlapping. The stiffness curves also confirm the similarity between the NPC and brush sample (Figure 5-7 b). Up to ~15 nm indentation, the curves from the NPC appear slightly steeper than those of the polymer brush. The small differences between the force curves can be easily spotted on the stiffness curves.

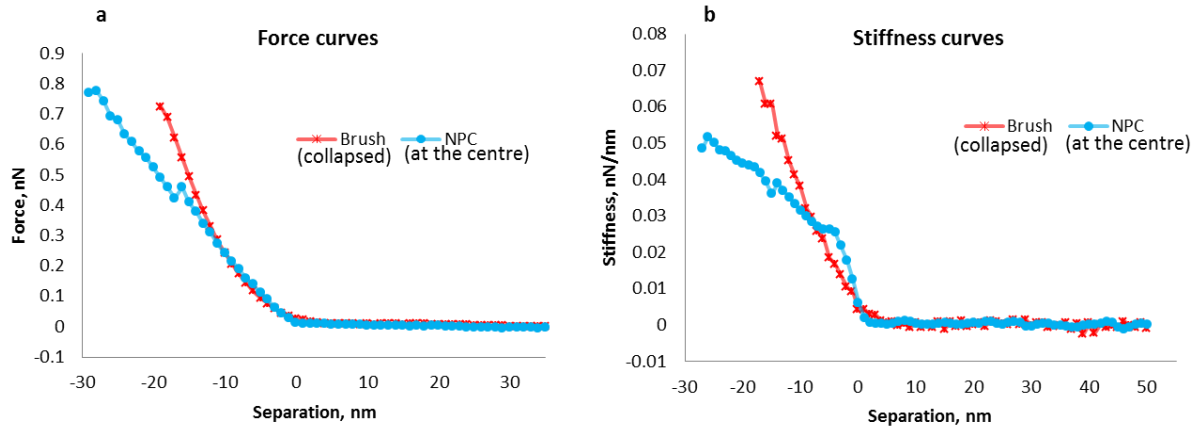

Figure 5-7 Averaged force (a) and stiffness (b) curves from the centre of NPCs (based on 76 individual curves) and from the collapsed polymer brush (based on 1024 curves). The red line corresponds to the 60 nm thick polymer brush at pH 9 (collapsed state) and the blue line - central channel of 19 NPCs.

Currently, biophysical descriptions of the permeability barrier's structure and selectivity remain hypothetical due to minimal information about the nanomechanical properties of FG Nups, which constitute the barrier.

The FG Nups studied *in vitro* showed that they can take up four different conformations. The first one is the brush-like extended state of the FG nucleoporins [23], [62], [61]. For example, AFM force measurements of the FG containing nucleoporins (cNup153), which were tethered to the gold nanodots, showed force curves with long-range repulsive steric forces, supporting the brush-like model. This polymer brush behaviour is not necessarily surprising for disordered, unstructured proteins [62], [61].

The second conformation is a collapsed state of FG Nups, which was also claimed to result when the FG domains were interacting with karyopherins [23], [26]. A collapsed polymer state would also greatly resemble a hydrogel structure, as observed for FG Nups *in vitro* [28], [27], [24], [26], [25]. The hydrogel has a functional selectivity, meaning it excludes cargo without nuclear transport receptors. Interestingly, the FG nucleoporin Nup153, which was mentioned above having a brush-like conformation, was observed in a gel state [26]. The latter indicates that the *in vitro* studies of FG Nups may not give a complete representation of the permeability barrier structure.

Our experiments were conducted on the intact NPCs and show that the permeability barrier of the central channel is quite similar in stiffness with the collapsed brush state. When the brush collapses, the conformation of the polymer chain alters and a meshwork of tangled brush strings form, thus, the compressibility increases [185]. This means that the central channel of the NPC is stiffer than the brush in its extended state. This conclusion excludes the entropic brush model as an explanation for the permeability barrier since if the barrier constituted from the brush-like filaments of FG-Nups, it would appear softer and easier to penetrate. The AFM results thus appear in better agreement with a hydrogel state, formed by cross-linked FG-repeats.

However, the stiffness at the central channel might still be due factors that are not intrinsic to the NPC, and might thus not allow any conclusions about the nature of the FG Nups in the transport barrier. In particular, the central stiffness feature appears

similar to previous observations of a central plug, the nature of which is rather controversial.

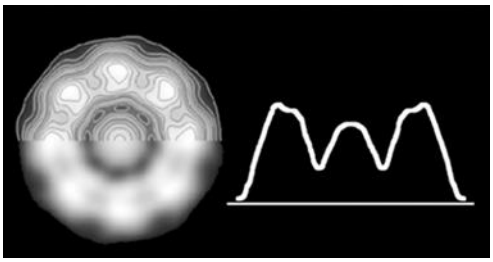

Figure 5-8 Averaged pore (>100) of thick-ice embedded Xenopus NPCs as measured by transmission electron microscopy. The central plug appears at the centre of the channel. On the right side there is a profile of averaged pore's cross section, where the protrusion is clearly observable [3].

In particular, this central plug (Figure 5-8) was considered as either a cargo trapped during the transport [14], [186] or as a meshwork of filaments from Nups [74], [187]. The central plug is mobile [110], [188] though it can disappear by applying a large force to the tip during AFM imaging [189]. It has also been claimed that it might be an artefact caused by the nuclear basket folding during fixation of a sample [99]. However it has been shown to exist even without fixation, although it may not be observable in every single NPC [37].

It has also been referred to as a transporter, which presumably helps the cargo to translocate the pore and acts as the central transport channel. The transporter is believed to be bound to the ring via eight internal filaments which seemingly open and close the gates of the transporter [5], [7], [186].

Therefore, the current data is not yet conclusive and requires further investigation with sharper and narrower tips to probe deeper inside the channel, and additionally, imply new sample preparation protocol to verify if stuck cargo is not a dominant factor in the NPC structure.

Therefore, the next chapter will present the nanomechanical properties of the NPC in a 'washed out' state, with little or no cargo present, and measured with tips that were sharper and had a higher aspect ratio. Consequently, the models of the permeability barrier will be tested. Thus, if the NPC is free of cargo, the FG Nups in central channel

should either demonstrate the characteristics of brush-like or hydrogel behaviour. Additionally, the nature of the central plug should be clarified.

5.3 Conclusion

The AFM Force Volume mode was able to generate height cross sections of the pore, indicating the true (non-indented) height and the deformed height under an applied force. Forces were measured over indentations of >20 nm. The topography and stiffness cross section of the pore matched well with EM data for NPCs of the same organism (*Xenopus laevis*).

The nanomechanical properties acquired from the central channel of the pore were compared to those from the model system – polymer brush – to answer the question whether the permeability barrier resembles an entropic brush structure or the gel-like structure. However, it is worth to mention that the conditions within NPC are different from the model sample for several reasons. Firstly, model sample used the synthetic material rather than FG-domains, though the physical properties appear rather similar. Secondly, in the NPC the FG-domains are confined within a nanoscale pore, whereas the polymer model sample has macroscale lateral dimensions. However, as it was noted earlier, this difference is not detectable in force curves. Thirdly, the density and concentration of the FG-domains is not strictly comparable with the polymer brush density.

Despite these limitations polymer brush is a convenient model: a sample that can show two different types of behaviour. By assuming that the densely grafted polymer brush in the collapsed state creates thick meshwork of polymers as in the hydrogel, we took the force measurements of the brush in extended and collapsed states to represent two proposed models for the structure of the permeability barrier.

As a result of the comparison of nanomechanical properties between the polymer brush and the NPC, we concluded that the structure of the FG Nups in the barrier resembles rather a collapsed than an extended brush. Although there was a good match for the force curves measured from the NPC central channel and the collapsed brush, there are few points to consider such as that different materials were probed (synthetic vs.

natural), with an ill-defined grafting density. In addition, the configuration of the nucleoporins within the NPC and the arrangement of the polymer brush upon collapse might differ drastically because the differences in scale and geometry as outlined above. Nevertheless, force curves from both samples exhibited stiffer material than the extended polymer brush.

However, these results needs further investigation due to the fact that NPCs imaged on AFM might still contain other macromolecules and karyopherins, which could contribute to the stiffness in the central channel. Moreover, according to the brush-model the entropic extended brush filaments collapsed when interacting with nuclear transport receptors. For this reason, it is important to verify to what extent the observed nanomechanical properties in the NPC can be interpreted as due to the FG-Nups (i.e., polymers) alone. Therefore, further experiments on ‘washed out’ NPCs are described in the next chapter to determine the nanomechanical properties of the permeability barrier with reduced amounts of possible cargoes and karyopherins.

Chapter 6 Nanomechanical Characterisation of the Permeability Barrier upon the NPC wash

6.1 Introduction

The transport mechanism in NPCs depends hugely on the structure of the permeability barrier. Various proposed models imply very different characteristics for the NPC nucleoporins in the permeability barrier, ranging from hydrogel behaviour to that of an entropic polymer brush. The hydrogel model assumes that the nucleoporins are a gel of cross-linked FG-repeat proteins, which are dissolved upon interaction with transport receptors. On the other hand, in the polymer brush model, the nucleoporins are fluctuating extended proteins, which in some views may collapse when transport receptors interact with them.

The results of the previous chapter show that the nanomechanical properties of the barrier in the central channel of the pore are drastically different from properties of the extended polymer brush, but agree reasonably well with the properties of the collapsed brush. Moreover, the pronounced stiffness at the central channel was observed, which might be attributable to a cargo molecule trapped inside the pore or the actual permeability barrier. In other words, it is not clear to what extent the observed nanomechanical properties in the NPC could be assigned to the nucleoporins in the transport channel. It was therefore decided to wash the pores, remove any remaining cargo molecules, and probe the NPC central channels once again. Additionally, to probe deeper and collect more accurate data the super sharp tips were used (Figure 6-1).

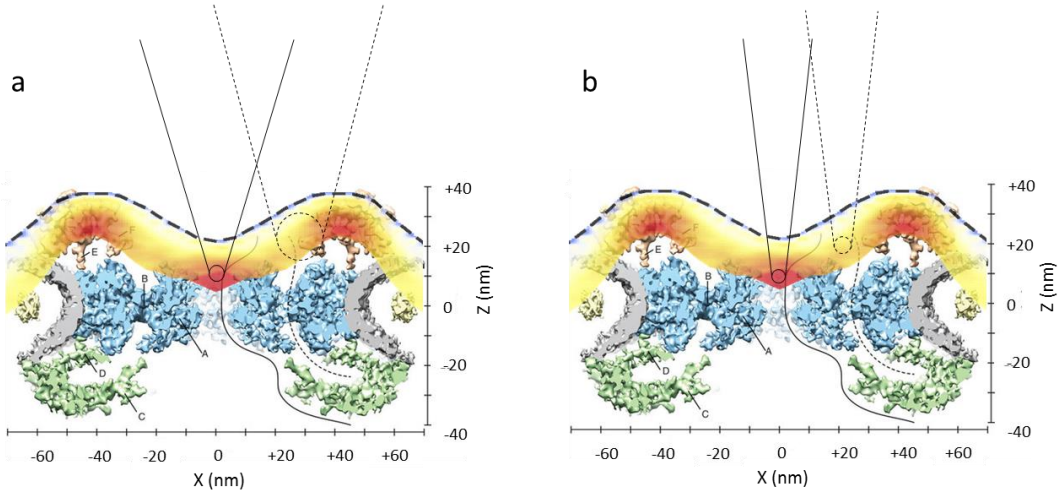

Figure 6-1 Probing the NPC with (a) MSNL tip with 18^o opening angle and nominal tip diameter 4 nm (solid line); and maximum tip diameter 16 nm (dashed line); b) probing with super sharp tip of ~8^o opening angle and 4 nm tip diameter (solid line); and maximum 8 nm in diameter (dashed line).

The experiment in this chapter was designed to probe the NPCs in their native state, i.e. probably including cargoes and nuclear transport receptors in transit; and in a state, where these have been depleted by adding transport enhancing reagents and enzymes digesting ribonucleic proteins, which are presumably some of the largest cargoes in the NPC.

The removal of cargoes from the central channel of the NPC was achieved by activating the Ran cycle for the isolated nuclei, causing a larger number of transport events to occur. Specifically, active transport was promoted by Ran-Mix and Energy-Mix (see Section 3.2.7, Chapter 3) containing the main components required for the transport cycle; and the nuclear transport receptor Importinβ. Ran-Mix contains proteins such as RanGTP, RanBP1, RanGAP and NTF2 that sustain the nuclear import process. The transport process is also energy-dependent, thus the Energy Mix was added to the system to provide the active transport cycle with the required chemical energy.

The transport activation was verified on the isolated nuclei by observing an accumulation of fluorescent cargo inside the nuclei using confocal microscopy. Additionally, the effect of transport activation was tested on fluorescent Importinβ to find out if it behaves as a cargo. The permeability barrier integrity was verified by

observing the leakage of fluorescent 70 kDa dextran in the presence and absence of cyclohexanediol (CHD) which is known to degrade the barrier.

Moreover, any remaining cargo was biochemically removed using the endonuclease Benzonase, designed for nucleic acid digestion, including DNA and RNA. The digestion was verified by observing the change in intensity of fluorescently tagged RNA in NPCs on isolated nuclear envelopes using confocal microscopy. Additionally, the process of digestion was also confirmed by applying the Western Blot analysis.

After verifying the transport activation and macromolecules digestion, the NPCs were probed on AFM in Force Volume mode to generate the stiffness cross section and compare the results on native NPCs and 'washed out' NPCs.

6.2 Results and Discussion

Prior to measuring the stiffness topography of 'empty' NPCs (no cargo) a number of control experiments on the confocal microscopy were run to ensure the transport was activated, nuclei were still functional and the cargo was digested after treatment with Ran-/E-mix and Benzonase (Figure 6-2).

Positive-control sample or "treated" samples were incubated with Ran- and E-mix after isolation of the nuclei, and with Benzonase nuclease and after nuclear envelope isolation. For a negative control sample for AFM measurements, confocal imaging and Western Blotting, a "mock-treated" sample was subjected exactly the same procedures except the inclusion of Ran-/E-Mix and Benzonase treatment in the used reagents.

Firstly, the integrity of the permeability barrier was assessed by observing the limited access of the fluorescent dextran which is > 40 kDa in size into the nuclei in comparison with easy flow of dextran upon barrier's damage.

Secondly, after the integrity of the selectivity barrier was verified, the transport activation was confirmed by monitoring the import of fluorescent cargo into the isolated nuclei. Similar experiments were carried out for fluorescently labelled Importins.

Thirdly, after confirming the transport activation on nuclei, the digestion of the cargo was verified on isolated nuclear envelope using confocal microscopy. The intensity of fluorescently tagged RNA was recorded upon the Ran-, E-Mix and Benzonase treatment. To support the findings, the same sample was analysed using Western Blotting.

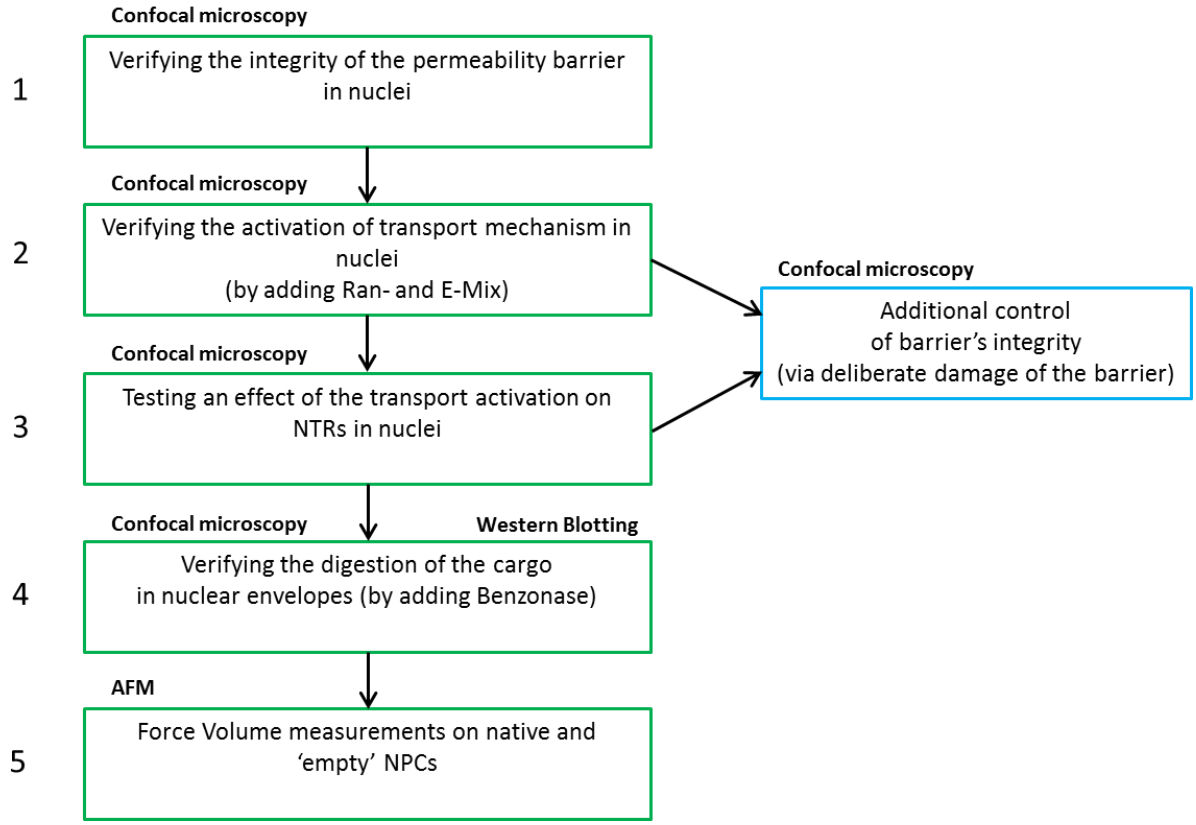

Figure 6-2 A diagram describing the experiments done in this chapter and their sequence.

To ensure that the positive and negative controls could be accurately compared, experiments for both controls were carried out on the same day, from the same batch of oocytes, and using AFM tips from the same batch. It should be emphasised that in this study functional nuclei [190], [191] and nuclear envelopes [192] were used.

6.2.1 Assessing the structural integrity of the permeability barrier

Trans-1,2-cyclohexanediol (CHD) is known to cause irreversible damage to the NPC barrier at 5% concentration. After exposure to CHD, NPCs, and hence the nuclei,

become ‘leaky’ for import of larger cargoes [193]. This was confirmed by observing the influx of 12 kDa and 70 kDa fluorescent dextran after nuclei exposure to the CHD using confocal microscopy.

The reason for the permeability barrier collapse upon CHD treatment is not well known yet. Some assume that it is related to the breaking of bonds between the FG-repeats [76] or dissociation of the Nups from the NPC (Nup62 and Nup98) [193]. The first scenario was tested by monitoring the FG-interaction using the fluorescence microscopy. In particular the Sepharose beads coated with GST-Nup116 had a binding with fluorescent CFP-Nup100, and upon CHD exposure, the FG-interaction was disrupted (Figure 6-3 a). The second scenario was tested by exposing the nuclei and nuclear envelopes to CHD and observing the increasing amount of the nuclear proteins leaking out from nuclei and nuclear envelope into the surrounding area. This was recorded by using sodium dodecyl sulfate polyacrylamide gel electrophoresis (SDS-PAGE), which is designed to separate proteins by their size (Figure 6-3 b,c). To test whether this outcome is due to the CHD effect on the barrier, the nuclei were incubated with WGA which is known for binding the glycosylated sites of Nups mainly at the cytoplasmic ring. As a result at high concentration of CHD, the medium around WGA pre-treated nuclei did not show any sign of nuclear proteins. This means that most likely CHD affects the barrier by affecting the nucleoporins.

Regardless of the exact mechanism, these results allow us to characterise and compare the permeability barrier for intact and damaged NPCs.

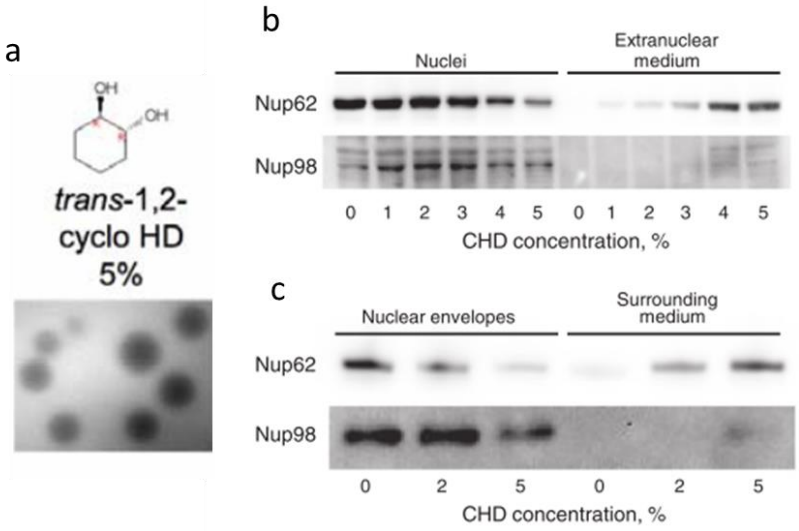

Figure 6-3 (a) The interaction of GST-Nup116 beads with fluorescent CFP-Nup100 in presence of 5% CHD has been broken [72]. *SDS-PAGE analysis applied to (b) nuclei and (c) nuclear envelopes to identify whether there is a signal for Nup98 and Nup62 in the surrounding medium upon exposure to CHD at various concentrations* [193].

Figure 6-4 (a) shows the nuclei with NPCs for which the permeability barrier is intact, since the interior of the nuclei appears dark restricting the surrounding fluorescent 70 kDa dextran from import. In contrast, Figure 6-4 (b) shows the nuclei filled with fluorescent dextran upon degradation of the barrier in the presence of CHD.

To quantify these observations the rate of diffusion of 70 kDa dextran across the nuclear envelope was calculated in the presence and absence of CHD. The rate of dextran influx upon a 5% CHD wash appeared to be ten times faster ($[1.6\pm0.1]x10^{-4}s^{-1}$) than in a sample with no CHD treatment ($[3.5\pm0.3]x10^{-5}\ s^{-1}$). Figure 6-5 shows the changes of intensity over time, before and after the addition of CHD, based on measurements on five nuclei. The background fluorescence intensity before the CHD injection was constant, although it increased over time after incubation with CHD. This is possibly due to the diffusion equilibration of the fluorescent dextran which was added into the buffer after the incubation with CHD to keep the same concentration of fluorophore (because prior to injection of CHD the corresponding amount of solution was removed).

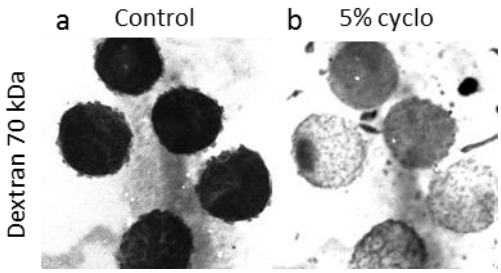

Figure 6-4 Confocal images of nuclei incubated in 70 kDa Dextran in: (a) the absence of, and (b) the presence of 5% CHD.

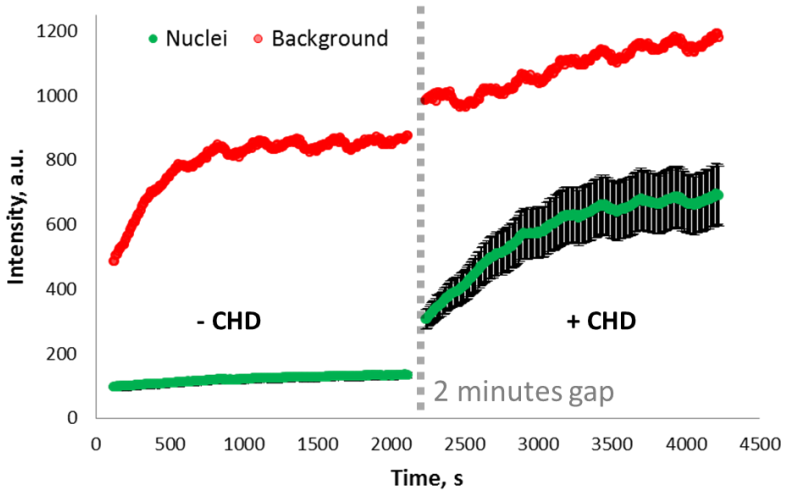

Figure 6-5 Average changes of fluorescence intensity over time in nuclei before and after injection of CHD. The fluorescent signal from dextran was recorded for 35 minutes before the CHD addition, then after a gap of 2 minutes during which the nuclei were incubated with the CHD, the scan continued for another 33 minutes. The error bars (in black) represent the standard error of the mean.

This experiment shows that the nuclei integrity remains intact after isolation of the nuclei, and that the barrier excludes molecules of sizes larger than 40 kDa, unless the barrier is deliberately broken.

6.2.2 Activation of the transport cycle and its effect on the cargo

The experiments on the enhancement of the Ran cycle on isolated nuclei from *X. laevis* oocytes were done in the presence of the fluorescent cargo (Rch1-MBP-IBB-GFP) with an Importinβ binding domain using confocal microscopy. This is a common test of the

transport functionality *in vitro* [194]. The nuclei were incubated with the fluorescent cargo and Importinβ, followed by a wash in Ran- and E-Mix. As a negative control, the nuclei were washed with a solution without Ran- and E-Mix.

Figure 6-6 (a) shows the image from the confocal microscope of the negative control sample, when the nuclei were incubated only with the fluorescent cargo and Importinβ. There is a fluorescence signal inside the nuclei and a slightly brighter signal on the edges of the nuclei. On the other hand, Figure 6-6 (b), which shows the positive control, i.e. the nuclei washed with the Ran- and E-Mix, renders an even distribution of intense fluorescence both on the rim and inside the nuclei. Additionally, the background in the first sample of mock-treated nuclei exhibit brighter signal than the background in the treated sample.

The fluorescence intensity over the nuclear envelope and the interior of the nuclei were compared for both controls, with the results showing a 6-fold increase in the nuclear envelope and 7-fold increase in the nuclei interior for the positive control (Figure 6-6 e). The images along the bottom of the Figure 6-6, (c) and (d), show the nuclei in the presence of the large fluorescently tagged 70 kDa dextran, and serve as validation for the integrity of the nuclei. This dextran molecule is significantly larger than the size exclusion limit for passive transport (40 kDa). Therefore, if the nuclei are intact, the dextran cannot translocate across the NPCs. Indeed, the dextran remained outside of the nucleus, as expected, for the period of the measurements, demonstrating the intactness of the selective barrier to transport.

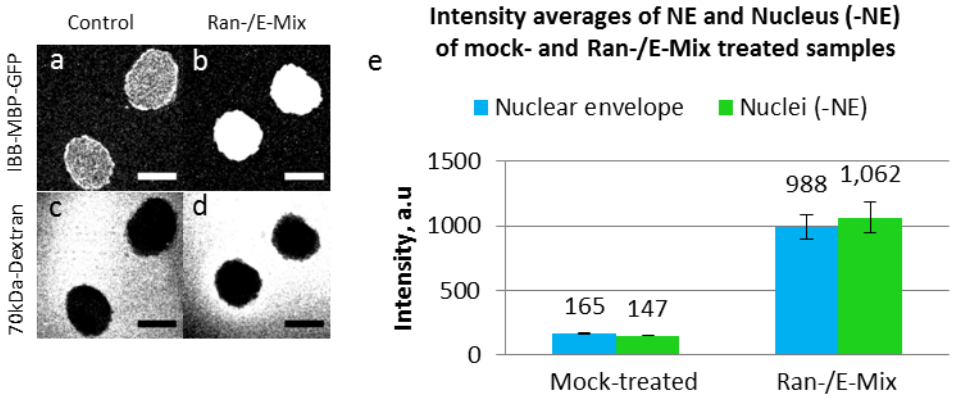

Figure 6-6 a) Mock treated and (b) Ran-/E-Mix treated samples incubated with Rch1-IBB-MBP-GFP to measure active transport. c) and (d) 70 kDa dextran was added to the corresponding nuclei to check the integrity of the nuclei. Scale bar: 400 µm. e) The plot represents the Rch1-IBB-MBP-GFP signal intensity in nuclear envelope and interior of the nuclei, in mock- and treated samples, with error bars indicating standard error of the mean. 15 mock-treated and 16 Ran-, E-Mix treated nuclei were analysed. The images were acquired at the same settings of the laser, photomultiplier gain and offset levels.

Compared to the experiments without Ran- and E-Mix ("untreated" nuclei), the bright fluorescence inside the treated nuclei demonstrates the activation of the transport process, where the cargo is translocated into the nucleoplasm, assisted by Importinβ and Ran-constituents. In these positive control samples, the fluorescent intensity in the nuclear envelope was 7% less than inside the nuclei. For the untreated nuclei, more of the cargo remains stuck at the nuclear envelope (11% larger than in the nuclei), since there is a deficiency of Ran, which is primarily active at the nucleoplasmic site of the NPC, and releases the cargo from the central channel to the nucleus. Therefore, in 'Ran deficient' conditions the fluorescent cargo tends to accumulate at the periphery of the nuclei by docking to the NPC via Importinβ [75].

To sum up, in this experiment there was an obvious influx of Importin-bound cargo into the nucleus, whereas no observable leaks were detected for passive transport. Since the signal in mock-treated samples from the nuclear envelope was larger than inside of the nuclei, while in the Ran-/E-Mix treated sample the highest intensity came from the nuclei, rather than nuclear envelope, we can conclude that fluorescent cargo has

successfully translocated across the pore and accumulated inside the nuclei with less cargo stuck in NPCs.

Behaviour of cargo upon damage to the permeability barrier

The breakdown of the permeability barrier and its subsequent effect on cargo import was shown by confocal microscopy images, as in Figure 6-7. The nuclei which were full of cargo (IBB-MBP-GFP) in Figure 6-7 (a) became almost empty upon the CHD wash (Figure 6-7 b). The GFP intensity dropped after cyclohexanediol treatment to ~70% (Figure 6-7 e), which means the majority of cargo was washed away from the nuclei. On the other hand, the dextran import into nuclei was slower (Figure 6-7 c, d), such that the increase of dextran fluorescence in the nuclei was ~30% (Figure 6-7 f).

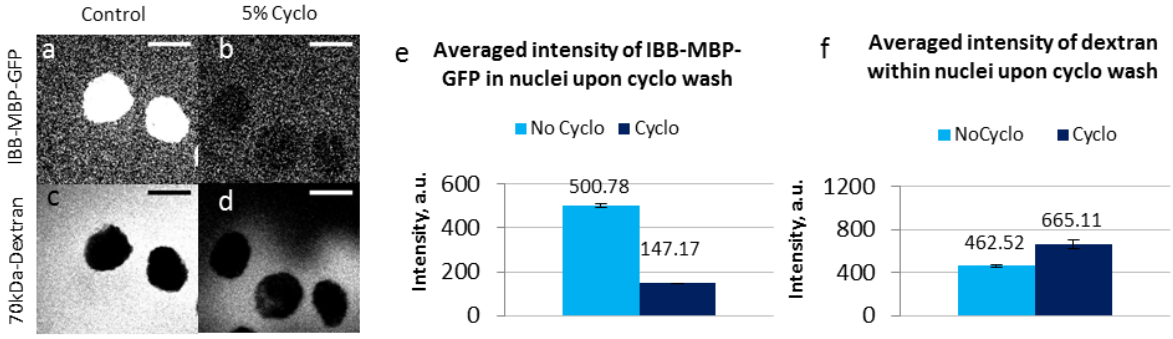

Figure 6-7 a) Control and (b) 5% trans-1,2-cyclohexanediol washed nuclei were incubated with IBB-MBP-GFP. In (c) and (d) structural integrity of the nuclei was tested by adding 70 kDa Dextran. Scale bar – 400 µm. Plots of averaged intensity of the (e) fluorescent cargo and (f) fluorescent dextran within nuclei in presence and absence of CHD.

These results demonstrate that upon damaging the permeability barrier, most of the cargo, which was trapped inside the nuclei, was released, and very little remains inside the nuclei. Thus, the intact permeability barrier holds the accumulated cargo inside the nuclei.

6.2.3 Effect of the transport activation on the depletion of the nuclear transport receptors (NTRs)

In this section the Importinβ influx into the nuclei was tested upon the transport initiation by Ran- and E-Mix.

Figure 6-8 (a) shows a confocal image of nuclei incubated with Importinβ tagged with the fluorophore GFP, in the buffer NIM 1.5% PVP. Similarly to the results shown in the previous section, the nuclei treated with Ran- and E-Mix show a strong fluorescence signal around the nuclear envelope and a much weaker signal within (Figure 6-8 b), whereas the control experiment, although also showing a high intensity around the periphery of the nucleus, has a much higher fluorescence signal inside (Figure 6-8 a). The integrity of the nuclei was tested by adding the 70 kDa dextran prior to measurements, which is excluded from translocation into the nuclei due to its large size and lack of a nuclear localisation signal (Figure 6-8 c, d).

The intensity of the nuclei and its periphery was quantified to compare the signal between the positive and negative control experiments (Figure 6-8 e). The intensity of the mock-treated nuclei (11 in total) excluding its periphery was 26% larger than in the Ran- and E-Mix treated nuclei (9 in total). The rim of the nuclei showed similar results: the intensity of the rim in mock-treated sample was 18% larger than in the treated nuclei. However, the statistical significance of these differences was insufficient to make any concluding statements about NTR depletion here. In both samples, the fluorescence intensity at the periphery of the nuclei was larger than inside.

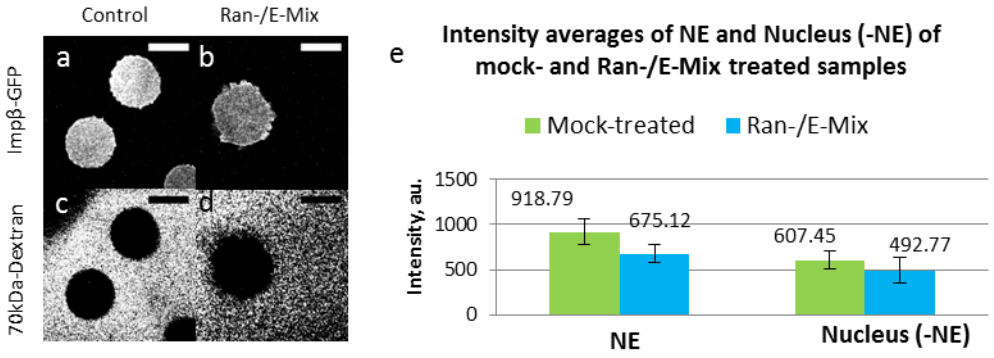

Figure 6-8 a) Control and (b) Ran-/E-Mix treated samples incubated with Impβ-GFP to verify the accumulation and wash-out of nuclear transport receptors and with (c) and (d) 70 kDa dextran to check the integrity of the nuclei. Scale bar: 400 µm; e) The Impβ-GFP signal intensity in the nuclei in control (mock-treated) and treated samples with standard error of the mean. 11 mock-treated and 9 Ran-, E-Mix treated nuclei were analysed.

Behaviour of NTRs upon permeability barrier leakage

A stronger depletion of Importinβ was obtained following exposure to CHD: fluorescent Importinβ had leaked out from the nuclei, but was still present in the nuclear envelope (Figure 6-9 a, b). Figure 6-9 (c) and (d) show the corresponding nuclei incubated in the 70 kDa dextran, validating the effect of CHD on the integrity of the permeability barrier.

The quantification of the fluorescence intensity showed that upon CHD treatment the intensity on the nuclear envelope and inside the nuclei dropped by 55% and 65% respectively (Figure 6-9 e). Conversely, the averaged intensity of dextran fluorescence within the nuclei before and after CHD wash increased by 57%, which confirmed the leakage of the pores.

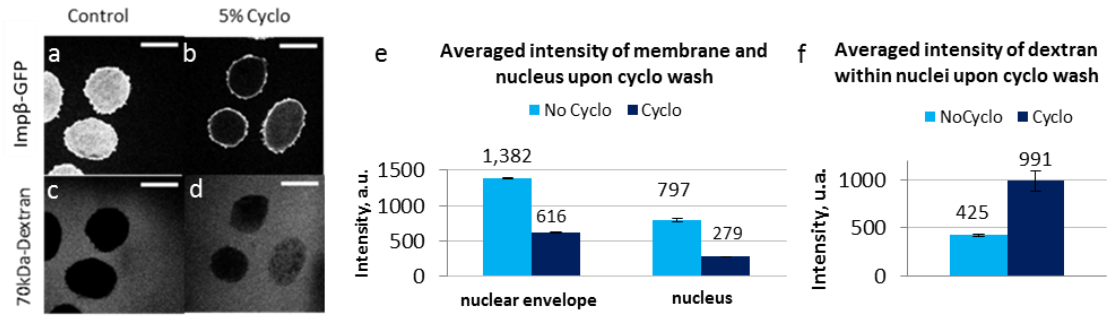

Figure 6-9 a) Isolated nuclei incubated with Importinβ-GFP and washed with (a) NIM 1.5% PVP or (b) 5% trans-1,2-cyclohexanediol. (c) and (d) nuclei incubated in 70 kDa dextran. Scale bar – 400 µm. e) Averaged intensity of the fluorescent Importinβ quantified from the nuclear envelope and the interior of the nuclei before and after the CHD wash. f) Averaged intensity of the dextran fluorophore inside the nuclei upon CHD wash.

These results demonstrate that CHD did not have a significant effect on the binding between FG-repeats and Importinβ: On the confocal images, the fluorescent Importinβ was clearly observed in the nuclear envelope, but not inside of the nucleus (Figure 6-9 b).

Hence the exposure to CHD leads to a significant leakage of Importinβ from the inside of the nuclei, but Importinβ molecules within the NPC are not washed away, even under harsh conditions.

6.2.4 Fluorescence verification of cargo removal from NPC

After verification of the transport activation on nuclei, further experiments were performed on isolated nuclear envelopes. It was assumed that the barrier properties of NPCs remained unchanged upon nuclear envelope isolation, as the nuclear envelope remained in buffer solution during the whole experiment. However, there might be a possibility of some alternation of the barrier when the Ran gradient is not maintained. The nuclear envelopes were isolated after the Ran-/E-Mix pre-treatment of the nuclei. The Benzonase nuclease was added to the nuclear envelope to digest any remaining nucleic acid cargoes.

The result of this treatment was monitored via the fluorescence of SYBR Gold, which stained RNA (YoYo fluorophore) and wheat germ agglutinin (WGA) lectin staining nuclear envelope with Alexa647 fluorescent tag. The WGA was chosen to label the nuclear envelope, because of its high affinity for N-acetylglucosamine residues contained in some nucleoporins [195]. Since the membrane is fully covered by NPCs, [196] the WGA is an optimal reagent to stain the membrane and accurately determine its shape on the substrate. The digested nucleic acids were washed away prior to confocal scanning.

Figure 6-10 shows a series of images of the nuclear envelopes spread over glass and scanned using the confocal microscope. In particular, Figure 6-10 (a) shows the nuclear envelope, which was not subject to any treatment, stained with SYBR Gold with the YoYo fluorescent tag. It shows a high signal for the SYBR Gold in comparison with a very weak signal from the treated NE (Figure 6-10 b). Both WGA controls of the NEs (Figure 6-10 c, d) gave a bright and clean image, showing the shape of the membrane.

The resultant fluorescence intensities of the samples were represented by the ratio of SYBR Gold to WGA intensity (YoYo/Alexa647) (Figure 6-10 e). The combined Ran-/E-Mix and Benzonase treatment reduced the signal from the SYBR Gold by about 50%. In total 11 different NEs for the negative control and 10 for the positive control were analysed.

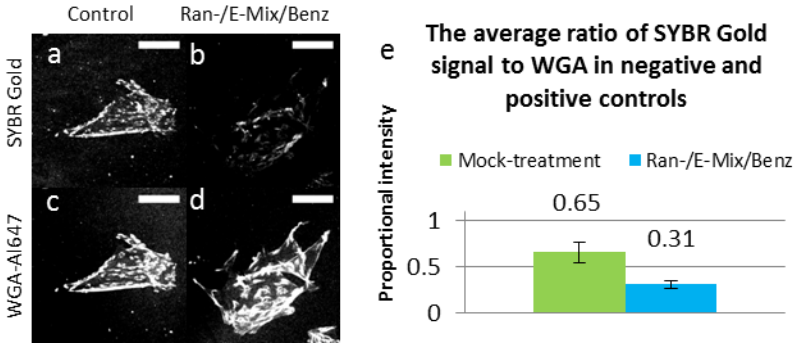

Figure 6-10 a) Control and (b) Ran-/E-Mix, Benzonase treated samples incubated in SYBR Gold (YoYo) to map RNA and (c) and (d) WGA-Alexa647 to identify the membrane. Scale bar: 400 µm; e) Ratio of signal intensity (YoYo/Alexa647) with standard error of the mean.

The drop in fluorescence intensity from the SYBR Gold indicated a reduction of RNA in the nuclear envelope due to the Ran-/E-mix and Benzonase treatment. RNA is one of the most common cargoes found in the NPC, due to its continuous export into the cytoplasm, where it is involved into protein synthesis [197], [1]. Hence, as expected, the treatment with Ran-, E-Mix and Benzonase significantly decreased the amount of the cargo inside the NPCs.

6.2.5 Biochemical verification of cargo removal from the NPC

For a biochemical validation of the wash-out procedure, Western Blotting was used carried out by Dr. Aksana Labokha, Infection and Immunity division, UCL. The Western Blot is a common technique used to identify the proteins in a tissue by separating them using electrophoresis. The separated proteins attach to a membrane and are then stained with the antibodies.

Isolated *Xenopus* nuclei were treated twice with Ran-/E-Mix. During the first wash 1 µM Rch1-IBB-MBP-GFP and 0.5 µM hsImpβ was added. Isolated NEs were treated with 2.5 units/µl Benzonase and solubilised in SDS Sample Buffer. The protein samples were separated on 10% SDS-PAGE and blotted on a Nitrocellulose membrane. 15 nuclear envelopes were loaded per lane. Membranes were incubated separately with primary antibodies 1:200 mouse anti-RNP K/J (3C2; sc-32307, Santo Cruz Biotechnology); 1:1000 mouse mAb anti-GFP; 1:2000 rabbit anti-Nup153 (HPA027896, Sigma). As the secondary antibody – 1:40 000 Goat anti-mouse-IRDye

680 (LI-COR) and 1:40 000 Goat anti-rabbit-IRDye 800 (LI-COR) were used. The membrane was scanned using an Infrared Odyssey scanner. The negative control samples were not subjected to Ran-/E-Mix and Benzonase treatment.

Figure 6-11 shows a membrane with stained proteins, seen as dark bands. The nuclear envelopes of the positive control samples were subjected to the Ran-, E-Mix and Benzonase treatment, whereas NEs in the negative control samples remained untreated. Due to this difference in sample preparation, the intensities of the stripes on the membrane changed. The intensity of a line is a measure of the amount of protein. The nucleoporin Nup153 acted as a loading control to ensure the consistency of the data in two types of samples. As expected, the intensity of Nup153 barely changed.

The bands in the negative control samples were of strong intensity, which means the RNA containing nucleoporin (RNP) and the cargo (Rch1-IBB-MBP-GFP) are present in the nuclear envelope. On the other hand, the positive control sample treated with Ran- and E-Mix, shows a weaker signal, indicating the reduction of RNPs and of Rch1-IBB-MBP-GFP.

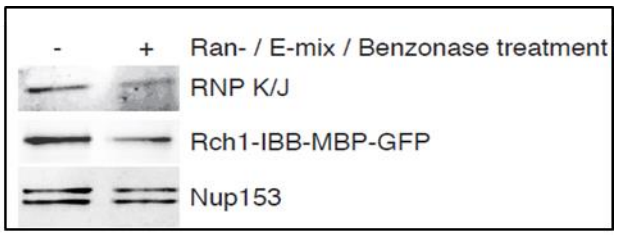

Figure 6-11 Results of the Western Blot analysis performed on 30 NEs, split equally between positive and negative controls. The nucleoporin Nup153 was used as a loading control. The negative control sample shows a strong line representing the presence of the cargo (Rch1-IBB-MBP-GFP; RNP K/J); whereas the positive control qualitatively shows its reduction.

Thus the Western Blot verified the reduction of the cargo (Rch1-IBB-MBP-GFP) and the component of messenger RNPs (RNP K/J) in isolated nuclear envelopes upon treatment with Ran-, E-Mix and Benzonase. The results confirmed that fewer cargo molecules remained in the treated nuclear envelopes, compared to the mock-treated NEs.

6.2.6 Stiffness topography of the NPC cross section

Stiffness topography measurements were carried out using AFM Force Volume mode on isolated nuclear envelopes to probe the structure of the NPC's central channel. This was done from the cytoplasmic side using high-aspect ratio super sharp tips (ShoconG-SS-20, AppNano, USA) to penetrate the pore over depths of tens of nanometres. The nanomechanical properties of the NPCs, in both the presence and absence of the transport enhancing reagents (such as Ran-/E-Mix and the nucleic acid digestive enzyme Benzonase), were observed. The resultant height and stiffness cross sections of the pore were produced from the force curves, as explained in Section 3.1.5 of Chapter 3. The force curves were selected from the multiple concentric shells of 4 nm in size built around the central axis of the pore to generate the rotational averaging of the data. Thus, the cross sections shown below are the result of the force curves averaging for each radial position for over 30 pores.

The height cross sections of the pores from the treated and mock-treated samples (Figure 6-12 a, b) do not exhibit any significant difference between each other. This means the shape of the pore was reserved after the treatment with Ran-, E-Mix and Benzonase. The indentation into the surface, in both samples was >30 nm.

Figure 6-12 (c) shows the stiffness cross section (generated from taking derivatives of the force curves) of the mock-treated sample which confirms the results obtained in Chapter 4 by showing the stiffness at the centre. Interestingly, in the treated samples the central stiffness still remains even after the washing procedure was applied (Figure 6-12 d).

Figure 6-12 (e) and (f) represent the values of the effective Young's modulus as a function of radius of the concentric shells, r. The effective Young's modulus is acquired for each r value by fitting the Hertz model to the initial 20 nm indentation of the corresponding force curves. The elastic modulus of the control sample overall is about 20% higher than of the treated sample. The cross section of the Young's modulus values confirms the presence of the central stiffness in both mock- and treated samples.

The resultant elasticity cross section in comparison with the one obtained with MSNL-E cantilever in Chapter 5, is twice softer according to effective Young's modulus. The discrepancy may be caused by the differences in type of the AFM tip: due to the high aspect ratio of the super sharp tip (>3.5) and smaller tip diameter, it was able to protrude the sample deeper, hence the indentation was larger, and the limitations of the Hertz model (which assumes a small indentation with a sphere) may become more or less apparent.

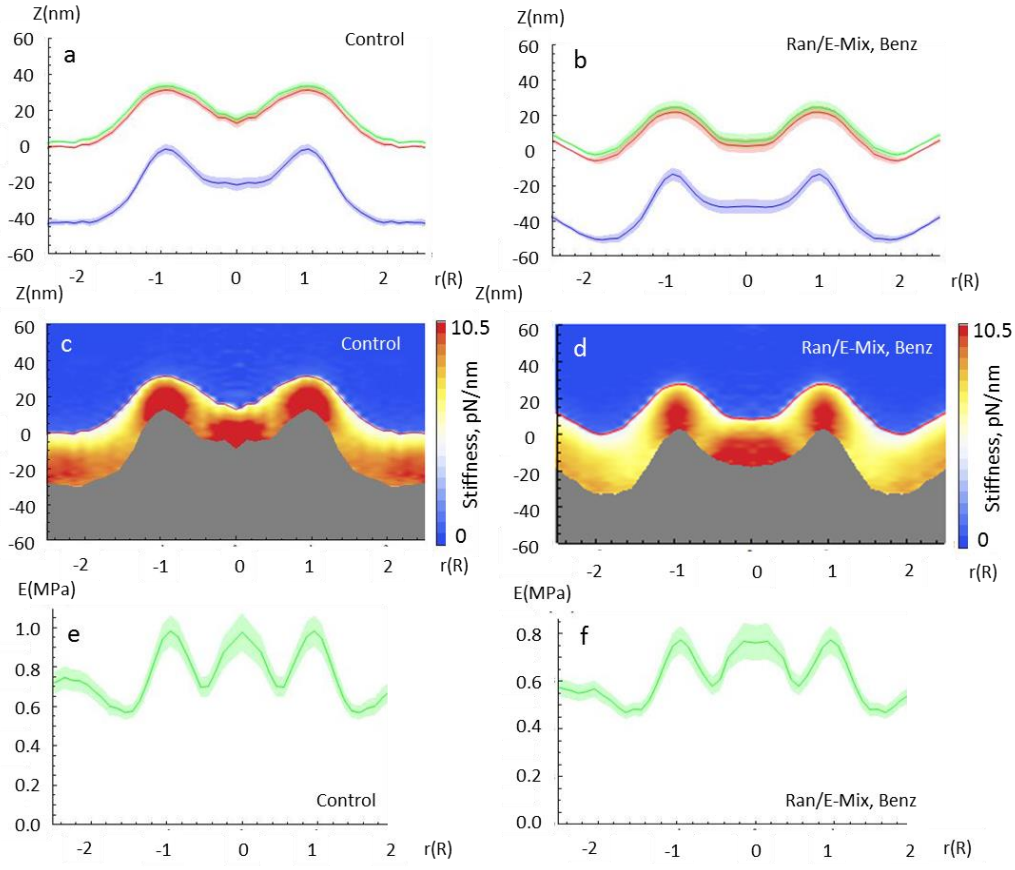

Figure 6-12 The first row shows the height cross sections of (a) mock-treated and (b) Ran-, E-Mix and Benzonase treated samples. The orange/green line corresponds to the unintended height, while the blue line – to the deformed height at the maximum force.

The second row represents the stiffness cross sections of c) mock-treated and d) Ran-, E-Mix and Benzonase treated samples. The distribution of stiffness is shown by a colour map, where red corresponds to the maximum value of 10.5 pN/nm.

The third row depicts an averaged effective Young's modulus (green line) with the standard error of the mean of e) 33 mock-treated NPCs and f) 36 Ran-/E-Mix and Benzonase treated NPCs. The stiffness at the central channel is in the same range as the stiffness at the periphery of the pore. The average stiffness is around 0.8 MPa for mock-treated sample and 1 MPa for Ran-, E-Mix and Benzonase treated.

The semi-transparent thick line around the main solid line represents the standard error of the mean. R(1)=42 nm; 'Zero' point in in Z-scale corresponds to the minimum value of the height at the contact point.

Figure 6-13 (a) represents the force curves acquired from the centre of the pore of native and 'empty' NPCs. The force curves are matching well with each other by demonstrating the same behaviour. The rapid increase of force with indentation can be observable in both of them. Subsequently, the stiffness curves overlapped demonstrating a significant increase of stiffness with only a few nanometres of indentation (Figure 6-13 b).

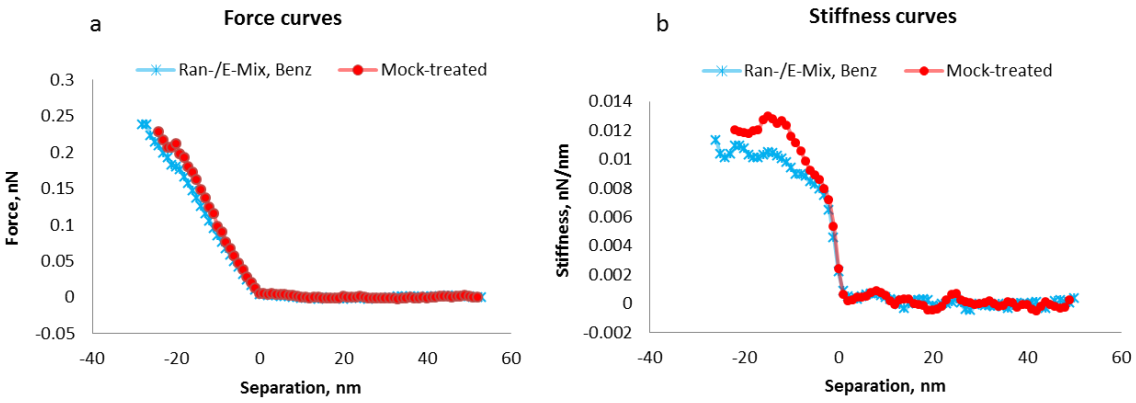

Figure 6-13 a) Force and (b) stiffness curves obtained from the centre of the pore and averaged over 33 and 36 pores from mock- and treated samples.

The resultant cross sections from AFM Force Volume suggest that the qualitative features such as stiffness of the scaffold and in the central channel are not affected by the washing procedures. This indicates that the central plug, which remains visible even after washing, represents a structural component of the central channel, rather than a cargo molecule. If this structural component was the FG Nups in the brush-like confirmation, the stiffness cross section would be expected to show soft material.

However, the cross section shows a rather stiff material, which is consistent with a meshwork of FG filaments in the hydrogel configuration.

6.3 Conclusion

We showed that we are able to significantly reduce the amount of cargo inside the NPCs (by >50%), possibly the quantity of Importinβ (~20%) in NPCs by enhancing the transport across the pore and digesting the nucleic acid which is the most common cargo. This was validated via the confocal microscopy and Western Blotting.

AFM force measurements were collected from native and thus 'washed out' pores. As a result of these measurements, we showed that the stiffness cross sections of the mock- and treated pores are matching well with each other. This was confirmed by the elasticity modulus. The part of the cross section which was identified as the cytoplasmic ring, using the EM images, appeared as stiff as the central channel of the pore, and force curves did not show significant differences inside the NPC channel. Since these were consistent features in both native and washed-out pores, we attribute it to the interaction of cohesive FG domains with each other or with Importinβ.

Combined with the results in the previous chapters, these experimental results are therefore consistent with a stronger cohesive than 'entropic' character of the permeability barrier, and thus more consistent with hydrogel/selective-phase model than with what is commonly understood as a brush model. In addition, they indicate that the cohesion of FG domains results in the plug-like structure as observed in the NPC conduit.

Chapter 7 Advanced AFM method to acquire the nanomechanical data

7.1 Introduction

Although Force Volume is a powerful technique, it has some drawbacks such as relatively low resolution and slow scan rates (which causes drift to be a significant problem). In principle, the nanomechanical properties acquired so far in the Force Volume mode can also be obtained in Peak Force QNM mode, which collects force curves much faster and while also enabling high-resolution imaging.

The Peak Force QNM was introduced by Bruker (Santa-Barbara, CA, US) as a fast and stable technique. It has the abilities to record the force curves at a ramp rates of 250-8000 Hz, compared to the ~1-20 Hz in Force Volume mode. The higher the ramping rate, the shorter the time per force curve, and the faster the scan. Therefore, in the Peak Force QNM the scanning time is much less than in the Force Volume: thousands of ramps can be obtained in a second, while in the Force Volume it would take several minutes. Switching to this faster technique would open opportunities to collect larger amount of data with higher throughput and less sensitivity to drift.

Such a high rate of ramping and quick imaging in Peak Force QNM is due to the ramping character of the tip along Z-piezo axis which is described by the sinusoidal wave unlike in the Force Volume where the ramping is linear (Figure 7-1).

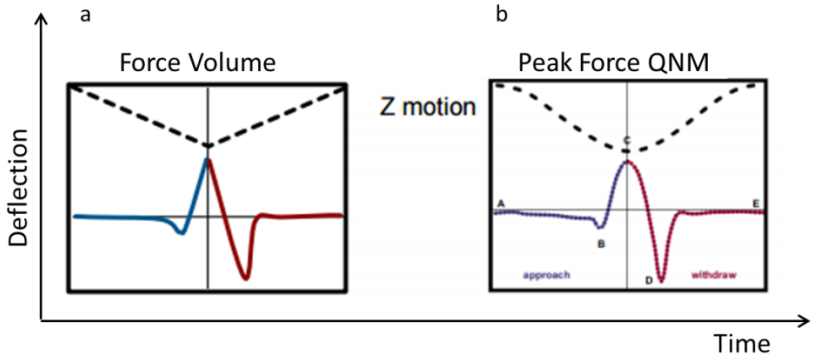

Figure 7-1 a) Linear ramping of Force Volume mode and (b) sinusoidal ramping of the Peak Force QNM [198].

In this chapter, preliminary data were collected for validating Peak Force QNM on NPCs. The nanomechanical properties and the imaging resolution of the NPCs obtained in the Force Volume/Tapping mode and Peak Force QNM were compared.

To cope with the differences in the file format between the Force Volume and Peak Force QNM, a new analysis code was developed and verified. Discrepancies between the codes along with the problems encountered are also described in this chapter.

7.2 Results and Discussion

7.2.1 Comparative study of the Tapping mode and Peak Force QNM

Peak Force QNM has been claimed as a high resolution imaging technique, which applies least force possible to the sample and thus preserves both the sharpness of the tip and the shape of the surface. Prior to AFM stiffness topography measurements in Force Volume and Peak Force QNM, the cytolplasmic side of isolated nuclear envelopes were imaged in Tapping mode (on the Multimode IV AFM) and Peak Force QNM (on the Multimode VIII AFM) respectively, using MSNL-F probes.

The most appropriate area for imaging is a densely packed arrangement of NPCs on a membrane. Figure 7-2 (a) demonstrates the part of the nuclear envelope free of contamination and rich of NPCs, as imaged in Tapping mode on the Multimode IV at the highest pixel resolution available (512 pixels per line). The NPCs appear as circular shaped rings.

However, the image resolution can be improved using Peak Force QNM on Multimode VIII even with the same tip type (Figure 7-2 b). The image in Figure 7-2 (b) was recorded at 1024x1024 pixel resolution and scanned at 0.8 Hz line rate. The image resolution has significantly improved and NPCs appear sharper, and thereby the 8-fold symmetry of the pore can be discerned.

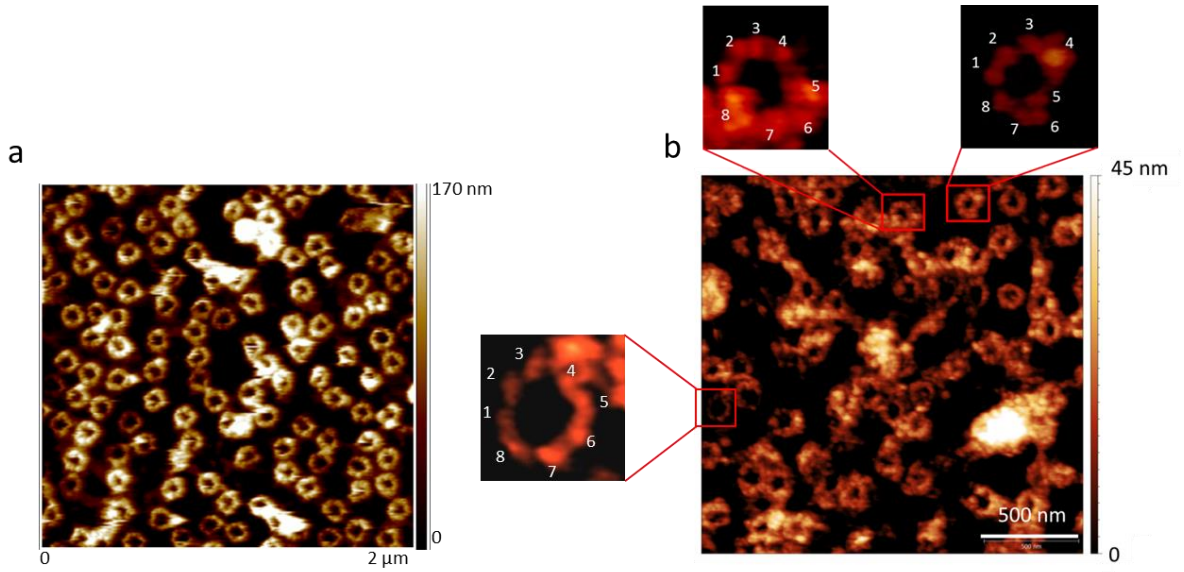

Figure 7-2 AFM images (2x2 µm^2) of a nuclear envelope using MSNL-F cantilevers obtained (a) on Multimode IV in Tapping mode at resolution of 512 pixels per line, line rate 1.9 Hz and (b) on Multimode VIII in Peak Force QNM displayed 8-fold symmetrical NPCs at resolution of 1024 pixels per line, line rate 0.8 Hz.

The Nanoscope software was used to extract the profile of the pore (Figure 7-3). The diameter acquired on both AFMs was measured as a distance between the two highest points on the rim of the pore. From the cross sections the diameter of the cytoplasmic ring appeared to be in the range ~70-90 nm which is in agreement with the height profiles of averaged NPC acquired from force volume measurements in Chapters 5 and 6.

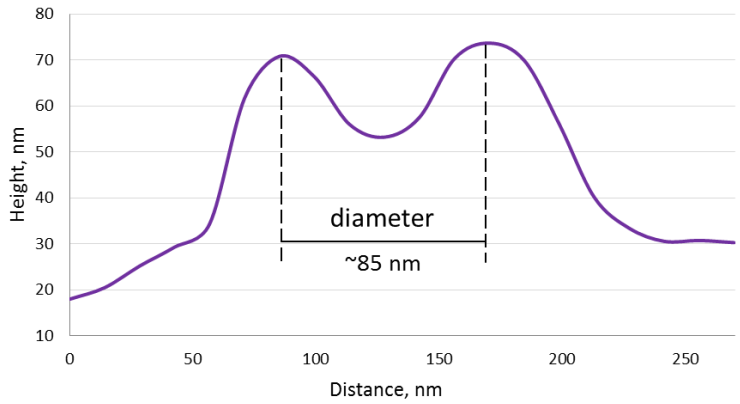

Figure 7-3 Cross section profile of a single NPC to measure the diameter.

7.2.2 Comparative study of nanomechanical properties as measured by Force Volume and Peak Force QNM

The Force Volume had a ramping rate 15.6 Hz, whilst the Peak Force QNM was at 250 Hz and 2 kHz. The comparison between the nanomechanical data among all frequencies was done using the same sample and tip (ShoconG-SS).

Topography of NPCs

Figure 7-4 shows topography images of NPCs acquired simultaneously with the force curves. The force applied during the force spectroscopy was around 500 pN. The same resolution across the modes was kept (1 pixel = 3.13 nm). The pore in the Force Volume image (Figure 7-4 a) appears with sharp edges and an elliptical shape that is due to the (lateral) thermal drift at the ~10 minutes time scale of the image. Because they are recorded more quickly, Peak Force QNM images do not suffer from this problem and show circular shaped pores.

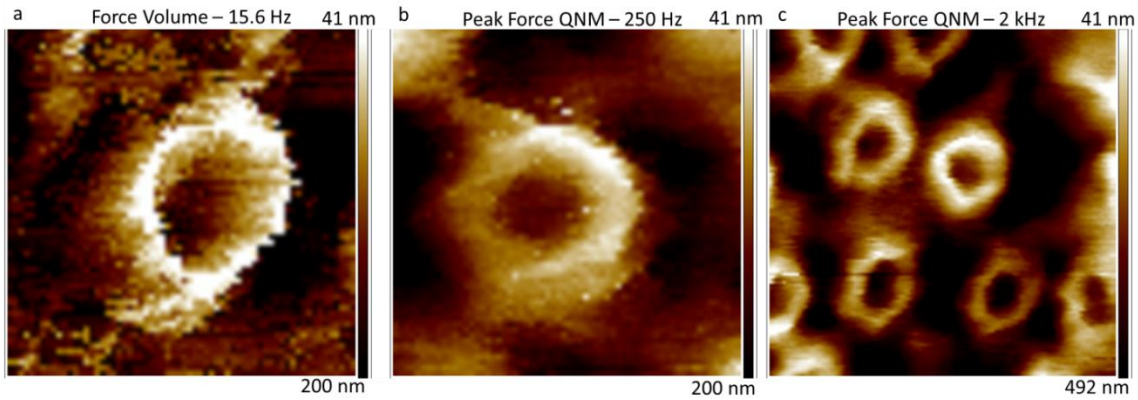

Figure 7-4 a) The NPC imaged in Force Volume mode. The pore appears elliptical due to the thermal drift caused because of the slow scan. b) The pore imaged in Peak Force QNM mode at 250 Hz and (c) 2 kHz. All images obtained at a resolution 1 pixel ~ 3 nm.

The time required to capture a single force curve with 512 data points in the Force Volume with a ramping rate 15.6 Hz was 64 ms. On the contrary, in Peak Force QNM, - at a ramping rate 250 Hz a single force curve (128 data points) was collected in 3.6 ms, whilst at a ramping rate 2 kHz the time to capture an individual force curve was 0.45 ms. The total time required for the frame capture then depends on the number of pixels/force curves in the frame.

This fast collection of force curves is allowed due to the sinusoidal movement of the tip during ramping which avoids piezo resonance and overshoot as it would be the case in Force Volume if the ramping rate had been increased up to frequencies of the Peak Force QNM. The velocity of the tip in Peak Force QNM changes along the ramp size: it starts from zero at the beginning of the ramp, increases to maximum 628 μm/s and 78.5 μm/s at 2 kHz and 250 Hz respectively (for the ramp size 100 nm) and decreases again to zero at the end of the ramp. This means when the tip is touching the surface it has a high speed (~500 μm/s at 2 kHz, and ~60 μm/s at 250 Hz in case of 20 nm indentation). This implies that the tip is in contact with the surface for a very short time at each ramp which helps to avoid the lateral drift.

On the other hand, in Force Volume the tip remains at the same velocity along the ramp size and can be set separately for extend and retract curves. It approaches the surface at the full speed as set from the beginning (~2 μm/s) that is few magnitudes less than in Peak Force QNM. To increase the scan time in Force Volume the retract velocity of the tip was set to 7.1 μm/s. It did not affect the results since in the analysis only the trace curves were used.

Validation of the new code for Peak Force QNM data analysis

To load the data acquired in Peak Force QNM mode, a new script had to be designed. The original script designed to analyse the Force Volume data was written in Mathematica[4] (Wolfram, Research, Champaign, IL, USA). For the new file formats, however, Bruker provide a toolbox for uploading the data into Matlab (MathWorks Inc, UK). To benefit from this, a new analysis script had to be written in this language[5]. This new script was designed to analyse the data in the same fashion as the Mathematica code - as much as this was possible.

One of the major differences in the new Matlab code, as compared to the original Mathematica code, is the method by which the NPC is identified, and subsequently the method by which the concentric shells are defined for the rotational averaging. In

[4] Designed by Dr. Bart Hoogenboom, Physics and Astronomy Department, UCL
[5] Designed by George Stanley, PhD student in Biosciences Division, UCL, and Sofya Mikhaleva, Master student in Department of Natural Sciences, UCL

Mathematica, the scaffold of each pore is traced manually. These pixels defined as the scaffold are then given a radial value of 1, and all other concentric bins are assigned relative to the scaffold. This means the code can adapt to shapes which are not perfectly circular, allowing for deformation of the images due to thermal drift. Matlab avoids this dependence on manual tracing, using automatic recognition of (roughly) circular shapes, but as of yet, no allowance has been made for shapes that are not rotationally symmetric. The centre of the circle is defined as the axis of rotation, and the concentric shells are made as perfect circles extending from this point. The current Matlab code is thus limited to circular pores only, which implies that it cannot compensate for drift-induced distortions of the pores. Although this is not a problem for the Peak Force QNM files, the slow rate of imaging in Force Volume means the effects of thermal drift can be more pronounced, causing a significant fraction of the pore measurements to be unsuitable for Matlab analysis. In this section only circular or nearly circular pores were analysed. The methods used in the rest of the code, such as: defining the contact point, fitting the Hertz model, averaging the force curves, and differentiating the force curves, are the same as those described in Section 3.1.5, Chapter 3.

To verify the code, previous Force Volume data from the Multimode IV AFM (three pores from the mock-treated samples from Chapter 6) were analysed. Figure 7-5 shows the results generated with the Mathematica analysis code (upper panel, Figure 7-5 a) compared to those generated by the Matlab code on the same experimental data (lower panel, Figure 7-5 b). The height profiles appear similar, although the indentation as determined by the Matlab analysis is smaller (by ~30%). This can be related to differences in the contact-point determination in the force curves by the Matlab and Mathematica code: The Matlab code tends to place the contact point more towards/inside the contact region than the Mathematica code. As a consequence, the effective Young's moduli appear somewhat higher in the Matlab analysis compared to the Mathematica analysis (Figure 7-5 a, b)

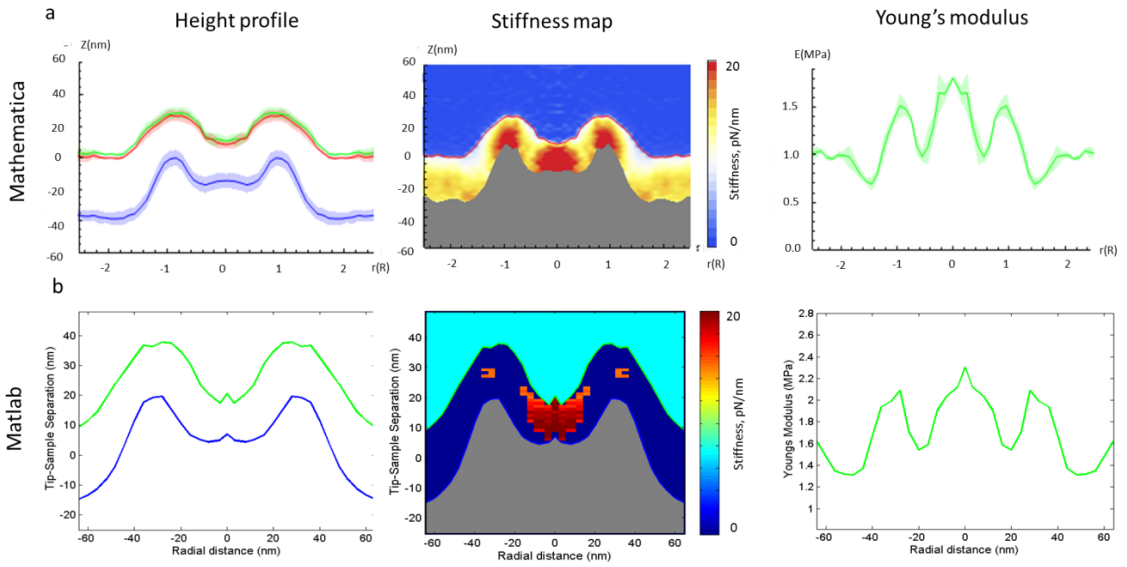

Figure 7-5 The height, stiffness and elasticity cross sections of the NPCs (average of 3) were generated using the same set of Force Volume data by (a) Mathematica and (b) Matlab codes. In the stiffness maps in (a) and (b) values increase from 0 pN/nm (blue) to 20 pN/nm (red). In Mathematica plots (a) R ~ 42.5 nm.

Notwithstanding these differences that still need to be addressed in having a more consistent contact-point determination between the codes, both analyses yield largely similar results. The Matlab stiffness map verified the existence of the stiffness in the central channel (20 pN/nm). The profiles of the Young's modulus are very similar in shape exhibiting stiff central channel and the rim of the pore.

Comparison of the nanomechanical data obtained in the Force Volume and Peak Force QNM

Once the code was tested and verified, the comparison between the Force Volume and Peak Force QNM, both implemented on AFM Multimode VIII, was carried out. The resolution of images across all frequencies was kept the same (1 pixel=3.13 nm). However, the number of data points in the force curves in the Peak Force QNM was 128, instead of 512 as in the Force Volume. The number of averaged pores in the Force Volume was 4, Peak Force QNM at 2 kHz – 4 pores, and 250 kHz - 5 pores.

Figure 7-6 shows the averaged height, stiffness and elasticity profiles for the pores scanned in the Force Volume at 15.6 Hz and the Peak Force QNM at 250 Hz and 2 kHz.

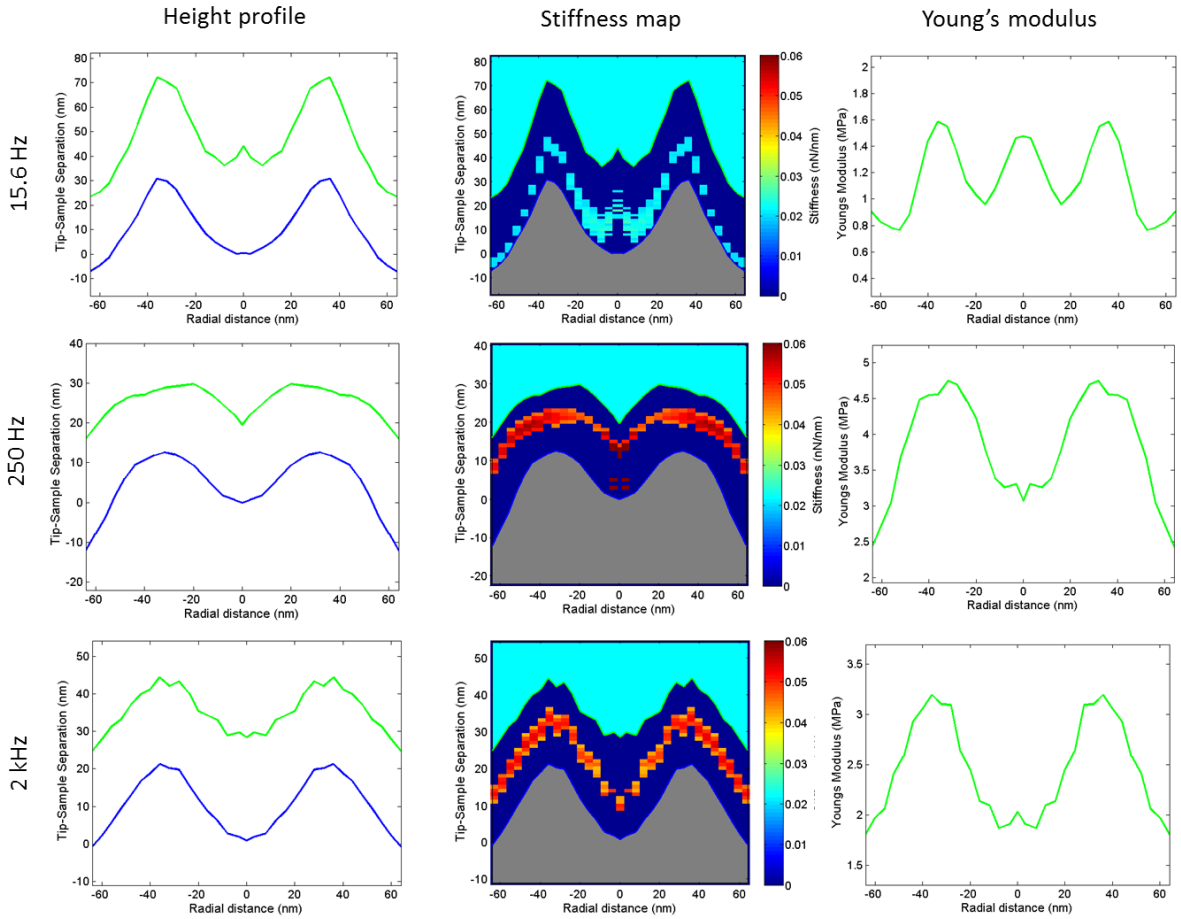

Figure 7-6 The averaged height, stiffness and Young's moduli profiles as a result of the measurements at (a) 15.6 Hz, (b) 250 Hz and (c) 2 kHz ramping rates. The results collected at 15.6 Hz are the average of 4 pores, at 250 Hz – 5 pores and 2 kHz – 4 pores.

The shape of the NPC was preserved in both low and high frequencies. The NPC shape at 250 Hz is outstanding the most due to the plumpness of the rim, which was depicted in Figure 7-4 (b), where the pore rim appears thick and thus the central channel is smaller in diameter. The pores measured in the Peak Force QNM appear slightly flatter by ~ 20 nm compared to the Force Volume. The indentation in the Force Volume is the largest: ~35 nm, while in the Peak Force QNM at 250 Hz and 2 kHz was ~20 nm and ~30 nm respectively.

The stiffness profile across the modes exhibits similar outcome: observation of the central stiffness in the channel of the pore. The effective Young's modulus of the cytoplasmic ring in the Force Volume mode was around 1.6 MPa, which is low compared to the values obtained in Peak Force QNM. The elasticity moduli of the NPCs cytoplasmic ring measured in the Peak Force QNM at 250 Hz and 2 kHz were 4.4 MPa and 3.2 MPa respectively. Both frequencies in the Peak Force QNM showed a little or no plug in the central channel, whilst in the Force Volume there a significant increase of the Young's modulus at the centre of the pore.

To find out the difference between the nanomechanical properties at various ramping rates the force curves and corresponding stiffness curves at the central channel should be considered. Figure 7-7 shows the averaged force and stiffness curves from both modes of operation. At the first glance it seems such as the indentation in the force curves at 15.6 Hz is larger than the others. Indeed, the force curve at 250 Hz frequency is the steepest among all and hence has smaller indentation. As a result, the stiffness curve of 250 Hz has the largest stiffness. On the other hand, force curves recorded at 2 kHz has much larger indentation, however due to inaccurate contact point determination, which identified it at the contact region, and thereby the maximum stiffness was also high.

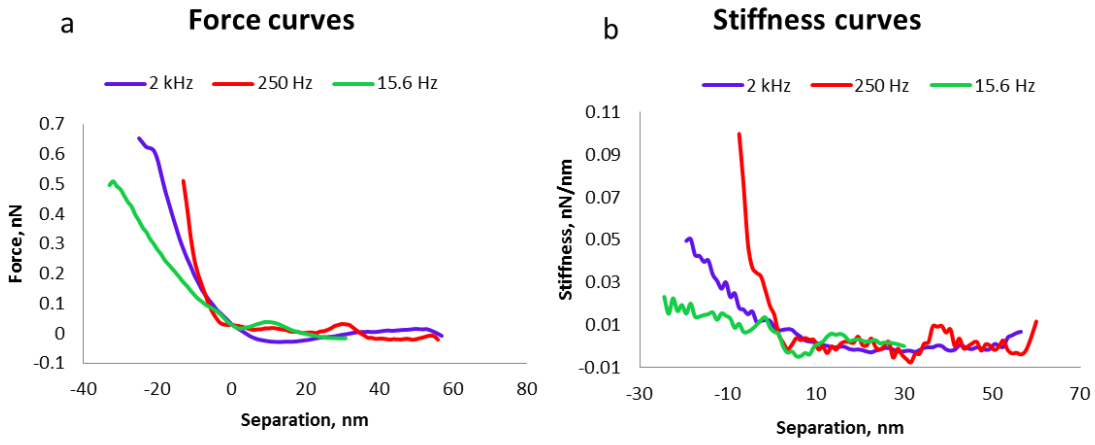

Figure 7-7 a) force and (b) stiffness curves obtained from the central channel in the Force Volume mode (15.6 Hz, green line, average of 35 force curves) and Peak Force QNM (2 kHz, blue line, average of 44 force curves; and 250 Hz, red line, average of 51 force curves).

Since there are not as many pixels in the central channel of the pore and given that some of them were removed during analysis, for the better comparison of the force curves behaviour the area with more pixels should be considered. Figure 7-8 shows the averaged force and stiffness curves corresponding to the cytoplasmic ring. The contact point determination is still a problem for the curves from 2 kHz frequency in Peak Force QNM: it still finds it in the contact area, and thus not surprising that the height profile showed less indentation than in the Force Volume. As for the 250 Hz, the force curves appear even steeper than before. Subsequently in the stiffness curves these two curves have the stiffness values twice larger than in the Force Volume (Figure 7-8 b).

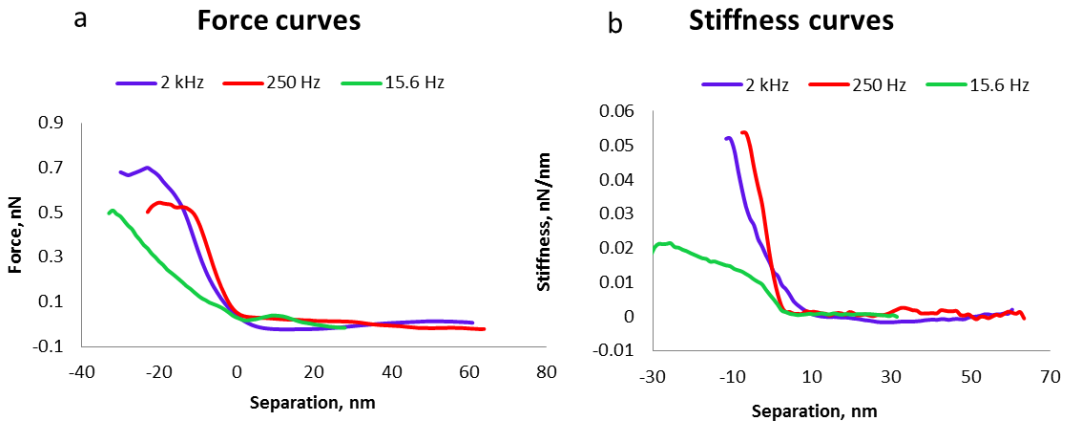

Figure 7-8 a) force and b) stiffness curves obtained from the cytoplasmic ring in the Force Volume mode (15.6 Hz, green line, average of 386 force curves) and Peak Force QNM (2 kHz, blue line, average of 227 force curves; and 250 Hz, red line, average of 400 force curves).

According to the total number of force curves used for analysis (which varied among frequencies) it is interesting to check which pixels were used for analysis. Figure 7-9 shows the graphical representation of the missing pixels (in images obtained at 15.6 Hz, 250 Hz and 2 kHz), where the code was unable to identify the contact point. Although in this analysis about 27% of the force curves were discarded in the Force Volume data because the analysis code detected poorly defined baselines, the majority of the discarded curves were related to positions at the nuclear envelope and not NPC itself, unlike in 2 kHz measurements, where 14% of the force curves were removed from random positions. The least amount of force curves were missing in the images obtained at 250 Hz (7%) since the contact point determination was easier for the steeper curves.

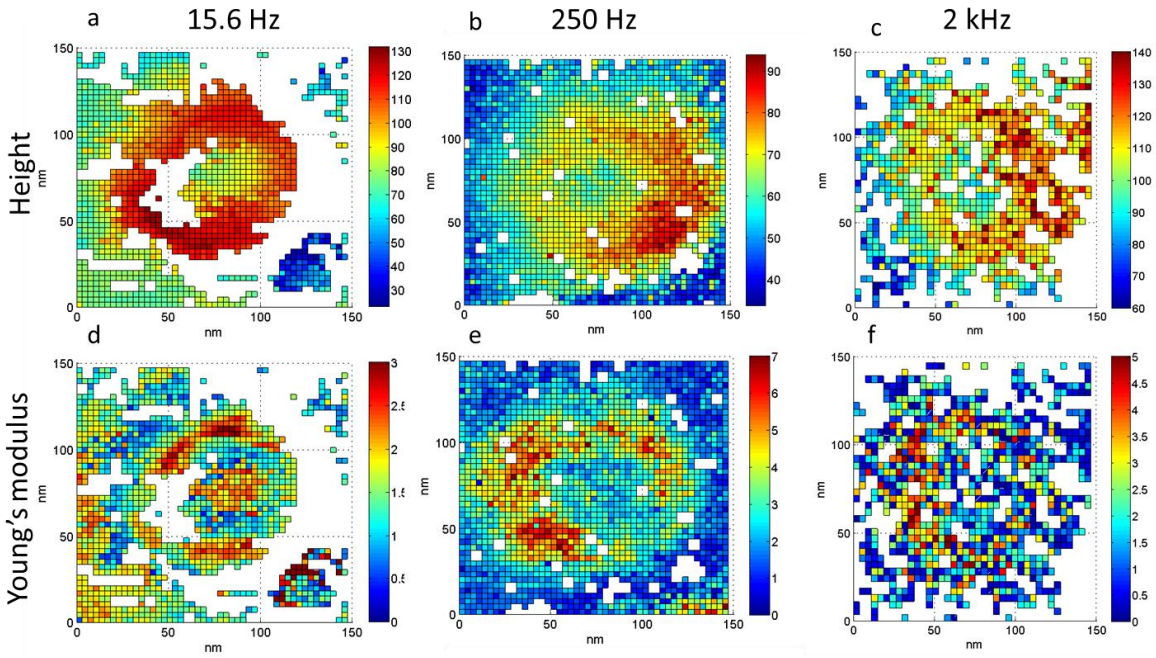

Figure 7-9 Graphical representation in 3D of the images acquired at (a) 15.6 Hz, (b) 250 Hz and (c) 2 kHz, where the missing pixels indicate that the corresponding force curves were binned. The lower row is a graphical representation in 3D of the Young's moduli calculated for each pixel in the images obtained at (d) 15.6 Hz, (e) 250 Hz and (f) 2 kHz.

The reason for the smaller indentation and steep force curves in Peak Force QNM at 250 Hz remains unknown and requires further investigation with larger amount of pores for analysis. Given the relatively large fraction of discarded/inappropriate force curves,

as well as the rather odd height profiles for the 250 Hz measurements, it is probable that further repeats experiments will be required for a sound comparison.

7.3 Conclusion

The Peak Force QNM showed its capabilities as a high resolution imaging technique and as a tool to obtain quickly the nanomechanical properties of the sample. It is able to significantly reduce the imaging time. Thus, the time spent on collection of the force data has improved from 10 minutes to ~30 seconds per pore with the same resolution.

The Peak Force QNM measurements of NPCs yielded well-defined shape of the pore, however, showed them at least twice stiffer than it was found via Force Volume. During the elastic modulus calculation, the nucleoporins were assumed as an elastic surface with no adhesion to the AFM tip. However, it is quite possible that confined nucleoporins within the central channel have the viscoelastic properties rather than elastic ones which would affect the interaction between the tip and the surface, in particular when probing the NPCs at higher speed as in the Peak Force QNM measurements. At present, it cannot be excluded that the relaxation time of the nucleoporin filaments is larger than the oscillation rate of the tip, such that during the next ramp the surface will not have enough time to relax and the tip will interact with more material [199]. This is confirmed indirectly by larger indentations into the central channel than into the cytoplasmic ring of the pore in Peak Force QNM, whereas in Force Volume the indentation in central channel is similar to the rim. The larger indentation means less steep force curves and as a result the Young's modulus will be less.

The potential of the Peak Force QNM lies in the quick imaging time. At present, however, there remains uncertainty about its accuracy compared for Force Volume measurements. Moreover, the analysis code should be improved in terms of identifying more precisely the centre of the pore and determining the contact point. Currently, Force Volume remains as a reliable technique for nanomechanical characterisation, which can provide with the accurate pore shape even in elasticity distribution. However,

the slow nature of these experiments makes it worthwhile to pursue higher-throughput measurements such as Peak Force QNM.

Chapter 8 The nanopore devices

8.1 Introduction

NPCs selectively regulate the translocation of RNA, proteins, and other small molecules, between the nucleus and the cytoplasm. Many, different methods have been employed to study this translocation process *in vivo*, specifically through studying a single molecule transport [52], [59], [200] using different types of super-resolution confocal microscopy [58], [94], [75], [201] and electron microscopy [15], [202]. However, due to the complexity of the NPC structure and its surrounding cellular environment, the mechanism of the selectivity barrier is not fully understood. Biomimetic assemblies provide an alternative approach to studying the transport across the NPC.

The NPCs can be imitated using artificially built nanopores with nucleoporins anchored to the inside of the channel. The artificial nanopores can be used as biodetectors and filters of DNA [203], RNA [204], proteins, dyes and polymers [205]. Selectivity is established according to size, charge, and hydrophobicity. However, most importantly they can be used to measure both passive diffusion of ions [206] and mediated transport across the NPC [207].

An artificial nanopore can be made using either biological or so-called solid-state materials (typically silicon) to design a channel on the nanometre scale (Figure 8-1 a, b). The biological channels are formed by the self-assembly of polypeptides [208], whereas the solid-state pores are formed by sculpting or drilling the solid state material.

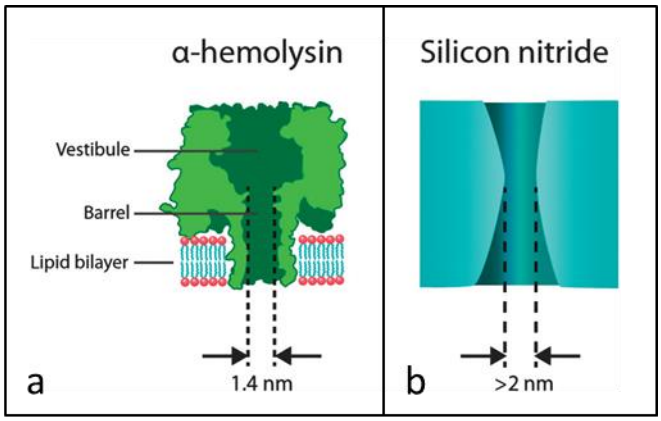

Figure 8-1 a) α-hemolysin: a protein assembly inserted into a lipid bilayer to form a channel of 1.4 nm in diameter; b) a silicon nitride nanopore of hour-glass shape with a diameter at the middle of about 2 nm [113].

Although both types of the pore can accommodate transport, the solid state nanopores have more flexibility in terms of tuning the parameters such as size, surface properties and possibility to be integrated in devices and arrays [209].

In general, the fabrication process of solid state nanopores involves two steps: substrate preparation and nanopore formation, which is implemented by either building the pore using a sculpting ion beam, or milling it with a focused ion beam or an electron beam.

The transport process in NPCs was successfully mimicked in the past by using a gold-coated polycarbonate membrane, which was perforated by an array of pores, each 30 nm in diameter [206] (Figure 8-2). Resulting channels, with a gold entrance of 15 nm thickness, were functionalised with the yeast protein Nsp1. The FG repeat domains presented in the Nsp1 created a selective transport barrier. By measuring signal from the fluorescently labelled protein-karyopherin complex, it was clearly shown that the presence of only one type of Nup can facilitate the active transport.

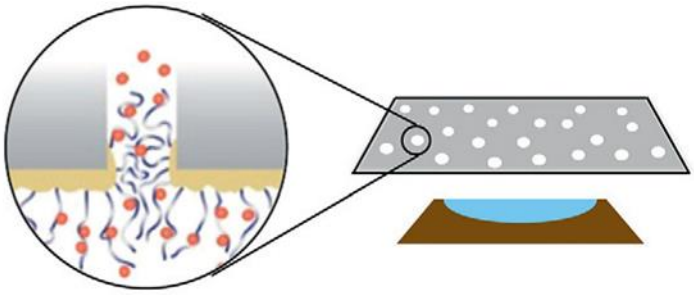

Figure 8-2 A schematic diagram of an array of pores on a membrane functionalised with the Nsp1 yeast protein [206].

Similar experiments were done using a single-pore model instead of an array [210]. The pore of 40 nm diameter was drilled by an electron beam into a 20 nm thick silicon nitride substrate. The selective barrier was built via tethering either Nup153 or Nup98 FG-containing nucleoporins. The transport of Importinβ with and without the protein was detected by monitoring the ion-current changes across the pore (Figure 8-3) which is possible due to the properties of the solid state materials.

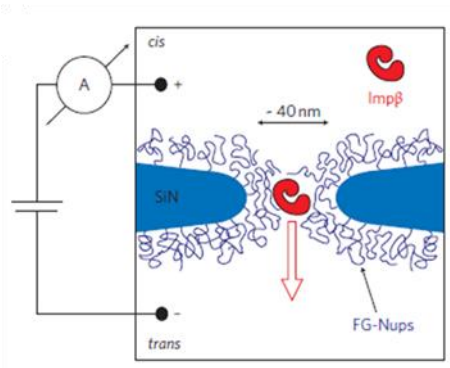

Figure 8-3 Schematic representation of the biomimetic silicon nitride pore functionalised with the nucleoporin, where each translocation was recorded via monitoring the ion current [210].

Moreover, depending on the size of the pore, the Nups formed different configurations in it. The smaller pores (~25 nm diameter) appeared as "closed" pores, whereas the larger pores were "open". The level of selectivity was dependent on the type of Nup. On average, the number of Importinβ translocations per second was 60 times higher than that of inert molecules.

These functionalised nanopores can mimic the permeability barrier, and thus regulate transport in various conditions: different pH [211], light [212] and ions [213]. Therefore, nanopores provide an easier approach of tuning parameters of interest than in NPCs.

This chapter presents the first steps towards a solid-state device that consists of an array of nanopores, sometimes also referred to as “channels”. The device is formed from a silicon substrate with a gold slice sandwiched in between, meaning that when the nanopores are milled using a focused ion beam, a gold ring is formed within each channel. This ring provides a well-defined anchoring location for selectively binding proteins, thus forming a barrier inside the channel only, rather than also binding to the surface at the entrance to the pore. This is a novel design of the functionalised nanopore - one which is more truthful to the native structure of the NPC.

The initial aim of this project was to visualise and acquire the stiffness of functionalised pores with various diameters and different nucleoporin concentrations. However, due to the time-consuming nature of each experiment, the growing scope of the project, and a shortage of time, only the preliminary data on the nanopore characterisation and passivation were collected.

8.2 Results and discussion

The nanopore devices were characterised with AFM and confocal microscopy. AFM was able to provide the topography of the device and qualitatively show the difference between the functionalised and non-functionalised surfaces using force spectroscopy mode. It was found that the Nsp1, as well as binding to gold, was also binding to silicon in a non-specific manner. Therefore, a new protocol was required in which the silicon surface would be covered by a blocking agent to prevent Nsp1 binding.

To test the success of the passivation process, a second nuclear transport factor 2 (NTF2), labelled with green fluorescent protein (GFP) was introduced. NTF2 has a strong affinity for the FG repeats found in Nsp1 [214], meaning they can bind to them and be detected using confocal microscopy, thus showing the presence of Nsp1 that should specifically bind via thiol-chemistry to the gold surface.

The nanopore devices were characterised using the AFM and confocal microscopy and the preliminary work on passivation was done.

8.2.1 Visualisation of the nanopores by AFM microscopy

The thicknesses of SiO_x and Au layers in the initial nanopore devices were 150 nm and 30 nm respectively. Samples were scanned on a JPK Nanowizard 1 in contact mode.

Figure 8-4 shows an AFM scan of regularly spaced dark spots (shown by white circles on the image) in an area of 25x25 μm^2.

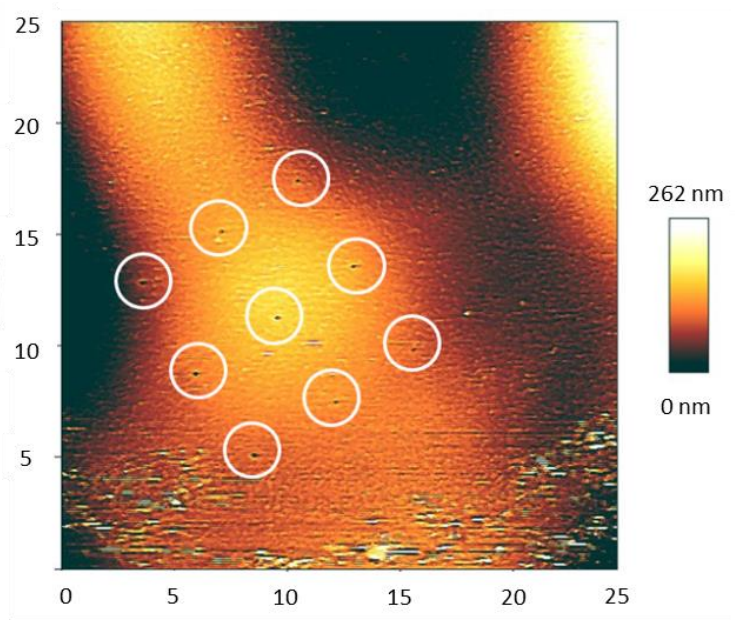

Figure 8-4 AFM image of the nanopore array scanned on the JPK Nanowizard 1 in contact mode in the area 25x25 μm^2. The pores are enclosed in white circles. Height colour scale: 262 nm.

Analysis of the cross sections of the individual pores from the AFM images enabled quantification of the diameter and depth of the nanopores (Figure 8-5 a, b). The depth was defined as a distance between the lowest point of the pore and the baseline, which is a surface of the device. The diameter was measured at the middle of the depth.

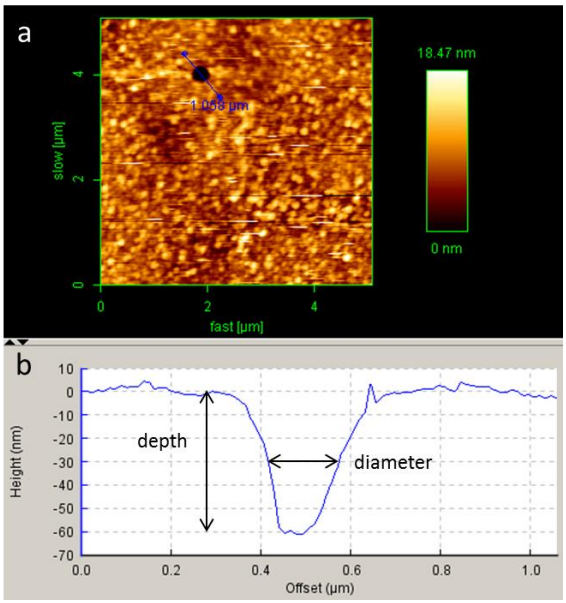

Figure 8-5 a) AFM image of a single nanopore (diameter, >100 nm); b) cross section of the nanopore acquired from JPK data Processing software.

The geometry of the pore can be explained by the technique applied at the preparation stage. When the focused ion beam drills the hole, it also sputters ions and atoms from the surrounding walls. As a result, at the entrance of the beam the diameter of the pore is much larger than the diameter of the channel. In the same way, but with a smaller impact, the exit of the beam is affected (see Figure 2-4, Chapter 2). Therefore, the geometry of the channel is not a perfect cylinder but rather an hourglass shape from both entrances. It is also possible that the cones of two pores have a similar exit diameter.

The analysis revealed that the diameters of the pores measured by AFM were in general about 20% larger than the diameters identified, for the same pores, by SEM (Figure 8-6).

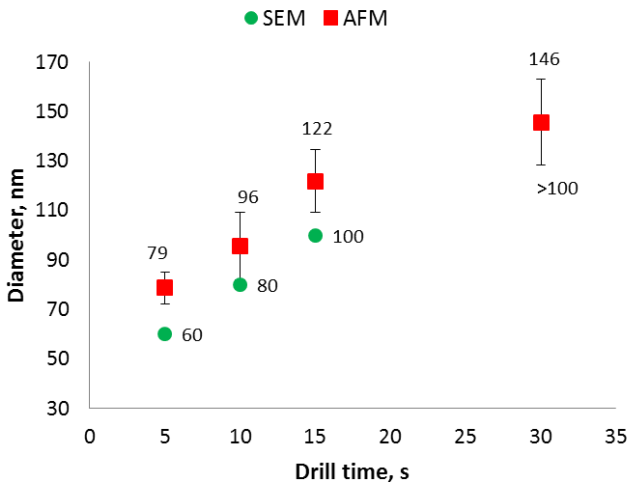

Figure 8-6 A comparison of the diameters between the nanopores imaged by SEM and AFM. The pore diameter which is larger than 100 nm was not accurately measured in SEM and thus, on the plot the random value above 100 nm was assigned to it. The nanopores were drilled at 50 pA and 30kV for 2 s, 10 s, 15 s and 30 s. The error bars correspond to the standard deviation.

The depth of the pore varied in accordance to the diameter. The larger the pore, the deeper it can be probed (Figure 8-7). The fabrication protocol suggested that the final depth of the pore is 215 nm. The deepest pore was 60±5 nm and the shallowest was 20±2 nm.

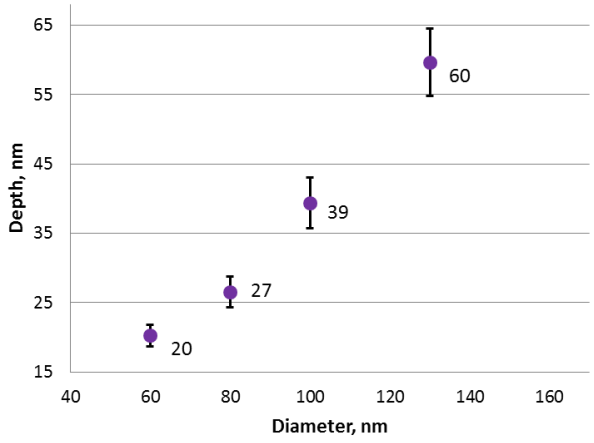

Figure 8-7 Correlation of the depth of the pore with the diameter. The error bars represent the standard deviation.

The diameter measurements by AFM are limited by the shape and size of the AFM tip. The nominal diameter of the MSNL tip is 4 nm; however, the maximum declared by a manufacturer is 20 nm which is already one third of the smallest diameter. Additionally the low aspect ratio MSNL tip cannot penetrate the nanopore deeper than the tip's geometry allows it (Figure 8-8 a). It is therefore likely that only the entrance of the pore was scanned, rather than the pore itself. Therefore, it is better to use another tip with reduced diameter (<4 nm) and a higher aspect ratio. Moreover, in order to protrude deeper inside the pore the tip should be tilt compensated, which ensures that the tip is perpendicular to the scanning surface (Figure 8-8 b).

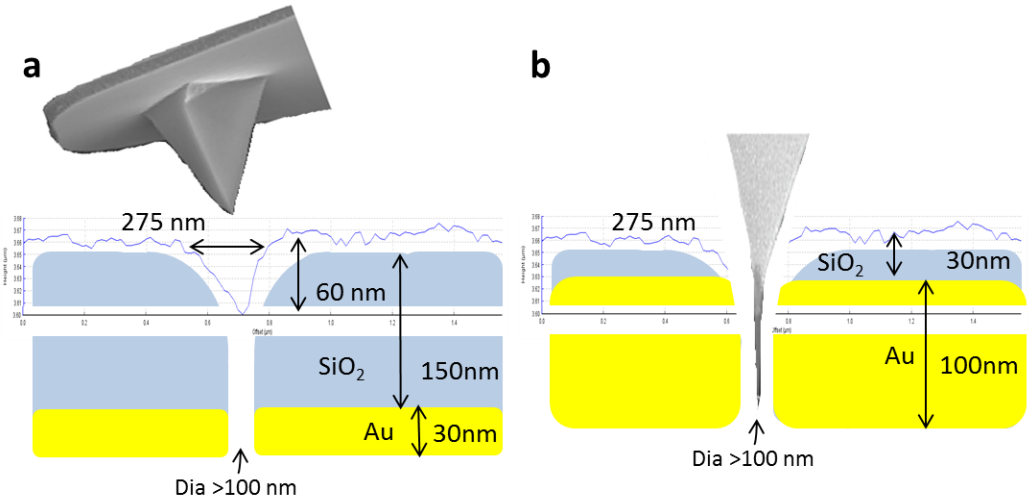

Figure 8-8 A cross section profile of a pore with a diameter of >100 nm (a) probed with a standard MSNL tip with a height of 2.5-8 µm, diameter of 4-16 nm, and a low aspect ratio; b) New design of the device with an enlarged gold section and a reduced thickness of the SiO_x layer. The representation of the pore probed with a tilt compensated tip, with a height of 100-200 nm, a spike diameter of ~1 nm, and a high aspect ratio. The images are not to scale.

After imaging, it was decided to change the design of the nanopore devices to ensure easy access to the permeability barrier created with proteins. Given that the pore with diameter of >100 nm was only probed up to 60 nm deep with a standard probe, the thicknesses of the gold and silicon oxide layers was amended. The thickness of the SiO_x layer was reduced from 150 nm to 30 nm to make it easier for the tips to reach the gold ring at a depth of 30 nm, where the proteins should be anchored. Thus, a standard tip should be able to probe a permeability barrier created by there-grafted nucleoporins. In

addition, the thickness of the gold ring was increased to 100 nm. With this new design, at least 30 nm of the upper region of the gold can be probed using a standard tip, in nanopores of >100 nm minimum diameter. Moreover, increasing the thickness of the gold layer would result in anchoring more FG-repeats, and hence, increase the selectivity of the barrier [215].

8.2.2 Visualisation of the nanopores using the confocal microscopy

The confocal scan of the nanopore devices (Figure 8-9 a), which were incubated with a fluorophore (4 kDa DiI cell tracker, diameter 1.4 nm) [216], revealed very bright spots on the surface (shown with blue arrows). The position of the spots in the confocal image matched the position of nanopores in the SEM image (Figure 8-9 b). This is attributed to the small sized fluorophore which filled the pores, due to the hydrophilic surface of the nanopore device after UV light treatment [217].

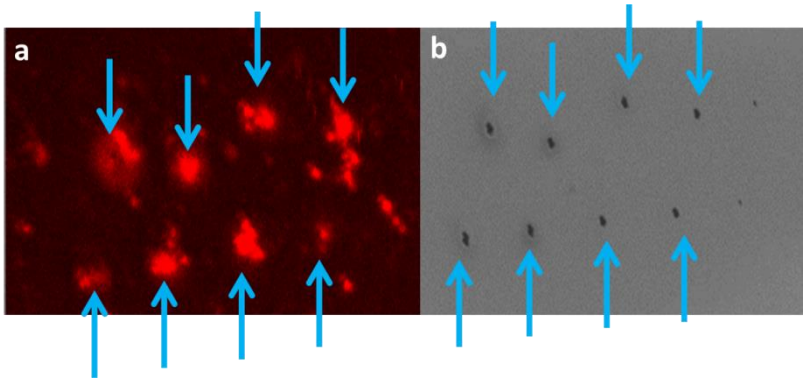

Figure 8-9 a) A confocal image obtained using a HeNe laser with excitation wavelength of 543 nm and a 100x oil immersion objective lens at a digital zoom of 7.3; b) A SEM image of the nanopore arrays (Image courtesy of Dr. Agniezska Rutkowska)

8.2.3 Assessing the Nsp1 binding to a silicon surface using force spectroscopy

To first verify if there may be unspecific (and unwanted) binding of Nsp1 to the silicon parts of the nanopore device, additional AFM topography and force measurements were done on a planar surface of silicon chips, in the presence and absence of Nsp1.

Figure 8-10 (a) represents an example of a raw force curve obtained from the silicon surface without Nsp1. In the non-contact region (i) the trace curve appeared as a flat line

showing no attraction of the tip to the surface until the tip suddenly “snaps in” to the sample. In the contact region (ii) the trace line became almost vertical, meaning that only a small indentation occurred with a relatively large bend of the cantilever. The difference in the behaviour of the trace and the retrace curves emerged at the retract stage (iii). The retrace curve entered the zone of negative deflection which determines a strong adhesion of the tip towards the surface. As soon as the tip was withdrawn from the surface, the retrace curve became flat again (iv).

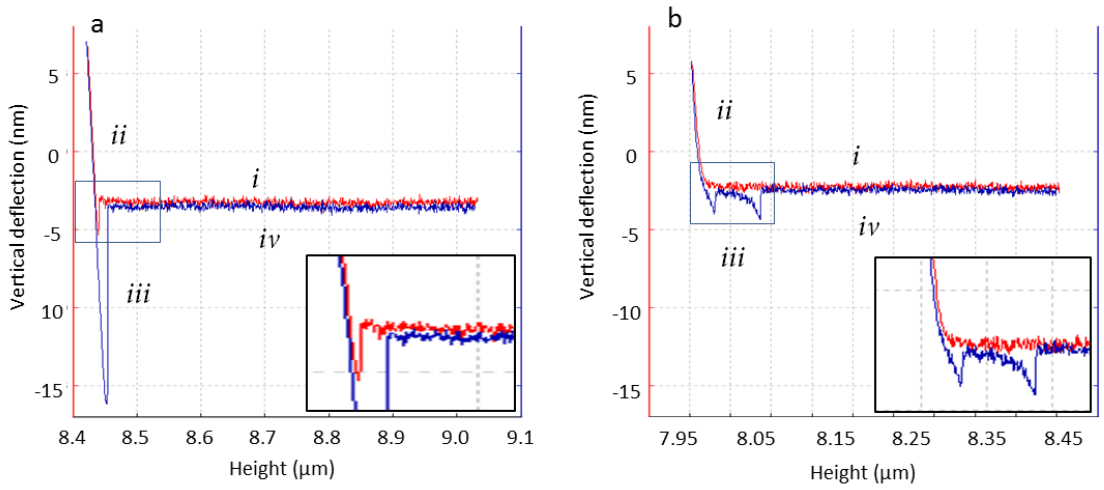

Figure 8-10 Force curves representing (a) the non-functionalised planar silicon surface scanned at 315pN; b) the functionalised surface with Nsp1 scanned at 270 pN

Figure 8-10 (b) represents one of the multiple force curves (total 20) collected from the silicon surface after exposure to Nsp1. The tip is gradually attracted to the surface by showing a smooth transfer from non-contact flat region (i) into contact (ii). Nevertheless, with an increase of the indentation, the deflection grew very fast. When the tip was pulled back, the retract curve showed few spikes for deflection (iii) until the tip was retracted, which means the tip was pulling molecules from the surface.

In the first plot, acquired from planar silicon surface without Nsp1, the contact point is very sharp and can be detected easily, which is typical for the case when the tip interacts with a hard surface. The adhesion behaviour of the tip towards the planar silicon surface, shown on Figure 8-10 (a), was an expected outcome. The negatively charged

silicon nitride tip is strongly attracted to the ‘p-doped’ silicon surface due to electrostatic force.

On the other hand, the force curve from a sample exposed to Nsp1 shows different behaviour. The contact point is more difficult to define since the tip after contact is indenting into the soft surface. However, the layer of this soft material is very shallow, since the tip quickly reaches the substrate and the force curve demonstrates a fast increase of the deflection with little indentation, indicative of a hard surface once again. Moreover, at the retract stage, the tip cannot easily withdraw and shows occasional negative spikes in the deflection, which can be attributed to longer molecules being pulled away from the surface. All 20 curves in this measurement displayed similar behaviour. We therefore interpret these observations as signatures of the presence of Nsp1 bound at the surface.

This was further validated by an analysis of the AFM topography; in particular, the roughness of the surface was estimated. The roughness of the bare silicon surface was 2.0±0.1 nm, whereas the roughness of surface with Nsp1 was 5.0±0.5 nm which is at least 2.5 times larger. We conclude that the change in the roughness is due to the presence of Nsp1. Hence the silicon surfaces will need to be passivated to prevent binding of Nsp1.

8.2.4 Characterisation of the surface before passivation

In an additional test for the binding of Nsp1 to the relevant surfaces of the nanopore devices, GFP-labelled NTF2 was used, and the surface was imaged by confocal microscopy. The rationale is that nuclear transport receptor NTF2 binds to the Nsp1, and can thus be used to detect the presence of Nsp1.

The fluorescence signal was detected for difference surfaces following exposure to NTF2-GFP: 1) bare silicon; 2) silicon that was pre-incubated with Nsp1; 3) bare gold; and 4) gold that was pre-incubated with Nsp1.

All surfaces were fluorescent on the microscope. Initially it was concluded that there is unspecific binding of NTF2 and/or Nsp1 to the gold and silicon surfaces respectively. However, after scanning the plain chips without the fluorophore, it was found that there

is a high reflectance of the excitation light coming from both surfaces, which was incorrectly interpreted as a fluorescent signal.

The LSCM Olympus FV1000 detected the direct fluorescence signal of 488 nm laser light, reflecting from silicon and gold surfaces, which could not be eliminated due to the inefficient blocking of the excitation light before the detectors. Thus, further experiments were carried out on the confocal microscope with extra filters (see Section 2.2.5, Chapter 2) to improve the selectivity for the fluorescent signal.

To verify an absence of direct deflection in the measured signal in the new setup, bare gold and silicon chips with no functionalisation was scanned on the microscope. The resultant fluorescent intensity was found to be low compared to that of functionalised surfaces. This intensity of the bare chips was used for normalisation. Since Nsp1 on its own does not yield a fluorescence signal, gold and silicon chips incubated with it showed the lowest values in the normalised intensity (Figure 8-11). The highest signal acquired was from the silicon chip incubated with NTF2 - 70% larger than on the gold chip.

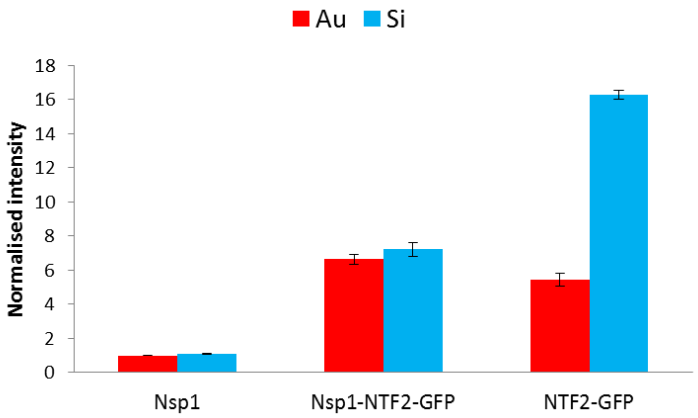

Figure 8-11 Normalised intensity of the silicon and gold chips incubated in Nsp1, Nsp1-NTF2-GFP and NTF2-GFP. The intensity values are normalised to the intensity of planar chips. The error bars corresponds to the standard deviation.

NTF2-GFP thus has a high affinity towards silicon and less towards gold. The presence of Nsp1 increased the NTF2-GFP signal on gold; however, it suppressed the signal on silicon. This confirms that Nsp1 binds not only to the gold but also to the silicon.

Apparently, the Nsp1 coverage of the silicon surface prevented the strong NTF2 adsorption to the silicon surface. The (lower) NTF2 affinity to explain the similar fluorescence signal of the silicon and the gold after Nsp1-NTF2-GFP incubation.

The encountered problem of non-specific binding of proteins to surfaces such as silicon, gold and glass is a common problem, but one which can be solved using various passivation techniques [218], [219]. One of the popular solutions is a passivation by synthetically formed polyethylene glycol (PEG), which can self-assemble on the surface [220], [221], [222], [223] - this is the technique I used next for passivating silicon and gold.

8.2.5 Characterisation of the surface after the passivation

To prevent any non-specific binding, the chips were incubated with the blocking agent polyethylene glycol (PEG) and tested on the confocal microscope. It is commonly accepted that for forming a protein-resistant surface on silicon, silane chemistry should be used [224]. On the other hand, for binding the passivation agent on a gold surface, the thiol bond should be used [219]. However there are not many configurations in which both are utilised [225].

To verify the success of PEG as a blocking agent, gold and silicon were functionalised with Nsp1 and/or NTF2-GFP after passivation. Any non-specific binding of Nsp1 and NTF2-GFP to silicon or of NTF2-GFP to gold was tested.

The steps of Au/Si chip passivation and functionalisation are explained in Figure 8-12. Initially all the chips were incubated with PEG-silane. Afterwards, depending on the purpose of the test, they were incubated with either: Nsp1, followed by the optional PEG-thiol passivation; or, with PEG-thiol passivation with no prior incubation with Nsp1. At the end of each preparation the incubation with NTF2-GFP followed.

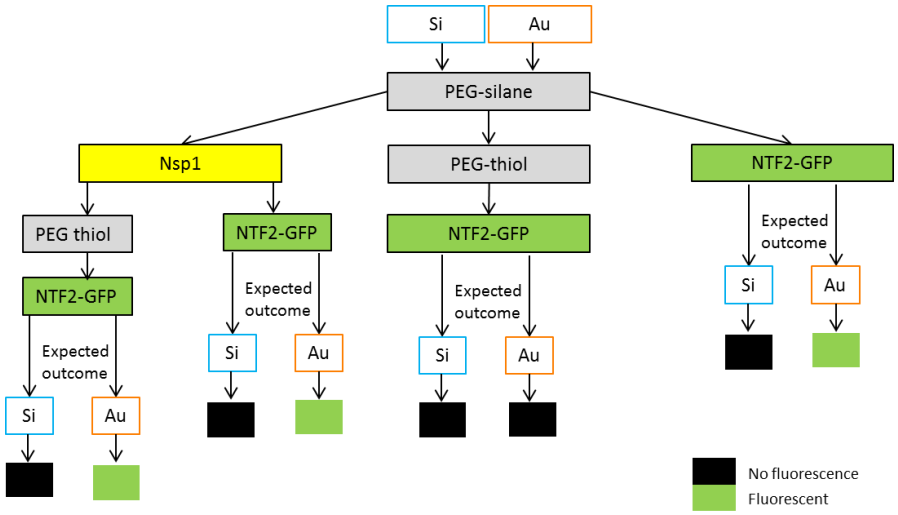

Figure 8-12 Schematic diagram of the gold and silicon chips incubation sequence prior to confocal scanning, and their expected results.

Figure 8-13 shows the experimental outcome from the various sample preparation methods outlined above. All the passivated samples rendered a weak signal barely discernible from the background noise. The fluorescence of the silicon, prepared by subsequent incubation with PEG and protein, was about 10% larger than the background and 4% larger than the corresponding gold surface. The situation was similar for the samples incubated with PEG-silane and proteins in the absence of PEG-thiol: the silicon surface was 6% higher than the background and 4% higher than the gold. All samples with no Nsp1 incubation exhibit similar results: the fluorescence of the gold and the silicon is equal to the background. The fluorescence of the silicon equals the fluorescence of the gold. The intensity from passivated samples were normalised to the intensity of the background.

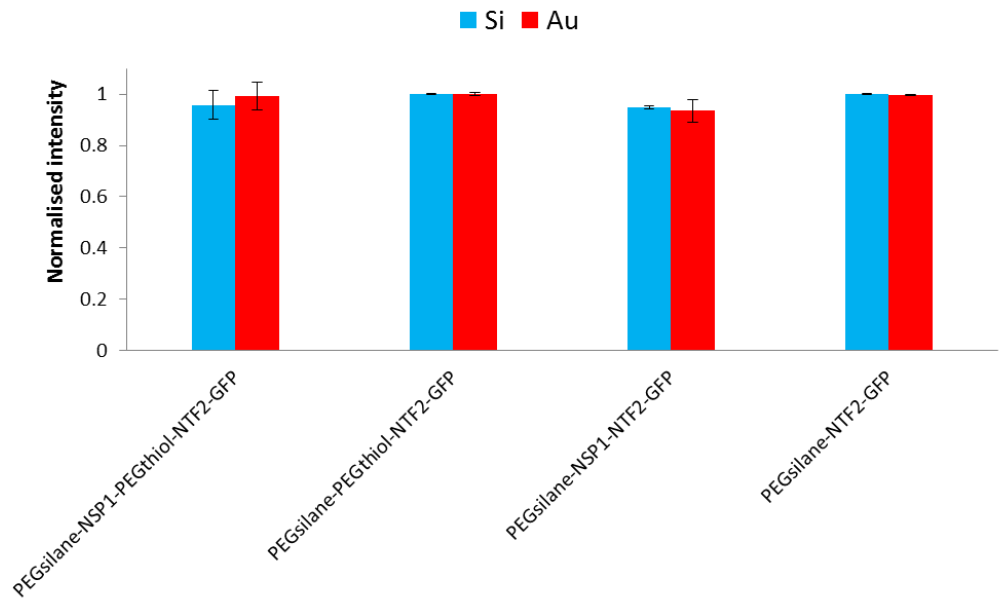

Figure 8-13 Intensity values of Si and Au chips after passivation and incubation with Nsp1 and/or NTF2-GFP. The intensity is normalised to the background. The error bars represent the standard deviation of the ratio of two means.

To understand these results, a further investigation of the interaction between the molecules at the silicon and gold surfaces is required. In particular, the possible scenarios of the thiol and silane binding to the gold and silicon at the molecular level are discussed below.

The air plasma clean or UV treatment which was used to reduce the amount of organic impurities on the surface, also promoted the sample's oxidation [226], [227]. The oxidized silicon surface is preferred for the silane interaction with silicon.

Figure 8-14 illustrates the steps required to form a bond between a silane group and the silicon oxide surface. Initially, PEG-silane is adsorbed onto the hydrated surface without interacting with any of the surface atoms. The interaction begins with the hydrolysis of the methoxy group $(CH_3O)_3$, producing hydroxylsilane $Si(OH)_3$ compounds called silanols. Afterwards, the silanols of PEG-silane start binding with hydroxyl groups on the silicon surface. Whilst binding, a condensation reaction occurs and water molecules are released. Finally, the covalent bond (Si-O-Si) is formed, eventually leading to a PEG monolayer on the surface [226], [228], [229], [230].

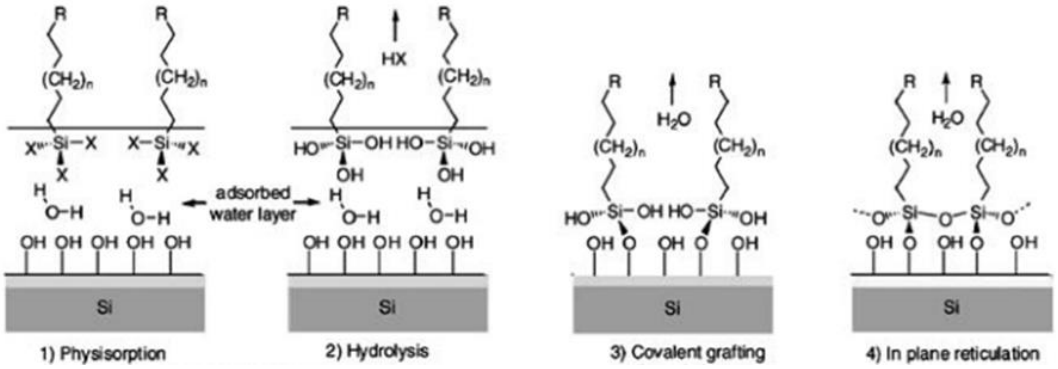

Figure 8-14 Steps required for the formation of the PEG-saline monolayer on the silicon oxide surface: 1) physisorption of PEG molecules; 2) hydrolysis of a methoxy group in the PEG-saline; 3) covalent bond formation between silane and silicon oxide; 4) alignment of PEG on the surface [228]. *'X' corresponds to CH_3O.*

The interaction between the thiol group and the gold surface is described below. Normally, if the gold surface is clean and oxide-free, then the thiol-gold interaction is formed via a covalent bond between the gold and sulfur atoms (RS-Au). Initially, the thiol moiety adsorbs onto the gold surface; the hydrogen atom preferring to remain bonded to the sulfur atom. Eventually, the sulfur-hydrogen bond dissociates to create a hydrogen radical, and a thiyl radical (Figure 8-15 a), which then forms a covalent bond with a gold atom (Figure 8-15 b). The hydrogen radicals are either chemisorbed onto the gold surface, or are lost as H_2, however, the role played by hydrogen during this process is not clearly understood [115], [231]. In fact, the entire mechanism of thiol binding to gold is still poorly understood and requires more research [232].

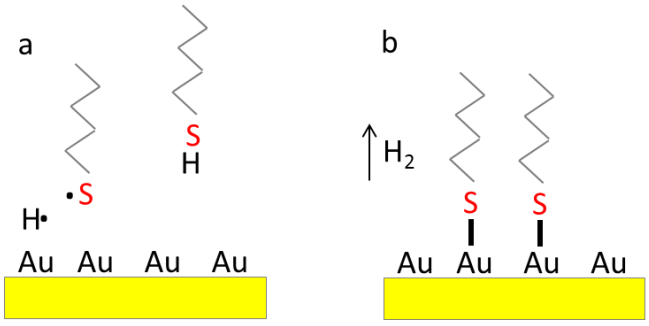

Figure 8-15 Schematic view of the gold-sulfur bond formation where (a) the thiol (S-H) bond dissociates and (b) the newly formed radical covalently binds with the gold atom upon hydrogen release.

If a protonated thiol (RS-H) interacts with the gold (RSH-Au), then the bonding occurs via a weaker coordinate covalent bond, in which sulfur donates a lone-pair of electrons [233]. However, this bond is not thermodynamically preferred [232], [234].

The oxidation of gold which might occur after the UV treatment [227], [235], on the other hand, can add difficulties for thiol binding. Thiol moieties from adjacent PEG molecules can be oxidised to form an intermolecular disulfide bond, and the same mechanism applies to the cysteine tag [236], [237], [238]. At this state the dimer formed can still bind to the gold atoms but via a weaker covalent bond [232]. In case when the gold-sulfur bond is created, it is still is much weaker on the oxidised surface than on the reduced surface [115]. Besides, the reactive oxygen species, formed on the surface after the UV treatment, might interact with Nsp1 and affect its functionality [239], [240].

Moreover, if the gold oxide was formed on gold surface, then it creates a good environment for the silane binding to anchor through oxygen, although silane generally has a propensity to anchor to the gold [241], [242], [243]. This might be another reason for the absence of fluorescence during the scanning, as all of the samples were passivated by the PEG-silane first.

No fluorescent signal from the sample can be associated with the reasons listed above, such as: silane attraction to gold, and oxidation of gold which leads to oxidation of the thiol group in both PEG and the cysteine tag. However, most likely the formation of the PEG-silane monolayer on the gold has restricted PEG-thiol and Nsp1 from binding to the gold surface. If silane easily self-assembles on both surfaces, then Nsp1 is blocked from binding to the gold by PEG-silane. Since no free site is available, then NTF2 cannot bind even non-specifically to either of the surfaces.

The oxygen free surface is an important step in the sample preparation for the passivation process. The reduction of gold oxidation helps thiol to directly interact with the gold. To reduce the oxidation state, various pre-treatment techniques [244], [245], [246] can be applied to stabilize the gold-thiol bond, in particular, ethanol can be used [235].

There are also ways to prevent the oxidation of gold. One of them is to use an anaerobic chamber to remove excess oxygen by applying nitrogen and hydrogen gases. The second method is using an argon plasma clean which reduces the organic contaminants without oxidizing the gold [247].

In the development of the passivation protocol, the following aspects should be taken into account: the binding chemistry between the blocking agent and the surface under the different conditions; surface pre-treatment mechanisms before the passivation and quality of the PEG coverage.

8.3 Conclusion

The nanopore devices prepared in Imperial College London were visualised using AFM and confocal microscopy. The AFM characterisation provided an estimate for the diameter of the pores and the depth that AFM probe could reach. These measurements lead to the amendments in the nanopore design. To ensure an easy reach of the functionalised golden ring with the AFM tip, the thickness of the golden ring was enlarged up to 100 nm, whilst the top layer of the silicon oxide, covering the gold, was reduced to 30 nm. Thus, the standard tip, which can probe to a depth of 60 nm within the pores of >100 nm in diameter, allows probing of at least the first 30 nm of the functionalised golden ring.

Prior to proceeding with the functionalisation of the ring, the non-specific binding of Nsp1 protein to the silicon was assessed using force spectroscopy. The silicon surface, functionalised with Nsp1, was softer, thus indicating the presence of the protein, which was confirmed by the roughness analysis. The same test was done on the confocal microscope, which suggested that Nsp1 has a non-specific affinity towards the silicon and NTF2 binds non-specifically to both gold and silicon.

To prevent the non-specific binding, a passivation method was attempted. Two types of PEG, one terminated by a thiol group and the other by a silane group, were used to create bonds with gold and silicon respectively. However, the protocol for the surface passivation needed improvement due to the possible silane affinity towards gold or oxidised gold. By studying the surface chemistry of the gold and silicon, which can be

amended during the sample preparation, the more appropriate blocking agents could be found. Additionally, the quality of the PEG coverage of the sample should be tested, which is important in terms of prevention of the non-specific binding of the proteins to the open space on the surface.

When the protocol of passivation is established, and functionalisation of only the golden ring is successful, then the stiffness measurements can be acquired by probing the permeability barrier created by Nsp1 in the channel.

Another option of examining the functionalised nanopore is to identify the spatial arrangement of Nsp1 within the channel. This can be done by finding the distance between two terminals of Nsp1 using Fluorescence resonance energy transfer (FRET) [248], [249]. This technique registers the energy transfer between two fluorophores, one of which is excited, in a distance dependent manner. The C and N terminals of Nsp1 would have to be labelled with an organic fluorescence tag. The configuration of Nsp1 in the pore is not known yet, thus it is scientifically important to attempt the implementation of these experiments.

Chapter 9 Conclusion

Different models have been proposed to describe the structure of the permeability barrier in the NPC and to explain the underlying transport mechanism. However, only two of them have been extensively explored: entropic brush and hydrogel. Experimental work in vitro showed that FG Nups can occur in both of these configurations [67], [61]. In this thesis the question on the nature of the permeability barrier was addressed by comparing the physical and mechanical properties of the model system built from polymer brushes by using the atomic force microscopy, which can study the NPCs at nanometre resolution in physiological buffer solution. In particular, sharp and narrow AFM tips probed the transport barrier in NPCs to measure its nanomechanical properties. The same procedure was applied to the polymer brushes.

Nanomechanical data were acquired using the so-called Force Volume mode, in which force-versus-indentation curves are measured at different position on a sample. For an interpretation in the context of the NPC, this measurement method was first validated on a model system: Artificial polymer brushes. Such brushes are easy to prepare and can serve as control data for comparison with NPCs, since entropic/extended polymer brushes represent one of the proposed models for the barrier. Moreover, these brushes are responsive to pH and can also appear in the collapsed state which to a certain degree may be used as a model for a hydrogel. The results acquired from the extended and collapsed brush in form of force curves were in agreement with previous results from elsewhere [61], [62], [63], [64], [22] acquired from the FG Nups/PEG brush (extended and collapsed) and from more cohesive, hydrogel materials.

The same Force Volume method with the same cantilever and force was applied to NPCs. The profile of the NPC built from the height and indentations data matched well with the EM representation of the NPC acquired at 2 nm resolution [10]. The cross sections were compared and the parameters such as location of the cytoplasmic ring and diameter of the central channel were similar. In terms of nanomechanical data a stiff plug was observed in the central channel. However, because the nature of this plug may be controversial and in the past has been attributed to cargo stuck in transport [14],

[186], experiments were done to effectively flush the pore, resulting in significantly less cargo molecules (>50%) and nuclear transport receptors in the pore (~20%) confirmed by confocal microscopy and Western Blot analysis.

The reduced presence of cargo did not change the qualitative appearance of the various features of NPC in our experiments, including the central plug. Moreover, the force curves from the central channel showed the same behaviour as the force curves of the collapsed brush, i.e., a steep increase of the force with the indentation, in clear contrast to the more exponential behaviour of the extended brush. This might mean that the entropic brush in the central channel got collapsed upon interaction with Importinβ; however, this "reversible collapse" was based on an the experiment [62] on FG-domains originating from the nuclear basket, whereas in this study we focused only onto the cytoplasmic side. Furthermore, a similar study on FG-domains from the cytoplasmic site did not confirm the collapse [64]. Moreover, even if some FG-domains collapsed due to the interaction with Importinβ, it was supposed to restore since the nuclei were also incubated with RanGTP, which was shown to disassemble the FG-repeat-Importinβ [62], and as a result the extended brush would appear again. Thus, the option of an importin-induced collapse of the brush was excluded. Another option causing the observed stiffness might be transport receptors themselves, however as it was demonstrated elsewhere [64] the interaction of transport receptors with FG-domains does not contribute into stiffness of the central channel [172]. On the other hand, the cohesive FG-domains can form a meshwork of filaments formed from FG-domains or hydrogel which is stiffer than the brush [22]. As it was shown earlier the cohesive hydrogel can maintain the selectivity of the barrier [25].

Therefore, we suggest that the stiffness in the central channel is an intrinsic part of the NPC represented by the meshwork of the FG Nups forming a hydrogel [37], [187]. Moreover, the recent EM images of the central channel [10] resolved part of it due to the fixed positions of the nucleoporins, which indirectly indicated that the barrier is most likely resembling a hydrogel. These findings let us conclude that the permeability barrier is better described as a gel-like material, than as an entropic/extended brush.

We have thus successfully applied the traditional Force Volume method for collecting nanomechanical data on the NPC. However, this method is slow and – because of this – suffers from drift during the data acquisition. This complicates the experiments and the data analysis, and affects the lateral resolution at which data are acquired. We therefore explored the more recently developed and higher-throughput Peak Force QNM method for simultaneous imaging and force curve acquisition at 10~100 times higher speeds. Force Volume data were compared to the data from Peak Force QNM, and it was shown that that force curves at 250 Hz (PF QNM) appear steeper than at 2 kHz (PF QNM) and 15.6 Hz (Force Volume), though further repeat experiments will be required to confirm this finding. Up to now, all three measurements resulted in the similar appearance of the pore, although the central plug in Hertz model was not observed as clearly as in Force Volume.

Finally, exploring a biomimetic approach for studying the NPC, nanopore devices with the pore size of ~100 nm in diameter were characterised using AFM and confocal microscopy. It was illustrated earlier [206], [210] that the nanopores functionalised with FG-domains can replicate the selective barrier. In our study the design of the nanopore was amended to bring it closer to the dimensions and configuration of the real NPC. The nanopore devices were fabricated from silicon with a layer of gold within the pore for nucleoporins to bind and form the barrier within the silicon pore. However, due to the complication of functionalisation, in this thesis only the passivation mechanisms for the nucleoporins to bind specifically to the gold were investigated. It was found that polyethylene glycol (PEG) passivation agent blocks both gold and silicon.

9.1 Future work

In terms of acquiring the nanomechanical properties, the Peak Force QNM requires further validation. Subsequently, it could be used for a high(er)-throughput nanomechanical characterisation of NPC under different conditions, e.g., buffer conditions that reduce the affinity between FG-nucleoporins and/or different concentrations of various transport receptors.

For preparing artificial nanopores, different agents for passivation can be used and the passivation protocol further developed. Finally, one would hope to create a nanopore with a selective transport barrier formed by specifically anchored Nsp1. This will allow the further experiments on identifying the configuration of Nsp1 proteins in the pore, among others via characterisation of their collective nanomechanical properties.

References

[1] M. G. Cooper, “The Nuclear Envelope and Traffic between the Nucleus and Cytoplasm,” in *The Cell: A Molecular Approach*, 2nd editio., Boston University, 2000.

[2] “Nuclear Envelope.” [Online]. Available: http://preuniversity.grkraj.org/html/1_CELL_STRUCTURE.htm. [Accessed: 21-Dec-2015].

[3] D. Stoffler, B. Feja, B. Fahrenkrog, J. Walz, D. Typke, and U. Aebi, “Cryo-electron Tomography Provides Novel Insights into Nuclear Pore Architecture: Implications for Nucleocytoplasmic Transport,” *J. Mol. Biol.*, vol. 328, no. 1, pp. 119–130, Apr. 2003.

[4] C. W. Akey and M. Radermacher, “Architecture of the Xenopus Nuclear Pore Complex Revealed by Microscopy,” *J. Cell Biol.*, vol. 122, no. 1, pp. 1–19, 1993.

[5] Q. Yang, M. P. Rout, and C. W. Akey, “Three-dimensional architecture of the isolated yeast nuclear pore complex: functional and evolutionary implications.,” *Mol. Cell*, vol. 1, no. 2, pp. 223–34, Jan. 1998.

[6] J. E. Hinshaw, B. O. Carragher, and R. a Milligan, “Architecture and design of the nuclear pore complex.,” *Cell*, vol. 69, no. 7, pp. 1133–41, Jun. 1992.

[7] E. Kiseleva, M. W. Goldberg, T. D. Allen, and C. W. Akey, “Active nuclear pore complexes in Chironomus: visualization of transporter configurations related to mRNP export.,” *J. Cell Sci.*, vol. 111, pp. 223–36, Jan. 1998.

[8] T. Maimon, N. Elad, I. Dahan, and O. Medalia, “The human nuclear pore complex as revealed by cryo-electron tomography.,” *Structure*, vol. 20, no. 6, pp. 998–1006, Jun. 2012.

[9] M. P. Rout, J. D. Aitchison, a Suprapto, K. Hjertaas, Y. Zhao, and B. T. Chait, “The yeast nuclear pore complex: composition, architecture, and transport mechanism.,” *J. Cell Biol.*, vol. 148, no. 4, pp. 635–51, Feb. 2000.

[10] M. Eibauer, M. Pellanda, Y. Turgay, A. Dubrovsky, A. Wild, and O. Medalia, “Structure and gating of the nuclear pore complex,” *Nat. Commun.*, vol. 6, no. May, p. 7532, Jun. 2015.

[11] M. Beck, F. Förster, M. Ecke, J. M. Plitzko, F. Melchior, G. Gerisch, W. Baumeister, and O. Medalia, “Nuclear pore complex structure and dynamics revealed by cryoelectron tomography.,” *Science*, vol. 306, no. 5700, pp. 1387–90, Nov. 2004.

[12] S. G. Brohawn, J. R. Partridge, J. R. R. Whittle, and T. U. Schwartz, “The nuclear pore complex has entered the atomic age.,” *Structure*, vol. 17, no. 9, pp. 1156–68, Sep. 2009.

[13] F. Alber, S. Dokudovskaya, L. M. Veenhoff, W. Zhang, J. Kipper, D. Devos, A. Suprapto, O. Karni-Schmidt, R. Williams, B. T. Chait, A. Sali, and M. P. Rout,

"The molecular architecture of the nuclear pore complex.," *Nature*, vol. 450, no. 7170, pp. 695–701, Nov. 2007.

[14] D. Stoffler, B. Fahrenkrogt, and U. Aebi, "The nuclear pore complex: from molecular functional dynamics," *Curr. Opin. Cell Biol.*, vol. 11, pp. 391–401, 1999.

[15] M. Kann, "Nuclear Pore Complex Is Able to Transport Macromolecules with Diameters of 39 nm," *Mol. Biol. Cell*, vol. 13, no. February, pp. 425–434, 2002.

[16] B. Fahrenkrog and U. Aebi, "The nuclear pore complex: nucleocytoplasmic transport and beyond.," *Nat. Rev. Mol. Cell Biol.*, vol. 4, no. 10, pp. 757–66, Oct. 2003.

[17] M. Beck, F. Förster, M. Ecke, J. M. Plitzko, F. Melchior, G. Gerisch, W. Baumeister, and O. Medalia, "Nuclear pore complex structure and dynamics revealed by cryoelectron tomography.," *Science*, vol. 306, no. 5700, pp. 1387–90, Nov. 2004.

[18] D. Frenkiel-Krispin, B. Maco, U. Aebi, and O. Medalia, "Structural analysis of a metazoan nuclear pore complex reveals a fused concentric ring architecture.," *J. Mol. Biol.*, vol. 395, no. 3, pp. 578–86, Jan. 2010.

[19] A. Hoelz, E. W. Debler, and G. Blobel, "The structure of the nuclear pore complex.," *Annu. Rev. Biochem.*, vol. 80, pp. 613–43, Jun. 2011.

[20] D. P. Denning, S. S. Patel, V. Uversky, A. L. Fink, and M. Rexach, "Disorder in the nuclear pore complex: the FG repeat regions of nucleoporins are natively unfolded.," *Proc. Natl. Acad. Sci. U. S. A.*, vol. 100, no. 5, pp. 2450–5, Mar. 2003.

[21] L. J. Terry and S. R. Wente, "Flexible gates: dynamic topologies and functions for FG nucleoporins in nucleocytoplasmic transport.," *Eukaryot. Cell*, vol. 8, no. 12, pp. 1814–27, Dec. 2009.

[22] N. B. Eisele, A. a Labokha, S. Frey, D. Görlich, and R. P. Richter, "Cohesiveness tunes assembly and morphology of FG nucleoporin domain meshworks - Implications for nuclear pore permeability.," *Biophys. J.*, vol. 105, no. 8, pp. 1860–70, Oct. 2013.

[23] J. Yamada, J. L. Phillips, S. Patel, G. Goldfien, A. Calestagne-Morelli, H. Huang, R. Reza, J. Acheson, V. V Krishnan, S. Newsam, A. Gopinathan, E. Y. Lau, M. E. Colvin, V. N. Uversky, and M. F. Rexach, "A bimodal distribution of two distinct categories of intrinsically disordered structures with separate functions in FG nucleoporins.," *Mol. Cell. Proteomics*, vol. 9, no. 10, pp. 2205–24, Oct. 2010.

[24] S. Frey and D. Görlich, "A saturated FG-repeat hydrogel can reproduce the permeability properties of nuclear pore complexes.," *Cell*, vol. 130, no. 3, pp. 512–23, Aug. 2007.

[25] S. Frey and D. Görlich, "FG/FxFG as well as GLFG repeats form a selective permeability barrier with self-healing properties.," *EMBO J.*, vol. 28, no. 17, pp. 2554–67, Sep. 2009.

[26] S. Milles and E. a Lemke, "Single molecule study of the intrinsically disordered

FG-repeat nucleoporin 153.," *Biophys. J.*, vol. 101, no. 7, pp. 1710–9, Oct. 2011.

[27] D. Mohr, S. Frey, T. Fischer, T. Güttler, and D. Görlich, "Characterisation of the passive permeability barrier of nuclear pore complexes.," *EMBO J.*, vol. 28, no. 17, pp. 2541–53, Sep. 2009.

[28] B. B. Hülsmann, A. A. Labokha, and D. Görlich, "The Permeability of Reconstituted Nuclear Pores Provides Direct Evidence for the Selective Phase Model," *Cell*, vol. 150, no. 4, pp. 738–751, Aug. 2012.

[29] H. B. Schmidt and D. Görlich, "Nup98 FG domains from diverse species spontaneously phase-separate into particles with nuclear pore-like permselectivity.," *Elife*, vol. 4, pp. 1–30, Jan. 2015.

[30] V. V Krishnan, E. Y. Lau, J. Yamada, D. P. Denning, S. S. Patel, M. E. Colvin, and M. F. Rexach, "Intramolecular cohesion of coils mediated by phenylalanine--glycine motifs in the natively unfolded domain of a nucleoporin.," *PLoS Comput. Biol.*, vol. 4, no. 8, p. e1000145, Jan. 2008.

[31] and R. P. R. Nico B. Eisele, Aksana A. Labokha, Steffen Frey, Dirk Gorlich, "Cohesiveness tunes assembly and morphology of FG nucleoporin domain meshworks – Implications for nuclear pore permeability," *Biophys. J.*, vol. 105, pp. 1860–1870, 2013.

[32] R. H. Kehlenbach, *Nuclear Transport*. Austin, Texas, USA: Landes Bioscience, 2009.

[33] E. Hurt and M. Beck, "Towards understanding nuclear pore complex architecture and dynamics in the age of integrative structural analysis.," *Curr. Opin. Cell Biol.*, vol. 34, no. i, pp. 31–8, Jun. 2015.

[34] S. Hutten, A. Flotho, F. Melchior, and R. H. Kehlenbach, "The Nup358-RanGAP Complex Is Required for Efficient Importin α/β -dependent Nuclear Import," *Mol. Biol. Cell*, vol. 19, no. May, pp. 2300–2310, 2008.

[35] M. Stewart, "Molecular mechanism of the nuclear protein import cycle.," *Nat. Rev. Mol. Cell Biol.*, vol. 8, no. 3, pp. 195–208, Mar. 2007.

[36] G. Riddick and I. G. Macara, "The adapter importin-alpha provides flexible control of nuclear import at the expense of efficiency.," *Mol. Syst. Biol.*, vol. 3, no. 118, p. 118, 2007.

[37] A. Kramer, I. Liashkovich, Y. Ludwig, and V. Shahin, "Atomic force microscopy visualises a hydrophobic meshwork in the central channel of the nuclear pore.," *Pflugers Arch.*, vol. 456, no. 1, pp. 155–62, May 2008.

[38] M. Mazzanti, J. O. Bustamante, and H. Oberleithner, "Electrical dimension of the nuclear envelope.," *Physiol. Rev.*, vol. 81, no. 1, pp. 1–19, Jan. 2001.

[39] A. Kramer, Y. Ludwig, V. Shahin, and H. Oberleithner, "A pathway separate from the central channel through the nuclear pore complex for inorganic ions and small macromolecules.," *J. Biol. Chem.*, vol. 282, no. 43, pp. 31437–43, Oct. 2007.

[40] B. Naim, V. Brumfeld, R. Kapon, V. Kiss, R. Nevo, and Z. Reich, "Passive and facilitated transport in nuclear pore complexes is largely uncoupled.," *J. Biol.*

Chem., vol. 282, no. 6, pp. 3881–8, Feb. 2007.

[41] J. Fiserova, S. a Richards, S. R. Wente, and M. W. Goldberg, “Facilitated transport and diffusion take distinct spatial routes through the nuclear pore complex.,” *J. Cell Sci.*, vol. 123, no. Pt 16, pp. 2773–80, Aug. 2010.

[42] P. L. Paine, L. C. Moore, and S. B. Horowitz, “Nuclear Envelope Permeability,” *Nature*, vol. 254, pp. 109–114, 1975.

[43] C. M. Feldherr and D. Akin, “The location of the transport gate in the nuclear pore complex.,” *J. Cell Sci.*, vol. 110, pp. 3065–70, Dec. 1997.

[44] M. Breeuwer and D. S. Goldfarb, “Facilitated nuclear transport of histone H1 and other small nucleophilic proteins.,” *Cell*, vol. 60, no. 6, pp. 999–1008, 1990.

[45] S. Jäkel, W. Albig, U. Kutay, F. R. Bischoff, K. Schwamborn, D. Doenecke, and D. Görlich, “The importin beta/importin 7 heterodimer is a functional nuclear import receptor for histone H1.,” *EMBO J.*, vol. 18, no. 9, pp. 2411–23, 1999.

[46] G. Dirk and U. Kutay, “TRANSPORT BETWEEN THE CELL NUCLEUS AND THE CYTOPLASM,” *Annu. Rev. Annu. Rev. Cell Dev. Biol.*, vol. 15, pp. 607–660, 1999.

[47] K. Ribbeck and D. Görlich, “Kinetic analysis of translocation through nuclear pore complexes.,” *EMBO J.*, vol. 20, no. 6, pp. 1320–30, Mar. 2001.

[48] M. Rout, J. Aitchison, M. Magnasco, and B. Chait, “Virtual gating and nuclear transport: the hole picture,” *Trends Cell Biol.*, vol. 13, no. 12, pp. 622–628, Dec. 2003.

[49] P. R. Clarke and C. Zhang, “Spatial and temporal coordination of mitosis by Ran GTPase.,” *Nat. Rev. Mol. Cell Biol.*, vol. 9, no. 6, pp. 464–77, Jun. 2008.

[50] S. J. Lee, Y. Matsuura, S. M. Liu, and M. Stewart, “Structural basis for nuclear import complex dissociation by RanGTP.,” *Nature*, vol. 435, no. 7042, pp. 693–696, 2005.

[51] J. Fu, Q. Jiang, and C. Zhang, “Coordination of Cell Cycle Events by Ran GTPase,” *Nat. Educ.*, vol. 3, no. 9, 2010.

[52] U. Kubitscheck, D. Grünwald, A. Hoekstra, D. Rohleder, T. Kues, J. P. Siebrasse, and R. Peters, “Nuclear transport of single molecules: dwell times at the nuclear pore complex.,” *J. Cell Biol.*, vol. 168, no. 2, pp. 233–43, Jan. 2005.

[53] M. P. Rout and J. D. Aitchison, “The nuclear pore complex as a transport machine.,” *J. Biol. Chem.*, vol. 276, no. 20, pp. 16593–6, May 2001.

[54] D. Grünwald, R. H. Singer, and M. Rout, “Nuclear export dynamics of RNA-protein complexes.,” *Nature*, vol. 475, no. 7356, pp. 333–41, Jul. 2011.

[55] A. R. Lowe, J. H. Tang, J. Yassif, M. Graf, W. Y. C. Huang, J. T. Groves, K. Weis, and J. T. Liphardt, “Importin-β modulates the permeability of the nuclear pore complex in a Ran-dependent manner.,” *Elife*, vol. 4, pp. 1–24, Jan. 2015.

[56] S. M. Paulillo, E. M. Phillips, J. Köser, U. Sauder, K. S. Ullman, M. a Powers, and B. Fahrenkrog, “Nucleoporin domain topology is linked to the transport status of the nuclear pore complex.,” *J. Mol. Biol.*, vol. 351, no. 4, pp. 784–98,

Aug. 2005.

[57] D. Görlich, M. J. Seewald, and K. Ribbeck, “Characterization of Ran-driven cargo transport and the RanGTPase system by kinetic measurements and computer simulation.,” *EMBO J.*, vol. 22, no. 5, pp. 1088–100, Mar. 2003.

[58] D. Grünwald and R. H. Singer, “In vivo imaging of labelled endogenous β-actin mRNA during nucleocytoplasmic transport.,” *Nature*, vol. 467, no. 7315, pp. 604–7, Sep. 2010.

[59] T. Dange, D. Grünwald, A. Grünwald, R. Peters, and U. Kubitscheck, “Autonomy and robustness of translocation through the nuclear pore complex: a single-molecule study.,” *J. Cell Biol.*, vol. 183, no. 1, pp. 77–86, Oct. 2008.

[60] A. Ghavami, “Coarse-grained molecular dynamics simulation of transport through the nuclear pore complex,” University of Groningen, 2014.

[61] R. Y. H. Lim, N.-P. Huang, J. Köser, J. Deng, K. H. A. Lau, K. Schwarz-Herion, B. Fahrenkrog, and U. Aebi, “Flexible phenylalanine-glycine nucleoporins as entropic barriers to nucleocytoplasmic transport,” *Proc. Natl. Acad. Sci. U. S. A.*, vol. 103, no. 25, pp. 9512–7, Jun. 2006.

[62] R. Y. H. Lim, B. Fahrenkrog, J. Köser, K. Schwarz-Herion, J. Deng, and U. Aebi, “Nanomechanical basis of selective gating by the nuclear pore complex.,” *Science*, vol. 318, no. 5850, pp. 640–3, Oct. 2007.

[63] R. Y. . Lim and J. Deng, “Interaction Forces and Reversible Collapse of a Polymer Brush-Gated Nanopore,” *ACS Nano*, vol. 3, no. 10, pp. 2911–2918, 2009.

[64] N. B. Eisele, S. Frey, J. Piehler, D. Görlich, and R. P. Richter, “Ultrathin nucleoporin phenylalanine–glycine repeat films and their interaction with nuclear transport receptors,” *EMBO Rep.*, vol. 11, no. 5, pp. 366–372, 2010.

[65] R. D. Jäggi, A. Franco-Obregón, and K. Ensslin, “Quantitative topographical analysis of nuclear pore complex function using scanning force microscopy.,” *Biophys. J.*, vol. 85, no. 6, pp. 4093–8, Dec. 2003.

[66] T. Bickel and R. Bruinsma, “The Nuclear Pore Complex Mystery and Anomalous Diffusion in Reversible Gels,” *Biophys. J.*, vol. 83, no. 6, pp. 3079–3087, Dec. 2002.

[67] S. Frey, R. P. Richter, and D. Görlich, “FG-rich repeats of nuclear pore proteins form a three-dimensional meshwork with hydrogel-like properties.,” *Science*, vol. 314, no. 5800, pp. 815–7, Nov. 2006.

[68] R. Peters, “Translocation through the nuclear pore complex: selectivity and speed by reduction-of-dimensionality.,” *Traffic*, vol. 6, no. 5, pp. 421–7, May 2005.

[69] R. Moussavi-Baygi, Y. Jamali, R. Karimi, and M. R. K. Mofrad, “Biophysical coarse-grained modeling provides insights into transport through the nuclear pore complex,” *Biophys. J.*, vol. 100, no. 6, pp. 1410–1419, 2011.

[70] A. Paradise, M. K. Levin, G. Korza, and J. H. Carson, “Significant proportions of nuclear transport proteins with reduced intracellular mobilities resolved by fluorescence correlation spectroscopy.,” *J. Mol. Biol.*, vol. 365, no. 1, pp. 50–65,

2007.

[71] R. D. Jäggi, A. Franco-Obregón, P. Mühlhäusser, F. Thomas, U. Kutay, and K. Ensslin, “Modulation of nuclear pore topology by transport modifiers.,” *Biophys. J.*, vol. 84, no. 1, pp. 665–70, Jan. 2003.

[72] S. S. Patel, B. J. Belmont, J. M. Sante, and M. F. Rexach, “Natively Unfolded Nucleoporins Gate Protein Diffusion across the Nuclear Pore Complex,” *Cell*, vol. 129, no. 1, pp. 83–96, 2007.

[73] J. Ma, A. Goryaynov, A. Sarma, and W. Yang, “Self-regulated viscous channel in the nuclear pore complex.,” *Proc. Natl. Acad. Sci. U. S. A.*, vol. 2012, pp. 1–6, Apr. 2012.

[74] C. W. Akey, “Visualization of transport-related configurations of the nuclear pore transporter.,” *Biophys. J.*, vol. 58, no. 2, pp. 341–55, Aug. 1990.

[75] A. R. Lowe, J. J. Siegel, P. Kalab, M. Siu, K. Weis, and J. T. Liphardt, “Selectivity mechanism of the nuclear pore complex characterized by single cargo tracking,” *Nature*, vol. 467, no. 7315, pp. 600–3, Sep. 2010.

[76] S. S. Patel, B. J. Belmont, J. M. Sante, and M. F. Rexach, “Natively unfolded nucleoporins gate protein diffusion across the nuclear pore complex.,” *Cell*, vol. 129, no. 1, pp. 83–96, Apr. 2007.

[77] I. Ben-efraim and L. Gerace, “Gradient of Increasing Affinity of Importin B for Nucleoporins along the Pathway of Nuclear Import,” *J. Cell Biol.*, vol. 152, no. 2, pp. 411–417, 2001.

[78] D. Osmanović, I. J. Ford, and B. W. Hoogenboom, “Model inspired by nuclear pore complex suggests possible roles for nuclear transport receptors in determining its structure.,” *Biophys. J.*, vol. 105, no. 12, pp. 2781–9, Dec. 2013.

[79] M. L. Watson, “Further observations on the nuclear envelope of the animal cell.,” *J. Biophys. Biochem. Cytol.*, vol. 6, no. 2, pp. 147–56, Oct. 1959.

[80] J. G. Gall, “Octagonal Nuclear Pores,” *J. Cell Biol.*, no. 1950, pp. 391–399, 1967.

[81] K. H. Bui, A. von Appen, A. L. DiGuilio, A. Ori, L. Sparks, M.-T. Mackmull, T. Bock, W. Hagen, A. Andrés-Pons, J. S. Glavy, and M. Beck, “Integrated structural analysis of the human nuclear pore complex scaffold.,” *Cell*, vol. 155, no. 6, pp. 1233–43, Dec. 2013.

[82] S. Siniossoglou, M. Lutzmann, H. Santos-Rosa, K. Leonard, S. Mueller, U. Aebi, and E. Hurt, “Structure and assembly of the Nup84p complex.,” *J. Cell Biol.*, vol. 149, no. 1, pp. 41–54, 2000.

[83] M. Lutzmann, R. Kunze, A. Buerer, U. Aebi, and E. Hurt, “Modular self-assembly of a Y-shaped multiprotein complex from seven nucleoporins.,” *EMBO J.*, vol. 21, no. 3, pp. 387–97, 2002.

[84] S. G. Brohawn, N. C. Leksa, E. D. Spear, K. R. Rajashankar, and T. U. Schwartz, “Structural Evidence for Common Ancestry of the Nuclear Pore Complex and Vesicle Coats,” *Science (80-.).*, vol. 322, no. 5906, pp. 1369–1373, 2009.

[85] M. Kampmann and G. Blobel, “Three-dimensional structure and flexibility of a membrane-coating module of the nuclear pore complex,” *Nat. Struct. & Mol.*

Biol., vol. 16, no. 7, pp. 782–788, 2009.

[86] R. P. Grant, D. Neuhaus, and M. Stewart, “Structural Basis for the Interaction Between the Tap/NXF1 UBA Domain and FG Nucleoporins at 1Å Resolution,” *J. Mol. Biol.*, vol. 326, no. 3, pp. 849–858, Feb. 2003.

[87] N. Schrader, C. Koerner, K. Koessmeier, J.-A. Bangert, A. Wittinghofer, R. Stoll, and I. R. Vetter, “The crystal structure of the Ran-Nup153ZnF2 complex: a general Ran docking site at the nuclear pore complex.,” *Structure*, vol. 16, no. 7, pp. 1116–25, Jul. 2008.

[88] U. Kubitscheck, P. Wedekind, O. Zeidler, M. Grote, and R. Peters, “Single nuclear pores visualized by confocal microscopy and image processing.,” *Biophys. J.*, vol. 70, no. 5, pp. 2067–77, May 1996.

[89] J. Hüve, R. Wesselmann, M. Kahms, and R. Peters, “4Pi microscopy of the nuclear pore complex.,” *Biophys. J.*, vol. 95, no. 2, pp. 877–85, Jul. 2008.

[90] A. Szymborska, A. de Marco, N. Daigle, V. C. Cordes, J. a G. Briggs, and J. Ellenberg, “Nuclear pore scaffold structure analyzed by super-resolution microscopy and particle averaging.,” *Science*, vol. 341, no. 6146, pp. 655–8, Aug. 2013.

[91] A. Löschberger, S. van de Linde, M.-C. Dabauvalle, B. Rieger, M. Heilemann, G. Krohne, and M. Sauer, “Super-resolution imaging visualizes the eightfold symmetry of gp210 proteins around the nuclear pore complex and resolves the central channel with nanometer resolution.,” *J. Cell Sci.*, vol. 125, no. Pt 3, pp. 570–5, Feb. 2012.

[92] R. Chéreau, J. Tønnesen, and U. V. Nägerl, “STED microscopy for nanoscale imaging in living brain slices.,” *Methods*, pp. 1–10, Jun. 2015.

[93] F. Göttfert, C. a Wurm, V. Mueller, S. Berning, V. C. Cordes, A. Honigmann, and S. W. Hell, “Coaligned dual-channel STED nanoscopy and molecular diffusion analysis at 20 nm resolution.,” *Biophys. J.*, vol. 105, no. 1, pp. L01–3, Jul. 2013.

[94] W. Yang, J. Gelles, and S. M. Musser, “Imaging of single-molecule translocation through nuclear pore complexes.,” *Proc. Natl. Acad. Sci. U. S. A.*, vol. 101, no. 35, pp. 12887–92, Aug. 2004.

[95] H. Oberleithner, H. Schillers, M. Wilhelmi, D. Butzke, and T. Danker, “Nuclear pores collapse in response to CO 2 imaged with atomic force microscopy,” *J. Cell Biol.*, vol. 439, pp. 251–255, 2000.

[96] M. A. Lee, R. C. Dunn, D. E. Clapham, and L. Stehno-bitte, “Calcium regulation permeability of nuclear pore,” *Cell Calcium*, vol. 23, pp. 91–101, 1998.

[97] L. Stehno-Bittel, C. Perez-Terzic, and D. Clapham, “Diffusion across the nuclear envelope inhibited by depletion of the nuclear Ca2+ store,” *Science (80-.).*, vol. 270, no. 5243, pp. 1835–1838, 1995.

[98] D. Stoffler, K. N. Goldie, B. Feja, and U. Aebi, “Calcium-mediated structural changes of native nuclear pore complexes monitored by time-lapse atomic force microscopy.,” *J. Mol. Biol.*, vol. 287, no. 4, pp. 741–52, Apr. 1999.

[99] H. Wang and D. E. Clapham, “Conformational changes of the in situ nuclear pore complex.,” *Biophys. J.*, vol. 77, no. 1, pp. 241–7, Jul. 1999.

[100] T. Rhen and J. a Cidlowski, “Antiinflammatory action of glucocorticoids--new mechanisms for old drugs.,” *N. Engl. J. Med.*, vol. 353, no. 16, pp. 1711–23, Oct. 2005.

[101] V. Shahin, Y. Ludwig, C. Schafer, D. Nikova, and H. Oberleithner, “Glucocorticoids remodel nuclear envelope structure and permeability.,” *J. Cell Sci.*, vol. 118, no. Pt 13, pp. 2881–9, Jul. 2005.

[102] Z. Liu, R. Kenworthy, C. Green, and H. Tang, “Molecular determinants of nucleolar translocation of RNA helicase A.,” *Exp. Cell Res.*, vol. 313, no. 17, pp. 3743–54, Oct. 2007.

[103] W. Matthew, “A Nuclear Export Signal in hnRNP Al : Nuclear Protein Export Pathway within PK-NLS,” *Cell*, vol. 83, pp. 415–422, 1995.

[104] B. Wolff, M. C. Willingham, and J. A. Hanover, “Nuclear protein import: specificity for transport across the nuclear pore.,” *Exp. Cell Res.*, vol. 178, no. 2, pp. 318–34, Oct. 1988.

[105] N. Shulga and D. S. Goldfarb, “Binding Dynamics of Structural Nucleoporins Govern Nuclear Pore Complex Permeability and May Mediate Channel Gating,” *Mol. Cell. Biol.*, vol. 23, no. 2, pp. 534–542, 2003.

[106] C. Schäfer, Y. Ludwig, V. Shahin, A. Kramer, P. Carl, H. Schillers, and H. Oberleithner, “Ethanol alters access to the cell nucleus.,” *Pflugers Arch.*, vol. 453, no. 6, pp. 809–18, Mar. 2007.

[107] R. L. Schoch, L. E. Kapinos, and R. Y. H. Lim, “Nuclear transport receptor binding avidity triggers a self-healing collapse transition in FG-nucleoporin molecular brushes.,” *Proc. Natl. Acad. Sci. U. S. A.*, vol. 109, no. 42, pp. 16911–6, 2012.

[108] L. E. Kapinos, R. L. Schoch, R. S. Wagner, K. D. Schleicher, and R. Y. H. Lim, “Karyopherin-centric control of nuclear pores based on molecular occupancy and kinetic analysis of multivalent binding with FG nucleoporins.,” *Biophys. J.*, vol. 106, no. 8, pp. 1751–62, Apr. 2014.

[109] X. J. Liu, *Xenopus Protocols.Cell Biology and Signal Transduction*. Humana Press, 2006.

[110] E. S. Erickson, O. L. Mooren, D. Moore-Nichols, and R. C. Dunn, “Activation of ryanodine receptors in the nuclear envelope alters the conformation of the nuclear pore complex.,” *Biophys. Chem.*, vol. 112, no. 1, pp. 1–7, Dec. 2004.

[111] E. Wedege and G. Svenneby, “Effects of the blocking agents bovine serum albumin and Tween 20 in different buffers on immunoblotting of brain proteins and marker proteins.,” *J. Immunol. Methods*, vol. 88, no. 2, pp. 233–7, Apr. 1986.

[112] N. Patterson, D. P. Adams, V. C. Hodges, M. J. Vasile, J. R. Michael, and P. G. Kotula, “Controlled fabrication of nanopores using a direct focused ion beam approach with back face particle detection.,” *Nanotechnology*, vol. 19, no. 23, p. 235304, Jun. 2008.

[113] B. N. Miles, A. P. Ivanov, K. a Wilson, F. Doğan, D. Japrung, and J. B. Edel, "Single molecule sensing with solid-state nanopores: novel materials, methods, and applications.," *Chem. Soc. Rev.*, vol. 42, no. 1, pp. 15–28, Jan. 2013.

[114] D. A. Hook, J. a. Olhausen, J. Krim, and M. T. Dugger, "Evaluation of Oxygen Plasma and UV Ozone Methods for Cleaning of Occluded Areas in MEMS Devices," *J. Microelectromechanical Syst.*, vol. 19, no. 6, pp. 1292–1298, Dec. 2010.

[115] Y. Xue, X. Li, H. Li, and W. Zhang, "Quantifying thiol-gold interactions towards the efficient strength control.," *Nat. Commun.*, vol. 5, p. 4348, Jan. 2014.

[116] C. G. G. Binnig and C. F. Quate, "Atomic Force Microscope," *Phys. Rev. Lett.*, vol. 56, no. 9, pp. 930–933, 1986.

[117] J. Varesi and a. Majumdar, "Scanning Joule expansion microscopy at nanometer scales," *Appl. Phys. Lett.*, vol. 72, no. 1, p. 37, 1998.

[118] B. W. Hoogenboom, "AFM in Liquids," in *Encyclopedia of Nanotechnology*, Springer Netherlands, Dordrecht, 2012.

[119] J. A. Gallego-Juarez, "Piezoelectric ceramics and u It rason ic transducers," *J. Phys. E Sci. Instrum.*, vol. 22, pp. 804–816, 1989.

[120] NT-MDT, "Atomic Force Microscopy - The Principles of Operation of Atomic Force Microscope," 2008. [Online]. Available: http://www.azom.com/article.aspx?ArticleID=4437#2.

[121] F. J. Giessibl, "Advances in atomic force microscopy," *Rev. Mod. Phys.*, vol. 75, no. 3, pp. 949–983, 2003.

[122] a. G. Onaran and F. L. Degertekin, "A fluid cell with integrated acoustic radiation pressure actuator for atomic force microscopy," *Rev. Sci. Instrum.*, vol. 76, no. 10, p. 103703, 2005.

[123] B. Mitra and A. Gaitas, "Thermally actuated tapping mode atomic force microscopy with polymer microcantilevers.," *Rev. Sci. Instrum.*, vol. 80, no. 2, p. 023703, Feb. 2009.

[124] G. R. Jayanth, Y. Jeong, and C.-H. Menq, "Direct tip-position control using magnetic actuation for achieving fast scanning in tapping mode atomic force microscopy," *Rev. Sci. Instrum.*, vol. 77, no. 5, p. 053704, 2006.

[125] F. Kienberger, A. Ebner, H. J. Gruber, and P. Hinterdorfer, "Molecular recognition imaging and force spectroscopy of single biomolecules.," *Acc. Chem. Res.*, vol. 39, no. 1, pp. 29–36, Jan. 2006.

[126] Veeco, "Force Measurements. Support Note N228," vol. 93117, no. 228. pp. 1–44, 2003.

[127] N. H. Green, S. Allen, M. C. Davies, C. J. Roberts, S. J. B. Tendler, and P. M. Williams, "Force sensing and mapping by atomic force microscopy," *Science (80-.).*, vol. 21, no. 1, pp. 64–73, 2002.

[128] F. L. Leite, C. C. Bueno, A. L. Da Róz, E. C. Ziemath, and O. N. Oliveira, *Theoretical models for surface forces and adhesion and their measurement using atomic force microscopy.*, vol. 13, no. 10. 2012.

[129] M. Radmacher, “Studying the mechanics of cellular processes by atomic force microscopy.,” *Methods Cell Biol.*, vol. 83, no. 07, pp. 347–72, Jan. 2007.

[130] R. Bassani, R. Solaro, M. Alderighi, C. D. I. Cesare, and M. Allegrini, “Nanoindentation with AFM,” *Int. Conf. Tribol.*, 2006.

[131] P. Trtik, J. Kaufmann, and U. Volz, “On the use of peak-force tapping atomic force microscopy for quantification of the local elastic modulus in hardened cement paste,” *Cem. Concr. Res.*, vol. 42, no. 1, pp. 215–221, Jan. 2012.

[132] D. C. Lin, E. K. Dimitriadis, and F. Horkay, “Robust strategies for automated AFM force curve analysis--I. Non-adhesive indentation of soft, inhomogeneous materials.,” *J. Biomech. Eng.*, vol. 129, no. 3, pp. 430–40, Jun. 2007.

[133] N. S. Claxton, T. J. Fellers, and M. W. Davidson, “Laser Scanning Confocal Microscopy,” *Microscopy, Confocal. Encyclopedia of Medical Devices and Instrumentation.*, vol. 1979, no. 21. pp. 1–37, 2006.

[134] M. Minsky, “MICROSCOPY APPARATUS,” 3,013,467, 1961.

[135] M. Minsky, “Memoir on inventing the confocal scanning microscope,” *Scanning*, vol. 10, no. 4, pp. 128–138, 1988.

[136] J. C. Robert Bagnell, *Chapter 13 Confocal Laser Scanning Microscopy*. 2012.

[137] I. Johnson and M. T. Z. Spence, Eds., *The Molecular Probes*. Life Technologies Corporation, 2010.

[138] L. Bei, “Acousto-optic tunable filters: fundamentals and applications as applied to chemical analysis techniques,” *Prog. Quantum Electron.*, vol. 28, no. 2, pp. 67–87, 2004.

[139] K. R. Spring and M. W. Davidson, “Nikon Microscopy. Concepts and Formulas.,” 2013. [Online]. Available: http://www.olympusmicro.com/primer/techniques/confocal/aotfintro.html.

[140] M. Abramowitz and M. W. Davidson, “Microscope Objectives,” 2004. [Online]. Available: http://micro.magnet.fsu.edu/primer/anatomy/numaperture.html.

[141] I. Kochevar, “Phototoxicity Mechanisms: Chlorpromazine Photosensitized Damage to DNA and Cell Membranes,” *J. Invest. Dermatol.*, no. 76, pp. 59–64, 1981.

[142] K. Ribbeck and D. Görlich, “The permeability barrier of nuclear pore complexes appears to operate via hydrophobic exclusion.,” *EMBO J.*, vol. 21, no. 11, pp. 2664–71, Jun. 2002.

[143] J. Rühe, M. Ballauff, M. Biesalski, P. Dziezok, F. Gröhn, D. Johannsmann, N. Houbenov, N. Hugenberg, R. Konradi, S. Minko, M. Motornov, R. R. Netz, M. Schmidt, C. Seidel, M. Stamm, and H. Zhang, “Polyelectrolyte Brushes,” in *Polyelectrolytes with Defined Molecular Architecture I*, M. Schmidt, Ed. Springer Berlin Heidelberg, 2004, pp. 79–150.

[144] S. Sanjuan, P. Perrin, N. Pantoustier, and Y. Tran, “Synthesis and swelling behavior of pH-responsive polybase brushes.,” *Langmuir*, vol. 23, no. 10, pp. 5769–78, May 2007.

[145] E. Katz, O. Lioubashevsky, and I. Willner, “Electromechanics of a redox-active rotaxane in a monolayer assembly on an electrode.,” *J. Am. Chem. Soc.*, vol. 126, no. 47, pp. 15520–32, Dec. 2004.

[146] M. Riskin, B. Basnar, E. Katz, and I. Willner, “Cyclic control of the surface properties of a monolayer-functionalized electrode by the electrochemical generation of Hg nanoclusters.,” *Chemistry*, vol. 12, no. 33, pp. 8549–57, Nov. 2006.

[147] W. Lu, A. G. Fadeev, B. Qi, E. Smela, B. R. Mattes, J. Ding, G. M. Spinks, J. Mazurkiewicz, D. Zhou, G. G. Wallace, D. R. Macfarlane, S. A. Forsyth, and M. Forsyth, “Use of Ionic Liquids for -Conjugated Polymer Electrochemical Devices,” *Science (80-.).*, vol. 297, no. August, pp. 983–988, 2002.

[148] S. Minko, “Responsive Polymer Brushes,” *J. Macromol. Sci. Part C Polym. Rev.*, vol. 46, no. 4, pp. 397–420, Dec. 2006.

[149] X. Wang, R. Berger, J. I. Ramos, T. Wang, K. Koynov, G. Liu, H.-J. Butt, and S. Wu, “Nanopatterns of polymer brushes for understanding protein adsorption on the nanoscale,” *RSC Adv.*, vol. 4, no. 85, pp. 45059–45064, 2014.

[150] J. E. Gautrot, B. Trappmann, F. Oceguera-Yanez, J. Connelly, X. He, F. M. Watt, and W. T. S. Huck, “Exploiting the superior protein resistance of polymer brushes to control single cell adhesion and polarisation at the micron scale.,” *Biomaterials*, vol. 31, no. 18, pp. 5030–41, Jun. 2010.

[151] E. B. Zhulina, T. M. Birshtein, V. A. Priamitsyn, and L. I. Klushin, “Inhomogeneous Structure of Collapsed Polymer Brushes under Deformation,” *Macromolecules*, vol. 28, pp. 8612–8620, 1995.

[152] T. Farhan, O. Azzaroni, and W. T. S. Huck, “AFM study of cationically charged polymer brushes: switching between soft and hard matter,” *Soft Matter*, vol. 1, no. 1, p. 66, 2005.

[153] J. L. Cuellar, I. Llarena, J. J. Iturri, E. Donath, and S. E. Moya, “A novel approach for measuring the intrinsic nanoscale thickness of polymer brushes by means of atomic force microscopy: application of a compressible fluid model,” *Nanoscale*, vol. 5, no. 23, p. 11679, 2013.

[154] R. B. . Sullan, A. B. Churnside, D. M. Nguyen, M. S. Bull, and T. T. Perkins, “Atomic force microscopy with sub-picoNewton force stability for biological applications,” *Methods*, vol. 60, no. 2, pp. 131–141, 2014.

[155] “Contact AFM Troubleshooting,” *Bruker Corporation*, 2013. [Online]. Available: http://www.nanophys.kth.se/nanophys/facilities/nfl/afm/fast-scan/bruker-help/Content/Contact AFM/Contact_AFM_Troubleshoot.htm. [Accessed: 20-Dec-2015].

[156] A. J. Parnell, S. J. Martin, R. a. L. Jones, C. Vasilev, C. J. Crook, and A. J. Ryan, “Direct visualization of the real time swelling and collapse of a poly(methacrylic acid) brush using atomic force microscopy,” *Soft Matter*, vol. 5, no. 2, pp. 296–299, 2009.

[157] K. L. Johnson, *Contact Mechanics*. Cambridge: Cambridge University Press, 1985.

[158] A. B. Mathur, A. M. Collinsworth, W. M. Reichert, W. E. Kraus, and G. a. Truskey, “Endothelial, cardiac muscle and skeletal muscle exhibit different viscous and elastic properties as determined by atomic force microscopy,” *J. Biomech.*, vol. 34, no. 12, pp. 1545–1553, Dec. 2001.

[159] M. Lekka, P. Laidler, D. Gil, J. Lekki, Z. Stachura, and a. Z. Hrynkiewicz, “Elasticity of normal and cancerous human bladder cells studied by scanning force microscopy,” *Eur. Biophys. J.*, vol. 28, no. 4, pp. 312–316, May 1999.

[160] S. C. Lieber, N. Aubry, J. Pain, G. Diaz, S. Kim, S. F. Vatner, and C. Samuel, “Aging increases stiffness of cardiac myocytes measured by atomic force microscopy nanoindentation,” *Am. J. Physiol. Hear. Circ. Physiol.*, vol. 287, pp. 645–651, 2004.

[161] W. F. Heinz and J. H. Hoh, “Spatially resolved force spectroscopy of biological surfaces using the atomic force microscope,” *Trends Biotechnol.*, vol. 17, no. 4, pp. 143–150, Apr. 1999.

[162] K. a Melzak, S. Moreno-Flores, K. Yu, J. Kizhakkedathu, and J. L. Toca-Herrera, “Rationalized approach to the determination of contact point in force-distance curves: application to polymer brushes in salt solutions and in water.,” *Microsc. Res. Tech.*, vol. 73, no. 10, pp. 959–64, Oct. 2010.

[163] S. Yamamoto, M. Ejaz, Y. Tsujii, and T. Fukuda, “Surface Interaction Forces of Well-Defined, High-Density Polymer Brushes Studied by Atomic Force Microscopy. 2. Effect of Graft Density,” *Macromolecules*, vol. 33, no. 15, pp. 5608–5612, Jul. 2000.

[164] W. F. Heinz and J. H. Hoh, “Spatially resolved force spectroscopy of biological surfaces using the atomic force microscope,” *Trends Biotechnol.*, vol. 17, no. 4, pp. 143–150, Apr. 1999.

[165] X. Sui, Q. Chen, M. a Hempenius, and G. J. Vancso, “Probing the collapse dynamics of poly(N-isopropylacrylamide) brushes by AFM: effects of co-nonsolvency and grafting densities.,” *Small*, vol. 7, no. 10, pp. 1440–7, May 2011.

[166] S. Radji, H. Alem, S. Demoustier-champagne, A. M. Jonas, and S. Cuenot, “Investigation of Thermoresponsive Nano- Confined Polymer Brushes by AFM-Based Force Spectroscopy,” *Macromol. Chem. Phys.*, vol. 213, pp. 580–586, 2012.

[167] I. Amin, M. Steenackers, N. Zhang, A. Beyer, X. Zhang, T. Pirzer, T. Hugel, R. Jordan, and A. Gölzhäuser, “Polymer carpets.,” *Small*, vol. 6, no. 15, pp. 1623–30, Aug. 2010.

[168] R. Y. H. Lim, B. Fahrenkrog, J. Köser, K. Schwarz-Herion, J. Deng, and U. Aebi, “Nanomechanical basis of selective gating by the nuclear pore complex.,” *Science*, vol. 318, no. 5850, pp. 640–3, Oct. 2007.

[169] K. a Melzak, S. Moreno-Flores, K. Yu, J. Kizhakkedathu, and J. L. Toca-Herrera, “Rationalized approach to the determination of contact point in force-distance curves: application to polymer brushes in salt solutions and in water.,” *Microsc. Res. Tech.*, vol. 73, no. 10, pp. 959–64, Oct. 2010.

[170] R. Y. H. Lim, U. Aebi, and D. Stoffler, “From the trap to the basket: getting to the bottom of the nuclear pore complex.,” *Chromosoma*, vol. 115, no. 1, pp. 15–26, Feb. 2006.

[171] K. Enss, T. Danker, a Schlune, I. Buchholz, and H. Oberleithner, “Passive transport of macromolecules through Xenopus laevis nuclear envelope.,” *J. Membr. Biol.*, vol. 196, no. 3, pp. 147–55, Dec. 2003.

[172] A. Bestembayeva, A. Kramer, A. a Labokha, D. Osmanović, I. Liashkovich, E. V Orlova, I. J. Ford, G. Charras, A. Fassati, and B. W. Hoogenboom, “Nanoscale stiffness topography reveals structure and mechanics of the transport barrier in intact nuclear pore complexes.,” *Nat. Nanotechnol.*, vol. 10, no. 1, pp. 60–64, Jan. 2015.

[173] M. Beck, V. Lucić, F. Förster, W. Baumeister, and O. Medalia, “Snapshots of nuclear pore complexes in action captured by cryo-electron tomography.,” *Nature*, vol. 449, no. 7162, pp. 611–5, Oct. 2007.

[174] K. Haase and A. E. Pelling, “Investigating cell mechanics with atomic force microscopy,” *J. R. Soc. Interface*, vol. 12, pp. 1–16, 2015.

[175] T. G. Kuznetsova, M. N. Starodubtseva, N. I. Yegorenkov, S. a Chizhik, and R. I. Zhdanov, “Atomic force microscopy probing of cell elasticity.,” *Micron*, vol. 38, no. 8, pp. 824–33, Jan. 2007.

[176] V. M. Laurent, S. Kasas, A. Yersin, T. E. Schäffer, S. Catsicas, G. Dietler, A. B. Verkhovsky, and J.-J. Meister, “Gradient of rigidity in the lamellipodia of migrating cells revealed by atomic force microscopy.,” *Biophys. J.*, vol. 89, no. 1, pp. 667–75, Jul. 2005.

[177] A. A. Soufivand and M. Navidbakhsh, “The effects of Hertz’s model parameters on analysis of Atomic Force Microscopy (AFM) data for cardiac cell,” *IEEE*, no. December, pp. 163–166, 2012.

[178] M. Yokokawa, K. Takeyasu, and S. H. Yoshimura, “Mechanical properties of plasma membrane and nuclear envelope measured by scanning probe microscope,” *J. Microsc.*, vol. 232, pp. 82–90, 2008.

[179] J. P. Straehla, F. T. Limpoco, N. V. Dolgova, B. G. Keselowsky, W. G. Sawyer, and S. S. Perry, “Nanomechanical Probes of Single Corneal Epithelial Cells: Shear Stress and Elastic Modulus,” *Tribol. Lett.*, vol. 38, no. 2, pp. 107–113, Jan. 2010.

[180] J. Domke and M. Radmacher, “Measuring the Elastic Properties of Thin Polymer Films with the Atomic Force Microscope,” *Langmuir*, vol. 14, pp. 3320–3325, 1998.

[181] T. Maimon and O. Medalia, “Perspective on the metazoan nuclear pore complex.,” *Nucleus*, vol. 1, no. 5, pp. 383–6, 2010.

[182] R. E. Mahaffy, C. K. Shih, F. C. MacKintosh, and J. Käs, “Scanning Probe-Based Frequency-Dependent Microrheology of Polymer Gels and Biological Cells,” *Phys. Rev. Lett.*, vol. 85, no. 4, pp. 880–883, Jul. 2000.

[183] C. Roduit, S. Sekatski, G. Dietler, S. Catsicas, F. Lafont, and S. Kasas, “Stiffness

tomography by atomic force microscopy.," *Biophys. J.*, vol. 97, no. 2, pp. 674–7, Jul. 2009.

[184] M. T. Ahmadian and A. A. Nikooyan, "Modeling and Prediction of Soft Tissue Directional Stiffness using in vitro Force-Displacement Data," *Int. J. Sci. Res.*, vol. 16, pp. 385–389, 2006.

[185] M. Gelbert, M. Biesalski, J. Ruhe, and D. Johannsmann, "Collapse of Polyelectrolyte Brushes Probed by Noise Analysis of a Scanning Force Microscope Cantilever," *Langmuir*, no. 14, 2000.

[186] H. Oberleithner, E. Brinckmann, G. Giebisch, and J. Geibel, "Visualizing life on biomembranes by atomic force microscopy.," *Kidney Int.*, vol. 48, no. 4, pp. 923–9, Oct. 1995.

[187] M. Jarnik and U. Aebi, "Toward a more complete 3-D structure of the nuclear pore complex.," *J. Struct. Biol.*, vol. 107, no. 3, pp. 291–308, Dec. 1991.

[188] D. Moore-Nichols, A. Arnott, and R. C. Dunn, "Regulation of nuclear pore complex conformation by IP(3) receptor activation.," *Biophys. J.*, vol. 83, no. 3, pp. 1421–8, Sep. 2002.

[189] T. Danker and H. Oberleithner, "Nuclear pore function viewed with atomic force microscopy.," *Pflugers Arch.*, vol. 439, no. 6, pp. 671–81, Apr. 2000.

[190] C. W. Lehman and D. Carrol, "Isolation of Large Quantities of Functional, Cytoplasm-Free Xenopus laevis Oocyte Nuclei," *Anal. Biochem.*, vol. 211, pp. 311–319, 1993.

[191] I. Ruberti, E. Beccari, E. Bianchi, and F. Carnevali, "Large scale isolation of nuclei from oocytes of Xenopus laevis," *Anal. Biochem.*, vol. 180, no. 1, pp. 177–180, Jul. 1989.

[192] A. Ewald, C. Zünkler, D. Lourim, and M. Dabauvalle, "Microtubule-dependent assembly of the nuclear envelope in Xenopus laevis egg extract," *Eur. J. Cell Biol.*, vol. 691, pp. 678–691, 2001.

[193] I. Liashkovich, A. Meyring, H. Oberleithner, and V. Shahin, "Structural organization of the nuclear pore permeability barrier," *J. Control. Release*, vol. 160, no. 3, pp. 601–8, Jun. 2012.

[194] R. B. Kopito and M. Elbaum, "Reversibility in nucleocytoplasmic transport.," *Proc. Natl. Acad. Sci. U. S. A.*, vol. 104, no. 31, pp. 12743–8, Jul. 2007.

[195] B. R. Miller, M. Powers, M. Park, W. Fischer, and D. J. Forbes, "Identification of a New Vertebrate Nucleoporin, Nup188, with the Use of a Novel Organelle Trap Assay," *Mol. Biol. Cell*, vol. 11, no. October, pp. 3381–3396, 2000.

[196] T. D. Allen, J. M. Cronshaw, S. Bagley, E. Kiseleva, and M. W. Goldberg, "The nuclear pore complex: mediator of translocation between nucleus and cytoplasm.," *J. Cell Sci.*, vol. 113 (Pt 1, pp. 1651–9, May 2000.

[197] B. Alberts, A. Johnson, J. Lewis, M. Raff, K. Roberts, and P. Walter, *Molecular Biology of the Cell*, 4th editio. New York, 2002.

[198] B. Pittenger, "Nanoscale mechanical property measurements in AFM modes with direct force control," vol. m. pp. 1–23, 2014.

[199] D. Haviland, C. A. van Eysden, D. Forchheimer, D. Platz, H. G. Kassa, and phil leclere, "Probing viscoelastic response of soft material surfaces at the nanoscale," *Soft Matter*, 2015.

[200] O. Keminer and R. Peters, "Permeability of single nuclear pores.," *Biophys. J.*, vol. 77, no. 1, pp. 217–28, Jul. 1999.

[201] T. Radtke, D. Schmalz, E. Coutavas, T. M. Soliman, and R. Peters, "Kinetics of protein import into isolated Xenopus oocyte nuclei," *PNAS*, vol. 98, no. 5, pp. 2407–2412, 2000.

[202] D. D. Newmeyer and D. J. Forbes, "Nuclear import can be separated into distinct steps in vitro: nuclear pore binding and translocation.," *Cell*, vol. 52, no. 5, pp. 641–53, Mar. 1988.

[203] J. Li, M. Gershow, D. Stein, E. Brandin, and J. a Golovchenko, "DNA molecules and configurations in a solid-state nanopore microscope.," *Nat. Mater.*, vol. 2, no. 9, pp. 611–5, Sep. 2003.

[204] G. M. Skinner, M. van den Hout, O. Broekmans, C. Dekker, and N. H. Dekker, "Distinguishing single- and double-stranded nucleic acid molecules using solid-state nanopores.," *Nano Lett.*, vol. 9, no. 8, pp. 2953–60, Aug. 2009.

[205] A. Han, G. Schürmann, G. Mondin, R. A. Bitterli, N. G. Hegelbach, N. F. de Rooij, and U. Staufer, "Sensing protein molecules using nanofabricated pores," *Appl. Phys. Lett.*, vol. 88, no. 9, p. 093901, 2006.

[206] S. W. Kowalczyk, T. R. Blosser, and C. Dekker, "Biomimetic nanopores: learning from and about nature.," *Trends Biotechnol.*, vol. 29, no. 12, pp. 607–14, Dec. 2011.

[207] S. W. Kowalczyk, L. Kapinos, T. R. Blosser, T. Magalhães, P. van Nies, R. Y. H. Lim, and C. Dekker, "Single-molecule transport across an individual biomimetic nuclear pore complex.," *Nat. Nanotechnol.*, vol. 6, no. 7, pp. 433–8, Jul. 2011.

[208] B. Division, C. Biology, and S. Cruz, "Characterization of individual polynucleotide molecules using a membrane channel," *Proc. Natl. Acad. Sci. USA*, vol. 93, no. November, pp. 13770–13773, 1996.

[209] C. Dekker, "Solid-state nanopores," *Nat. Nanotechnol.*, vol. 2, pp. 209–215, 2007.

[210] S. W. Kowalczyk, L. Kapinos, T. R. Blosser, T. Magalhães, P. van Nies, R. Y. H. Lim, and C. Dekker, "Single-molecule transport across an individual biomimetic nuclear pore complex.," *Nat. Nanotechnol.*, vol. 6, no. 7, pp. 433–8, Jul. 2011.

[211] F. Xia, W. Guo, Y. Mao, X. Hou, J. Xue, H. Xia, L. Wang, Y. Song, H. Ji, Q. Ouyang, Y. Wang, and L. Jiang, "Gating of Single Synthetic Nanopores by Proton-Driven DNA Molecular Motors," *J. Am. Chem. Soc.*, vol. 130, no. 26, pp. 8345–8350, 2008.

[212] G. Wang, A. K. Bohaty, I. Zharov, and H. S. White, "Photon Gated Transport at the Glass Nanopore Electrode," *J. Am. Chem. Soc.*, vol. 128, no. 41, pp. 13553–13558, 2006.

[213] X. Hou, W. Guo, F. Xia, F.-Q. Nie, H. Dong, Y. Tian, L. Wen, L. Wang, L. Cao,

Y. Yang, J. Xue, Y. Song, Y. Wang, D. Liu, and L. Jiang, “A biomimetic potassium responsive nanochannel: G-quadruplex DNA conformational switching in a synthetic nanopore.,” *J. Am. Chem. Soc.*, vol. 131, no. 22, pp. 7800–5, Jun. 2009.

[214] C. Chaillan-Huntington, C. Villa, and M. Stewart, “Dissecting the Interactions between NTF2 , RanGDP , and the Nucleoporin X F X FG Repeats *,” *J. Biol. Chem.*, vol. 275, no. 8, pp. 5874–5879, 2000.

[215] T. Jovanovic-Talisman, J. Tetenbaum-Novatt, A. S. McKenney, A. Zilman, R. Peters, M. P. Rout, and B. T. Chait, “Artificial nanopores that mimic the transport selectivity of the nuclear pore complex.,” *Nature*, vol. 457, no. 7232, pp. 1023–7, Feb. 2009.

[216] H. Watarai, N. Teramae, and T. Sawada, *Interfacial Nanochemistry: Molecular Science and Engineering at Liquid-Liquid Interfaces*. Kluwer Academic/Plenum Publishers, 2006.

[217] J. Fan, G. Y. Chong, and C. S. Tan, “Study of Hydrophilic Si Direct Bonding with Ultraviolet Ozone Activation for 3D Integration,” *ECS J. Solid State Sci. Technol.*, vol. 1, no. 6, pp. P291–P296, Oct. 2012.

[218] K. Awsiuk, a. Psarouli, P. Petrou, a. Budkowski, S. Kakabakos, a. Bernasik, J. Rysz, and I. Raptis, “Spectroscopic and microscopic examination of protein adsorption and blocking of non-specific binding to silicon surfaces modified with APTES and GOPS,” *Procedia Eng.*, vol. 25, pp. 334–337, 2011.

[219] M. Furuya, M. Haramura, and A. Tanaka, “Reduction of nonspecific binding proteins to self-assembled monolayer on gold surface.,” *Bioorg. Med. Chem.*, vol. 14, no. 2, pp. 537–43, Jan. 2006.

[220] D. L. Elbert and J. A. Hubbell, “Surface treatments of polymers for biocompatibility,” *Annu. Rev.*, pp. 365–394, 1996.

[221] A. Jain, R. Liu, Y. K. Xiang, and T. Ha, “Single-molecule pull-down for studying protein interactions.,” *Nat. Protoc.*, vol. 7, no. 3, pp. 445–52, Mar. 2012.

[222] F. Tao and S. Bernasek, *Functionalization of Semiconductor Surfaces*, John Wiley. 2012.

[223] S. Sharma, K. C. Popat, and T. a. Desai, “Controlling Nonspecific Protein Interactions in Silicon Biomicrosystems with Nanostructured Poly(ethylene glycol) Films,” *Langmuir*, vol. 18, no. 23, pp. 8728–8731, Nov. 2002.

[224] Q. He, J. Zhang, J. Shi, Z. Zhu, L. Zhang, W. Bu, L. Guo, and Y. Chen, “The effect of PEGylation of mesoporous silica nanoparticles on nonspecific binding of serum proteins and cellular responses.,” *Biomaterials*, vol. 31, no. 6, pp. 1085–92, Feb. 2010.

[225] M. Cerruti, S. Fissolo, C. Carraro, C. Ricciardi, A. Majumdar, and R. Maboudian, “Poly(ethylene glycol) monolayer formation and stability on gold and silicon nitride substrates.,” *Langmuir*, vol. 24, no. 19, pp. 10646–53, Oct. 2008.

[226] L. C. P. M. De Smet, D. Ullien, M. Mescher, and E. J. R. Sudhölter, “Organic

Surface Modification of Silicon Nanowire-Based Sensor Devices," in *Organic Surface Modification of Silicon Nanowire-Based Sensor Devices, Nanowires - Implementations and Applications*, no. step 1, 2011, p. 538.

[227] D. E. King, "Oxidation of gold by ultraviolet light and ozone at 25 ° C," *J. Vac. Sci. Technol.A*, vol. 13, no. 3, pp. 1247–1253, 1995.

[228] D. K. Aswal, S. Lenfant, D. Guerin, J. V Yakhmi, and D. Vuillaume, "Self assembled monolayers on silicon for molecular electronics.," *Anal. Chim. Acta*, vol. 568, no. 1–2, pp. 84–108, May 2006.

[229] A. Sarkar and T. Daniels-Race, "Electrophoretic Deposition of Carbon Nanotubes on 3-Amino-Propyl-Triethoxysilane (APTES) Surface Functionalized Silicon Substrates," *Nanomaterials*, vol. 3, no. 2, pp. 272–288, May 2013.

[230] S. Pal, M. J. Kim, and J. M. Song, "Quantitation of surface coverage of oligonucleotides bound to chip surfaces: a fluorescence-based approach using alkaline phosphatase digestion," *Lab Chip*, vol. 8, no. 8, p. 1332, 2008.

[231] J. C. Love, L. a Estroff, J. K. Kriebel, R. G. Nuzzo, and G. M. Whitesides, *Self-assembled monolayers of thiolates on metals as a form of nanotechnology.*, vol. 105, no. 4. 2005.

[232] H. Gro, A. Curioni, and W. Andreoni, "Thiols and Disulfides on the Au (111) Surface : The Headgroup - Gold Interaction," *J. Am. Chem. Soc*, no. 122, pp. 3839–3842, 2000.

[233] H. Häkkinen, "The gold-sulfur interface at the nanoscale.," *Nat. Chem.*, vol. 4, no. 6, pp. 443–55, Jun. 2012.

[234] C. Vericat, M. E. Vela, G. Benitez, P. Carro, and R. C. Salvarezza, "Self-assembled monolayers of thiols and dithiols on gold: new challenges for a well-known system.," *Chem. Soc. Rev.*, vol. 39, no. 5, pp. 1805–34, May 2010.

[235] H. Ron, S. Matlis, and I. Rubinstein, "Self-Assembled Monolayers on Oxidized Metals . 2 . Gold Surface Oxidative Pretreatment , Monolayer Properties , and Depression Formation," vol. 7463, no. 14, pp. 1116–1121, 1998.

[236] C. M. Furdui and L. B. Poole, "Chemical approaches to detect and analyze protein sulfenic acids," *Mass Spectrom. Rev.*, vol. 33, pp. 126–146, 2014.

[237] J. Qian, R. Wani, C. Klomsiri, L. B. Poole, A. W. Tsang, and C. M. Furdui, "A simple and effective strategy for labeling cysteine sulfenic acid in proteins by utilization of β-ketoesters as cleavable probes.," *Chem. Commun. (Camb).*, vol. 48, no. 34, pp. 4091–3, Apr. 2012.

[238] G. Roos and J. Messens, "Protein sulfenic acid formation: from cellular damage to redox regulation.," *Free Radic. Biol. Med.*, vol. 51, no. 2, pp. 314–26, Jul. 2011.

[239] E. Cabiscol, J. Ros, and J. Tamarit, "Oxidative stress in bacteria and protein damage by reactive oxygen species," *Int. Microbiol.*, vol. 3, pp. 3–8, 2000.

[240] M. Misawa and J. Takahashi, "Generation of reactive oxygen species induced by gold nanoparticles under x-ray and UV Irradiations.," *Nanomedicine*, vol. 7, no. 5, pp. 604–14, Oct. 2011.

[241] M. J. S. Spencer and G. L. Nyberg, “Adsorption of silane and methylsilane on gold surfaces,” *Surf. Sci.*, vol. 573, no. 2, pp. 151–168, Dec. 2004.

[242] S. Yochelis, E. Katzir, Y. Kalcheim, V. Gutkin, O. Millo, and Y. Paltiel, “Formation of Au-Silane Bonds,” *J. Nanotechnol.*, vol. 2012, pp. 1–8, 2012.

[243] C. D. Kinz-thompson, M. Palma, D. K. Pulukkunat, D. Chenet, J. Hone, S. J. Wind, and R. L. Gonzalez, “Robustly Passivated, Gold Nanoaperture Arrays for Single- Molecule Fluorescence Microscopy,” *ACS Nano*, vol. 7, no. 9, pp. 8158–8166, 2013.

[244] M. Lynch and T. Furtsch, “Blocking Oriented Monolayers of Alkyl Mercaptans on Gold Electrodes,” vol. XII, no. 8, pp. 409–413, 1987.

[245] R. . Carvalhal, R. . Friere, and L. . Kubota, “Polycrystalline gold electrodes: a comparative study of pretreatment procedures used for cleaning and thiol self-assembly monolayer formation,” *Electroanalysis*, vol. 17, no. 14, pp. 1251–1259, 2005.

[246] H. Ron and I. Rubinstein, “Alkanethiol Monolayers on Preoxidized Gold. Encapsulation of Gold Oxide under an Organic Monolayer,” *Langmuir*, vol. 10, pp. 4566–4573, 1994.

[247] J.-M. Koo, J.-B. Lee, Y. Moon, W.-C. Moon, and S.-B. Jung, “Atmospheric pressure plasma cleaning of gold flip chip bump for ultrasonic flip chip bonding,” *J. Phys. Conf. Ser.*, vol. 100, no. 1, p. 012034, Mar. 2008.

[248] P. R. Selvin, “The renaissance of fluorescence resonance energy transfer,” *Nat. Struct. Biol.*, vol. 7, no. 9, pp. 730–734, 2000.

[249] R. M. Clegg, “Fluorescence resonance energy transfer,” *Curr. Opin. Biotechnol.*, vol. 6, no. 1, pp. 103–110, Jan. 1995.

Appendix

List of the reagents used

Table 1 Reagents required for the nuclear envelope isolation

Name	Concentration/Composition
Barth's solution	88 mM NaCL, 1 mM KCl, 0.41 $CaCl_2$, 10 mM HEPES, 0.33 mM $Ca(NO_3)_2$, 0.82 mM $MgSO_4$, 2.4 mM $NaHCO_3$, pH 7.4
Nuclear isolation medium (NIM)	17 mM NaCl, 90 mM KCl, 10 mM $MgCl_2$, 10 mM TRIS, pH 7.4
Polyvinylpyrrolidone (PVP), 40 kDa, in addition to NIM	1.5% and 8%
Poly-l-Lysine, Mw 150,000-300,000	0.01%
Bovine serum albumin (BSA)	1%

Table 2 Reagents required for the 'wash-out' experiments

Name	Concentration/Composition
Ran-Mix	0.3 µM Ran, 0.3 µM GDP, 0.06 µM NTF2, 0.03 µM RanGAP, 4 nM Ran BP1
E-Mix	0.75 mM ATP, 0.75 mM GTP, 15 mM creatinP, 0.075 mM $Mg(OAC)_2$, 0.075 mM DTT, 0.075 mg/ml creatin kinase in HEPES/KOH pH 7.5
Benzonase®Nuclease	25 units/µl
Rch1-IBB-MBP-GFP, 70 kDa	1 µM
hsImpβ-GFP, 120 kDa	0.5 µM
hsImpβ 90 kDa	0.5 µM
Dextran-Texas Red, 70 kDa	0.2 mg/ml
Wheat Germ Agglutinin (WGA)-Alexa647	0.04 µM
SYBR Gold	1:5000
trans-1,2-cyclohexanediol (CHD)	5%

Table 3 Reagents required for Western Blot analysis

Name	Concentration/Composition
mouse mAb anti-GFP	1:1000
Rabbit anti-Nup153	1:2000
Goat anti-mouse-IRDye 680	1:40 000
Goat anti-rabbit-IRDye 800	1:40 000

Table 4 Reagents required for nanopores preparation and characterisation

Name	Concentration/Composition
HEPES buffer	10 mM KCl, 90 mM HEPES, pH 7.5
NTF2-GFP	100 µg/ml
Nsp1	600 µg/ml
PEG-silane: (2-[Methoxy (polyethyleneoxy)propyl] trimethoxysilane)	40 mg/ml in absolute EtOH
PEG-thiol: HS-C16-EG3-OMe	10 mg/ml in EtOH